Evolution of short-period massive binary stars in the Magellanic Clouds

Dissertation
zur
Erlangung des Doktorgrades (Dr. rer. nat.)
der
Mathematisch-Naturwissenschaftlichen Fakultät
der
Rheinischen Friedrich-Wilhelms-Universität Bonn

vorgelegt von
Koushik Sen
aus
West Bengal, India

Bonn 2022

Two roads diverged in a wood, and I–
I took the one less traveled by,
And that has made all the difference.

— *The Road Not Taken*, Robert Frost

Acknowledgements

There are many people who were an integral part of my academic journey. First of all, I would like to thank my doctoral supervisor, Prof. Dr. Norbert Langer, who gave me the right amount of freedom- to explore the vast expanses of the subject, and direction- to keep me focussed on the major goal of my thesis. Apart from his vast academic wisdom, he has been empathetic during this ongoing COVID-19 pandemic and kept my morale high even though more than half of my thesis work had to be done from home. I would also like to mention some of my collaborators: Xiao-Tian Xu, Ileyk El Mellah, David Ramon Aguilera-Dena, Abel Schootemeijer, Athira Menon and Chen Wang for their help on numerous occasions to carry out this work. Many others have lent their helping hand- Christoph Schurmann, Ben Hastings, Gotz Grafener, Martin Quast, Pablo Marchant, Selma De Mink, Laurent Mahy, Nathan Grin- to make my thesis stand where it is today. Thanks as well to all the past and present members of the stellar group in Bonn and Leuven for the countless discussions, fun and healthy work environment. Thanks also to members of the lunch crew for quite the interesting discussions! Thank you to Elisabeth Kramer and Sabine Derdau for always making me feel welcome right from my first day in Bonn.

My heartfelt gratitude goes towards two very special individuals- Joachim Puls and Rodrigo Fernandez, who, not only gave me the opportunity but also mentored me towards pursuing a career in the field of Astronomy during my undergraduate days. On a similar line of thought, I want to thank Debashish Nath, Kripa Sindhu Ballav, Basab Ranjan Bhattacharya for making me excited about science in general since my school days. The memories of you grinding with us through evenings of no electricity to get us kids like me educated are humbling to say the least, and will always serve as a reminder to keep my feet grounded and strive to get better.

Beyond my professional life, I thank my parents Jaya Sen and Asish Sen, my partner Shalini Sengupta, my brother Souparno Sen and sister Debeshi Sen for their neverending patience and emotional support during the last three years, and especially during the pandemic for keeping me mentally healthy and functioning properly. I thank the members of the Soccer Centre Bonn, the Pokemon Go community of Bonn, the members of the various Counter-Strike Global Offensive groups I am a part of, T90's Age of Empires II community and Agadmator's chess community for always making my after-work hours fun, entertaining and enjoyable. A big thank you to the members of the IMPRS- Kevin, Prajwal, Vishnu, Madhuri, Parichay, Surya for the numerous hangouts we had during my stay. Then there are my gym buddies- Shalini, Abel, David, Patrick and Xiao-Tian for providing each other with mutual motivation to go the gym regularly and take care of our physical well-being, when it was possible to do so.

Last but not the least, thank you to all my friends from my college and school days- Arinjoy, Hillol, Gaurav, Sweta, Gokul, Jayanta, Aneesh, Amit, Tathagata, Kunal, Dibyojoti, Arijit, Arkaprabha, Moloy, Mohanto, Srijeet, Bijay, Baibhav, Rijul, Sarbartha, Sankarsan, Debaditya, the 'Subham' pair, Angshuman, Ankit, Souparno, Sayan, Aakash, Anirban, Poulam and Arijit- for, well, making my life a life-long comedy! Honestly, I would not have it any other way.

Abstract

Massive stars play a central role in the evolution of the Universe. They enrich the interstellar medium with matter via strong winds and highly energetic transient events, thereby influencing the evolution of their host galaxies. However, massive star evolution is riddled with sparsely understood uncertainties. Recent observational studies have revealed that massive stars form in binaries that can interact during their lifetime, further complicating their evolution.

Depending on the mass, up to two-thirds of them are so close that they undergo mass transfer during core hydrogen burning and yield most of the observable post-interaction binaries. Of particular interest are the observed Algol binaries that are thought to be undergoing nuclear timescale mass transfer from a less massive star to a more massive star. Since rapid binary evolution codes cannot provide accurate predictions for these systems, we study them here using large grids of detailed binary evolution models that include internal differential rotation and magnetic angular momentum transport, time-dependent tidal coupling, and a self-consistently derived mass and angular momentum transfer prescription.

Through follow-up population synthesis, we derive the observable properties of massive Algol binaries, Wolf-Rayet/helium star binaries, black hole/neutron star binaries, pre-supernova stars and their companions, both for constant star formation and for coeval populations. We find that our tide and spin dependant mass transfer efficiency model can reproduce most properties of the observed massive Algol binaries, while a purely conservative or non-conservative model does not.

Using state-of-the-art prescriptions to decide the fate of massive stars upon core collapse, we predict the position of the neutron star or black hole progenitors and their companions on the Hertzsprung-Russell diagram to aid the large observational efforts recently undertaken to search for these supernovae and their progenitors. We also look at the expected number and properties of compact object binaries in a coeval population of binary stars as a function of their age.

Finally, we find that Bondi-Hoyle wind accretion in our black hole+O star binary models is expected to lead to observable X-ray emission only in exceptionally favourable cases such as high angular momentum accretion efficiency and low wind velocities, and is biased towards binaries with rapidly spinning black holes. Our results provide important constraints for the evolution of massive binaries towards detectable gravitational wave sources.

Contents

Introduction

1.1 A brief history of astronomy

The word 'astronomy' comes from a Greek word $\alpha\sigma\tau\rho\text{o}\nu\text{o}\mu\iota\alpha$ that means the science of the laws of the stars. Despite its originally limited definition, the word now encompasses the study of everything that we can see in the sky, not just via our naked eyes but also via modern-day telescopes, such as the inter-stellar medium, galaxies and transients. It is considered to be one of the oldest of the natural sciences, where we apply the knowledge gained from various other branches of science such as the likes of physics and chemistry to explain the things we see in the sky.

The earliest civilizations in recorded history, such as the Babylonians, Greeks, Indians, Egyptians, Chinese and Mayans are known to have used astronomy, or more precisely- the position of stars for navigation and making calenders. They also associated celestial objects with Gods, as seen from the names of constellations. They also associated Earthly phenomena such as rain, floods, droughts, tides and seasons to the movement of stars and believed them to be a manifestation of the Divine. Although their belief was unscientific, some phenomena like the changing of seasons and tides are indeed linked to the movement of the Sun and Moon around the Earth.

The earliest Babylonian star catalogues date back to 1200 BC, while indirect evidence of Sumerian astronomy dating back to 3000 BC comes from a unique form of writing known as the *cuneiform*. The importance given to celestial Gods in mythology and religion started from the Sumerians, as well as the modern concensus of dividing a circle into 360 degrees and an hour into 60 minutes. During the reign of Nabonassar and also during the Seleucid Empire, there was a significant rise in Babylonian observational astronomy where they discovered the existence of a periodicity in the lunar eclipse. Mathematical models were constructed that could predict the future occurence of periodic events, without having to base their prediction on past observations.

Indian astronomy started during the Indus Valley civilization (Ashfaque, 1977). The first written record of Indian astronomy is the text *Vedanga Jotisha* from the Vedic period, where the motion of Sun and Moon is described for ritualistic purposes. Many star catalogues were produced during the Shunga Empire, also known as the 'golden age of Indian astronomy'. Many calculations of the motion of planets, their conjunction and eclipses were developed during this period. Aryabhatta, in his book *Aryabhatiya*, accurately calculated the orbital period of planets, solar-lunar eclipse timescales and the instantaneous motion of the Moon. By the 6th century, Indian astronomers had estimated the periods of some comets, but the accuracy of their estimates are unknown. In the 11th century, Bhaskara II,

Figure 1.1: *Left panel:* The historical Jantar Mantar observatory in Jaipur, India. *Right panel:* The Antikythera Mechanism was an analog computer from 150–100 BC designed to calculate the positions of astronomical objects. Credits: Wikipedia, Marsyas

who was the head of the Ujjain astronomical observatory, calculated the orbital period of the Earth around the Sun to nine decimal places. The very famous Nalanda University where many scholars from around the world came to study, offered formal astronomical courses.

The ancient Greeks treated astronomy as a branch of mathematics. They developed sophisticated geometrical, three-dimensional models to explain the motion of the planets already in the fourth century BC. The likes of Plato and Aristotle proposed the first cosmological models: the Universe is a spherical body that is divided into circles that carry the planets (Plato), or the Universe is a series of concentric spheres (Aristotle) whose motion would make planets move about each other. The multi-talented Erastothenes estimated the circumference of the Earth to great accuracy (Pedersen, *Early Physics and Astronomy*). Depending on one's viewpoint, the peak or corruption of ancient Greek astronomy came with Ptolemy of Alexandria, who postulated that the Universe is centered around the Earth. This geocentric model had a long-lasting impact on astronomy up to the age of Renaissance.

The Renaissance period saw a revolution in the field of astronomy, as in many other disciplines, starting with Nicolaus Copernicus who proposed the heliocentric model of our solar system. In the beginning, this view gained a lot of traction because a lot of notable figures like Galileo Galilei, Johannes Kepler and Isaac Newton improved upon this work. However, in the long term, this claim created a lot of controversies, not only with the church, but also some well-known astronomers such as Tycho Brahe did not completely adopt this theory. Tycho Brahe created his own system, the Tychonic system, where the Sun and Moon and the stars revolve around the Earth, but the other five planets revolve around the Sun. It was after the death of Brahe, and after a lot of religious and political struggles, that Kepler was able to publish his, now famous, laws of planetary motion.

Galileo was the first person to make his own telescope and discovered that the Moon has craters, Jupiter has moons, the Sun has spots, and Venus has phases like the Moon. It was most unfortunate that Galileo had to spend a considerable fraction of his late life trying to fight against the Catholic

Church, who accused him of heresy, banned his book, and put him under house arrest until he died in 1642. Isaac Newton established further connections between physics and astronomy, via his theory of gravitation and derived Kepler's laws from first principles in his book *Principia Mathematica*.

This brings us to the astronomy in the 19th century, when Joseph von Fraunhofer discovered that sunlight consists of a variety of spectral lines when dispersed, and the same lines could be observed in the spectra of gas lamps, where different lines correspond to different elements. Cecilia Payne discovered that the composition of the Sun was different from that of the Earth, and that hydrogen is the most abundant element in the Universe. Her thesis was hailed as 'the most brilliant Ph.D. thesis ever written in astronomy' by Otto Strauve.

Modern astronomy is now divided into many subsections based on the part of the electromagnetic spectrum used to observe celestial objects, namely, optical astronomy (uses the visible part of the spectrum), radio astronomy (measurements are taken at radio wavelengths), infrared astronomy (for objects that mostly emit in infrared), ultraviolet, X-ray and gamma ray astronomy. Recently, two more branches are emerging: neutrino astronomy (that records neutrinos emitted from celestial sources) and gravitational wave astronomy (that observes ripples in space-time caused by gravitational waves).

1.2 Stars, stellar equilibrium and timescales

Stars are self-gravitating balls of gas that radiate energy from internal sources. The two most common sources of energy in stars are the nuclear fusion of lighter elements into heavier elements, which releases nuclear energy, and the gravitational contraction of the star, which releases potential energy. For a large fraction of the lifetime of the star, the energy per unit volume or pressure gradient generated from burning nuclear fuel at the core of the star balance the force of gravity. Applying momentum and energy conservation, we show below two different types of equilibrium in stars.

The long life-time of a star compared to the time-span of observation of a star implies no noticable acceleration of an unit mass inside the star within timescales of human lifetimes. The sum of all forces acting on any unit volume inside the star balance each other. In such a situation, the star is said to be in a state of mechanical or hydrostatic equilibrium. For a star in hydrostatic equilibrium, when the internal energy sources inside a star due to nuclear burning can compensate for the energy radiated from the surface of the star, the star is said to be in thermal equilibrium. Assuming the star to be made of ideal gas, which is typically true in most stars, the virial theorem can be used to show that the star remains in a stationary state, it neither contracts nor expands.

Based on these two equilibriums, three different timescales are relevant in stellar evolution. These timescales are based on changes to the mechanical structure of the star, the thermal structure of the star, or change in composition of the star. When the force balance equation is violated, changes to the hydrostatic structure of the star take place in what we call the dynamical timescale. If the internal pressure of the star is suddenly removed, the star is expected to collapse under its own gravity. Thus, the dynamical timescale (τ_{dyn}) can be approximated by

$$\tau_{\mathrm{dyn}} \sim \sqrt{R/g} \sim \sqrt{R^3/GM} \approx 5 \times 10^{-5} \left(\frac{M}{M_\odot}\right)^{-1/2} \left(\frac{R}{R_\odot}\right)^{3/2} yr \qquad (1.1)$$

where R and M are the radius and mass of the star and G is the gravitational constant. For the Sun, this turns out to be ~1600 sec. In comparison, the current age of the Sun is 4.6 Gyrs or ~1.5 X 10^{17} sec.

The second timescale describes how a star in thermal equilibrium reacts when perturbed. To obtain an estimate of the thermal timescale, we note that a star without a nuclear energy source will contract by radiating away its internal energy. For a star made up of ideal gas, the timescale on which this thermal contraction will occur is then approximated by

$$\tau_{th} = \frac{E_{int}}{L} \approx \frac{GM^2}{2RL} \approx 1.5 \times 10^7 \left(\frac{M}{M_\odot}\right)^2 \frac{R_\odot}{R} \frac{L_\odot}{L} yr, \tag{1.2}$$

where L is the luminosity of the star. A few phases of stellar evolution, such as the contraction of the star after core hydrogen burning, where the nuclear burning is nearly absent to keep thermal equilibrium, occur at the thermal timescale.

A star can stay in thermal equilibrium as long as the nuclear fuel in its center lasts. The timescale of this nuclear burning is called the nuclear timescale. Since nuclear burning turns lighter elements into heavier elements, this is also the timescale at which composition changes occur in the core of the star (composition changes at the surface of the star can occur due to various other factors). The nuclear timescale is given by

$$\tau_{nuc} = \phi f_{nuc} \frac{Mc^2}{L} \approx 10^{10} \frac{M}{M_\odot} \frac{L_\odot}{L} yr \tag{1.3}$$

where ϕ is the fraction of rest mass of the nuclear fuel converted to its equivalent energy, f_{nuc} is the fraction of the mass of the star that can be burnt as nuclear fuel. The last approximation holds for a star that is burning hydrogen at the core. Hence, we see that $\tau_{dyn} \ll \tau_{th} \ll \tau_{nuc}$.

1.3 Massive stars

Stars that are significantly heavier than our Sun, typically more than ~eight times more massive are called massive stars. The study of massive stars is of central importance in the field of astrophysics (Langer, 2012; Crowther, 2019). Owing to their high surface temperatures and luminosity, massive stars give out ionising radiation and strong stellar winds, respectively, that influence the evolution of star-forming galaxies by polluting the interstellar medium, providing chemical enrichment and mechanical feedback to its environment (Mac Low et al., 2004; Hopkins et al., 2014; Crowther et al., 2016). It has also been shown that massive stars might have played a role in re-ionising the Universe (Haiman et al., 1997), even before galaxies were formed.

Most massive stars end their lives producing highly energetic transient events such as an ordinary or superluminous supernova (except Type Ia supernovae) and gamma ray bursts (Smartt, 2009; Smith et al., 2011; Quimby et al., 2011; Aguilera-Dena et al., 2018), signifying that a neutron star is born (Heger et al., 2003; Metzger et al., 2017) and enrich the interstellar medium with elements heavier than iron (Hoyle et al., 1960). As we can see, it is very important for many avenues of astrophysics to use accurate and reliable models of massive stars.

1.3.1 Evolution of massive stars

To understand the life of a massive star, we explain its evolution on the Hertzsprung-Russell diagram (H. N. Russell, 1914) and point out the salient features and phases of its life by using Fig. 1.2 as an
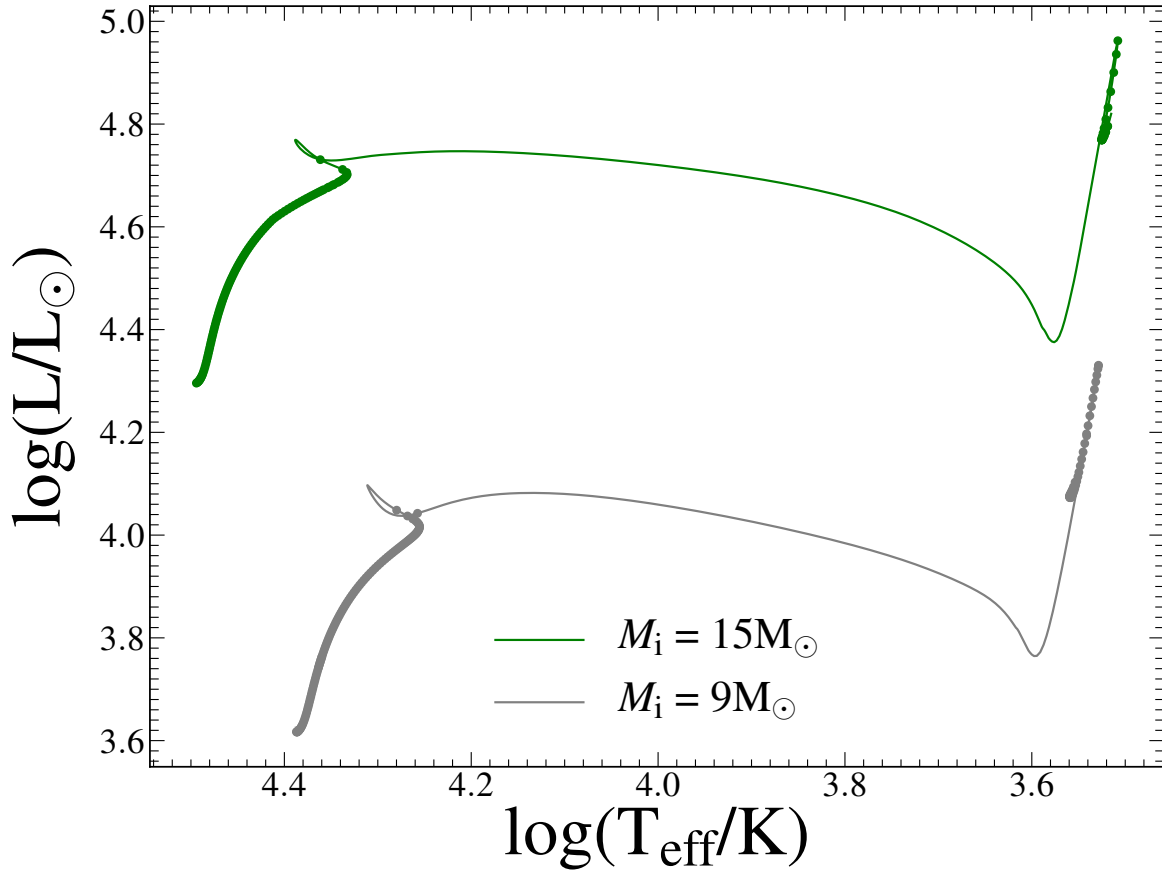
Figure 1.2: Hertzsprung-Russell diagram showing the evolution of two massive stars of masses 15 $M_\odot$ (green) and 9 $M_\odot$ (gray). The Y-axis shows the logarithm of the stellar luminosity in units of solar luminosity and the X-axis shows the logarithm of the surface temperature of the star in Kelvin. Circles on the evolutionary tracks are plotted at every 50,000 years of the lifetime of the star.

example.

New stars form from the gravitational collapse of giant molecular clouds present within galaxies, alternatively called star forming regions. Depending on the various physical properties of different star forming regions, the rates of star formation may vary. Thousands of stars can form from a single giant molecular cloud, and are thought to have the same initial composition and age, forming a gravitationally bound group of stars known as a star cluster. The collapse of gaint molecular clouds is triggered as soon as the internal pressure of the molecular cloud is unable to counteract the force of gravity (Jeans instability, Jeans, 1902). This cloud of gas keeps collapsing and the interior of the star keeps heating up. The radius of this cloud keeps decreasing until the core of the collapsing gas is hot enough to ignite hydrogen at the core, at which point the gravitational force is balanced by the pressure gradient generated due to core hydrogen burning. The onset of core hydrogen burning is usually referred to as the zero age main sequence (ZAMS) of the star (bottom left of the evolutionary tracks in Fig. 1.2). Depending on the mass of the star, the luminosity and effective temperature at ZAMS is different (compare green and gray tracks in Fig. 1.2). Corresponding to their different surface

temperatures, stars come in different flavours- based on their spectral types they are classified into O, B, A, F, G, K, M. Stars spend most of their lifetime burning hydrogen and constitute the main sequnce in the HR diagram (thick line formed after ZAMS by the superposition of circles in each track of Fig. 1.2).

The theory of stellar structure and evolution is based on five simplifying assumptions that lead to five coupled differential equations. They are then solved numerically with various boundary conditions motivated by physical assumptions. The assumptions generally used to model stellar evolution are:

1. Stars are self-gravitating, hot spherical balls of gas.

2. Stars are in hydrostatic equilibrium, where the pressure gradient inside the star balances gravity.

3. Stars are in global thermal equilibrium, where the rate of energy lost from the surface is the same as the rate of energy generation in the interior of the star.

4. Stars are in local thermal equilibrium, where the energy generated in the interior is transported to outer layers via radiative diffusion or convective motion.

5. The initial chemical composition of the star is the same as the molecular cloud it formed from, and the composition slowly changes due to nuclear burning and various mixing processes inside the star.

Given an equation of state which describes the relation between different thermodynamic variables inside the star, a prescription for calculating opacity (determines how much light is absorbed by the gas inside the star), the nuclear reaction rates and the assumed mass loss rate from the star, one can fully determine the structure of a star and try to explain the life of many types of stars.

As the stars evolve, nuclear reactions at the core of the star continually turn lighter elements to heavier elements. Thus the composition of the interior of the star gradually changes from hydrogen and helium to elements heavier than them, namely carbon, oxygen, nitrogen, magnesium, etc. Due to various mixing processes arising from convection or rotational circulation, some of the heavier elements can be churned out to the surface which then can be lost from the star via stellar winds, especially in massive stars. As the strength of stellar winds scale with luminosity, massive stars are considered as one of the key agents of polluting the interstellar medium with elements heavier than He- collectively also called 'metals' in astronomy.

The rate of nuclear fuel burning is set by the combined efforts of the electromagnetic force of repulsion, the thermal properties of the gas and and the quantum tunneling probability. It was the quantum tunneling probabilility that resolved the question of nuclear fuel burning in stars. Accordingly, the reaction rates are very sensitive to the density of the nuclear fuel and the temperature of the gas, that sets the velocity distribution of the gas particles. Hydrogen burning in stars occurs via two reactions: the proton-proton or PP chain, and the carbon-nitrogen-oxygen or CNO cycle. For stars below $1.4\,M_\odot$, nuclear burning occurs mainly via the PP chain while for stars above $1.4\,M_\odot$, most of the hydrogen fuel is burnt via the CNO cycle. Both reactions eventually convert four hydrogen atoms into a helium atom with an associated release of energy, but the intermediate steps are vastly different. In the CNO cycle, the sum of the abundances of carbon, oxygen and nitrogen remain same, but their relative abundance changes before CNO equilibrium is reached, with more nitrogen being produced at the expense of carbon and oxygen. Once CNO equilibrium is reached, which happens very soon after the onset of hydrogen burning in massive stars, the relative abundances of carbon, nitrogen and

oxygen also get fixed to the CNO equilibrium values. Since the hydrogen burning phase is the longest in the lifetime of the star, the main sequence is the most populated region of the HR diagram.

When all the hydrogen in the core is converted into helium, thermal equilibrium is disrupted as no energy is generated in the core from nuclear reactions that can sustain the rate of energy lost from the surface. Hence, at the end of core hydrogen burning, the star contracts (see the small leftward transition of the evolutionary tracks after the end of the main sequence in Fig. 1.2). As the star contracts, the region around the now inert helium core starts getting hotter until it is hot enough to burn hydrogen in a shell around the contracting helium core (hook feature in Fig. 1.2). This results in the increase of the helium core mass, as more helium is added to the core from the burning hydrogen shell. However, the helium core keeps contracting as there is no nuclear burning to counterbalance gravity in the core. Stars during this phase move from the main sequence branch to the giant and supergiant branch (see rapid transition of the evolutionary track for hot to cool temperatures in Fig. 1.2). This phase is much shorter than the main sequence phase as it occurs at the thermal timescale.

If the helium core is massive enough, the temperature inside the star core will get high enough for helium to get ignited. Helium burning proceeds via the so-called triple alpha process, where one carbon nucleus is created from three helium nuclei. A secondary process also converts some of the carbon to oxygen, creating a carbon-oxygen core as the outcome of core helium burning. During the helium burning lifetime, the stars occupy the giant and supergiant branch in the HR diagram (see cluster of circles on the far right-side of the evolutionary tracks). The helium burning lifetime is ~10% of the hydrogen burning lifetime due to the fact that the mass of the helium core that a star burns is smaller the the core mass during hydrogen burning, as well as the fact that nuclear reactions of elements heavier than hydrogen are decreasingly less efficient at producing energy through fusion.

If the star is massive enough, their carbon-oxygen core begins to burn first carbon, then neon, then oxygen and finally silicon. This chain of core burning reactions produce a core of iron, with layers of less heavy elements in shells around the core. The burning process is accelerated at each phase, and silicon burning only takes one day. However, the chain ends at iron because fusing iron to create more heavier elements actually requires energy, instead of releasing energy. As soon as the iron core forms, there is no further support against gravity and the core starts to collapse. This results in the formation of neutron stars or black holes, depending minutely on the structure of the star prior to core collapse. It is these stars that form either a neutron star or a black hole that we call 'massive stars' and is one of the central components of this thesis.

1.3.2 Wolf-Rayet stars

Wolf-Rayet stars (Murdin, 2000) are a class of stars that show prominent broad emission lines of ionised helium, nitrogen, carbon and/or oxygen (A. Fowler, 1912; Beals, 1929). Classical Wolf-Rayet stars show significantly high enhancement of heavier elements than hydrogen and helium at their stellar surface and have very strong stellar winds. They are conventionally thought to be core helium burning stars that have optically thick winds (*Wolf-Rayet stars: Observations, physics, evolution* 1982). This is because many of them were observed to be much hotter than main sequence stars (Beals, 1940). Based on the spectral signature, they are broadly classified into WN (nitrogen rich, see Hamann et al., 2006), WC (carbon rich, see Sander et al., 2012) and WO (oxygen-rich, see Barlow et al., 1982) subtypes. However, recent studies have shown that some of the observed hydrogen-rich WN stars can also be core hydrogen burning stars (de Koter et al., 1997; Martins et al., 2013). Hence, it is of utmost importance to explain the origin of the various subclasses of these stars through detailed

stellar models.

1.3.3 Supernovae

The majority of massive stars are expected to end their lives in a spectacular explosion called the supernova. Supernovae constitute an important part of this thesis, so we discuss them in some detail here. Supernovae have been observed since ancient history, due to their spectacular brightness which can rival that of an entire galaxy.

Supernovae are observed both via photometry and spectroscopy. The photometric observations are used to study how their brightness changes as a function of time, called their light-curve. One can obtain the total radiative energy released in a supernova by integrating the light-curve. Studying the photometric light curve and the spectroscopic features of a supernova provides provides clues about how the explosion is powered and how it interacts with its environment. They are now routinely discovered by large-scale supernova surveys such as the Zwicky Transient Factory, etc.

The spectroscopic classification of supernovae (Filippenko, 1997) distinguishes supernova based on the presence of hydrogen and helium in their spectral lines. Type I supernovae do not show hydrogen lines at maximum brightness while Type II supernovae show hydrogen lines at maximum brightness. Type Ia supernovae also show silicon lines, while Type Ib supernovae show strong helium lines and Type Ic supernovae does not even show helium lines in its spectra. The absence of the most abundant elements in the Universe, hydrogen and helium, make Type Ic supernovae very intriguing objects for detailed observational and theoretical studies.

Type II supernovae are also subdivided based on their light curves. Type IIp supernovae show a plateau in their light curve after maximum brightness. Type IIL supernovae light curves show a linear decay after peak brightness. Recently, a new subclass of supernovae has been abundantly discovered: Type IIb supernovae that shows the spectra of ordinary Type II supernovae at early times, but their spectra changes to that of Type Ib supernovae at late times. This Type IIb supernovae, along with Type Ib and Type Ic supernovae constitute the family of stripped-envelope supernovae, that are believed to originate majorly from massive binaries, especially at low metallicity.

In addition to these typical types of supernova, a host of exotic transients have been discovered recently. One of them is the so-called superluminous supernovae (Gal-Yam, 2012) that are 10-100 times brighter than ordinary supernovae. These are also subdivided into Type I and Type II, based on the presence of hydrogen and helium in their light curves. Another class of transients are gamma-ray bursts, whose discovery has a very interesting story. They were discovered by chance during the Cold War by military satellites employed to search for nuclear warhead testing. They are further classified into short and long gamma-ray bursts. Short gamma-ray bursts have been recently confirmed to orginate from the merger of two neutron stars (Ruffert et al., 1998) while long gamma-ray bursts are associated with the death of massive stars, with the most likely explanation being that they are also associated with the formation of magnetars.

1.3.4 Neutron stars and black holes

After a supernova event, a variety of remnants can be formed. The core of the star can contract until it reaches a radius of ~10 kms after which neutron degeneracy pressure halts further collapse of the core, leading to the formation of an object that is over 10^{14} times the density of water at normal temperature and pressure. These objects are called neutron stars (Baade et al., 1934) because they are

composed of neutrons and their gravitational collapse is balanced by the neutron degeneracy pressure. The general consensus is that neutron stars are formed from massive stars having masses between 8-20 $M_\odot$ (O'Connor et al., 2011a; Ertl et al., 2016), although, as recently found out, the explodability of stars depend complexly on the interior structure of the star prior to core collapse (see, for e.g., Sukhbold et al., 2016; Woosley et al., 2020).

Recently, a lot of work has been done to understand the collapse of massive stars (O'Connor et al., 2011b; Ugliano et al., 2012; Ertl et al., 2016; Müller et al., 2016; Sukhbold et al., 2018; Ertl et al., 2020; Woosley et al., 2020). These works have lead to the theoretical prediction of the existence of "islands of explodability", which are mass ranges in the continuous mass spectrum of very massive stars where neutron stars may form instead of a black hole. It has also been shown that the mass range of pulsational pair-instability supernova can vary based on various physics assumptions (Farmer et al., 2016).

On the other hand, if the core is so massive such that even neutron degeneracy pressure cannot halt the gravitational collapse, the entire star may collapse to form an object from which even light cannot escape. Such objects are called black holes. The formation of black holes may not even be associated with a energetic event (Heger et al., 2003), but the star might just vanish from the sky as it collapses into a black hole. Last but not the least, it may also be possible that the explosion of a massive star does not leave any remnant at all, as in the case of pair-instability supernova (W. A. Fowler et al., 1964; Langer, 2009; Kozyreva et al., 2014), where the pressure support in massive oxygen cores are suddenly removed due to the creation of electron-positron pairs. This leads to the collapse of the oxygen core, and a subsequent thermonuclear explosion of the oxygen core due to explosive oxygen burning that completely disrupts the star, leaving behind no remnant.

1.3.5 Uncertainties in massive star evolution

Despite the success of stellar modelling towards explaining most of the important features on the HR diagram, a lot of unconstrained physics still pervade the theory of stellar evolution. Here, we discuss a few important ones that are present in massive single star evolution.

Internal mixing processes

Internal mixing processes such as semiconvection, convective overshooting and meridonial circulation (due to rotation) are calibrated via indirect methods because we cannot peek into the interior of the stars directly. Recent developments in astroseismology has revealed many important aspects, especially regarding the extent of convective overshooting, but the picture is far from complete (Bowman, 2020). Especially in massive stars, studies have shown that a significant amount of overshooting is necessary to explain the evolution of log g vs $v \sin i$ and the extent of the main sequence band (Brott et al., 2011; Castro et al., 2014). Recent work has also revealed that a mass dependent parameterization of convective overshooting explains the observations more accurately (Claret et al., 2019).

To explain the fractional number of blue to red supergiants in the Small Magellanic Cloud, it has recently been found that a high semiconvective efficiency is preferred (Schootemeijer et al., 2019). Semiconvective mixing efficiency not only influences the evolution of single stars, but also of binaries. A high semiconvective efficiency leads to mass accretors of binaries to rejuvenate (Braun et al., 1995), that is, the mixing of additional hydrogen in the convective core that increases the size of their core and the central hydrogen mass fraction.

Wind mass loss rates

The wind mass loss rates of massive stars are emperically calibrated based on observations (see, for e.g., Muijres et al., 2012). However, there is still a lack of clear consensus on the mass loss rates of stars during each phase of stellar evolution, especially during the post mass transfer phases (see, for e.g., review by Smith, 2014). The red supergiant and Wolf-Rayet mass-loss rates have uncertainty of an order of magnitude, with various studies proposing their own 'best-fit' mass-loss rates for these phases. The wind mass-loss rates affect the amount of material lost to the interstellar medium prior to core collapse, and determine the type of Wolf-Rayet spectrum observed and the fraction of the Wolf-Rayet lifetime it is observed for.

1.4 Massive binary evolution

When two stars are so close that they revolve around each other under the influence of each others gravitational force of attraction, they are called to exist as a stellar binary. Recent photometric and spectroscopic surveys of massive stars have revealed that most massive stars prefer to form in binaries (Sana et al., 2012; Moe et al., 2017; Banyard et al., 2021), with the binary fraction increasing with increase in mass of the massive stars (Moe et al., 2017). This has the implication that understanding massive star evolution gets further complicated as these stars in binaries can interact with their companion, and significantly alter their observable properties (Podsiadlowski et al., 1992; de Mink et al., 2013). Since 50-90% of massive stars are in binaries, almost all properties of massive stars have to be explained keeping in mind the contribution from binary evolution.

From emperical observations (Sana et al., 2012; Sana et al., 2013), it has been found that short orbital period binaries are more abundant than long orbital period binaries, even after accounting for an observational bias. As stars are known to get larger in radius with age, one of the stars is expected to expand to such a large radius that the outer layers of the star will be attracted more strongly by its companion. As a result, some of the material of one star will get transferred to the other star.

1.4.1 Geometry and the Roche lobe

The initially more massive star is called the primary (denoted by M_1) and the less massive star is called the secondary (denoted by M_2). The mass ratio (q) of the binary is defined as the mass of the secondary to the mass of the primary (q = M_2/M_1). The orbital separation is denoted by a, orbital period by P, orbital angular frequency by ω and the total mass of the system is denoted by $M_T = M_1 + M_2$. Kepler's laws can be written as

$$\omega^2 = \left(\frac{2\pi}{P}\right)^2 \frac{GM_T}{a^3}, \text{ or} \tag{1.4}$$

$$P = \left(\frac{4\pi^2}{GM_T}\right)^{1/2} a^{3/2}. \tag{1.5}$$

The total potential in a frame co-rotating with the binary components is called the Roche potential
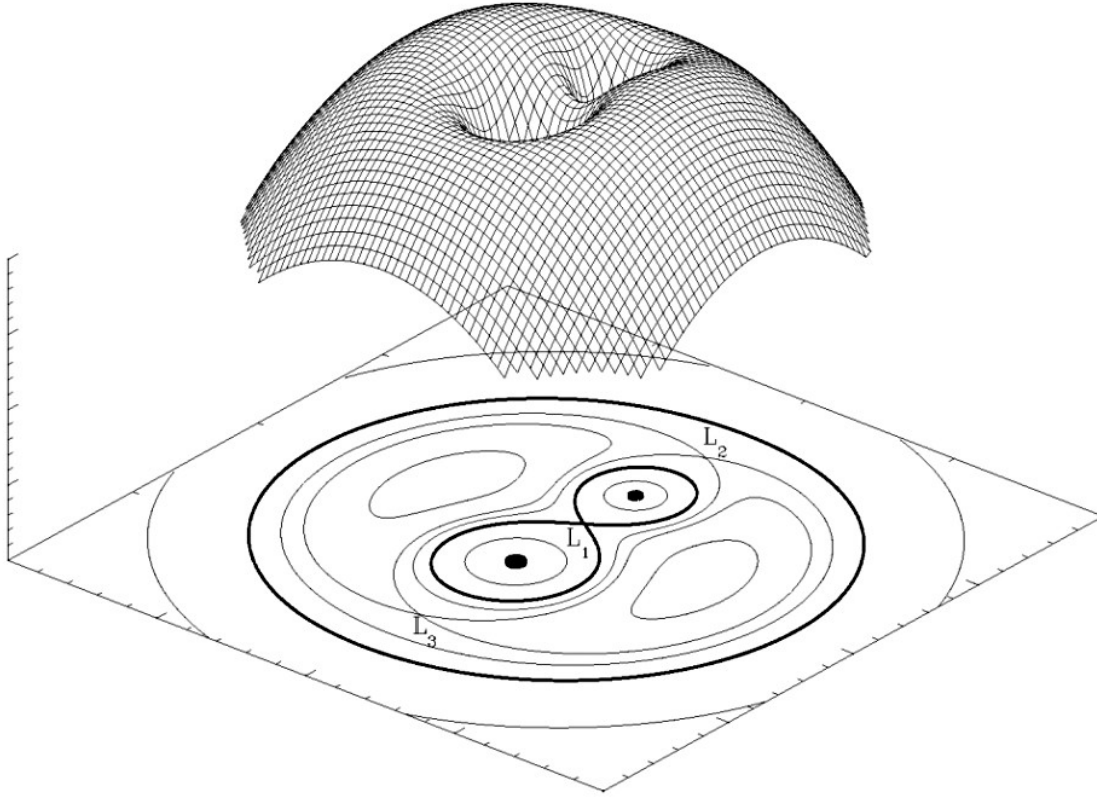
Figure 1.3: Roche potential for a binary with mass ratio of two. The droplet-shaped equipotential curve engulfing both the stars consititutes the Roche lobes of both stars (thick lines, with the more massive star having the larger lobe). The points L1, L2 and L3 are the Lagrangian points where forces cancel (L2 lies behind the lower-mass companion). Credits: Marc van der Sluys, Ph.D. thesis.

and is given by

$$\Phi_{\text{roche}}(\vec{r}) = -\frac{GM_1}{|\vec{r} - \vec{r_1}|} - \frac{GM_2}{|\vec{r} - \vec{r_2}|} - \frac{1}{2}(\vec{\omega} \times \vec{r})^2 \tag{1.6}$$

where $\vec{r}$ is any arbitrary point from the origin, $\vec{r_1}$ and $\vec{r_2}$ are the positions of the two stars with respect to the origin and the last term denotes the centrifugal force due to rotation. The negative gradient of this potential will then give the force on a test particle placed at $\vec{r}$.

Figure 1.3 shows the equipotential curves of the Roche potential given by the above equation. Notably, we see one equipotential curve that just engulfs both the stars (bold). The point of intersection is called the first Lagrangian point (L1) and the almond shaped curves crossing through the point L1 defines the Roche volumes of the two stars. A particle placed at the L1 point is attracted by both the stars with equal force. Hence, if a star expands such that its radius exceeds the L1 point, also called the Roche lobe radius, the matter will fall under the gravity of the other star onto its surface. This is called Roche lobe overflow, and is the central idea behind mass transfer in binaries.

Eggleton (1983) derived an approximation for estimating the Roche lobe radius, defining $R_{\text{Roche, i}}$ to be the radius of a sphere around star i (i = 1 or 2) that has the same volume as its Roche volume. This

is given by

$$\frac{R_{\text{Roche, i}}}{a} \approx \frac{0.49 q_i^{2/3}}{0.6 q_i^{2/3} + \ln(1 + q_i^{1/3})}.$$

(1.7)

Here $q_i = M_i/M_{2-i}$. This equation hence defines an equivalent radius of the Roche volume a star needs to fill such that it overflows its Roche lobe, to an accuracy of 1%. This is particularly useful for stellar evolution codes that are written in one dimension.

1.4.2 Mass transfer

In the rest of this thesis, we will call the primary star as the donor star and the secondary star as the accretor star. The transfer of mass from the donor to the accretor occurs when the donor fills its Roche lobe, and the mass transfer rate is usually set by the timescale of the instability occuring in the donor star. Intrinsically, mass transfer can happen at the dynamical, thermal or nuclear timescale of the donor. Mass transfer can also be driven by extrinsic factors such as loss of angular momentum leading to shortening of orbit. Loss of angular momentum can happen via mass-loss, gravitational waves, magnetic braking or tidal dissipation.

1.4.3 Types of mass transfer

Depending on the time at which the donor star fills its Roche lobe and transfers mass to the accretor, mass transfer can be divided into four types:

Case A mass transfer

When the donor fills its Roche lobe while it is in its core hydrogen burning phase, it is called Case A mass transfer. The first mass transfer phase occurs at the thermal timescale, followed by a slow nuclear timescale mass transfer that lasts upto core hydrogen depletion of the donor. Models in the slow mass transfer phase are thought to be the theoretical counterparts to observed Algol binaries where the currently less massive star is filling its Roche lobe. A detailed description of this mass transfer phase can be found in Chapter 2 (see also, Nelson et al., 2001; de Mink et al., 2007; Mennekens et al., 2017).

Case B mass transfer

For longer orbital period binaries, the donor can only fill its Roche lobe when it completes core hydrogen burning and expands rapidly to the supergiant phase. This leads to the donor filling its Roche lobe and a thermal timescale mass transfer phase occurs where the donor almost completely loses its hydrogen envelope. In Case A systems too, as soon as the donor completes core hydrogen burning, it is also expected to undergo another mass transfer phase, referred to as the Case AB mass transfer phase.

Case C mass transfer

For a very small number of binaries where their orbital separation is large enough such that the donor can avoid filling its Roche lobe after core hydrogen depletion, the donor again expands after core helium depletion. If at this stage, the donor can fill its Roche lobe, then the mass transfer phase is

called the Case C mass transfer phase. For high mass stars, the orbital period range where this happens is very narrow and decreases with increasing mass of the donor star.

Wind accretion

Even if the donor does not fill its Roche lobe, mass transfer can occur in binaries when the companion star can capture a significant portion of the wind of the donor star. Mohamed et al. (2007) showed that this is efficient only when the wind acceleration region lies close to the Roche lobe of the donor.

1.4.4 Stability of mass transfer

The stability of mass transfer depends on the reaction of the radius of the mass donor to the mass loss. This is usually expressed in terms of the logarithmic mass derivative of the logarithm of the radius such that $R(M) \sim M^{\xi}$ and ξ is then given by (Soberman et al., 1997)

$$\xi = \left(\frac{d\log R}{d\log M} \right).$$

(1.8)

From the physical point of view, the mass transfer will be stable if the radius of the donor increases less rapidly than the increase in its Roche lobe radius or decrease more rapidly than the decrease in its Roche lobe radius. When this criterion is violated, the mass transfer rate should increase. If the increased mass transfer rate can make the star react in such a way that the above criterion is satisfied again, the mass transfer will be stabilised after a brief period of mass transfer where the mass transfer rate is very high. However, if the above criterion is violated for an extended period of time, the mass transfer will be unstable.

There are three regimes of the stability of mass transfer based on the timescale of the response of the donor star to the mass transfer:

1. Thermally stable mass transfer: In this case, mass transfer is driven by the nuclear evolution of the star and occurs at the nuclear timescale, for e.g. the slow Case A mass transfer phase.

2. Dynamically stable but thermally unstable mass transfer: In this case, mass transfer occurs at the thermal timescale, for e.g. the fast Case A, Case AB and Case B mass transfer.

3. Dynamically unstable mass transfer: In this case, mass transfer is totally unstable and takes place at the dynamical timescale, for e.g. common envelope evolution (described later).

To determine the timescale at which the mass transfer will occur, one has to compare $\xi_{\mathrm{roche, donor}}$ to the Kelvin-Helmholtz mass-radius exponent $\xi_{\mathrm{KH, donor}}$ to check for thermally unstable mass transfer and to the adiabatic mass-radius exponent $\xi_{\mathrm{ad, donor}}$ to check for dynamically unstable mass transfer.

Conservative and non-conservative mass transfer

If all the mass lost by the donor from the first Lagrangian point is accreted by the accretor, and ignoring mass-loss via stellar winds and other sources of angular momentum loss, the orbital period evolution can be analytically determined by the following equation:

$$\frac{\dot{P}}{P} = 3 \frac{\dot{M_1}}{M_1}(q - 1)$$

(1.9)

where is $\dot{P}$ is the orbital period derivative and $\dot{M}_1$ is the mass transfer rate from the donor. If

1. the mass of the donor is greater than the mass of the accretor, then $\dot{P}$ is negative and the orbital period decreases.

2. the mass of the donor is smaller than the mass of the accretor, then $\dot{P}$ is positive and the orbital period increases.

However, stable mass transfer is not always fully conservative, especially when the mass transfer rates are high, and stars only need to accrete a few percent of their mass to spin up to critical rotation (Packet, 1981). When a star spins up to critical rotation, it is plausible that the star will not be able to accrete any more matter. This leads us to define a mass transfer efficiency β in binary evolution calculations that sets the fraction of mass accreted by the accretor to that transferred by the donor. One way to stop stars from reaching critical rotation is if the tidal forces are strong enough to stop the spin-up of the accretor (Zahn, 1977). In our models, it is this interplay between the tidal forces and spin-up due to mass accretion that determines our mass transfer efficiency. Hotspots produced on the surface of the accretor due to the infalling matter from the donor can provide an additional source of energy to remove matter from the accretor (van Rensbergen et al., 2008).

The mass transfer efficiency in massive binary evolution is very ill-constrained. While some studies indicate the need for a very conservative mass transfer (Wellstein et al., 1999; Schootemeijer et al., 2018), others argue in favour of a very low mass transfer efficiency (Petrovic et al., 2005; Ritchie et al., 2012; Shao et al., 2016). Constraints on the binary mass transfer efficiency is one of the central results of this thesis that we address in Chapter 2.

1.4.5 The isolated binary evolution channel

Figure 1.4 (Kruckow et al., 2018) gives the schematic representation of one of the formation paths of double compact objects: the close massive binary star evolution channel involving the common envelope phase. This channel involves a lot of phases for which current theoretical predictions are quite unconstrained, for example, the Roche-lobe Overflow phase, the common envelope phase, and the compact object formation phase. Ideally, it will be very advantageous to have observational constraints on as many as these individual evolutionary stages as possible to constrain the theoretical models.

It is essential to note that many of the binaries will merge or disrupt (de Mink et al., 2014; Renzo et al., 2019) during their evolution, and the final number of binaries reaching the compact binary stage will be many orders of magnitude lower than the number of main sequence binaries (Kruckow et al., 2018, Fig. 20). Hence, observational tests for earlier stages will be easier, where we expect more observational counterparts to our theoretical predictions. This idea was developed by Langer et al., 2020 who investigated the black hole phase (where there is a black hole with an OB star companion) and predicted that ∼3 out of every 100 massive binaries should host a black hole.

We explicate the assumptions that pervade each of the above phases now. The first phase, which consists of two detached massive stars in orbit with each other, is reasonably well-constrained. We have a fairly good understanding of the initial binary distribution functions (Sana et al., 2012; Sana et al., 2013) and the initial mass function (Salpeter, 1955). So we can use a grid of detailed binary evolution models and do population synthesis studies with the binary distribution functions. However,
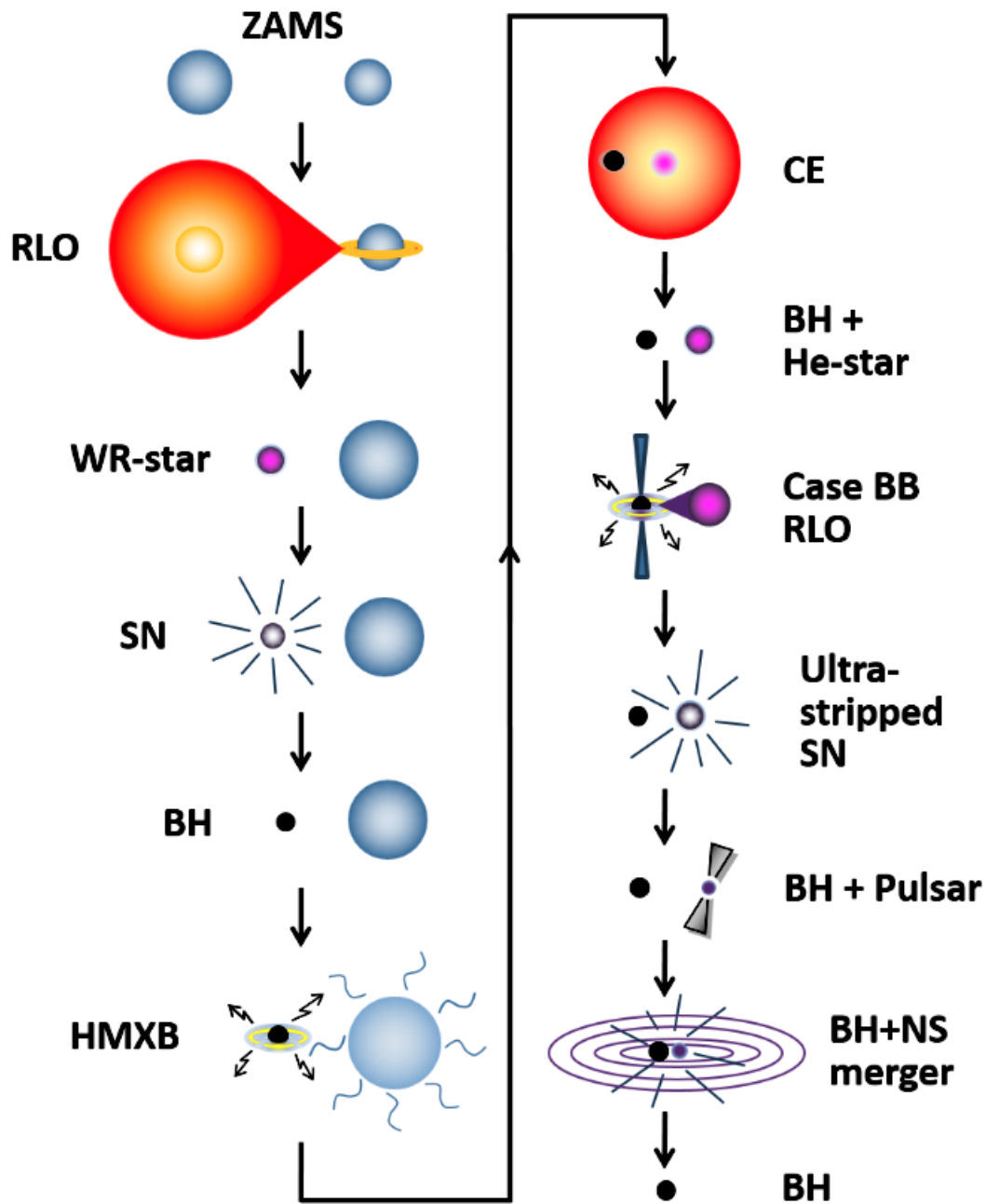
Figure 1.4: The close binary evolution channel towards the formation of compact object binaries that involve mass transfer. ZAMS: Zero age main sequence, RLO: Roche-lobe overflow, WR: Wolf-Rayet, SN: supernova, BH: black hole, HMXB: high-mass X-ray binary, CE: common envelope, BH+He: black hole+helium, Case BB: mass transfer phase after core helium burning, Pulsar: magnetised, fast rotating neutron star. Credits: Matthias Kruckow (Kruckow et al., 2018).

each of the next phases have unconstrained physics assumptions that we aim to constrain by comparing observations with the predictions of our population synthesis.

As already alluded to, the mass transfer efficiency of the Roche lobe overflow (RLO) phase is unconstrained. The silver lining is that this is one of the first mass transfer phases, so there are comparatively larger number of observed systems that we can compare our models to. More precisely, the Algol binaries are the observational counterparts to the binaries in our model grid that are undergoing slow Case A mass transfer. Since they are in the mass transfer phase, we can devise methods that can allow us to constrain the mass transfer efficiency of this phase (see, for e.g., de Mink et al., 2007).

After the Case AB or Case B mass transfer phase, the donor is almost completely stripped of its outer hydrogen envelope and becomes a naked helium star. For helium stars that have optically thick winds, they are observed as Wolf-Rayet stars. A lot of aspects of Wolf-Rayet stars are not well-understood. The winds of Wolf-Rayet stars are uncertain by an order of magnitude. The origin of these stars are also debated: whether they were single stars and were stripped by wind mass-loss or they were stripped in binaries (see, for e.g., Shenar et al., 2020, and references within).

Collapsing of Wolf-Rayet stars are believed to form compact objects, either neutron stars or black holes. A lot of work has been done to investigate the outcome of stripped envelope stars (see O'Connor et al., 2011a; Ertl et al., 2016; Müller et al., 2016; Woosley et al., 2020). Moreover, the natal kick received by the black holes during the collapse of the Wolf-Rayet stars are also unconstrained. Some studies require the assumption of a high natal kick to explain observations (Repetto et al., 2012; Repetto et al., 2017; Vanbeveren et al., 2020), while others require low natal kicks (Wong et al., 2012; Belczynski et al., 2016).

Since black holes by themselves do not emit any electromagnetic radiation that can observed, we have to rely on the formation of accretion disks around black holes that will emit X-ray radiation that we can observe here from Earth, as a high-mass X-ray binary (HMXB). The formation of accretion disks around black holes depend on many unconstrained physical assumptions like the amount of angular momentum available for accretion, the efficiency with which the black hole can accrete the available angular momentum and the effect of the spin of the black hole in the accretion disk formation process.

In the common envelope (CE) phase, the mass transfer is unstable, due to which the transferred matter from the donor does not get accreted by the accretor and instead engulfs both the donor and accretor inside itself, referred to as the common envelope. Both the donor and accretor are expected to spiral in during the common envelope phase and the orbital energy lost heats up the common envelope. If enough energy is released, this can eject the common envelope, leaving two very stripped stars in a close orbit with each other. However, the efficiency of the common envelope phase is largely unknown, since it happens at the dynamical timescale and observational counterparts are very hard to find (see review by Ivanova et al., 2013).

Finally, there is another core collapse event following the CE event that leads to the formation of the second compact object. As for the formation of the first compact object, the impact of kicks is unknown. Not all the compact object binaries will merge in Hubble time either. The compact objects need to be sufficiently close to each other so that the angular momentum lost via gravitational wave radiation can lead to a merger within Hubble time.

Unfortunately, all the compact object merger rates depend on each of these uncertainties discussed above and can change the predictions by over one order of magnitude. Hence, it is paramount that we start to constrain these uncertainties to get accurate predictions of compact object merger rates. In

Sect. 1.5, we describe how we aim to answer some of the uncertainties in this thesis.

1.4.6 Algol binaries

Algol binaries are a special class of interacting binaries where the currently less massive component of the binary is filling its Roche lobe and transferring mass to a more massive star which is not filling its Roche lobe. The study of Algol binaries was started centuries ago, with arguably the first systematic study of the light variability from an Algol binary being recorded by Goodricke (1783). The observations were only visual estimates of the stars' brightness and not measurements. Even then, these observations were the setting stones for more detailed works in this field. For a detailed review of the work done in the ancient past and the next two centuries since Goodricke's work, we encourage the interested reader to refer to the works of Budding (1988) and Batten (1989), respectively.

Theoretical treatments of the light variability were difficult as the observed changes were too complex to be explained by the then simple models. Concurrently with the series of theoretical papers by Henry Norris Russell in the early 1900s (see, for example H. N. Russell, 1912; I. H. N. Russell et al., 1912), photographic measurements were being made by the use of photometers. This infused renewed interest in the study of Algol binaries as astronomers started to realise the potential of eclipsing binaries to accurately determine the stellar and orbital parameters of stars using Newtonian dynamics. These realisations were of course not without hurdles. To quote Frank Bradshaw Wood "I remember one astronomical meeting, in which I suggested mass loss as a possible cause for changes in orbital period, where early in the discussion one member of the audience announced emphatically that, if there was one thing out of which we could be certain, it was that no star could ever lose mass. This statement would scarcely attract much support today". Interestingly, the now commonly known Roche model was first called the 'Jacobian' limiting surface, which F. B. Wood used in his Ph. D. thesis (Wood, 1946) to determine the configuration of the eclipsing binary variable stars AG Virginis, AR Lacertae, TX Ursae Majoris, VV Orionis, R Canis Majoris, SV Camelopardalis, ST Persei, RY Persei and VZ Hydrae. In the modern era, a lot more work has been done on Algol binaries, which we will discuss in Chapter 2.

1.4.7 Gravitational waves

On 14th of September 2015, gravitational waves were detected for the first time by the LIGO observatory (B. P. Abbott et al., 2016). Two black holes of masses ~36 and $29\,M_\odot$ were 'observed' to merge into a single black hole of mass ~$62\,M_\odot$. The energy released 7×10^{54} ergs during the merger event (in about a tenth of a second) meant that for a brief moment, this event was more luminous than all the stars in the visible Universe combined. The waveform of the gravitational wave event was in unison with the that prediction using the general theory of relativity, thereby confirming Einstein's theory yet again. Also, the masses of the black holes detected were the highest that ever has been measured for stellar mass black holes.

Four major formation channels were proposed for these merging black hole binaries. i) the isolated binary evolution channel, where two close massive binaries undergo stable mass transfer and then an unstable common envelope phase that brings both the stars close enough for them to merge within Hubble time (Kruckow et al., 2018). van den Heuvel et al. (2017) also proposed a close binary evolution channel that only involves stable mass transfer phases. ii) the chemically homogeneous evolution channel (de Mink et al., 2009; Marchant et al., 2016; Mandel et al., 2016), where two
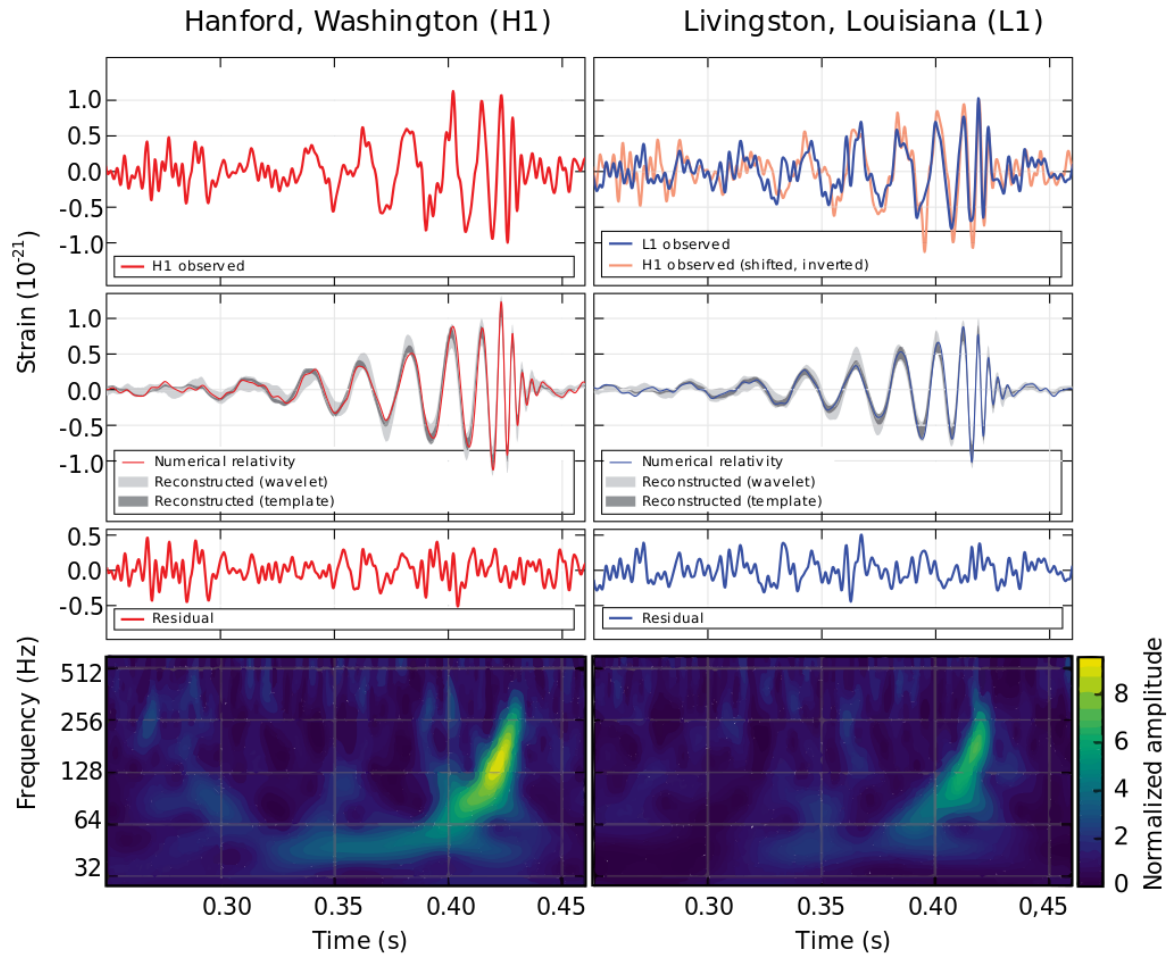
Figure 1.5: LIGO measurement of the gravitational waves at the Hanford (left) and Livingston (right) detectors, compared to the theoretical predicted values. Image taken from B. P. Abbott et al. (2016).

near contact binaries are tidally locked and the rapid rotation induces strong internal mixing that homogenises the entire star and the stars remain compact and collapse to form black holes without any mass transfer episodes. iii) the primordial channel (Carr et al., 1974; Bird et al., 2016; Nishikawa et al., 2019) and iv) the dynamical channel (Kulkarni et al., 1993; Fragione et al., 2019; Di Carlo et al., 2019). In this thesis, we study the close binary evolution channel that involves both stable and unstable mass transfer.

1.5 This thesis

The primary aim of this thesis is to study the evolution of short-period massive binaries that undergo their first mass transfer phase via Roche-lobe overflow during their main sequence. In turn, we constrain various physics assumptions taken in the modelling of the close massive binary evolution channel, such as the binary mass transfer efficiency and internal mixing. For this, we use grids of detailed binary evolution models calculated using the one dimentional stellar evolution code Modules for Experiments in Stellar Astrophysics (MESA, Paxton et al., 2011; Paxton et al., 2013; Paxton et al., 2015; Paxton et al., 2018). We derive observable stellar parameters of our models during relevant stages of stellar evolution and compare our predictions with observed massive binaries.

1.5.1 Detailed models of interacting short-period massive binary stars

In this project, we compare the properties of our models during the slow Case A mass transfer phase with the observed massive Algol binaries in the Large Magellanic Cloud. These models generally have orbital periods less than 10 days, such that tidal forces are strong in some of the most short period binaries. This fact enables us to study the interplay between the strength of tidal synchronisation and spin-up of the accretor during mass transfer and the effect it has on the mass transfer efficiency. We find that a purely conservative or purely non-conservative mass transfer is unable to explain the orbital period and mass ratio distribution of the observed massive Algol binaries, while our accretor spin-up dependent mass transfer efficiency can adequately explain most of the Algol binaries. We also derive the surface abundances, rotational and orbital velocities, orbital period derivatives of our models in the slow Case A mass transfer phase. We find that the binaries that survive the Case A mass transfer phase, show a high surface nitrogen enhancement during the slow Case A phase, while models that eventually merge on the main sequence have much lower surface nitrogen enhancement.

1.5.2 The evolution of massive short-period binaries at low metallicity

We then test our mass transfer efficiency prescription on the observed Algol binaries in the Small Magellanic Cloud. We confirm that the same mass transfer prescription that explains most of the Algol binaries in the Large Magellanic Cloud and Galaxy is able to explain the distribution of the massive Algols in the Small Magellanic Cloud. We find that the Ledoux criterion for convection along with efficient semiconvective mixing assumed in our models is able to reproduce the radius of the accretors better than previous work that adopted the Schwarzschild criterion. We also find that the efficiency of semiconvection plays a major role in the extent of envelope stripping in Case B binaries. We finally compare our models in the helium star/ Wolf-Rayet star + main sequence phase to the observed Wolf-Rayet binaries in the Small Magellanic Cloud and find that our binary models are able to explain the observed binary Wolf-Rayet stars in the Small Magellanic Cloud.

1.5.3 Compact object progenitors on the Hertzsprung-Russell diagram

Having a reasonable understanding of the mass transfer efficiency in close massive binaries, we move forward to look at the compact object phases of the close binary evolution channel. We use a grid of Monte Carlo generated models that resembles a $\sim 10^5$ M$_\odot$ co-eval population of binary stars. We study the position of the compact object progenitors on the Hertzsprung-Russell diagram to aid the observational search for such objects prior to core collapse. We also look at the expected number of compact object binaries in a binary cluster such as NGC 330 as a function of the binary age. We find that the Case A and Case B donors form two separate sub-populations of stripped envelope supernovae. We confirm the observational fact that stripped envelope supernova seem to have progenitors that are on average younger than the progenitors of ordinary Type II supernova.

1.5.4 X-ray emission from BH+O star binaries expected to descend from the observed galactic WR+O binaries

In this project, we look at the criterion for the formation of accretion disks in black hole + main sequence binaries and their observability as a high mass X-ray binary. We derive an analytical criterion to determine the formation of accretion disks that depend on the efficiency of angular momentum accretion and the spin of the black hole. We find that most of the black hole + main sequence binaries in our Galaxy are expected to be quiet in X-rays. A high spin of the black hole can increase the lifetime of the X-ray active phase of the black hole binary. Considering that stellar evolution models predict that the spin of the first formed black hole will be low, we conclude that a high black hole kick velocity is not necessary to explain the lack of observed black hole binaries compared to Wolf-Rayet binaries.

References

Abbott, B. P., R. Abbott, T. D. Abbott, M. R. Abernathy, F. Acernese, K. Ackley, C. Adams, T. Adams, P. Addesso, R. X. Adhikari, V. B. Adya, C. Affeldt, M. Agathos, K. Agatsuma, N. Aggarwal, O. D. Aguiar et al. (2016), *Binary Black Hole Mergers in the First Advanced LIGO Observing Run*, Physical Review X **6** 041015, arXiv: `1606.04856 [gr-qc]` (cit. on p. 17).

Abbott, B. P., R. Abbott, T. D. Abbott, M. R. Abernathy, F. Acernese, K. Ackley, C. Adams, T. Adams, P. Addesso, R. X. Adhikari, V. B. Adya, C. Affeldt, M. Agathos, K. Agatsuma, N. Aggarwal, LIGO Scientific Collaboration et al. (2016), *Observation of Gravitational Waves from a Binary Black Hole Merger*, Physical Review Letters **116** 061102, arXiv: `1602.03837 [gr-qc]` (cit. on p. 18).

Aguilera-Dena, D. R., N. Langer, T. J. Moriya and A. Schootemeijer (2018), *Related Progenitor Models for Long-duration Gamma-Ray Bursts and Type Ic Superluminous Supernovae*, The Astrophysical Journal **858** 115, arXiv: `1804.07317 [astro-ph.SR]` (cit. on p. 4).

Ashfaque, S. M. (1977), *Astronomy in the Indus Valley Civilization: A Survey of the Problems and Possibilities of the Ancient Indian Astronomy and Cosmology in the Light of Indus Script Decipherment by the Finnish Scholars*, Centaurus **21** 149 (cit. on p. 1).

Baade, W. and F. Zwicky (1934), *Remarks on Super-Novae and Cosmic Rays*, Physical Review **46** 76 (cit. on p. 8).

Banyard, G. et al. (2021), *The observed multiplicity properties of B-type stars in the Galactic young open cluster NGC 6231*, arXiv e-prints arXiv:2108.07814, arXiv: `2108.07814 [astro-ph.SR]` (cit. on p. 10).

Barlow, M. J. and D. G. Hummer (1982), "The WO Wolf-rayet stars.", *Wolf-Rayet Stars: Observations, Physics, Evolution*, ed. by C. W. H. De Loore and A. J. Willis, vol. 99 387 (cit. on p. 7).

Batten, A. H. (1989), *Two Centuries of Study of Algol Systems*, Space Science Reviews **50** 1 (cit. on p. 17).

Beals, C. S. (1929), *On the nature of Wolf-Rayet emission*, Monthly Notices of the Royal Astronomical Society **90** 202 (cit. on p. 7).

– (1940), *On the Physical Characteristics of the Wolf Rayet Stars and their Relation to Other Objects of Early Type (with Plates VIII, IX)*, Journal of the Royal Astronomical Society of Canada **34** 169 (cit. on p. 7).

Belczynski, K., D. E. Holz, T. Bulik and R. O'Shaughnessy (2016), *The first gravitational-wave source from the isolated evolution of two stars in the 40-100 solar mass range*, Nature **534** 512, arXiv: `1602.04531 [astro-ph.HE]` (cit. on p. 16).

Bird, S. et al. (2016), *Did LIGO Detect Dark Matter?*, Physical Review Letters **116** 201301, arXiv: `1603.00464 [astro-ph.CO]` (cit. on p. 19).

Bowman, D. M. (2020), *Asteroseismology of high-mass stars: new insights of stellar interiors with space telescopes*, Frontiers in Astronomy and Space Sciences **7** 70, arXiv: `2008.11162 [astro-ph.SR]` (cit. on p. 9).

Braun, H. and N. Langer (1995), *Effects of accretion onto massive main sequence stars.*, Astronomy and Astrophysics **297** 483 (cit. on p. 9).

Brott, I. et al. (2011), *Rotating massive main-sequence stars. I. Grids of evolutionary models and isochrones*, Astronomy and Astrophysics **530** A115, arXiv: `1102.0530 [astro-ph.SR]` (cit. on p. 9).

Budding, E. (1988), *Was There an Ancient Knowledge of Algol's Variability?*, Southern Stars **32** 180 (cit. on p. 17).

Carr, B. J. and S. W. Hawking (1974), *Black holes in the early Universe*, Monthly Notices of the Royal Astronomical Society **168** 399 (cit. on p. 19).

Castro, N. et al. (2014), *The spectroscopic Hertzsprung-Russell diagram of Galactic massive stars*, Astronomy and Astrophysics **570** L13, arXiv: `1410.3499 [astro-ph.SR]` (cit. on p. 9).

Claret, A. and G. Torres (2019), *The Dependence of Convective Core Overshooting on Stellar Mass: Reality Check and Additional Evidence*, The Astrophysical Journal **876** 134, arXiv: `1904.02714 [astro-ph.SR]` (cit. on p. 9).

Crowther, P. A. (2019), *Massive Stars in the Tarantula Nebula: A Rosetta Stone for Extragalactic Supergiant HII Regions*, Galaxies **7** 88, arXiv: `1911.02047 [astro-ph.SR]` (cit. on p. 4).

Crowther, P. A. et al. (2016), *The R136 star cluster dissected with Hubble Space Telescope/STIS. I. Far-ultraviolet spectroscopic census and the origin of He II λ1640 in young star clusters*, Monthly Notices of the Royal Astronomical Society **458** 624, arXiv: `1603.04994 [astro-ph.SR]` (cit. on p. 4).

de Koter, A., S. R. Heap and I. Hubeny (1997), *On the Evolutionary Phase and Mass Loss of the Wolf-Rayet–like Stars in R136a*, The Astrophysical Journal **477** 792 (cit. on p. 7).

de Mink, S. E., M. Cantiello et al. (2009), *Rotational mixing in massive binaries. Detached short-period systems*, Astronomy and Astrophysics **497** 243, arXiv: `0902.1751 [astro-ph.SR]` (cit. on p. 17).

de Mink, S. E., N. Langer, R. G. Izzard, H. Sana and A. de Koter (2013), *The Rotation Rates of Massive Stars: The Role of Binary Interaction through Tides, Mass Transfer, and Mergers*, The Astrophysical Journal **764** 166, arXiv: `1211.3742 [astro-ph.SR]` (cit. on p. 10).

de Mink, S. E., O. R. Pols and R. W. Hilditch (2007), *Efficiency of mass transfer in massive close binaries. Tests from double-lined eclipsing binaries in the SMC*, Astronomy and Astrophysics **467** 1181, arXiv: `astro-ph/0703480 [astro-ph]` (cit. on pp. 12, 16).

de Mink, S. E., H. Sana, N. Langer, R. G. Izzard and F. R. N. Schneider (2014), *The Incidence of Stellar Mergers and Mass Gainers among Massive Stars*, The Astrophysical Journal **782** 7, arXiv: `1312.3650 [astro-ph.SR]` (cit. on p. 14).

Di Carlo, U. N. et al. (2019), *Merging black holes in young star clusters*, Monthly Notices of the Royal Astronomical Society **487** 2947, arXiv: `1901.00863 [astro-ph.HE]` (cit. on p. 19).

Eggleton, P. P. (1983), *Aproximations to the radii of Roche lobes.*, The Astrophysical Journal **268** 368 (cit. on p. 11).

Ertl, T., H. .-.-T. Janka, S. E. Woosley, T. Sukhbold and M. Ugliano (2016), *A Two-parameter Criterion for Classifying the Explodability of Massive Stars by the Neutrino-driven Mechanism*, The Astrophysical Journal **818** 124, arXiv: `1503.07522 [astro-ph.SR]` (cit. on pp. 9, 16).

Ertl, T., S. E. Woosley, T. Sukhbold and H. .-.-T. Janka (2020), *The Explosion of Helium Stars Evolved with Mass Loss*, The Astrophysical Journal **890** 51, arXiv: `1910.01641 [astro-ph.HE]` (cit. on p. 9).

Farmer, R. et al. (2016), *On Variations Of Pre-supernova Model Properties*, The Astrophysical Journal Supplement Series **227** 22, arXiv: `1611.01207 [astro-ph.SR]` (cit. on p. 9).

Filippenko, A. V. (1997), *Optical Spectra of Supernovae*, Annual Review of Astronomy and Astrophysics **35** 309 (cit. on p. 8).

Fowler, A. (1912), *Observations of the principal and other series of lines in the spectrum of Hydrogen (Plates 2-4)*, Monthly Notices of the Royal Astronomical Society **73** 62 (cit. on p. 7).

Fowler, W. A. and F. Hoyle (1964), *Neutrino Processes and Pair Formation in Massive Stars and Supernovae.*, The Astrophysical Journal Supplement Series **9** 201 (cit. on p. 9).

Fragione, G., E. Grishin, N. W. C. Leigh, H. B. Perets and R. Perna (2019), *Black hole and neutron star mergers in galactic nuclei*, Monthly Notices of the Royal Astronomical Society **488** 47, arXiv: `1811.10627 [astro-ph.GA]` (cit. on p. 19).

Gal-Yam, A. (2012), *Luminous Supernovae*, Science **337** 927, arXiv: `1208.3217 [astro-ph.CO]` (cit. on p. 8).

Goodricke, J. (1783), *A Series of Observations on, and a Discovery of, the Period of the Variation of the Light of the Bright Star in the Head of Medusa, Called Algol. In a Letter from John Goodricke, Esq. to the Rev. Anthony Shepherd, D. D. F. R. S. and Plumian Professor at Cambridge*, Philosophical Transactions of the Royal Society of London Series I **73** 474 (cit. on p. 17).

Haiman, Z. and A. Loeb (1997), *Signatures of Stellar Reionization of the Universe*, The Astrophysical Journal **483** 21, arXiv: `astro-ph/9611028 [astro-ph]` (cit. on p. 4).

Hamann, W. .-.-R., G. Gräfener and A. Liermann (2006), *The Galactic WN stars. Spectral analyses with line-blanketed model atmospheres versus stellar evolution models with and without rotation*, Astronomy and Astrophysics **457** 1015, arXiv: `astro-ph/0608078 [astro-ph]` (cit. on p. 7).

Heger, A., C. L. Fryer, S. E. Woosley, N. Langer and D. H. Hartmann (2003), *How Massive Single Stars End Their Life*, The Astrophysical Journal **591** 288, arXiv: `astro-ph/0212469 [astro-ph]` (cit. on pp. 4, 9).

Hopkins, P. F. et al. (2014), *Galaxies on FIRE (Feedback In Realistic Environments): stellar feedback explains cosmologically inefficient star formation*, Monthly Notices of the Royal Astronomical Society **445** 581, arXiv: `1311.2073 [astro-ph.CO]` (cit. on p. 4).

Hoyle, F. and W. A. Fowler (1960), *Nucleosynthesis in Supernovae.*, The Astrophysical Journal **132** 565 (cit. on p. 4).

Ivanova, N. et al. (2013), *Common envelope evolution: where we stand and how we can move forward*, Astronomy and Astrophysicsr **21** 59, arXiv: `1209.4302 [astro-ph.HE]` (cit. on p. 16).

Jeans, J. H. (1902), *The Stability of a Spherical Nebula*, Philosophical Transactions of the Royal Society of London Series A **199** 1 (cit. on p. 5).

Kozyreva, A., S. .-.-C. Yoon and N. Langer (2014), *Explosion and nucleosynthesis of low-redshift pair-instability supernovae*, Astronomy and Astrophysics **566** A146, arXiv: `1405.6340 [astro-ph.HE]` (cit. on p. 9).

Kruckow, M. U., T. M. Tauris, N. Langer, M. Kramer and R. G. Izzard (2018), *Progenitors of gravitational wave mergers: binary evolution with the stellar grid-based code COMBINE*, Monthly Notices of the Royal Astronomical Society **481** 1908, arXiv: `1801.05433 [astro-ph.SR]` (cit. on pp. 14, 15, 17).

Kulkarni, S. R., P. Hut and S. McMillan (1993), *Stellar black holes in globular clusters*, Nature **364** 421 (cit. on p. 19).

Langer, N. (2012), *Presupernova Evolution of Massive Single and Binary Stars*, Annual Review of Astronomy and Astrophysics **50** 107, arXiv: `1206.5443 [astro-ph.SR]` (cit. on p. 4).

Langer, N. et al. (2020), *Properties of OB star-black hole systems derived from detailed binary evolution models*, Astronomy and Astrophysics **638** A39, arXiv: `1912.09826 [astro-ph.SR]` (cit. on p. 14).

Langer, N. (2009), *Astrophysics: Different stellar demise*, Nature **462** 579 (cit. on p. 9).

Mac Low, M.-M. and R. S. Klessen (2004), *Control of star formation by supersonic turbulence*, Reviews of Modern Physics **76** 125, arXiv: `astro-ph/0301093 [astro-ph]` (cit. on p. 4).

Mandel, I. and S. E. de Mink (2016), *Merging binary black holes formed through chemically homogeneous evolution in short-period stellar binaries*, Monthly Notices of the Royal Astronomical Society **458** 2634, arXiv: `1601.00007` `[astro-ph.HE]` (cit. on p. 17).

Marchant, P., N. Langer, P. Podsiadlowski, T. M. Tauris and T. J. Moriya (2016), *A new route towards merging massive black holes*, Astronomy and Astrophysics **588** A50, arXiv: `1601.03718` `[astro-ph.SR]` (cit. on p. 17).

Martins, F., E. Depagne, D. Russeil and L. Mahy (2013), *Evidence of quasi-chemically homogeneous evolution of massive stars up to solar metallicity*, Astronomy and Astrophysics **554** A23, arXiv: `1304.3337` `[astro-ph.SR]` (cit. on p. 7).

Mennekens, N. and D. Vanbeveren (2017), *A comparison between observed Algol-type double stars in the solar neighborhood and evolutionary computations of galactic case A binaries with a B-type primary at birth*, Astronomy and Astrophysics **599** A84, arXiv: `1611.08398` `[astro-ph.SR]` (cit. on p. 12).

Metzger, B. D., E. Berger and B. Margalit (2017), *Millisecond Magnetar Birth Connects FRB 121102 to Superluminous Supernovae and Long-duration Gamma-Ray Bursts*, The Astrophysical Journal **841** 14, arXiv: `1701.02370` `[astro-ph.HE]` (cit. on p. 4).

Moe, M. and R. Di Stefano (2017), *Mind Your Ps and Qs: The Interrelation between Period (P) and Mass-ratio (Q) Distributions of Binary Stars*, The Astrophysical Journal Supplement Series **230** 15, arXiv: `1606.05347` `[astro-ph.SR]` (cit. on p. 10).

Mohamed, S. and P. Podsiadlowski (2007), "Wind Roche-Lobe Overflow: a New Mass-Transfer Mode for Wide Binaries", *15th European Workshop on White Dwarfs*, ed. by R. Napiwotzki and M. R. Burleigh, vol. 372, Astronomical Society of the Pacific Conference Series 397 (cit. on p. 13).

Muijres, L. E., J. S. Vink, A. de Koter, P. E. Muller and N. Langer (2012), *Predictions for mass-loss rates and terminal wind velocities of massive O-type stars*, Astronomy and Astrophysics **537** A37, arXiv: `1112.0944` `[astro-ph.SR]` (cit. on p. 10).

Müller, B., A. Heger, D. Liptai and J. B. Cameron (2016), *A simple approach to the supernova progenitor-explosion connection*, Monthly Notices of the Royal Astronomical Society **460** 742, arXiv: `1602.05956` `[astro-ph.SR]` (cit. on pp. 9, 16).

"Wolf, Charles J E (1827-1918)" (2000), *Encyclopedia of Astronomy and Astrophysics*, ed. by P. Murdin 4101 (cit. on p. 7).

Nelson, C. A. and P. P. Eggleton (2001), *A Complete Survey of Case A Binary Evolution with Comparison to Observed Algol-type Systems*, The Astrophysical Journal **552** 664, arXiv: `astro-ph/0009258` `[astro-ph]` (cit. on p. 12).

Nishikawa, H., E. D. Kovetz, M. Kamionkowski and J. Silk (2019), *Primordial-black-hole mergers in dark-matter spikes*, Physical Reviews D **99** 043533 (cit. on p. 19).

O'Connor, E. and C. D. Ott (2011a), *Black Hole Formation in Failing Core-Collapse Supernovae*, The Astrophysical Journal **730** 70, arXiv: `1010.5550` `[astro-ph.HE]` (cit. on pp. 9, 16).

– (2011b), *Black Hole Formation in Failing Core-Collapse Supernovae*, The Astrophysical Journal **730** 70, arXiv: `1010.5550` `[astro-ph.HE]` (cit. on p. 9).

Packet, W. (1981), *On the spin-up of the mass accreting component in a close binary system*, Astronomy and Astrophysics **102** 17 (cit. on p. 14).

Paxton, B., L. Bildsten et al. (2011), *Modules for Experiments in Stellar Astrophysics (MESA)*, The Astrophysical Journal Supplement Series **192** 3, arXiv: `1009.1622` `[astro-ph.SR]` (cit. on p. 19).

Paxton, B., M. Cantiello et al. (2013), *Modules for Experiments in Stellar Astrophysics (MESA): Planets, Oscillations, Rotation, and Massive Stars*, The Astrophysical Journal Supplement Series **208** 4, arXiv: `1301.0319` [`astro-ph.SR`] (cit. on p. 19).

Paxton, B., P. Marchant et al. (2015), *Modules for Experiments in Stellar Astrophysics (MESA): Binaries, Pulsations, and Explosions*, The Astrophysical Journal Supplement Series **220** 15, arXiv: `1506.03146` [`astro-ph.SR`] (cit. on p. 19).

Paxton, B., J. Schwab et al. (2018), *Modules for Experiments in Stellar Astrophysics (MESA): Convective Boundaries, Element Diffusion, and Massive Star Explosions*, The Astrophysical Journal Supplement Series **234** 34, arXiv: `1710.08424` [`astro-ph.SR`] (cit. on p. 19).

Petrovic, J., N. Langer and K. A. van der Hucht (2005), *Constraining the mass transfer in massive binaries through progenitor evolution models of Wolf-Rayet+O binaries*, Astronomy and Astrophysics **435** 1013, arXiv: `astro-ph/0504242` [`astro-ph`] (cit. on p. 14).

Podsiadlowski, P., P. C. Joss and J. J. L. Hsu (1992), *Presupernova Evolution in Massive Interacting Binaries*, The Astrophysical Journal **391** 246 (cit. on p. 10).

Quimby, R. M. et al. (2011), *Hydrogen-poor superluminous stellar explosions*, Nature **474** 487, arXiv: `0910.0059` [`astro-ph.CO`] (cit. on p. 4).

Renzo, M. et al. (2019), *Massive runaway and walkaway stars. A study of the kinematical imprints of the physical processes governing the evolution and explosion of their binary progenitors*, Astronomy and Astrophysics **624** A66 (cit. on p. 14).

Repetto, S., M. B. Davies and S. Sigurdsson (2012), *Investigating stellar-mass black hole kicks*, Monthly Notices of the Royal Astronomical Society **425** 2799, arXiv: `1203.3077` [`astro-ph.GA`] (cit. on p. 16).

Repetto, S., A. P. Igoshev and G. Nelemans (2017), *The Galactic distribution of X-ray binaries and its implications for compact object formation and natal kicks*, Monthly Notices of the Royal Astronomical Society **467** 298, arXiv: `1701.01347` [`astro-ph.HE`] (cit. on p. 16).

Ritchie, B. W. et al. (2012), *The VLT-FLAMES survey of massive stars: NGC 346-013 as a test case for massive close binary evolution*, Astronomy and Astrophysics **537** A29, arXiv: `1110.6325` [`astro-ph.SR`] (cit. on p. 14).

Ruffert, M. and H. .-.-T. Janka (1998), *Colliding neutron stars. Gravitational waves, neutrino emission, and gamma-ray bursts*, Astronomy and Astrophysics **338** 535, arXiv: `astro-ph/9804132` [`astro-ph`] (cit. on p. 8).

Russell, H. N. (1912), *On the Determination of the Orbital Elements of Eclipsing Variable Stars. I.*, Astrophysical Journal **35** 315 (cit. on p. 17).

– (1914), *Relations Between the Spectra and Other Characteristics of the Stars*, Popular Astronomy **22** 275 (cit. on p. 4).

Russell, I. H. N. and H. Shapley (1912), *On Darkening at the Limb in Eclipsing Variables*, Astrophysical Journal **36** 239 (cit. on p. 17).

Salpeter, E. E. (1955), *The Luminosity Function and Stellar Evolution.*, The Astrophysical Journal **121** 161 (cit. on p. 14).

Sana, H., A. de Koter et al. (2013), *The VLT-FLAMES Tarantula Survey. VIII. Multiplicity properties of the O-type star population*, Astronomy and Astrophysics **550** A107, arXiv: `1209.4638` [`astro-ph.SR`] (cit. on pp. 10, 14).

Sana, H., S. E. de Mink et al. (2012), *Binary Interaction Dominates the Evolution of Massive Stars*, Science **337** 444, arXiv: `1207.6397` [`astro-ph.SR`] (cit. on pp. 10, 14).

Sander, A., W. .-.-R. Hamann and H. Todt (2012), *The Galactic WC stars. Stellar parameters from spectral analyses indicate a new evolutionary sequence*, Astronomy and Astrophysics **540** A144, arXiv: `1201.6354` `[astro-ph.SR]` (cit. on p. 7).

Schootemeijer, A. and N. Langer (2018), *Wolf-Rayet stars in the Small Magellanic Cloud as testbed for massive star evolution*, Astronomy and Astrophysics **611** A75, arXiv: `1709.08727` `[astro-ph.SR]` (cit. on p. 14).

Schootemeijer, A., N. Langer, N. J. Grin and C. Wang (2019), *Constraining mixing in massive stars in the Small Magellanic Cloud*, Astronomy and Astrophysics **625** A132, arXiv: `1903.10423` `[astro-ph.SR]` (cit. on p. 9).

Shao, Y. and X.-D. Li (2016), *NONCONSERVATIVE MASS TRANSFER IN MASSIVE BINARIES AND THE FORMATION OF WOLF–RAYETO BINARIES*, The Astrophysical Journal **833** 108 (cit. on p. 14).

Shenar, T., A. Gilkis, J. S. Vink, H. Sana and A. A. C. Sander (2020), *Why binary interaction does not necessarily dominate the formation of Wolf-Rayet stars at low metallicity*, Astronomy and Astrophysics **634** A79, arXiv: `2001.04476` `[astro-ph.SR]` (cit. on p. 16).

Smartt, S. J. (2009), *Progenitors of Core-Collapse Supernovae*, Annual Review of Astronomy and Astrophysics **47** 63, arXiv: `0908.0700` `[astro-ph.SR]` (cit. on p. 4).

Smith, N. (2014), *Mass Loss: Its Effect on the Evolution and Fate of High-Mass Stars*, Annual Review of Astronomy and Astrophysics **52** 487, arXiv: `1402.1237` `[astro-ph.SR]` (cit. on p. 10).

Smith, N., W. Li, A. V. Filippenko and R. Chornock (2011), *Observed fractions of core-collapse supernova types and initial masses of their single and binary progenitor stars*, Monthly Notices of the Royal Astronomical Society **412** 1522, arXiv: `1006.3899` `[astro-ph.HE]` (cit. on p. 4).

Soberman, G. E., E. S. Phinney and E. P. J. van den Heuvel (1997), *Stability criteria for mass transfer in binary stellar evolution.*, Astronomy and Astrophysics **327** 620, arXiv: `astro-ph/9703016` `[astro-ph]` (cit. on p. 13).

Sukhbold, T., T. Ertl, S. E. Woosley, J. M. Brown and H. .-.-T. Janka (2016), *Core-collapse Supernovae from 9 to 120 Solar Masses Based on Neutrino-powered Explosions*, The Astrophysical Journal **821** 38, arXiv: `1510.04643` `[astro-ph.HE]` (cit. on p. 9).

Sukhbold, T., S. E. Woosley and A. Heger (2018), *A High-resolution Study of Presupernova Core Structure*, The Astrophysical Journal **860** 93, arXiv: `1710.03243` `[astro-ph.HE]` (cit. on p. 9).

Ugliano, M., H.-T. Janka, A. Marek and A. Arcones (2012), *Progenitor-explosion Connection and Remnant Birth Masses for Neutrino-driven Supernovae of Iron-core Progenitors*, The Astrophysical Journal **757** 69, arXiv: `1205.3657` `[astro-ph.SR]` (cit. on p. 9).

van den Heuvel, E. P. J., S. F. Portegies Zwart and S. E. de Mink (2017), *Forming short-period Wolf-Rayet X-ray binaries and double black holes through stable mass transfer*, Monthly Notices of the Royal Astronomical Society **471** 4256, arXiv: `1701.02355` `[astro-ph.SR]` (cit. on p. 17).

van Rensbergen, W., J. P. De Greve, C. De Loore and N. Mennekens (2008), *Spin-up and hot spots can drive mass out of a binary*, Astronomy and Astrophysics **487** 1129, arXiv: `0804.1215` `[astro-ph]` (cit. on p. 14).

Vanbeveren, D., N. Mennekens, E. P. J. van den Heuvel and J. Van Bever (2020), *Evidence from high-mass X-ray binaries that Galactic WR components of WR+O binaries end their life with a supernova explosion*, Astronomy and Astrophysics **636** A99, arXiv: `1912.01256` `[astro-ph.SR]` (cit. on p. 16).

Wellstein, S. and N. Langer (1999), *Implications of massive close binaries for black hole formation and supernovae*, Astronomy and Astrophysics **350** 148, arXiv: `astro-ph/9904256` `[astro-ph]` (cit. on p. 14).

Wolf-Rayet stars: Observations, physics, evolution (1982), vol. 99 (cit. on p. 7).

Wong, T.-W., F. Valsecchi, T. Fragos and V. Kalogera (2012), *Understanding Compact Object Formation and Natal Kicks. III. The Case of Cygnus X-1*, The Astrophysical Journal **747** 111, arXiv: `1107.5585` `[astro-ph.HE]` (cit. on p. 16).

Wood, F. B. (1946), *The Eclipsing Variables AG Virginis, AR Lacertae, TX Ursae Majoris, VV Orionis, R Canis Majoris, SV Camelopardalis, ST Persei, RY Persei, VZ Hydrae*, Contributions from the Princeton University Observatory **22** 1 (cit. on p. 17).

Woosley, S. E., T. Sukhbold and H. .-.-T. Janka (2020), *The Birth Function for Black Holes and Neutron Stars in Close Binaries*, The Astrophysical Journal **896** 56, arXiv: `2001.10492` `[astro-ph.HE]` (cit. on pp. 9, 16).

Zahn, J. .-.-P. (1977), *Reprint of 1977A&A....57..383Z. Tidal friction in close binary stars.*, Astronomy and Astrophysics **500** 121 (cit. on p. 14).

Detailed models of interacting short-period massive binary stars

K. Sen[a], N. Langer[a,b], P. Marchant[c,d], A. Menon[a,e], S. E. de Mink[f,e,g], C. Schürmann[a,b], L. Mahy[c], H. Sana[c], A. Schootemeijer[a], K. Nathaniel[a], X.-T. Xu[a,b], C. Wang[a,b] & B. Hastings[a]

[a] Argelander-Institüt für Astronomie, Universität Bonn, Auf dem Hügel 71, 53121 Bonn, Germany

[b] Max-Planck-Institut für Radioastronomie, Auf dem Hügel 69, 53121 Bonn, Germany

[c] Institute of Astrophysics, KU Leuven, Celestijnenlaan 200D, 3001 Leuven, Belgium

[d] Center for Interdisciplinary Exploration and Research in Astrophysics (CIERA) and Department of Physics and Astronomy, Northwestern University, 2145 Sheridan Road, Evanston, IL 60208, USA

[e] Astronomical Institute "Anton Pannekoek", University of Amsterdam, Science Park 904, 1098 XH Amsterdam, The Netherlands

[f] Max Planck Institute for Astrophysics, Karl-Schwarzschild-Strasse 1, 85748 Garching, Germany

[g] Center for Astrophysics, Harvard-Smithsonian, 60 Garden Street, Cambridge, MA 02138, USA

Summary: Double-lined eclipsing binaries provide a unique testing ground to understand the physics of stellar evolution as the stellar parameters of the individual binary components can be very precisely determined. Moreover, the binary parameters of such systems can also be measured accurately, providing valuable information to constrain our models of binary evolution. Of particular importance are short-period semi-detached systems, where one binary component is found to fill its Roche lobe. Hence, in these semi-detached systems, the binary components are physically interacting with each other, providing a one-of-a-kind opportunity to study the physics of mass transfer in binaries. Most of these semi-detached binaries fall in the class of Algol binaries (named after β Persei or more commonly, Algol), where the currently less massive star is over-flowing its Roche lobe. Since hundreds of such binaries have been observed, the mass transfer in these binaries is thought to occur at the

nuclear timescale, which is also corroborated by measurements of the ratio of the orbital period to its time derivative of such systems being of the same order.

The existence of such systems has been explained through detailed binary evolution models, where the Algol configuration corresponds to a nuclear timescale slow mass transfer phase during the main sequence of the donor. In a binary model having a sufficiently short orbital period, the initially more massive star fills its Roche lobe during the main sequence and mass transfer first occurs at the thermal timescale. The orbital period decreases as the binary evolves towards a mass ratio of unity. As soon as the mass ratio inverts, that is, the Roche lobe filling donor star becomes the less massive star of the system, further mass transfer leads to the widening of the orbit of the binary. Mass transfer continues at the thermal timescale until the donor regains thermal equilibrium, after which the mass transfer is governed by the nuclear timescale expansion of the radius of the donor, leading to a slow mass transfer phase where the binary model stays in the Algol configuration for the remainder of the main sequence lifetime of the donor.

A significant amount of work has been done in the low-to-intermediate mass range of Algol binaries in the last century. In this work, we look at the observable properties of massive Algol binaries using detailed models of massive binary stars computed using the 1D stellar evolution code MESA (Modules for Experiments in Stellar Astrophysics) and compare our model predictions with observations of massive Algol binaries in the Large Magellanic Cloud and the Milky Way. Taking into account the empirical distribution of initial donor masses, orbital period, mass ratio of our binary models, and the amount of time our models spend in the semi-detached configuration, we define the probability distribution functions of observable stellar and binary parameters such as the orbital period and its derivative, mass ratio, rotational and orbital velocities and surface abundances. We carefully define the binary mass transfer efficiency in our models, that is the ratio of the amount of mass accreted to the amount of mass transferred by the donor, by removing the contribution of the wind mass-loss of the individual binary components from the mass transfer and accretion rates. This is particularly important during the nuclear timescale mass transfer phase as the wind mass-loss rate can be a significant fraction of the mass transfer and accretion rates. We implement an accretor spin-up dependent mass transfer efficiency, where the mass transfer efficiency is assumed to be conservative until the accretor spins up to critical rotation through mass accretion. When tidal forces are not efficient to stop the accretor from spinning up to critical rotation, we assume that the excess transferred mass is lost from the accretor via stellar winds.

One of the central results of this chapter is the constraint on the binary mass transfer efficiency. Due to our particular implementation of the binary mass transfer efficiency, our shortest period binary models undergo conservative mass transfer where tides are efficient, while the longer orbital period models undergo non-conservative mass transfer, that is, the mass transfer efficiency decreases for increasing orbital periods. We find that such an orbital period dependence on the mass transfer efficiency can explain most of the observed massive Algol binaries in the Large Magellanic Cloud and the Milky Way. The shortest period and extreme mass ratio Algols require a conservative mass transfer, while the longer period Algols have mass ratios much closer to unity, signifying that a much less efficient mass transfer episode has taken place. We also study the distribution of the surface abundances of the donors and accretors during the slow mass transfer phase. The slow stripping of the hydrogen-helium gradient region in our donor models is corroborated by the donors of observed massive Algols showing elevated helium and nitrogen mass fractions at their surface. Future observations of more Algol binaries, both photometric and spectroscopic, harbour immense potential to give precise constraints on the rotational velocities, mass ratios and surface abundances that can

update and revise our understanding of massive binary evolution.

The evolution of massive short-period binaries at low metallicity

Koushik Sen[a], Norbert Langer[a,b], Selma De Mink[c,d,e], Xiao-Tian Xu[a,b],
Chen Wang[c,a], Pablo Marchant[f,g], Christoph Schürmann[a,b],
Abel Schootemeijer[a] & Ben Hastings[a]

[a] Argelander-Institüt für Astronomie, Universität Bonn, Auf dem Hügel 71, 53121 Bonn, Germany

[b] Max-Planck-Institut für Radioastronomie, Auf dem Hügel 69, 53121 Bonn, Germany

[c] Max Planck Institute for Astrophysics, Karl-Schwarzschild-Strasse 1, 85748 Garching, Germany

[d] Astronomical Institute "Anton Pannekoek", University of Amsterdam, Science Park 904, 1098 XH Amsterdam, The Netherlands

[e] Center for Astrophysics, Harvard-Smithsonian, 60 Garden Street, Cambridge, MA 02138, USA

[f] Institute of Astrophysics, KU Leuven, Celestijnenlaan 200D, 3001 Leuven, Belgium

[g] Center for Interdisciplinary Exploration and Research in Astrophysics (CIERA) and Department of Physics and Astronomy, Northwestern University, 2145 Sheridan Road, Evanston, IL 60208, USA

In preparation for *Astronomy & Astrophysics*

ABSTRACT

Context: Low metallicity environments are suitable for studying massive star evolution as major uncertainties such as the stellar wind mass loss rate and envelope inflation are not expected to play a major role in their evolution. Recently, massive stars have also been found to preferentially exist in binaries, where mass transfer lead to features unobtainable via single star evolution.

Aims: We study the predicted observable properties of binary models that interact during core hydrogen burning (Case A) and/or have interacted just after core hydrogen depletion (Case AB/Case B). We also study the effect varying the semiconvective mixing efficiency and provide predictions to constrain it via observations of stripped-envelope stars.

Method: We use detailed binary evolution models with initial donor masses greater than $5\,M_\odot$ and orbital periods above ~1 day at a metallicity suitable for the Small Magellanic Cloud (SMC).

Through follow-up population synthesis, we study the distributions of observable properties of massive semi-detached binaries and Wolf-Rayet binaries, both for constant star formation and for a co-evolving population.

Results: In a ~10^5 $M_\odot$ co-eval population of binary stars, we expect to find ~10 massive Algol binaries at ages of 5-30 Myrs. Our models predict that more massive Algols have longer orbital periods, lower donor to accretor mass ratios and higher surface enhancement of helium and nitrogen than less massive Algols. The observed population of massive Algol binaries in the SMC is well reproduced by our models during the slow Case A phase, except for their effective temperatures where there is an established bias in the observed sample. We show that our models with the Ledoux criterion for convection can explain the radius of the accretors of observed Algol binaries, while previous models in the literature that used the Schwarzschild criterion for convection could not. We show that very efficient semiconvective mixing can lead to partial stripping of the hydrogen envelope in donors of Case B binaries. Our donors of Case AB models are able to match the observed properties of binary WR stars in the SMC while the Case B donors are comparatively much cooler during their core helium burning lifetime, owing to their lower extent of envelope stripping as compared to Case AB donors.

Conclusions: We find evidence for a mass dependence in the observed properties of Algol binaries. We also find observational evidence for the Ledoux criterion for convection over the Schwarzschild criterion. We outline a procedure to constrain semiconvective mixing efficiency from observed populations of Wolf-Rayet and helium star binaries. A detailed spectroscopic survey of the observed massive Algol binaries can provide further constraints to our model predictions.

Key words. stars: massive – stars: evolution – binaries: close – Stars: rotation – Stars: statistics

3.1 Introduction

Low metallicity environments are thought to harbour the first stars which are also very massive (Abel et al., 2002; Bromm et al., 2004; Frebel et al., 2005). Although we cannot directly observe the first stars as yet, some low metallicity dwarf galaxies such as the Small Magellanic Cloud (Venn, 1999; Hunter et al., 2007) are present in our Local Universe. Some of them form massive stars at a high rate (Tolstoy et al., 2009; Weisz et al., 2014). These can indeed be observed and individual massive stars can be studied. Hence, these dwarf galaxies can serve as a proxy to understand the evolution of the very first stars.

Observational studies of massive stars provide strong evidence that most stars are part of multiple systems instead of solitary objects (Sana et al., 2012; Kobulnicky et al., 2014; Moe et al., 2017; Mahy et al., 2021; Banyard et al., 2021). Binary population synthesis studies have already shown the potential of binary effects to help understand the plethora of features visible in the Hertzsprung-Russell (HR) diagrams of stellar clusters (A. P. Milone et al., 2018; Bodensteiner et al., 2020; C. Wang et al., 2020; Sun et al., 2021). de Mink et al., 2013 showed that binary evolution can account for a rapidly rotating population of stars that can explain the emission line stars observed. Binary mergers can also account for blue stragglers and large scale magnetic field observed in a few percentage of stars (Schneider et al., 2016; Schneider et al., 2019; C. Wang et al., 2022).

In binaries with initial donor masses between 10-40 $M_\odot$ (Chapter 2), up to one-third of the them are so close that they undergo mass transfer during core hydrogen burning (Case A). Case A mass transferring binaries serve as excellent test-bed to study massive binary evolution as they have the

many Algol binaries as their observed counterparts (Surkova et al., 2004; Malkov, 2020). In particular, they are ideal for understanding the binary mass transfer efficiency (de Mink et al., 2007; Mennekens et al., 2017; Sen et al., 2022). Understanding their evolution not only enables us to understand the slow nuclear timescale Case A mass transfer phase, but also the preceeding fast thermal timescale Case A phase, where most of the hydrogen envelope of the donor is removed (Sen et al., 2022).

However, the evolution of interacting binaries on the main sequence cannot be studied using rapid binary evolution codes (see, for e.g. Kruckow et al., 2018). Hence, we use detailed binary evolution models to study them here, for a metallicity suitable for the Small Magellanic Cloud (SMC), to compliment the work in Chapter 2 and investigate any metallicity dependence on the observable properties of Algol binaries. The lower metallicity of the SMC (about one-fifth of Solar, Venn, 1999; Hunter et al., 2007) also implies that wind mass-loss and inflation is not expected to play a major role in the evolution of the majority of our models (Kudritzki et al., 1987; Mokiem et al., 2007; Sanyal et al., 2015; Sanyal et al., 2017).

The study of close binary evolution was started by a series of papers by Paczynski (1966), Paczynski (1967a) and Paczynski (1967b), followed by Kippenhahn et al. (1967), Tutukov et al. (1971) and Tutukov et al. (1981) for low and intermediate mass binaries (see also Nelson et al., 2001). van Rensbergen et al. (2010a) (see also van Rensbergen et al., 2011) studied the Case A mass transfer phase in low and intermediate mass binaries, with particular emphasis on spin-up and hot-spots (van Rensbergen et al., 2008) and the formation of accretion disks (Van Rensbergen et al., 2016).

Sen et al. (2022) studied the slow Case A phase of binary evolution using a detailed grid of binary evolution models at a metallicity suitable for the Large Magellanic Cloud (LMC), with initial donor masses from 10-40 $M_\odot$ and orbital periods ≥ 1 day (see also van Rensbergen et al., 2021, for lower mass range). They found that the observed properties of the massive so-called Algol binaries (Mahy et al., 2020; Mahy et al., 2020) are well reproduced by their binary evolution models. They concluded that their accretor spin-up dependent mass transfer efficiency is a viable prescription to model the mass transfer phase in massive binaries. They predict to find ~ 90 binary systems above $10\,M_\odot$ to be in the semi-detached configuration in the LMC.

Schootemeijer et al. (2018) studied the observed binary and apparently single Wolf-Rayet (WR) stars in the SMC (Hainich et al., 2015; Shenar et al., 2016) using single star models and found that the effective temperatures of the binary WR stars can be explained by a shallow hydrogen gradient between the core and the envelope. To reproduce the apparently single WR stars, they found that their stellar models needed very steep hydrogen gradients. Close binary evolution leads to models with a shallow hydrogen gradient. To create steep gradients, they found that the internal semiconvective mixing efficiency has to be very high. Schootemeijer et al., 2019 found that the relative number of blue and red supergiants are also better reproduced with a high semiconvective mixing efficiency.

In this work, as a first part of a two paper study, we study the evolution of close binary systems both during and after the main sequence phase, using grids of detailed binary evolution models. We study the observable properties of massive Algols and WR/helium star+main sequence systems, both for a co-eval population of binary stars as well as a for constant star formation. We comprehensively show the time evolution of these systems in the Hertzsprung-Russell diagram with the help of an animation (Sen, 2020). We then study the observable properties of semi-detached models as a function of its donor mass, where the initial donor mass in our models range from 5-100 $M_\odot$, and compare our model predictions with observed Algol binaries in the SMC (Harries et al., 2003; Hilditch et al., 2005). We also study the properties of the apparently single and binary WR stars in the SMC and compare them with our binary models to derive constraints on the internal semiconvective mixing efficiency in binary

stars.

Section 3.2 gives a description of our model grids and the various physics assumptions. We discuss our results in Sect. 3.4 and compare our models with observed binaries in Sect. 3.5. In Sect. 3.6, we compare our work with relevant works in this field and discuss the implications of our physics assumptions on our results in Sect. 3.7. We give a brief summary and take-home messages in Sect. 3.8.

3.2 Method

In this section, we describe the physics assumptions used in our detailed binary model grids to study the properties of binary systems during the main sequence and post main sequence evolution. We use two sets of models, one where the initial binary parameters are chosen via a Monte Carlo method to emulate a co-eval population of binary stars, and the other where the investigated binary parameter space is sampled at constant intervals. The models were computed using the 1D stellar evolution code MESA[1] (Modules for Experiments in Stellar Astrophysics, Paxton et al., 2011; Paxton et al., 2013; Paxton et al., 2015; Paxton et al., 2018, version 8845).

3.2.1 The synthetic co-eval population of binary stars

This grid consists of 2078 binary models with initial donor masses greater than $5\,M_\odot$. The grid covers an initial mass ratio (ratio of mass of accretor to mass of donor) range of 0.3-0.95 and orbital periods of 1 day to 8.6 yrs. In this range of donor masses, mass ratios and orbital periods, a Monte Carlo method (C. Wang et al., 2020) was used to sample initial binary model parameters assuming a Salpeter initial mass function (IMF) (Salpeter, 1955), a flat distribution of mass ratios and logarithm of initial orbital periods. This translates to a total mass of $\sim 10^5\,M_\odot$ in binary stars between 0.1-100 $M_\odot$. The models are evolved from the beginning of core hydrogen burning to simulate the co-evolution of a population of binary stars.

The chemical composition and stellar physics assumptions of the individual components in a binary model are identical to the single rotating models of Brott et al. (2011). These include differential rotation and internal rotational mixing (Heger et al., 2000), magnetic angular momentum transport (Heger et al., 2005), non-equilibrium CNO nucleosynthesis and stellar wind mass loss. Convection is modelled using standard Mixing Length Theory Böhm-Vitense, 1960, assuming a mixing length parameter of 1.5. We use a moderately efficient value of the semiconvective efficiency ($\alpha_{sc} = 1.0$) following the implementation of Langer (1991) in the super-adiabatic layers of the star that are convectively stable against the Ledoux criterion. To study the effects of increased semi-convective efficiency in binaries, we study another grid of binary models having a semiconvective efficiency $\alpha_{sc} = 10$. Thermohaline mixing physics is modelled as in Cantiello et al. (2010) with efficiency $\alpha_{th} = 1$. Convective overshooting is applied to layers above the core convective zone which are chemically homogeneous using the step function formalism up to 0.335 times the pressure scale height above the convective core. With this formalism, the composition gradients are adequately considered during the rejuvenation process of the mass gaining stars (Braun et al., 1995).

The binary physics follows that of Marchant (2016) and the relevant physical assumptions are described as follows. In the grid with $\alpha_{sc} = 1$, the rotation of both components of the binary are assumed to be synchronised to the orbital period at their zero-age main sequence (ZAMS). In the

---

[1] http://mesa.sourceforge.net/

grid with $\alpha_{\mathrm{sc}} = 10$, the rotation of both components of the binary are assumed to be equal to 0.2 times the critical velocity of the star. Time-dependent tidal interactions are modelled following the implementation of Detmers et al. (2008). While there is no physical reason to assume all stellar components in a co-eval population of binary stars would be tidally synchronised at birth or rotating at exactly the same fraction of its critical velocity, studies have shown that moderate rotation does not significantly affect the evolution of single stars (Brott et al., 2011; Choi et al., 2016). de Mink et al. (2013) and C. Wang et al. (2020) have also shown that the fastest rotating stars might be products of binary interaction.

The mass and angular momentum transfer is taken from Langer et al. (2003a) and Petrovic et al. (2005) while the accretion of angular momentum follows de Mink et al. (2013), based on the results of Lubow et al. (1975) and Ulrich et al. (1976). A distinction is made between disk and ballistic modes of accretion. Mass accretion is also stopped when the accretor reaches critical rotation (Sen et al., 2022), where tidal forces are insufficient to halt the accretor spin-up. This is implemented using a rotational enhancement of the wind mass loss rate, which stops the accreting star from exceeding critical rotation. We assume that the increased mass loss rate is driven by the combined luminosity of both the stars. When this luminosity is not sufficient to drive the excess mass loss, it is assumed that both the stars are engulfed in the transferred material and the binary merges.

Otherwise, we follow the evolution of the binary models until i) core carbon exhaustion of each component whose helium core mass at core helium depletion is less than $13\,M_\odot$, ii) core helium depletion for components whose core helium mass at the end of core helium burning is greater than $13\,M_\odot$, due to numerical reasons, iii) until a model underwent L2 overflow. At the end of core carbon/helium burning of the first component, we compute the evolution of the remaining component as a single star. We note that we only model and follow the evolution of mergers originating from binary models that overflow their second Lagrangian point during the main sequence evolution, and not the mergers coming from the Case B channel.

The assumption of increased mass loss rates at close to critical rotation also leads to a self-consistent way of determining the mass transfer efficiency, without having to resort to a constant efficiency parameter for all our models. The ensuing dependence of the mass transfer efficiency with orbital period has also been found by comparing models with observed binaries (de Mink et al., 2007; Sen et al., 2022). They find evidence for a lower mass transfer efficiency for higher orbital periods. Moreover, in Chapter 2 we found that the accretor spin-up dependent mass accretion prescription, that self-consistently calculates the mass transfer efficiency in our models, is able to explain the observed distribution of Algol binaries in the LMC and Galaxy.

We use the prescription of Marchant et al. (2016) to compute the mass transfer phase when both components of the binary have overflown its' Roche Lobe and the binary model is in a contact configuration. When the individual binary components in the contact binary configuration starts to overflow its' second Lagrangian point, we assume that the binary will merge. If the binary overflows the second Lagrangian point while both stars are burning hydrogen at their core, we model the evolution of the merger as a single star model according to Schneider et al. (2016), where we adopt an appropriate stellar mass, age and central hydrogen abundance for the initial single stellar model after the merger happens. Following Schneider et al. (2019), we treat the mergers as non-rotating stars.

We note that binary models that are in the semi-detached configuration while both stellar components are burning hydrogen at the core are undergoing fast or slow Case A mass transfer phase (O. R. Pols, 1994; Vanbeveren et al., 1998; de Mink et al., 2007; Sen et al., 2022). The slow Case A mass transfer happens at the nuclear timescale while the fast Case A mass transfer occurs at the thermal timescale

(Wellstein et al., 2001). As such, the semi-detached configuration of a binary model during core hydrogen burning essentially captures the slow Case A mass transfer phase, with their observational counterparts being the massive Algol binaries.

3.3 The detailed binary evolution grid

In addition to the above simulation of a co-evolving population of binary stars, we also use a detailed grid of binary evolution models to compare our predictions of the observable properties of semi-detached binaries in the SMC to that of the LMC (Sen et al., 2022), for constant star formation. To make the comparison consistent, we take the same initial donor mass range of 10-40 $M_\odot$ and the population synthesis tools to calculate the distribution functions of the stellar and binary observables. We note that the orbital period boundary for which the binary models undergo Case A mass transfer is smaller for the SMC grid than that of the LMC grid, because the stars are more compact at SMC metallicity. The stellar and binary physics assumptions are the same as is used in our models for the simulation of the co-eval population of binary stars.

3.4 Results

In Sect. 3.4.1, we describe the evolution of the co-eval population of binary stars in the HR diagram, focussing on the models that interact during or just after core hydrogen burning of the donor. Section 3.4.2 reports the number of massive binary systems in different evolutionary stages during the first 40 Myrs of the evolution of a $10^5 M_\odot$ co-eval population of binary stars. In Sect. 3.4.3, we study the evolution of the observable properties of binaries in the semi-detached configuration, as function of the donor mass of the binary. Section 3.4.4 shows the metallicity dependence (between the LMC and SMC) in the observable properties of massive Algol binaries. Section 3.4.5 discusses the observable properties of our models after the main sequence evolution of the donor.

3.4.1 Evolution of the co-eval population of binary stars in the HR diagram

The study of star clusters is of fundamental importance in the understanding of evolution of stars (see, for e.g. Portegies Zwart et al., 2010; Krumholz, 2014; Adamo et al., 2018; Renaud, 2018; Krumholz et al., 2019). For example, studying the morphology of stars in a HR diagram (Russell, 1914) has revealed many essential hints to model the internal structure of stars (Eddington, 1916; Eddington, 1920; Jao et al., 2018). Recently, it has been observed that the distribution of stars in the HR diagram is not one dimensional but is rich with features that are currently not well understood (D'Antona et al., 2017; A. P. Milone et al., 2018; Li et al., 2019; Song et al., 2021).

Moreover, the assumptions taken to study star clusters like co-evolution, same initial composition, singularity of individual objects and minimal impact of rotation are being tested by modern precise measurements of stellar parameters (Harbeck et al., 2003; Lardo et al., 2012; Ferraro et al., 2012; Gerber et al., 2021). For example, photometric studies have revealed a rich variety of features: the extended main sequence turnoff, emission line stars and split main sequences itself (Niederhofer et al., 2017; A. P. Milone et al., 2018; Bodensteiner et al., 2020).

Here, we show the evolution of the simulated co-eval population of binary stars as a function of

their age, through an animation in the HR diagram. The animation can be found at Sen (2020)[2]. We did not need to interpolate between the binary evolution models and required only an interpolation in time for each binary model. Due to the high time resolution in MESA, it did not lead to undesirable errors in the animation. We discuss the features seen in our animation relevant to this chapter here. We use Fig. 3.1 as a reference, which is a zoomed-in snapshot of the animation at 14 Myrs.

The grey line traced on the HR diagram by the collection of pre-interaction binaries (marked by grey circles) denote the Single Star Isochrone (SSI). The binary merger products are marked by grey squares. We note that we only model and follow the evolution of mergers originating from binary models that overflow their second Lagrangian point during the main sequence evolution, and not the mergers coming from the Case B channel. Hence, the number of mergers is likely to be the lower limit to the expected number of merger products. Single star tracks at SMC metallicity are also plotted in the background from 5-100 $M_\odot$ (single star models taken from Schootemeijer et al., 2019).

The animation starts at 0.23 Myrs where we see that all the binaries together form the ZAMS line of the SMC. With time, we see the top of the ZAMS line move to cooler temperatures, as the most massive stars evolve faster than the others. One interesting feature we already see in our simulation at ~1.50 Myrs is that there is one grey circle that is moving to the left of the SSI. Inspection into the binary model revealed that the leftwards migrating grey circle is the donor of a short period binary and is undergoing chemically homogeneous evolution (CHE). We see the first binary undergoing slow Case A mass transfer in the animation at ~1.54 Myrs (the arrow indicates that the binary system is interacting). More such systems start appearing at later ages.

At very early ages (≤ 4.5 Myrs), we find that the mass donating star in the slow Case A phase can be more luminous than the mass accreting star. However, at higher ages, a pattern gradually develops in the slow Case A systems where the accretor is brighter and hotter than the donor. The slow Case A systems have small orbital periods and the binary components are tidally locked. The accretor keeps accreting mass from the donor without reaching critical rotation and rejuvenates, making it hotter, brighter and apparently looking younger than the rest of the co-eval population, and is situated to the left of the SSI in the HR diagram. The accretors of the slow Case A systems, along with the main sequence mergers, eventually gives rise to a Blue main sequence to the left of the SSI (~1.54 Myrs) which remains for the entire evolution of the co-eval population (see also C. Wang et al., 2020).

There is another class of binaries that undergo mass transfer after their primaries have completed core hydrogen burning, or Case B systems. The orbital period of these binaries are such that tides are ineffective and mass transfer from the donor to the accretor is very inefficient. The accretors, due to lack of tidal coupling, spin-up to critical rotation and possibly manifest themselves as OBe stars (at low metallicity such as for the SMC where winds are weak). Owing to the very high rotation, these stars show gravity darkening and their effective temperatures are lower than pre-interaction binaries that are rotating with moderate velocity. The donors, having got stripped of most of their hydrogen envelope resembles a WR/helium star and are seen even further to the left of the hydrogen ZAMS.

The WR/helium stars originating from the Case A channel are hotter than the ones originating from the Case B channel. This is because the envelope of the Case A donors are more severely stripped than the Case B systems due to the shorter orbital period. Hence, the Case A donors have much less hydrogen in their envelopes than the Case B donors and are subsequently much hotter at the surface or, in other words, much closer to the helium main sequence. We notice that the most massive helium stars ($\log L > 5.5$) usually keep moving towards the left of the Hydrogen ZAMS and even may become

---

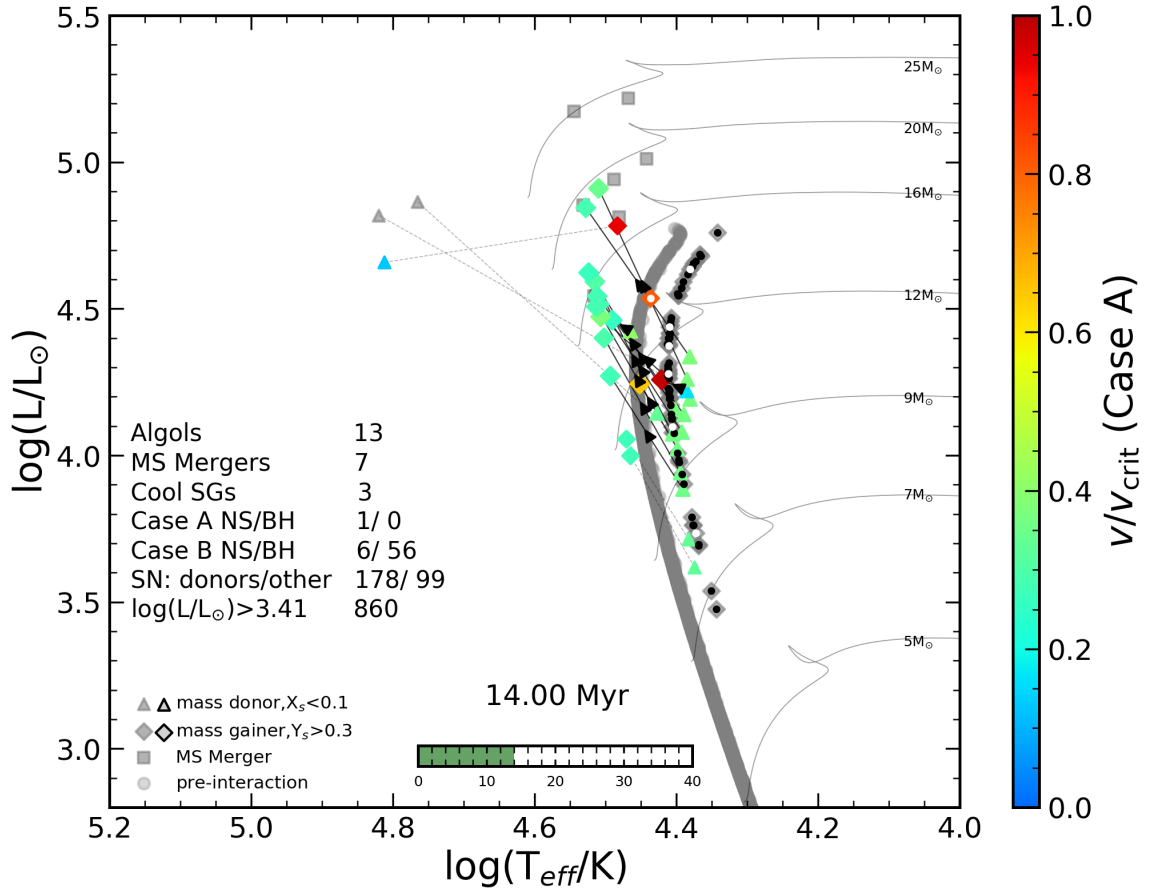[2] https://zenodo.org/record/4068428

Figure 3.1: A zoomed-in snapshot of the animation at 14 Myrs. Translucent grey circles indicate pre-interaction binaries - binaries that have not yet undergone a mass transfer phase via Roche-lobe overflow. Grey squares indicate the merger product when we expect a binary to merge during the Case A mass transfer phase. Mass donors and accretors are indicated by triangles and diamonds respectively. Models that are interacting or have interacted in the past via Case A mass transfer are shown in color, with the colormap showing the rotation of the components as a fraction of its critical rotational velocity (v/v_{crit}). All donors and accretors of binaries that have interacted via Case B/C are shown in grey. A black frame around the triangles for the mass donor indicate that the surface hydrogen mass fraction is less than 0.1. Similarly, a black frame around the diamonds for the mass accretors indicate that the surface helium mass fraction is greater than 0.3. The current age of the co-eval population is displayed in the center bottom with a time bar that fills up as the animation moves forward in time. The table above the legend indicates (from top) i) the number of Algol binaries i.e. models in the nuclear timescale slow Case A mass transfer phase; ii) the number of main sequence merger products that are still burning hydrogen at the core and, iii) the number of cool red supergiants (log T_{eff} < 3.7). The next two rows show the number of main sequence accretors that have a neutron star (white dots) or black hole (black dots) companion, arising from Case A and Case B evolution channels, at that age of the co-eval population. In the next row, we indicate the number of supernova that has already happened up to the current age of the animation. The last line gives the number of pre-interacting binaries having luminosity lesser than the brightest non-interacted binary component by upto 1.5 dex. The individual components of the binaries that are in the semi-detached configuration are joined together with solid black lines with an arrow indicating the direction of mass transfer (donor to the accretor). The individual components that have interacted in the past are connected to each other with grey dotted lines.

hotter than stars in the helium ZAMS (Köhler et al., 2015). Our post-interaction models do not seem to inflate during core helium burning like the single helium star models of Köhler et al. (2015).

Petrovic et al. (2006) investigated the inflation of WR stars as a function of mass-loss and metallicity. They found that their SMC metallicity models do not inflate. Moreover, the inflation is dependent on the mass loss rate of the systems. They found the existence of the critical mass loss rate above which even their Solar metallicity models do not inflate. Noting that our WR/helium stars had undergone a Case AB mass transfer phase where the mass transfer rate was much above the standard critical mass loss rates derived for such systems, we speculate that the previous Case AB mass transfer phase might have an effect on the structure of the star during the core helium burning phase.

3.4.2 Number of binary systems with age

Since the initial donor masses, mass ratio and orbital period of the binaries is derived from a Monte-Carlo simulation with their respective empirical weights, we can study the number of objects in different stages of binary evolution directly as a function of the age of the co-eval population. Fig. 4.1 shows the various numbers of binary systems as function of the age of the co-eval population as shown in the animation that is relevant to the scope of our work. The definition of each of the numbers are as described in the previous section.

Following Shenar et al. (2020), we distinguish between helium stars and helium stars that can show WR like emission features. We assume that stars with luminosity greater than $\log L = 5.5$ can exhibit the WR phenomena, at SMC metallicity. Additionally, the Case A or Case B WR+O star system means that the WR+O star binary is an outcome of Case A or Case B mass transfer phase respectively. Similarly, Case A or Case B helium+OB star systems are those where the system is an outcome of Case A or Case B evolution. At ages less than ~1 Myr we only have pre-interaction binaries and no other types of binary.

At ~ 1.5 Myrs, we see the first Algol system. The number of these systems rise to the order of 10 for the entire simulation. In comparison to the pre-interaction binaries, it is around 1-3%. This is in agreement with the numbers stated in the study of Case A mass transfer phase in Chapter 2 where we find 3% of massive binaries to be in the Algol configuration assuming constant star formation for the LMC.

The number of binary models in our simulation was calculated assuming a co-eval population mass of $10^5 M_\odot$ with stellar masses distributed between 100 and 0.1 $M_\odot$. This lead to 2078 binary models with donor masses above 5 $M_\odot$. Hence, we predict that for a usual cluster like NGC 330 in the SMC (Bodensteiner et al., 2021), we expect to find ~ 10 massive Algol binaries at ages between 0-40 Myrs.

It is to be noted that the number of pre-interaction binaries in our co-eval population decreases after 30 Myrs while in a real cluster the number should always be increasing in accordance with the IMF favouring lower and lower mass stars. We attribute this decrease to the incompleteness caused by modelling stars only upto 5 $M_\odot$. Hence, our predictions are only meaningful up to ~30 Myrs. We see that the number of main sequence mergers and cool supergiants are also of the order of ten during the evolution of the co-eval population. Since we only model the evolution of mergers that happen while both stars are still burning hydrogen at the core, the predicted numbers of mergers and cool RSGs are a lower limit.

We only see the presence of Wolf Rayet stars in our co-eval population till ~ 7 Myrs, with a peak of about 10 systems in each of the Case A and Case B channel. Throughout the remainder of the evolution of the co-eval population, we find 1-10 helium+OB star systems from each mass transfer
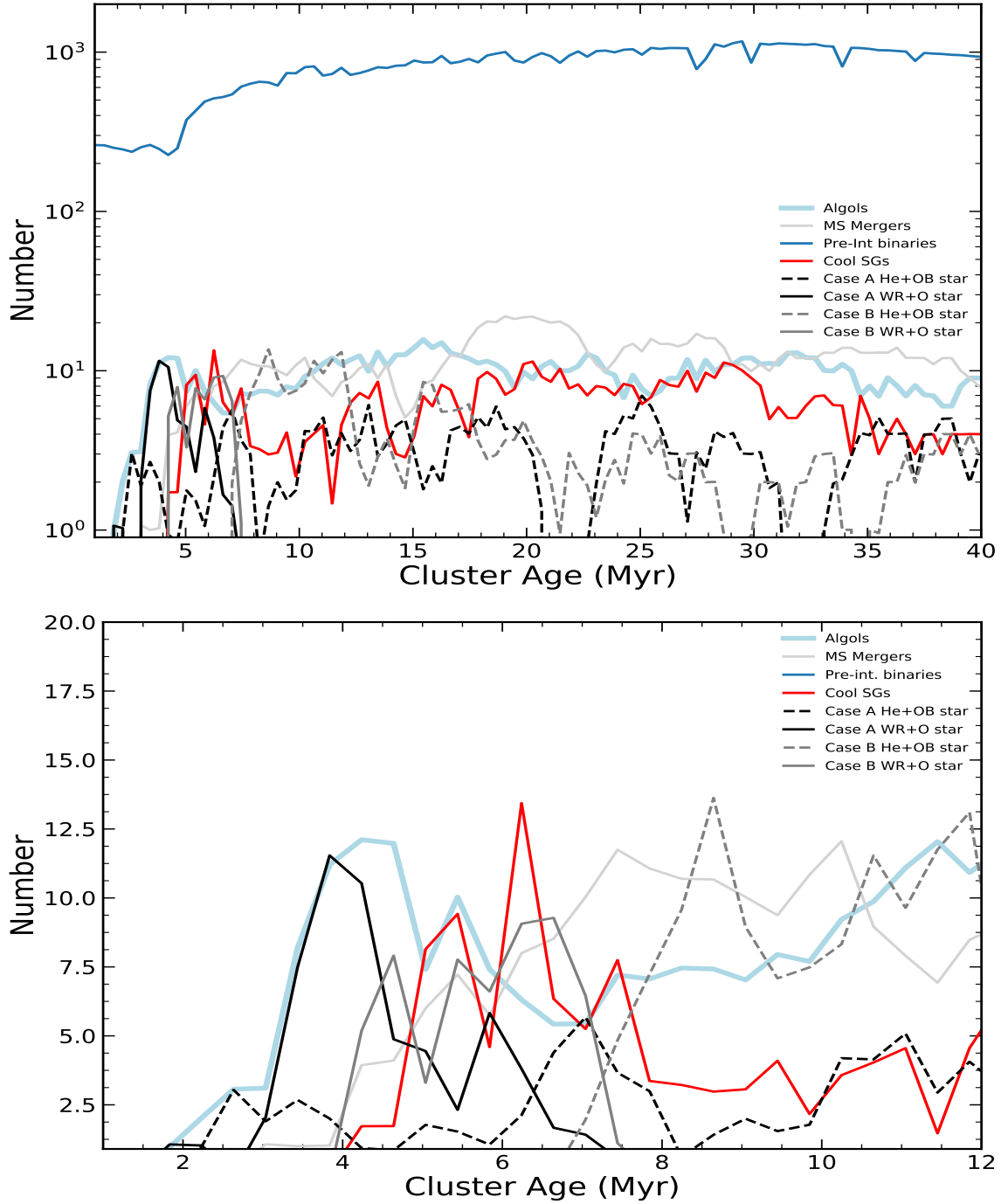
Figure 3.2: Numbers of binary systems in distinct evolutionary phases as a function of the age of the co-eval population for the first 40 Myrs after star formation (top panel). The Algols (thick light-blue line) are the binary systems that are in the slow Case A mass transfer phase. MS mergers (thin light-grey line) give the number of Case A merger products present in the co-eval population and still burning hydrogen. The purple line gives the number of pre-interaction binaries having luminosity less than the brightest non-interacted binary component by upto 1.5 dex. The red line give the number of stars having log T_{eff} < 3.7. We separately plot the number of Wolf Rayet+O star (solid lines) or helium+OB (dotted lines) star binaries originating from Case A (black) and Case B (grey) mass transfer. The bottom panel shows a zoomed-in view of the first 12 Myrs.
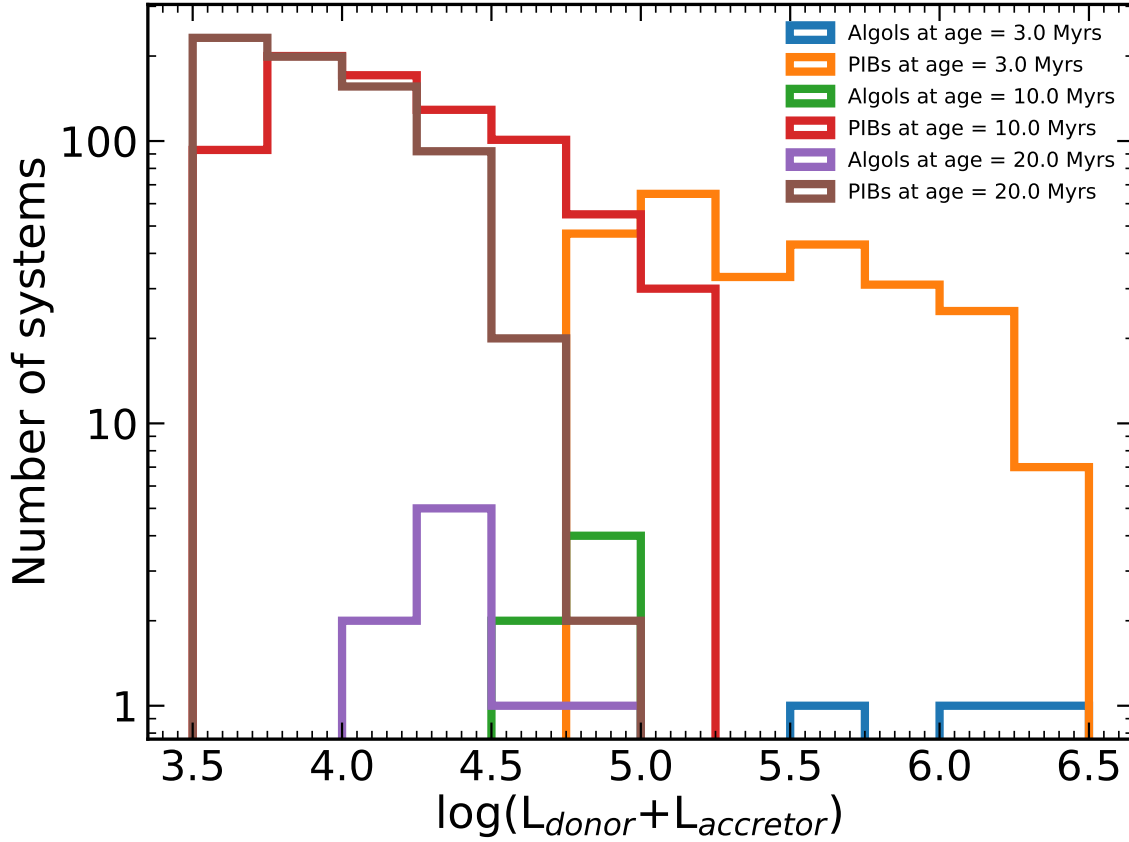
Figure 3.3: Predicted luminosity distribution of Algol binaries and pre-interaction binaries (PIBs) at three specific times after formation in a $10^5 \, M_\odot$ co-eval population of binary stars. The luminosity of a binary model is assumed to be the sum of the luminosities of the individual components.

channel. However, following the discussion in Shenar et al. (2020), we do not expect these systems to show the emission features in their spectra that is unique to WR stars at this metallicity.

Figure 3.3 shows the distribution of the combined luminosity of the Algol binaries and pre-interaction binaries at three different ages of the synthetic co-eval population: 3, 10 and 20 Myrs. We see that the combined luminosity of the Algol binaries are generally on the higher end of the distribution of luminosities of the pre-interaction binaries. Hence, the Algol binaries are more likely to be observed than the comparatively lower luminosity pre-interaction binaries at any given age of the co-eval population. As such, the observational probability to detect Algol binaries amongst pre-interaction main sequence binaries may be slightly greater than just 1%.

3.4.3 Properties of semi-detached systems with donor mass

In Chapter 2, we found evidence of a mass dependence in the binary and stellar parameters of their models in the Algol configuration. To study and explore this dependence further, we show the evolution of our models parameters in the semi-detached phase as a function of the mass of the Roche-lobe filling donor star, keeping in mind that the mass of the donor star can be used as a proxy for the age

Figure 3.4: The evolution of the orbital period (top panel) and mass ratio (bottom panel) versus donor mass during the semi-detached phase of the binary models is marked by small coloured stars, placed with a time difference of 100 000 yr. Coloured squares with a black frame show the position of the observed massive Algol binaries in the SMC (Harries et al., 2003; Hilditch et al., 2005). The colour-bar in the left and right panel shows the mass ratio and orbital period respectively.

of the co-eval population itself. Along with our theoretical predictions, we also mark the position of the observed Algol systems in the SMC. However, we compare our model predictions with the observations in a separate section (Sect. 3.5).
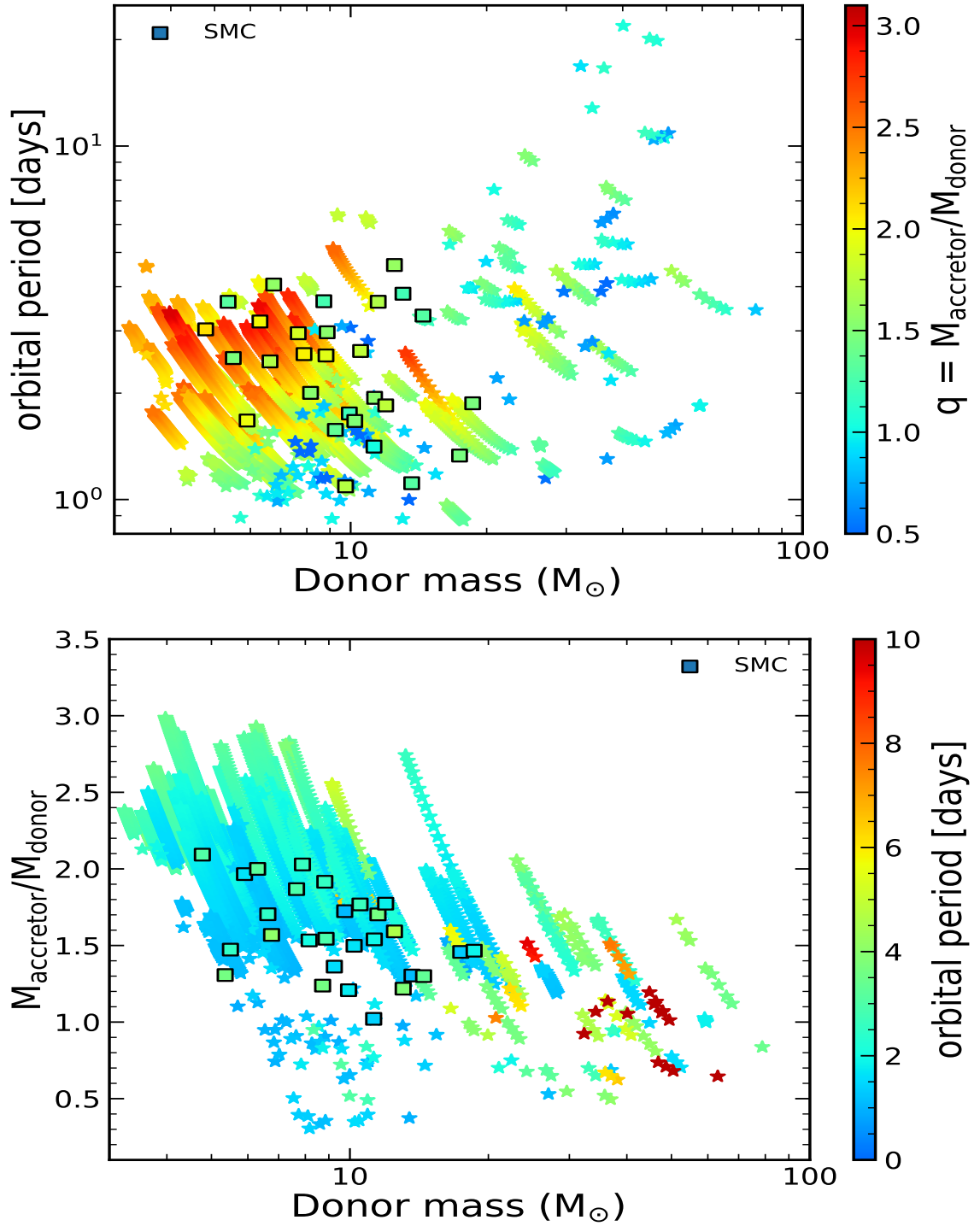
Figure 3.4 shows the evolution of the orbital period (top panel) and mass ratio (bottom panel) of our models during the semi-detached phase as a function of donor mass. Points are plotted at every 0.1 Myrs during the semi-detached phase. We note that since the initial binary parameters in our models was chosen by taking into account the initial mass function and binary distribution functions, the relative number of points are representative of the relative number of systems with the shown orbital periods in a given mass range. Another advantage of using a co-eval population of binary models is that we can study the dependence of a third observable, shown in colourbar, on the evolution of the other two observables. We define the mass ratio as the ratio of the mass of the initially less massive accretor to the initially more massive donor. Since the mass ratio inverts during the thermal timescale fast Case A mass transfer (Wellstein et al., 2001; de Mink et al., 2007), we see that the mass ratio of most of the models during the semi-detached phase is greater than 1 (Chapter 2). In general, the orbital period and mass ratio during the slow Case A phase increase due to the transfer of mass from the currently less massive Roche-lobe filling donor star to the more massive star.

We note that there are some singular 'asterisk' marks in both the panels. These points pick out the semi-detached systems in the fast Case A phase while a series of 'asterisk' markers consecutively signify the slow Case A phase of the model. We see that at donor masses $\geq 25\,M_\odot$, the orbital period of the semi-detached models can be as high as 20 days, in contrast to the maximum of 4 days for the lower donor masses ($\leq 10 M_\odot$). The very massive Algol binaries are predicted to have a larger range (1-10 days) of orbital periods than lower mass Algol binaries (1-4 days). Hence, we expect very young co-eval populations of massive binaries to host Algol binaries with longer orbital periods than older co-eval populations. Similarly, the most massive Algol models ($\geq 25\,M_\odot$) have mass ratios closer to 1 while the less massive models have mass ratios around 2. This is because of the larger core to envelope fraction of the more massive donors compared to lower mass donors.

At donor masses above $\sim 30\,M_\odot$, we find models in the semi-detached configuration with a mass ratio less than 1. Counter-intuitively, in these models the orbital period (top panel) is increasing while the mass ratio is going towards unity (bottom panel). Inspection into the models show that they are undergoing slow Case A mass transfer where the initially more massive star is still the donor star which has been stripped of its hydrogen envelope. The mass ratio has not inverted after the fast Case A mass transfer due to the increased core mass to envelope mass of the very massive stars. The increase in orbital period of these models is due to the elevated wind mass-loss rates from the envelope-stripped donor star. As such, the mass of the current donor star is also higher than the current accretor star, signified by the bluish colour of the markers in the top panel.

Figure 3.5 shows the evolution of the surface helium mass fraction (Y_s, top panel) and nitrogen surface enhancement (bottom panel) of the donors and accretors in the semi-detached configuration during core hydrogen burning. Since both helium and nitrogen are products of the CNO cycle, which is the dominant hydrogen burning cycle in massive stars, their enrichment are related. Shortly after the onset of core hydrogen burning, CNO-equilibrium is established in the convective cores of massive stars. Hence, nitrogen reaches its CNO-equilibrium value while only little hydrogen has been converted into helium.

As the convective core of massive main sequence stars recedes during the main sequence, a hydrogen-helium gradient region (Schootemeijer et al., 2018) is formed in-between the core and the outer envelope. In this gradient region, the helium mass fraction drops from its value at ZAMS to
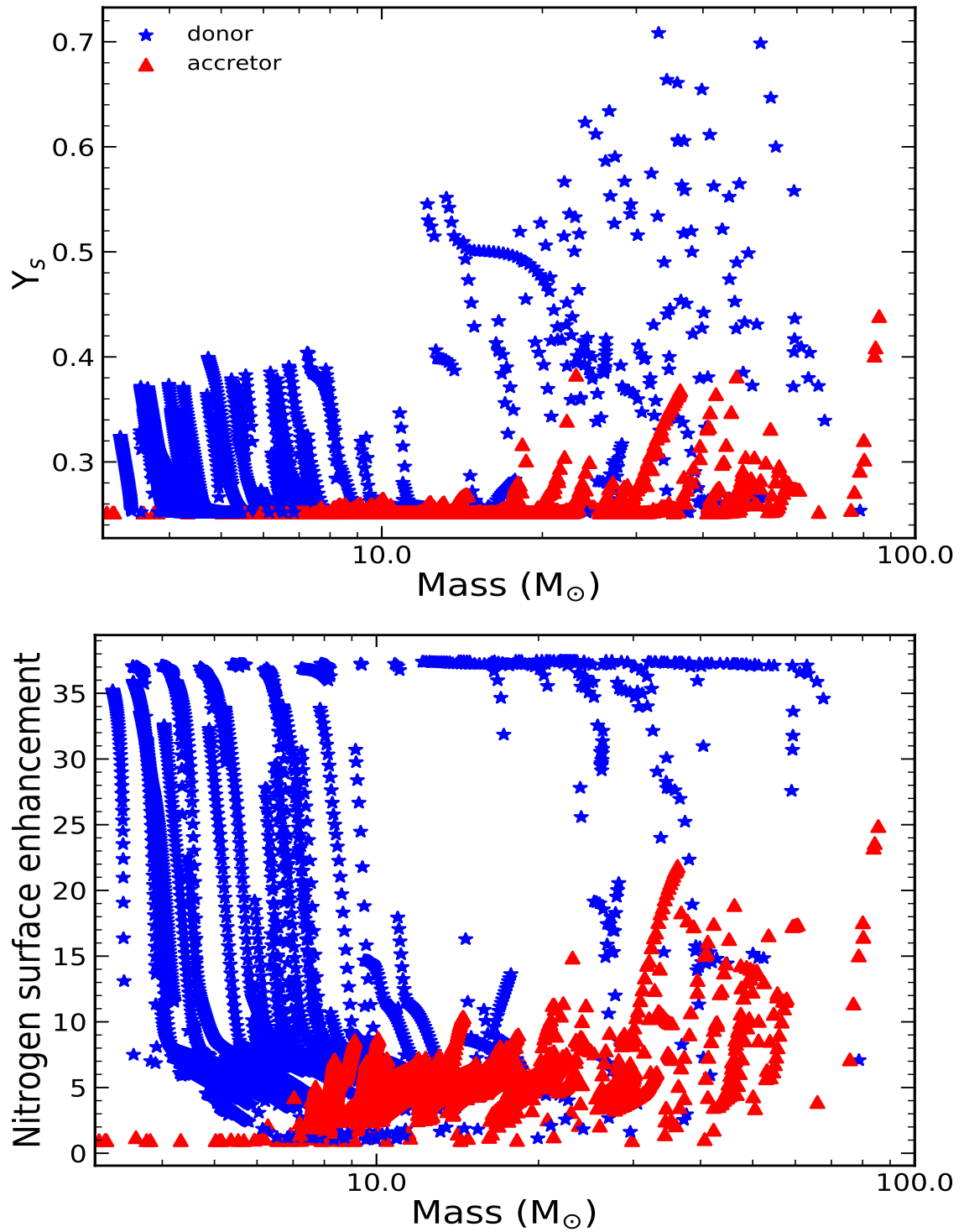
Figure 3.5: The evolution of the surface helium mass fraction (top panel) and surface nitrogen enhancement (bottom panel) of donors (blue asterisks) and accretors (red triangles) versus their respective masses during the semi-detached phase of the binary models. The markers are placed at a time difference of 100 000 yr.

the one currently inside the core. Depending on the semiconvective mixing efficiency, this gradient layer can be mixed with overlying unprocessed matter by semiconvection, thus extending the gradient region to layers above the initial convective core, where both helium and nitrogen are enhanced, but with a nitrogen abundance below the CNO-equilibrium value (Langer, 1991).

Moreover, incomplete hydrogen burning via the CNO cycle can occur just above the outer edge of the gradient region if the temperature is high enough, where some carbon is transformed into nitrogen, but oxygen is not. In the donor stars during the slow Case A mass transfer phase, all these layers are successively removed and their underlying helium and nitrogen enriched layers appear at the surface. These layers also determine the abundances of the matter accreted by the accretor star, where thermohaline mixing dilutes the enrichment as soon as even a small helium enrichment is present in the accreted matter.

We again find distinct differences in the evolution of surface helium mass fraction and nitrogen enhancement between lower mass and higher mass models during the semi-detached phase. Mass donors (blue asterisks) more massive than $\sim 12\,M_\odot$ can have surface helium mass fractions greater than 0.4 and reach upto 0.7 during the slow Case A mass transfer phase while mass donors below $12\,M_\odot$ reach up to 0.4 in surface helium mass fraction. We see a qualitatively similar feature in the surface helium mass fraction of the mass accretors where only mass accretors greater $\sim 15\,M_\odot$ have surface helium enrichment while all lower mass massive accretors do not show helium enrichment at the surface. This is again due to the larger core to envelope fraction of more massive stars, making it easier to expose the CNO enriched layers in more massive stars via envelope stripping.

A similar trend in surface helium mass fraction was found in the Algol models at LMC metallicity in Chapter 2, where higher mass donors and accretors show higher surface helium abundances. However, due to the higher metallicity, the LMC models are less compact than our SMC models and the borderline between the enhancement and no enhancement of surface helium in accretors is expected to be shifted to a lower donor mass.

This mass dependence is even more pronounced in the surface nitrogen enhancement of these systems (Fig. 3.5, bottom panel) where mass donors above $20\,M_\odot$ almost exclusively show CNO-equilibrium surface nitrogen enhancement during the slow Case A phase and the lower mass donors show a gradual increase in the surface nitrogen enhancement towards CNO equilibrium values during the course of the slow Case A mass transfer. On the other hand, the mass accretors show mild nitrogen enhancement with only the most massive accretors showing nitrogen enhancement above 10, due to the high efficiency of thermohaline mixing.

Figure 3.6 shows the evolution of the radii (R_{donor} and $R_{accretor}$) and effective temperatures ($T_{eff,d}$ and $T_{eff,a}$) of the donors and accretors, respectively, as a function of their respective masses during the semi-detached phase. The radius of the donors during the semi-detached phase are determined by the Roche geometry, that is, it depends on mass ratio and orbital period of the binary. For a fixed mass ratio, the radius of the donor has to be larger for longer orbital periods. The top left panel shows that for a fixed donor mass, the radius of the donor is larger for longer orbital periods since the orbital separation is larger, implying a larger Roche-lobe filling radius of the donor. The overall increase of the donor radius with mass captures the mass-radius relation of main sequence stars, as is for the accretor stars.

The radii of the accretor stars depend on the reaction of the stars to the mass accretion, hence, primarily on the mass accretion efficiency. For long period models, the mass accretion efficiency is low, and the radius of the accretors are similar to single stars of the same mass. However, for short-period models, the mass accretion efficiency of our models can be quite high (Chapter 2), and
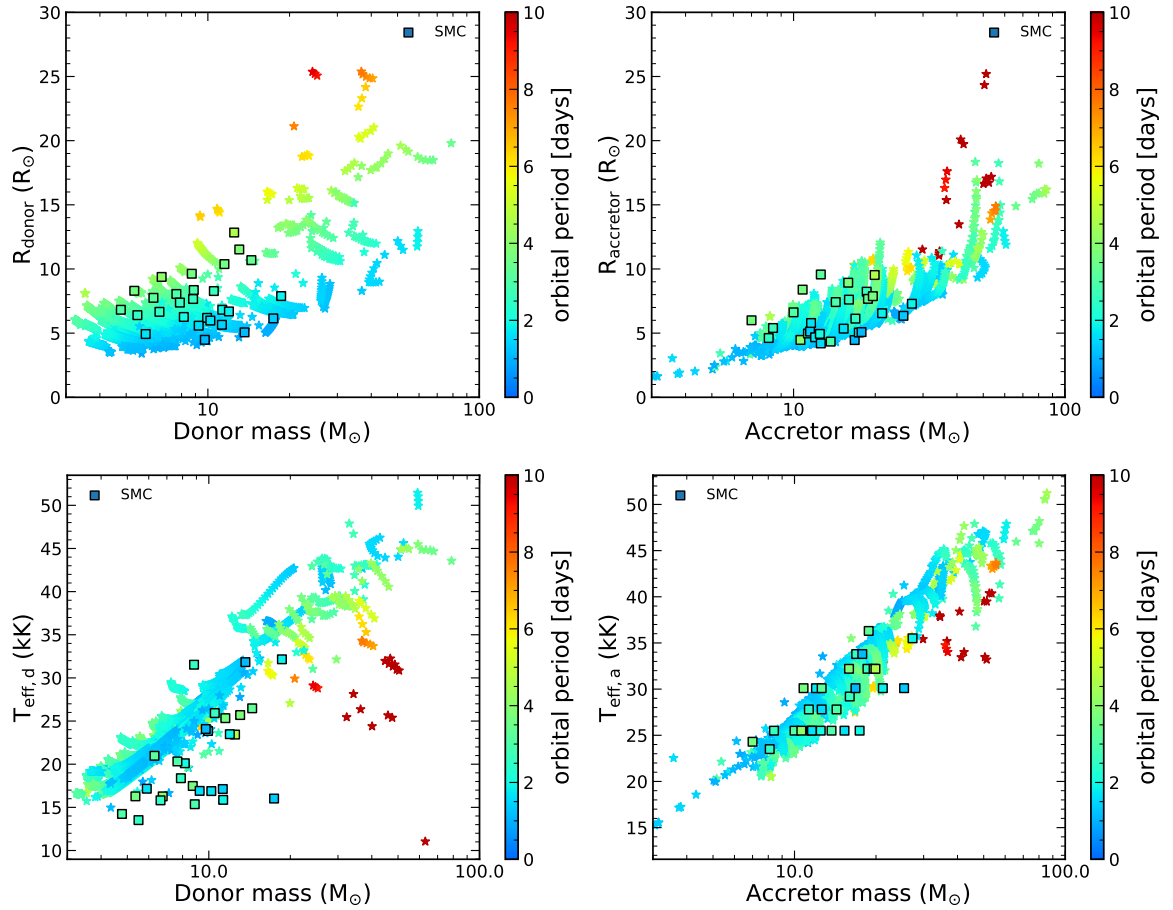
Figure 3.6: The evolution of the stellar radii (top panels) and effective temperatures (bottom panels) of donors (left panels) and accretors (right panels) of the binary models (marked by coloured stars) as a function of their respective masses during the semi-detached phase. The markers are placed at a time difference of 100 000 yr. The radii and effective temperatures of the observed massive Algols in the SMC are marked by coloured squares. The colour-bar shows the current orbital period of the models and observations.
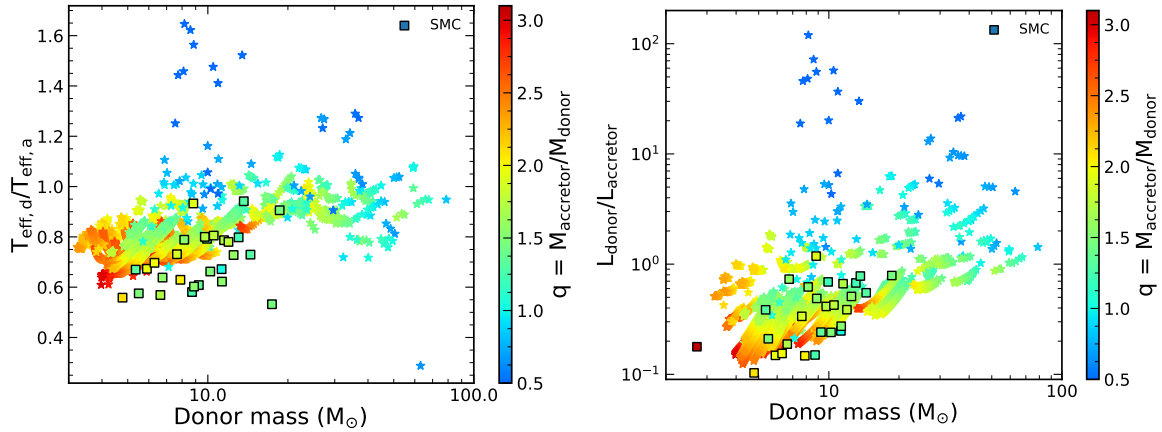
Figure 3.7: The evolution of the ratio of the effective temperatures (left panel) and luminosity (right panel) of the donors to the accretors in the semi-detached configuration. The data is sampled at every 0.1 Myrs. The observed massive Algols in the SMC are marked by coloured squares. The colour-bar denotes the mass ratio of the models at that time-step.

the radius of the accretors then depend on the efficiency of internal mixing, mainly semiconvective mixing (Braun et al., 1995). For efficient semiconvective mixing as is implemented in our models, the accretors are more compact than models with inefficient semiconvection (c.f. model numbers 47 and 48 of Wellstein et al., 2001). We also note that at a fixed accretor mass, models having longer orbital periods during the semi-detached phase have a larger radii (top right panel) because they undergo Case A mass transfer later during the core hydrogen burning and stars tend to expand with age.

The effective temperature of the donors and accretors (bottom panels of Fig. 3.6)) with respect to their respective masses span a narrow range at each mass. Since the radius of the donor is fixed by the Roche lobe radius, the effective temperature is set by the luminosity of the donor. Since the mass of the donor is almost equal to its core mass for binaries in the Algol configuration, and the mass luminosity relation holds during the main sequence evolution, we see that the effective temperature of the donors at a given donor mass is almost independent of the orbital period of the binary. On the other hand, due to the main sequence evolution of the accretors, we see that the effective temperature of the accretors slowly decrease with the simultaneous increase in its mass and the binary orbital period. The effect of the main sequence evolution is suppressed in the mass donating stars as hotter and hotter layers are exposed to the surface due to the loss of the envelope during slow Case A phase.

Figure 3.7 shows the evolution of the ratio of the effective temperatures ($T_{eff,d}/T_{eff,a}$, left panel) and luminosities ($L_{donor}/L_{accretor}$, right panel) of the donor to the accretor as a function of the mass of the donor during the semi-detached phase. We find that, generally, the ratio of effective temperatures and luminosities decrease with the decrease in the mass of the donor. The decrease in the luminosity ratios is attributed to the rising exponent in the mass-luminosity relation for lower mass stars. The difference in luminosity between the components in a lower mass Algol system is higher than that between components in a high mass Algol system because the mass-luminosity relation gets flatter with increasing mass of a star.

For the least massive Algol models in our grid, the ratio between the luminosity can be a factor of 10 or 2.5 magnitudes. We also find that, due to our accretor spin-up dependent mass transfer

efficiency prescription, the ratio of the luminosity depends on the orbital period of the binary. Low orbital period models usually undergo a more conservative mass transfer and the accretors become much more luminous than the donor. This also correlates to the high mass ratio of the models whose luminosity ratios are lowest. These less massive and low luminosity ratio systems are likely to be more difficult to observe than more massive Algol systems.

A similar explanation holds for the effective temperature ratios. We also see that the temperature and luminosity ratios decrease with increasing mass ratio of the models during the semi-detached phase. This signifies that the increase in luminosity of the mass accretor due to accretion of mass is relatively larger than the increase in luminosity of the mass donor due to core hydrogen burning. For the most massive Algols, we see that the luminosity ratio can be larger than one. The mass ratio being lower than one signify that they are currently undergoing slow Case A mass transfer from a more massive donor to a less massive donor.

3.4.4 Dependence on metallicity

Here, we compare model predictions of massive Algol binaries for two different metallicity environments, namely the SMC and the LMC. To do this, we use a similar grid of detailed binary evolution models as in Chapter 2 and assume constant star formation to derive the observable properties of the population of massive Algol binaries in the SMC. The initial donor mass of the binary models range from 10-40 $M_\odot$. The initial mass ratio and orbital period range from 0.30-0.95 and 1-3 000 d respectively. The physics assumptions implemented in these SMC models are the same as discussed in Sect. 3.2. For the ease of comparison, we again show the predictions derived in Chapter 2 for the LMC metallicity in the top panels and compare them with similar population synthesis predictions for the SMC metallicity in the bottom panels.

We note that our co-eval population of binary stars had initial donor masses between 5-100 $M_\odot$. Since the physics assumptions in the SMC models are the same, the predictions from the co-eval population scenario should coincide with the predictions for the constant star formation scenario in the mass range 10-40 $M_\odot$, which we discuss below.

Figure 3.8 shows orbital period distribution of our binary models in the LMC (top panel) and SMC (bottom panel) during Case A mass transfer. We see that the predicted distribution of orbital period of massive Algol binaries in both the dwarf galaxies is expected to be similar, with a peak at ~2 d. There is slightly more number of Algol models above 5 d in the LMC than in the SMC as longer orbital period models can undergo Case A mass transfer at LMC metallicity than in the SMC. Due to stars being more compact in the SMC than in the LMC, we also see that the relative number of contact systems with respect to Algol systems is smaller in the SMC than in the LMC (compare area under hatched histograms in top and bottom panels).

As for the predicted orbital period distribution of our Algol models, we see that our predicted distribution of mass ratio (Fig. 3.9, bottom panel) of Algol binaries in the SMC is similar to that for the LMC, with the peak in mass ratio at $q \sim 2$. We note that the small peak at a mass ratio near 0.5 is not present at SMC metallicity. This is because our accretor models at SMC metallicity are more compact such that none of our models goes through an Algol phase where the initial accretor expands upon mass accretion such that it fills its Roche lobe and transfers mass back to the initial donor star that is now underfilling its Roche lobe (c.f. Chapter 2).

Figure 3.10 compares the orbital period and mass ratio distribution during the semi-detached phase predicted from our binary models in the LMC (top panel) and SMC (bottom panel). We see that
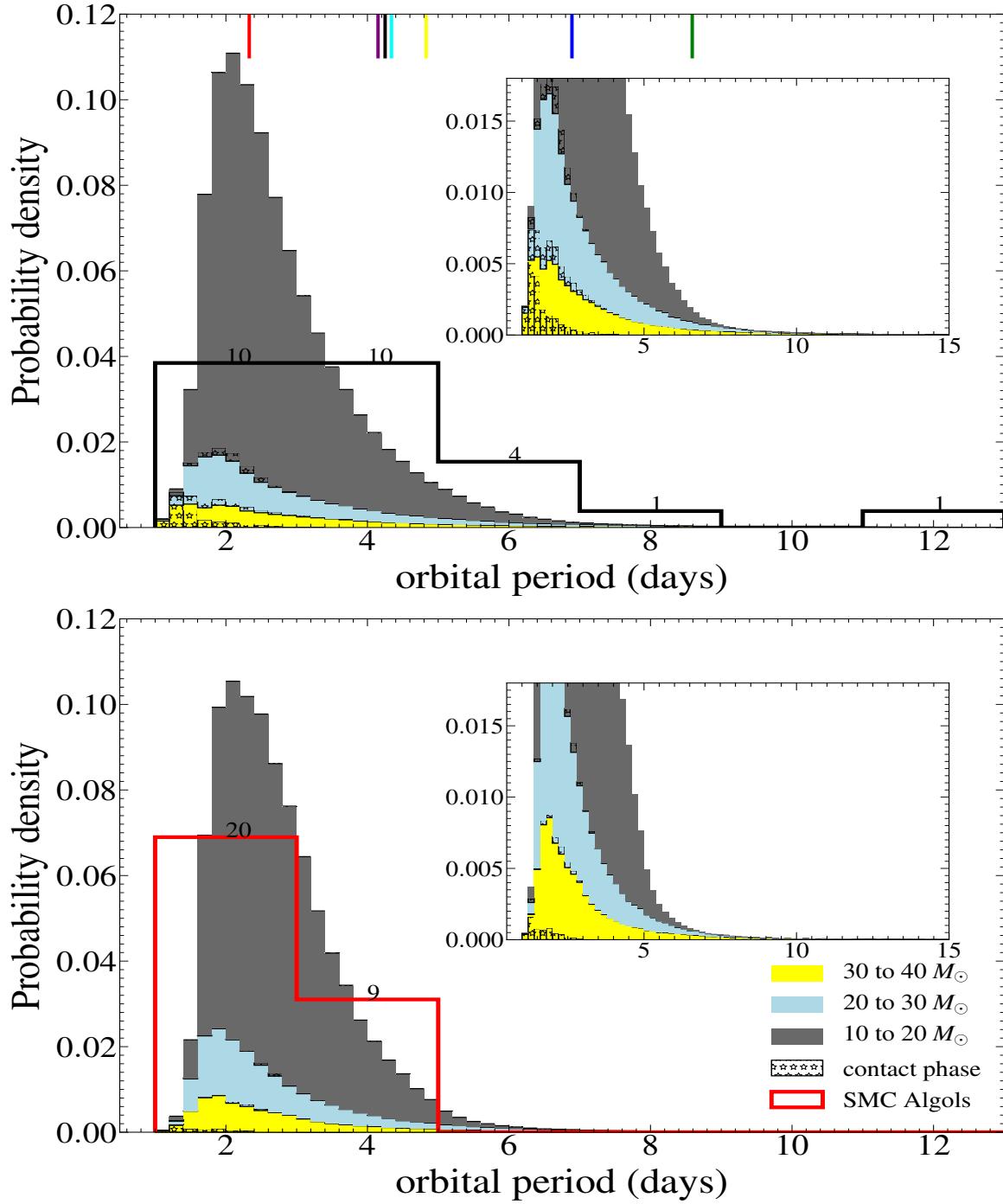
Figure 3.8: Distribution of orbital period of our models during the semi detached phase (unhatched) or contact phase (hatched with stars) of Case A mass transfer. The top panel and bottom panel show the distribution for the LMC and SMC respectively. Color coding marks three different initial mass ranges, as indicated. The ordinate values are normalized such that the sum of the number fractions in all bins equals unity. Vertical lines at the top of the LMC plot denote the orbital periods of the observed Algol systems in the LMC, identified through their color (see legend). The inset shows a zoomed-in distribution of the yellow and blue models. The black and red step-histogram denotes the distribution of orbital periods of 26 observed massive Algol systems in the Galaxy and 29 observed massive Algols in the SMC, respectively. They are normalized such that the area under the individual step histograms (red and black) is equal to the area under the histograms showing the predicted distributions.

51
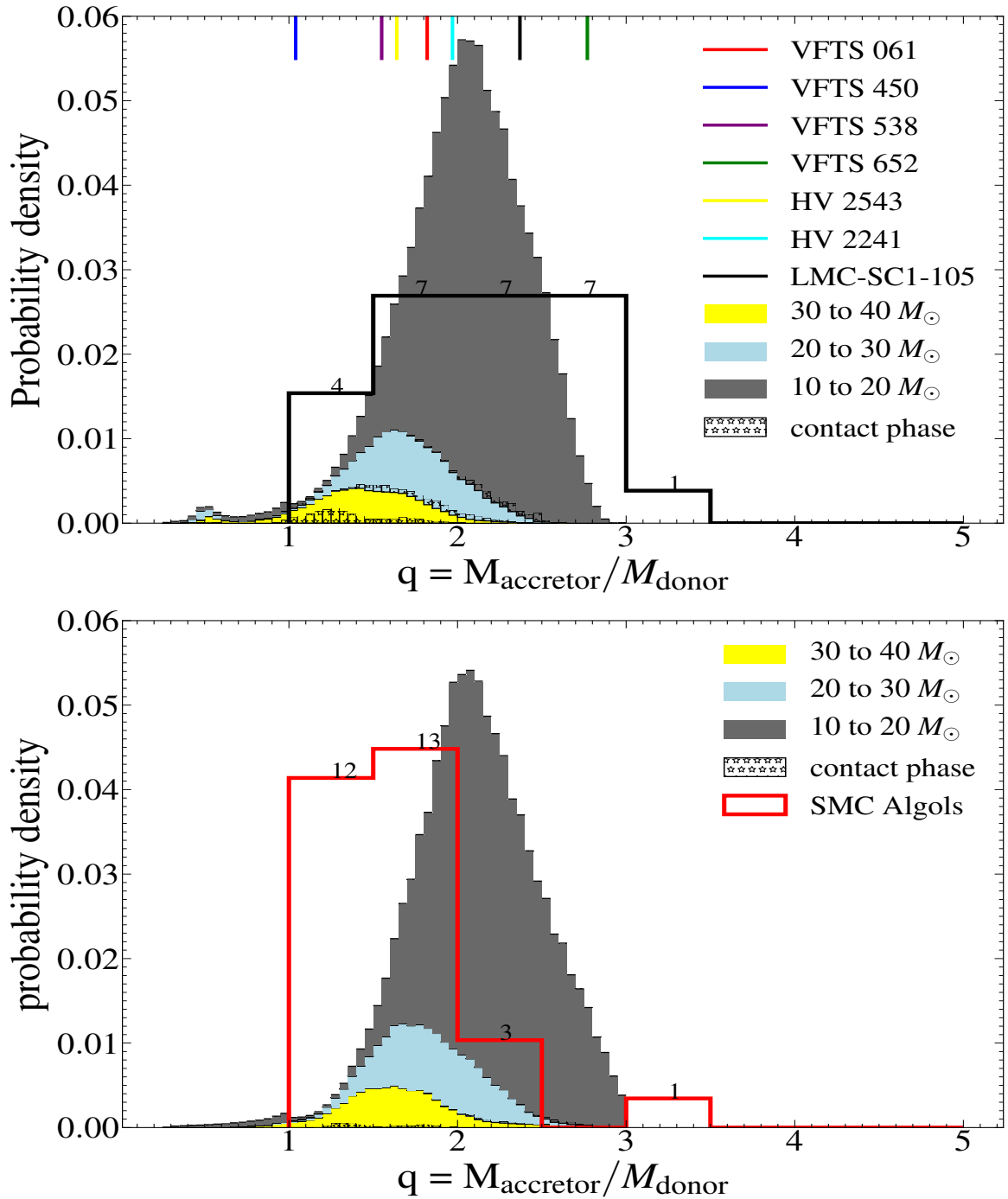
Figure 3.9: Distribution of mass ratio of our models during the semi detached phase (unhatched) or contact phase (hatched with stars) of Case A mass transfer. The top panel and bottom panel show the distribution for the LMC and SMC respectively. Color coding marks three different initial mass ranges, as indicated. The ordinate values are normalized such that the sum of the number fractions in all bins equals unity. Vertical lines at the top of the LMC plot denote the mass ratios of the observed Algol systems in the LMC, identified through their color (see legend). The inset shows a zoomed-in distribution of the yellow and blue models. The black and red step-histogram denotes the distribution of mass ratios of 26 observed massive Algol systems in the Galaxy and 29 observed massive Algols in the SMC, respectively. They are normalized such that the area under the individual step histograms (red and black) is equal to the area under the histograms showing the predicted distributions.
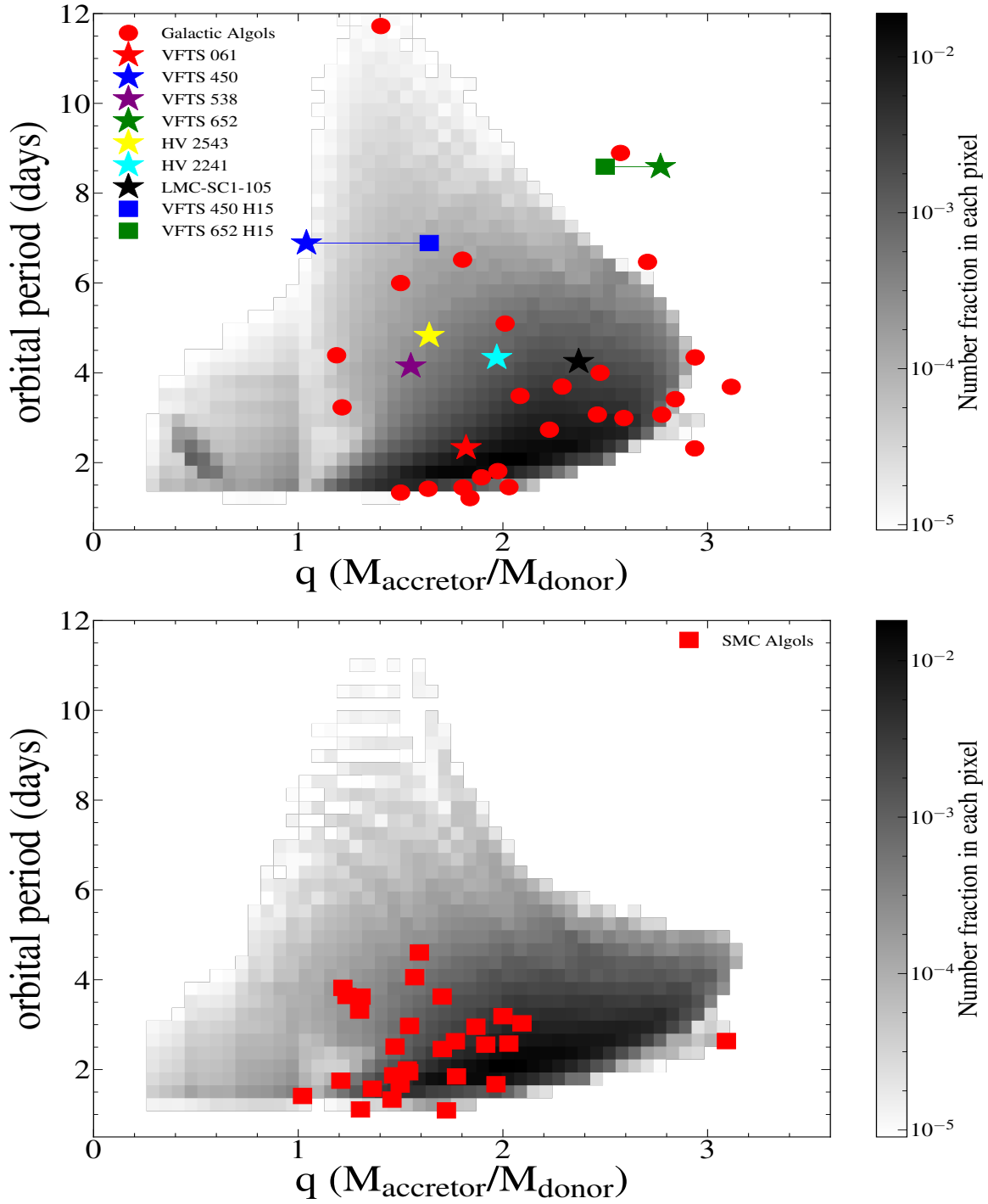
Figure 3.10: Probability distribution of orbital periods and mass ratios of our synthetic populations of semi-detached binaries in the LMC (top panel) and SMC (bottom panel). The grey-scale gives the probability fraction in each pixel. The total probability is normalised such that the sum over the entire area is 1. The different coloured star symbols denote the position of the semi-detached systems in the LMC, and squares denote the binary parameters of VFTS 450 and 652 derived by Howarth et al. (2015). Red circles and squares denote the parameters for the Galactic and SMC Algol systems respectively.
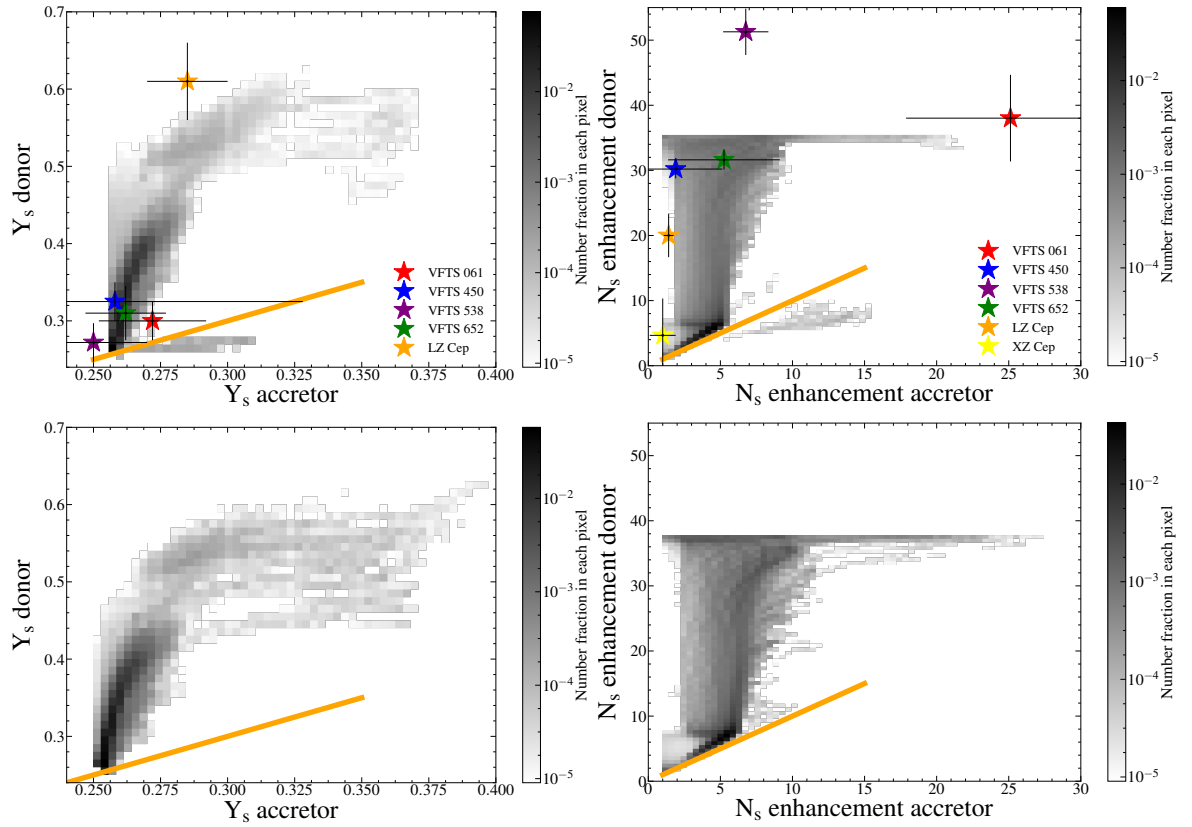
Figure 3.11: Probability distribution of the surface helium mass fraction (Y_s, left panels) and surface nitrogen mass fraction (N_s) enhancement (right panels) of the donor vs the accretor that is predicted to be observed in the semi-detached configuration of the Case A mass transfer phase based on the model grids at the LMC (top panels) and SMC metallicity (bottom panels). The different coloured 'stars' with error bars denote the position of the semi-detached systems of the TMBM survey and the Milky Way. The surface nitrogen mass fraction enhancement of the LMC systems are evaluated w.r.t. to the LMC nitrogen abundance baseline, while the enhancement for LZ Cep and XZ Cep are evaluated w.r.t to the Solar baseline. The grey-scale gives the probability fraction in each pixel. The total probability is normalised such that the integrated sum over the entire area is 1. The orange line indicates where the surface helium mass fraction or surface nitrogen enrichment of the donor and accretor is the same.

the most likely orbital periods and mass ratios predicted by our models are similar in both the two metallicity environments. Above an orbital period of 5 d, there is a sharper decline in the maximum mass ratio of the Algol models with orbital period in the SMC than the LMC. This is because the accretor models at LMC metallicity are less compact compared to those at SMC metallicity. Hence, the tidal forces are marginally more efficient in halting the spin-up of the accretor in the LMC, leading to a slightly greater mass transfer efficiency in the LMC binary models. This leads to a higher maximum mass ratio being able to be reached at long orbital periods in the LMC compared to SMC.

The predicted surface helium and nitrogen mass fraction enhancements are very similar at both metallicities (Fig. 3.11), except that the accretors of the SMC models have a higher maximum helium and nitrogen mass fraction enhancement than the accretors in the LMC. This is because the Algol models in the SMC are less likely to undergo a contact phase. The short-period models that undergo

conservative mass transfer do not have their accretors filling its Roche lobe and undergoing reverse mass transfer on the main sequence, that would lead to the accretor transferring the accreted mass back to the donor (note the absence of models where the accretor has higher surface abundances than the donor in the SMC). Hence, their surface helium and nitrogen abundances remain high.

Last but not the least, we note that the observable properties of the Algol models such as the mass ratio, orbital period and surface abundances are nearly identical for the case of the co-eval population study (Sect. 3.4.3) and the constant star formation assumption as they probe the same evolutionary phase of massive binary evolution, using the same physics assumptions.

3.4.5 Properties of post main sequence systems

After core hydrogen depletion of one of the binary components (which can be the initially more massive or less massive component based on the initial mass ratio of the model, c.f. Nelson et al., 2001), the contraction of the helium core leads to a rapid expansion of the remaining hydrogen envelope, leading to a thermal timescale mass transfer phase. For short-period models that had previously undergone Case A mass transfer, this mass transfer phase is called the Case AB phase, while for long period models that do not interact during core hydrogen burning, it is called the Case B mass transfer phase.

In this section, we focus on the properties of post Case AB models in our grid. However, we also compare their properties with those of post Case B models. The most common and obvious distinguishing feature between models originating from the two mass transfer channels is the orbital period of the binaries. Case AB systems usually have lower orbital periods than Case B systems. In the following paragraphs, we study their distinguishing features in more detail. We note that the donor stars in this stage are stripped envelope stars. Owing to their very high temperatures and the presence of a optically brighter OB star companion, they are harder to observe (Wellstein et al., 2001; Götberg et al., 2020; L. Wang et al., 2021).

Figure 3.12 shows the position of post- Case AB and Case B models in the HR diagram at every 0.3 Myrs during their core helium burning lifetime. As such, the absolute numbers of these points do not have direct physical significance. However, the relative number of points in different regions of the HR diagram denote the likelihood of finding a post- Case AB or Case B model there.

We see that the Case AB donors (coloured triangles) and Case B donors (grey asterisks) are quite distinctly separated in the HR diagram. The Case AB donors are hotter than the Case B donors at the same luminosity. Yoon et al. (2017) found that shorter orbital periods lead to more efficient stripping of the hydrogen envelope in binaries. Hence, Case AB donors are more efficiently stripped than the Case B donors, owing to the short orbital periods. In other words, the Case AB donors are more closer to the helium main sequence and are expected to have smaller surface hydrogen abundance than the Case B donors, which we show later (Fig. 3.13).

Our models predict two different populations of WR/helium star binaries: one with short periods which are more easily observable and one with longer orbital periods that are harder to identify as binary systems. Only the most luminous Case AB donors get sufficiently stripped such that their surface hydrogen mass fraction falls below 0.1 (black frames around triangle markers).

We find that most of the Case AB accretors are critically rotating while a few of the Case AB accretors have moderate rotation and surface helium enrichment (black frames). This is primarily due to the fact that the orbital period increases further during the Case AB mass transfer and tidal forces become weaker, such that most binaries are not tidally locked (see Chapter 2). Only the shortest period Case A binaries stay tidally locked through the Case AB mass transfer phase, enabling them to

Figure 3.12: The evolution of the binary models during the core helium burning phase (central core helium mass fraction between 0.95 to 0.05) of the mass donor. Markers showing their position in the HR diagram are plotted at every 0.3 Myrs during the core helium burning lifetime of the donor. The Case AB donors and accretors are marked with colored triangles and diamonds, respectively, while the Case B ones are marked with grey asterisks and squares. If a donor star has a surface hydrogen mass fraction less than 0.1, the triangles and asterisks are marked with black frames. If the accretor has a surface helium mass fraction greater than 0.3, the diamonds and squares are marked with black frames. The black circles denote the observed single WR stars in the SMC while black squares are the binary WR stars in the SMC (Table 3.1). The colour-bar indicates the rotational velocity of the binary components as a fraction of its' critical velocity. In the background are plotted single star tracks in the SMC from Schootemeijer et al. (2019).

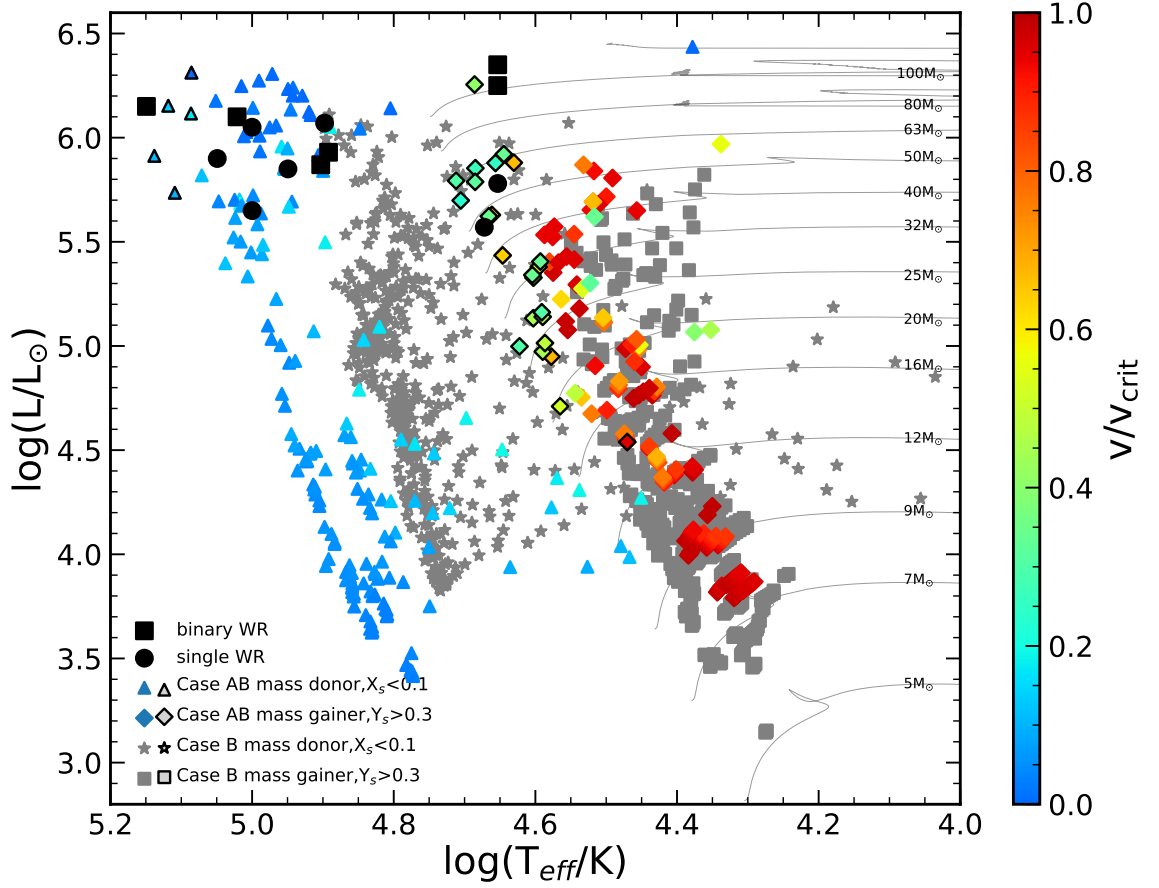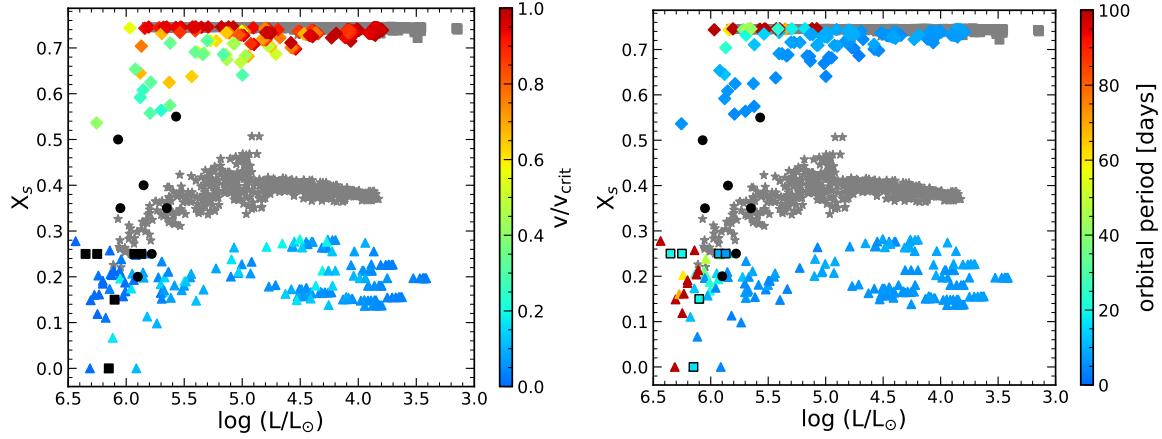Figure 3.13: The evolution of the surface hydrogen mass fraction and luminosity of the donors and accretors of the binary models during the core helium burning phase (central core helium mass fraction between 0.95 to 0.05) of the mass donor. The markers are at every 0.3 Myrs during the core helium burning of the mass donor. The symbols have the same meaning as in Fig. 3.12. The colour-bars indicate the ratio of the rotational velocity to the critical velocity of the binary components in the left panel and the orbital period of the binary in the right panel. The observed binary WR stars are marked with black squares (left panel) or coloured squares with black frames (right panel). The single WR stars are marked with black circles in both panels.

undergo fairly conservative mass transfer, which manifests as an increase in the surface helium mass fraction in the accretors.

Tides are ineffective for the Case B models, having orbital periods greater than 10 days, which make their accretors spin up to critical rotation as soon as they start accreting mass from the donor (Packet, 1981). Moreover, our mass transfer algorithm evaluates the mass transfer efficiency based on the spin-up of the accretor. Hence, the Case B models undergo inefficient mass transfer, where the accretor does not increase in mass or luminosity. These Case B donor stars get significantly cool towards the end of core helium burning and reach or cross the hydrogen ZAMS. These stars, owing to their stripped envelopes and a correspondingly higher luminosity-to-mass ratio, are expected to have higher wind mass-loss rates. For the luminous donors, their companions may still be the less massive star of the binary, and hence be hard to be detected. These Case B donors, towards the end of their helium burning lifetime, can be observed as O dwarfs with high surface helium abundances, which might explain the observed OB stars with abnormally high helium surface abundances (see Sec. 5.5.3 of Holgado, 2018).

Figure 3.13 shows the surface hydrogen mass fraction as a function of the luminosity for the binary components that has undergone Case AB or Case B mass transfer at 0.3 Myr intervals during core helium burning of the mass donor. As expected from the positions in the HR diagram (Fig. 3.12), the Case AB donors have lower surface hydrogen mass fraction than the Case B donors. The Case AB donors have ~0.2 surface helium mass fraction while the Case B donors with $\log L/L_\odot \leq 5.5$ have surface hydrogen mass fraction ~0.4. This is because the envelope stripping is more efficient in the short-period Case AB binaries (with orbital periods less than 20 days, see right panel) when compared to long-period Case B binaries. Above $\log L/L_\odot \simeq 5.5$, in the SMC, stripped envelope stars are expected to manifest themselves as WR stars (Shenar et al., 2020), with much higher wind mass loss rates than ordinary helium stars. Hence, the most luminous Case B donors have a lower surface

hydrogen mass fraction than 0.4.

On the other hand, we see that the Case AB accretors which are not critically rotating (left panel) show lower surface hydrogen mass fraction than ~0.72 (i.e. helium is enhanced), while the critically rotating Case AB accretors show no surface helium enhancement. Moreover, we only see that the more luminous Case AB accretors show surface hydrogen depletion. This is because the strength of tidal interactions increase with stellar mass, and thereby the with the stellar luminosity. None of the Case B accretors show any surface hydrogen depletion (they start rotating critically very soon after the onset of mass transfer) as our mass transfer efficiency is a strong function of the orbital period of the binary.

Here, we again see that the Case AB and Case B models can give rise to two separate populations of WR/helium stars with main sequence companions. Hence, the surface hydrogen abundance/effective temperature of the binary components, orbital period of the binary and luminosity of the binary components constitute a triplet of observable parameters that can be used to distinguish between Case AB and Case B binary systems. We also note that our models predict a larger number of Case B systems but the higher orbital period of these models means that they are harder to be detected as binaries.

3.5 Comparison with observations

In this section, we compare the predicted properties of our models during core hydrogen burning (Case A) and after core hydrogen depletion (post- Case AB and Case B) with observations. First, we compare observed Algol binaries in the SMC, LMC and Milky Way with the properties of the models during the semi-detached phase and then the observed WR+main sequence binaries in the SMC with the properties of post- Case AB and Case B models.

3.5.1 Algol binaries in the SMC

Harries et al. (2003) and Hilditch et al. (2005) derived the stellar parameters of 50 double-lined spectroscopic binaries in the SMC, having B-band magnitude less than 16 and orbital period less than 5 days. Of them, 29 systems are in the semi-detached configuration (see table 1 of de Mink et al., 2007). Their orbital solution of the light curves did not reveal any eccentric orbits in the observed Algol systems. The orbital periods and mass ratios were taken from Udalski et al. (1998) and Wyrzykowski et al. (2004). The effective temperatures of the more massive components were determined from its spectral type, with the average temperature difference between spectral sub-types in the range O6-B2 being ~1800 K (see Fig. 3.6). However, there exists significant uncertainty in estimating the temperature from spectral type at SMC metallicity (Massey et al., 2004). Moreover, the effective temperature of the Roche-lobe filling component is derived from the I-band flux ratio, which is not very sensitive to the temperature for massive OB stars (de Mink et al., 2007).

From Fig. 3.4, we see that the orbital periods of the observed Algol binaries are in good agreement with our model predictions in the semi-detached phase (top panel). However, the mass ratios (colour coded in the top panel) of the observed Algols are slightly lower than that of our models at the corresponding orbital periods. This feature is more clearly visible from the bottom panel where we see that our models reach mass ratios up to three while the observed Algols have a maximum mass ratio around two. We note that observationally it is harder to detect high mass ratio binaries. We also see a weak trend of decreasing mass ratios with increasing donors masses in the right panel, in agreement

with our models. The absence of observed massive Algols with mass ratios below unity in the mass range 5-20 $M_\odot$ is because the predicted counterparts are in fast Case A mass transfer phase that occurs at the thermal timescale, so it is hard to catch such binaries in observations. We also note the absence of observed binaries in the high mass range, where our models predict longer orbital periods and lower mass ratios of massive Algol binaries.

The radius of the donor stars are in excellent agreement with the models in the semi-detached, being constrained by the Roche-lobe geometry (Fig. 3.6, top left panel), along with its trend with the orbital period of the binary. The accretor radii (top right panel) are also in good agreement, although the trend with the binary orbital period is not seen in some of the observed Algols. The agreement of the predicted radii of our accretor models with that of the observed binaries gives credence to our implementation of moderately efficient semiconvection with the Ledoux criterion for convection in our models (c.f. models of de Mink et al., 2007). The accretor models of (de Mink et al., 2007), that adopted a Schwarzschild criterion for convection, were reported to be consistently smaller in radii than the observed radii of the observed accretors in the massive Algol binaries in the SMC.

The largest discrepancy is seen in the effective temperatures of the donors and accretors with our models. The donor temperatures of the observed Algols are significantly lower than our model predictions. The effective temperatures of the accretors are in better agreement, though the difference in effective temperatures between adjacent spectral types are too large to make a concrete conclusion. A careful comparison of the trend with orbital period (bottom left panel) reveals that most of the accretor temperatures and their binary orbital period are not simultaneously reproduced adequately by our models.

The left panel of Fig. 3.7 shows that the ratio of the donor to accretor effective temperatures of our models are indeed higher than the observed Algol binaries derived from the I-band flux ratio. We calculate the luminosity of the observed binaries assuming that the stars are in thermal equilibrium and the Stefan-Boltzmann equation holds. The right panel of Fig. 3.7 shows that even though the luminosity ratios of our models seem to reproduce the luminosity ratio of the observed Algols well, the mass ratios of the binaries are not simultaneously reproduced. The mass ratios of our models are in general higher at a particular value of the luminosity ratio than the observations.

A detailed spectroscopic survey of these massive Algol binaries in the SMC, with updated effective temperatures and surface abundances are expected to provide more constraints to test our model predictions further. Photometric observations in additional bands would also improve the determination of the donor temperatures and the temperature ratios.

3.5.2 Metallicity dependence

We see relatively more number of observed short-period Algol systems in the SMC than in the LMC and Milky Way (Fig. 3.8). Also, there is a tail of observed long-period Algol binaries in the LMC and the Milky Way above 5 d. We note however that the observational sample of Harries et al. (2003) and Hilditch et al. (2005) was limited to a maximum orbital period of 5 d. However, considering how our predicted distribution of orbital period drops of in the SMC, we do not expect more than 1-2 Algol binaries in the SMC above 5 d. We predicted ~90 massive Algol binaries in the LMC. Since the star formation rate of SMC is one-fourth of that of the LMC, and assuming constant star formation, we expect that the massive Algol population in the SMC is nearly complete.

Moreover, we see that the peak in the mass ratio distribution of the observed Algol binaries in the SMC (Fig. 3.9) is at a smaller value than what is predicted by our models. If the observed sample

in the SMC is indeed complete, we see that the mass transfer efficiency in the SMC Algol models need to be lower than what is assumed in our work. On the other hand, if the observed sample is not complete, we have already discussed that high mass ratio binaries are difficult to detect and most of them may not have been found yet in the SMC. This can lead to a skewing of the distribution of the mass ratios of the currently observed Algols to lower values in the SMC.

We note that the simultaneous distribution of the orbital period and mass ratio of the observed Algol binaries in the SMC (Fig. 3.10) does not match with the most likely orbital periods and mass ratios predicted by our SMC models. The observed binaries have in general smaller mass ratios than what is predicted by our binary evolution models. As discussed earlier, either we are still missing the high mass ratio Algols in the SMC because it is harder to detect them, or our mass transfer efficiency is too conservative to reproduce the massive Algols in the SMC, if they constitute a complete sample.

3.5.3 WR stars in the SMC

Ever since the first discovery of WR stars in the SMC (Breysacher et al., 1978; Azzopardi et al., 1979), the total number of WR systems has grown to twelve, after the work by Massey et al. (2001) and Massey et al. (2003). Radial velocity measurements on all these WR stars (Foellmi et al., 2003; Foellmi, 2004) find 5 of the 12 WR stars to have a binary star companion. Recently, the stellar parameters of both the apparently-single and binary WR stars have been derived using stellar atmosphere calculations by Hainich et al. (2015) and Shenar et al. (2016) respectively. Their deduced parameters are listed in Table 3.1, using the nomenclature introduced by Azzopardi et al. (1979) for the SMC systems.

The position of the WR stars in the HR diagram are shown in Fig. 3.12. Shenar et al. (2016) found that the luminosity of the SMC AB6 greatly exceeded its Eddington luminosity. They remarked that it might be due to light contamination from a third stellar object. Shenar et al. (2018) re-investigated this system and derived more accurate physical parameters. They conclude that it is probably a quintuple system, where the WR star (star A) is in a 6.5 day period with an O star (star B), with another single star C, and star D forms a 140 days period wide binary with a BH or B2 V star. Lastly, we call the WR stars that are to the left (right) of the hydrogen ZAMS as hot (cool) WR stars respectively.

We focus on comparing our binary models with the binary WR stars in the SMC. We find that (Fig. 3.12) the position of the binary WR stars in the HRD is well reproduced by our post Case AB mass donors, with the only exception of SMC AB5a/b which is a quintuple system (Shenar et al., 2018). This system in particular may be a product of chemically homogeneous evolution, as studied by Koenigsberger et al. (2014).

The orbital periods (Fig. 3.13) and the surface hydrogen mass fraction (Fig. 3.13) of the binary WR stars are also in decent agreement with our models, especially when the error-bar in the surface abundance (± 0.05) is taken into consideration. We predict, owing to the short orbital periods of these binaries and the high masses of these systems, that the remaining four of them (SMC AB3, AB6, AB7, AB8) may be products of Case AB mass transfer and their companion may show surface helium enrichment (Fig. 3.5).

There is a large spread in the surface hydrogen mass fraction (Fig. 3.13) and effective temperatures (Fig. 3.12) of the apparently single WR stars. We see that the surface temperatures of the hot apparently-single WR stars resemble those of Case AB donors but show much higher surface hydrogen mass fraction than what is predicted by post Case AB donor models. Despite being very hot, their surface hydrogen resembles that of post Case B mass donors. Hence, there is a clear discrepancy between the stellar parameters of the apparently-single WR stars in the SMC with the predicted

Table 3.1: List of WR stars in the SMC and their properties.

Name	Period (days)	log L ($L_\odot$)	Teff (kK)	X_s
SMC AB 1		$6.07^{+0.2}_{-0.2}$	79^{+6}_{-6}	$0.50^{+0.05}_{-0.05}$
SMC AB 2		$5.57^{+0.1}_{-0.2}$	47^{+3}_{-3}	$0.55^{+0.05}_{-0.05}$
SMC AB 3	10.1	$5.93^{+0.05}_{-0.05}$	78^{+5}_{-5}	$0.25^{+0.05}_{-0.05}$
SMC AB 4		$5.78^{+0.1}_{-0.2}$	45^{+3}_{-3}	$0.25^{+0.05}_{-0.05}$
SMC AB 5a	19.3	$6.35^{+0.1}_{-0.2}$	45^{+5}_{-5}	$0.25^{+0.05}_{-0.05}$
SMC AB 5b	19.3	$6.25^{+0.15}_{-0.15}$	45^{+10}_{-7}	$0.25^{+0.20}_{-0.20}$
SMC AB 6	6.5	$5.87^{+0.15}_{-0.15}$	80^{+20}_{-5}	$0.25^{+0.05}_{-0.05}$
SMC AB 7	19.6	$6.10^{+0.1}_{-0.1}$	105^{+20}_{-10}	$0.15^{+0.05}_{-0.05}$
SMC AB 8	16.6	$6.15^{+0.1}_{-0.1}$	141^{+60}_{-20}	$0.00^{+0.15}_{-0.15}$
SMC AB 9		$6.05^{+0.2}_{-0.2}$	100^{+6}_{-6}	$0.35^{+0.05}_{-0.05}$
SMC AB 10		$5.65^{+0.2}_{-0.2}$	100^{+6}_{-6}	$0.35^{+0.05}_{-0.05}$
SMC AB 11		$5.85^{+0.2}_{-0.2}$	89^{+6}_{-6}	$0.40^{+0.05}_{-0.05}$
SMC AB 12		$5.90^{+0.2}_{-0.2}$	112^{+6}_{-6}	$0.20^{+0.05}_{-0.05}$

The apparently single WR stars do not have any orbital period value. The list is adapted from Hainich et al. (2015) and Shenar et al. (2016). The parameters of SMC AB6 are taken from Shenar et al. (2018).

properties of our binary models.

3.5.4 Peculiar O dwarfs

Holgado (2018, page 107, Sec. 5.3.3) found a small number of O dwarfs with surface helium mass fraction ~0.6 in the Galaxy. The spectroscopic masses of these systems are above 20 $M_\odot$ and they also show clear signatures of binarity. These systems may be long period post Case B systems towards the end of core helium burning where the post Case B mass donors starts to inflate past the hydrogen ZAMS, while having surface helium mass fraction ≥ 0.6 (c.f. Fig. 3.12 and Fig. 3.13).

3.5.5 Be+helium star binaries

L. Wang et al. (2018) studied a sample of 264 Be stars using archival ultraviolet spectra from the International Ultraviolet Explorer Satellite (see also, Götberg et al., 2020; L. Wang et al., 2021). Their analysis lead to the confirmation of already detected Be+helium star binaries ϕ Per, FY CMa, 59 Cyg, and 60 Cyg. Moreover, they found twelve new candidate Be+helium star binaries. D. Gies et al. (2019) report that they have started spectroscopic observations at the Apache Point Observatory and Cerro Tololo Inter-american Observatory to measure the orbital motion of the Be star and search for spectral features from the helium star in the optical band. D. Gies et al. (2019) also report the commencement of a new program of the Hubble Space Telescope under Cycle 26 where they will collect ultraviolet spectra that can be used to characterise the binary and stellar parameters of the candidate binaries. As such, their results will provide new constraints to our models of binary evolution post the mass transfer phase.

3.6 Comparison with earlier work

3.6.1 Properties of Case A binaries

The properties of Case A binaries at the SMC metallicity was earlier studied by de Mink et al. (2007) where they concluded that their models were unable to explain a large fraction of the observed Algol binaries in the SMC. In particular, the radius of the accretor stars were often under-predicted by their models. Our models are able to reproduce the radius of the accretors much better. We attribute this difference to the lower overshooting assumed in their models when compared to our models, and their use of the Schwarzschild criterion to model convection instead of the Ledoux criterion used in our models. Both these assumptions lead to stellar models that have smaller radius (see, for e.g., Wellstein et al., 2001).

As in our work, de Mink et al. (2007) were unable to explain the extreme temperature ratios of the Algol binaries and attributed this discrepancy to the I-band flux ratios from which they were determined. The I-band flux ratios are not very sensitive to temperature differences as they cover only the Raleigh-Jeans tail of the spectrum. Hence, we expect a detailed spectroscopic survey of the Algol binaries in the SMC will provide more accurate and precise temperatures of their binary components as well as provide surface abundance measurements which can be used to constrain our model predictions further.

In Chapter 2 we performed a detailed study of the Case A mass transfer phase using a model grid consisting of detailed binary evolution models suitable for the LMC metallicity. We find that our results at SMC metallicity are similar in terms of the general properties of systems in the slow Case A mass transfer phase. As such, we also find most of our models to spend a large fraction of their slow Case A mass transfer phase in the orbital period range of 1-4 days and mass ratios around 2. Moreover, we also find that the properties of very massive Algol binaries are quite different from the lower mass massive binaries. The most massive binaries can have orbital periods of up to 10 days and mass ratios around 1 during the slow Case A phase.

As such, the contribution to the Algol phase from very massive binaries come from relatively higher orbital period binaries. Since the mass transfer efficiency of higher period systems are low in our mass transfer prescription (Chapter 2), we see that the mass ratios of the higher mass Algol binaries are also lower, nearer to unity. Moreover, more massive stars also have a higher core to envelope ratio. An example of such a massive Algol system is VFTS 450, where we see it has a orbital period of 6.89 days and mass ratio near unity.

A similar trend is found in the distribution of surface abundances where the most massive mass donors (> $10\,M_{\odot}$) show surface helium mass fraction (Fig. 3.5, top panel) above 0.4 and mass accretors show slight helium enhancement. This is in contrast to lower mass massive Algols where the mass donors reach a maximum surface helium abundance of 0.4 and the accretors are not helium enriched at all. A similar trend is seen in the study in Chapter 2 where we find that the helium and nitrogen enhancement of their binary models are mass dependent, with the highest enhancement seen in the most massive models. We see the same behaviour in our models with respect to their surface nitrogen enhancement (Fig. 3.5, bottom panel).

Most of the earlier work on Algol binaries were done for low to intermediate mass binaries. Mennekens et al. (2017) found evidence of non-conservative mass transfer in Algol binaries in the mass range of $0.1...8\,M_{\odot}$ (van Rensbergen et al., 2010b). While our mass transfer efficiency prescription was able to explain most of the Algol binaries in the LMC and Milky Way (Chapter 2),

we find that a more non-conservative mass transfer episode may have to be adopted to explain the massive Algol binaries in the SMC.

3.6.2 Properties of post Case AB and Case B systems

Schootemeijer et al. (2018) did a detailed theoretical study of the physical properties of the 12 WR stars in the SMC using MESA single stellar evolution models to determine their probable formation channels. Using their novel definition of the slope of the hydrogen gradient in the stellar envelope, they find that the WR stars in binaries agree (in particular, their effective temperatures with surface hydrogen mass fraction) with stellar models with shallow hydrogen gradient above the convective core of the star. On the other hand, the properties of apparently single WR stars are well reproduced by single star models having a steep hydrogen gradient.

Then they investigate the evolution of the slope of the hydrogen profiles in single star models with their evolution. They find that the hydrogen gradient remains shallow until the end of core hydrogen burning and starts to rapidly increase post hydrogen depletion when the star expands to red supergiant dimensions. Hence, stars that get stripped in binaries during Case A or early Case B evolution should have shallow hydrogen gradients. On the other hand, very wide binaries that interact via late Case B/ Case C, or survive a common envelope phase should have a steep hydrogen gradient. Moreover, they find that accretors that are able to accrete mass during the Case A mass transfer phase from its companion may also develop steep hydrogen gradients due to the growth of the convective core.

They conclude that the observed WR binaries might be a product of stable Case A or early Case AB mass transfer which leads to shallow hydrogen gradients while the apparently single WR stars, after arguing that single star stripping is unlikely at SMC metallicity (see, however, Shenar et al., 2020), may be products of late Case B/C evolution or be the accretors of previous Case A mass transfer that eventually goes through a common envelope phase with a compact object.

We find that both our post Case AB and Case B donors show similar hydrogen gradients. This is because of the moderately efficient semiconvection ($\alpha_{sc} = 1$) that we use in our models. Regardless of the mass transfer channel, the hydrogen gradient region in the donor stars face the same semiconvective instability post the depletion of central hydrogen and hence show similar gradients in the hydrogen profile. We find the hydrogen profile in our donor models to be similar to the ones shown in the top panel of fig. 9 in Schootemeijer et al. (2018). This is expected because we use the same mixing physics in our binary models as their work.

Our Case AB donors, that have shallow hydrogen profiles, are able to reproduce the stellar parameters of the binary WR stars, and their binary orbital periods. However, our Case B donors not only have much higher orbital periods than what is observed in the binaries, but also are cooler than most of the binary WR stars discovered. This is because our Case AB donors are more stripped than the Case B donors, containing a much smaller hydrogen envelope. Accordingly, the Case AB mass transfer phase has removed more of the hydrogen gradient region and the hydrogen surface mass fraction is lower and they are hotter.

As already predicted in Schootemeijer et al. (2018), the stable mass transfer channel is unable to reproduce the population of the apparently single WR stars in the SMC. Very steep hydrogen profiles are needed to simultaneously reproduce the high effective temperature and surface abundance combination of the apparently single WR stars, while our Case AB/B donors show shallow hydrogen profiles. However, this leads to the exciting prospect of finding compact objects around the apparently single WR stars as the remaining channel to form these systems (Schootemeijer et al., 2018). It

remains to be investigated how likely this channel is to account for almost all of the apparently single WR stars.

Götberg et al. (2017) and Götberg et al. (2018) studied the effect of metallicity on the envelope stripping of binary donors and the resulting ionising radiation from the stripped stars. Their models covered a mass range of 2-20 $M_\odot$ and they only considered binaries that undergo mass transfer after core hydrogen depletion of the donor. As we have seen, our Case A donors are hotter than our Case B donors during their core helium burning lifetime. Moreover, the total amount of hydrogen remaining after mass transfer is also lower for our Case A models than the Case B models. Hence, we predict two separate populations of stripped stars arising from the two mass transfer channels.

3.6.3 Effect of semiconvective mixing efficiency

Schootemeijer et al. (2018) showed that the observed apparently single WR stars can be better reproduced by models that have a very steep hydrogen gradient between the core and the envelope. To explore this possibility, we compute another grid of binary models with a semiconvective mixing efficiency of $\alpha_{sc} = 10$. In these models, we find that the hydrogen gradient is very steep for the mass donors that undergo Case B mass transfer. However, these models also have a large hydrogen envelope remaining even after a Case B mass transfer when compared to the models with moderately efficient semiconvective mixing (i.e. $\alpha_{sc} = 1$).

We illustrate the difference in the structure and evolution of models with different semiconvective mixing efficiency in Fig. 3.14, where we show two models with similar initial binary parameters from the two grids. The initial mass ratio of both the models are 0.58. The initial donor mass and orbital period of the $\alpha_{sc} = 1$ model is equal to 48.6 $M_\odot$ and 944 days respectively. The initial donor mass and orbital period of the $\alpha_{sc} = 10$ model is equal to 47.9 $M_\odot$ and 996 days respectively. Both these models undergo mass transfer after core hydrogen depletion of the donor. However, we find significant differences in the structure of the mass donors after the Case B mass transfer phase.

For the $\alpha_{sc} = 10$ model, the Case B mass transfer does not strip the outer hydrogen envelope completely up to the composition gradient region whereas in the $\alpha_{sc} = 1$ model the envelope stripping is much more efficient and strips the mass donor all the way down to the hydrogen gradient region. The $\alpha_{sc} = 10$ model gets stripped down only to 35 $M_\odot$ while the $\alpha_{sc} = 1$ model gets stripped to 28.5 $M_\odot$ (top panel of Fig. 3.14). This is because models with very efficient semiconvective mixing efficiency are more compact, and tend to live their helium burning phase as blue supergiants rather than red supergiants (Schootemeijer et al., 2019; Klencki et al., 2022). As such, these models do not expand to extremely large sizes after core hydrogen depletion and their response to mass loss is different. The bottom panel shows the hydrogen profile of the mass donors of both the models at central helium burning mass fraction of 0.75. We see that the higher semiconvective efficiency model has a very steep hydrogen gradient but also a more massive hydrogen envelope than the moderately efficient semiconvection model.

The model with $\alpha_{sc} = 10$, despite having a very steep hydrogen gradient has a lower effective temperature than the model with $\alpha_{sc} = 1$ because it retains a more massive hydrogen envelope. Due to convergence issues with massive helium cores, our models were stopped at core helium depletion. However, we see that a mass transfer phase post central helium depletion (Case BC) in the $\alpha_{sc} = 10$ model has the potential to strip the remaining hydrogen envelope, exposing the steep hydrogen gradient at the surface. This resulting structure of the star will be similar to the structure of stars Schootemeijer et al. (2018) found necessary to reproduce the observed properties of apparently single WR stars in

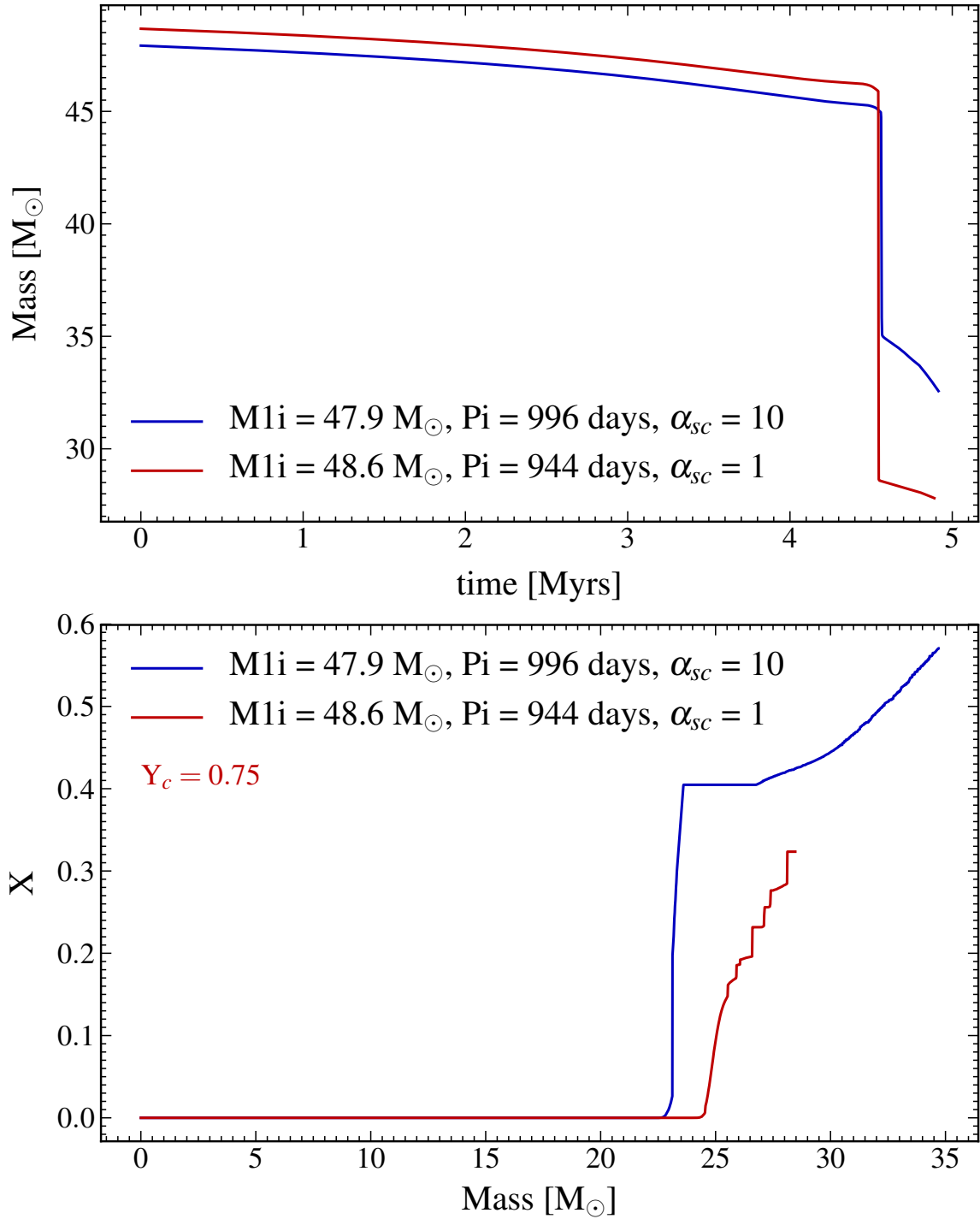Figure 3.14: *Top panel:* The evolution of the donor mass with binary age for the two example binary models from the two grids. *Bottom panel:* The hydrogen profile in the mass donor of the two example models during core helium burning when the central helium mass fraction has reduced to 0.75. The initial mass ratio of the binary in both the models is ~0.58. The other parameters are given in the legend.

the SMC. The donor being a Wolf-Rayet star, it may be difficult to identify it as part of a binary in the observations. Since the apparently single WR stars are also very massive, their companions are expected to remain the less massive star of the binary, as the mass transfer phase may not lead to an inversion of the mass ratio of the binary (see Fig. 3.4, bottom panel).

Figure B.1 shows the distribution of the individual binary components of models in the HR diagram having semiconvective efficiency $\alpha_{sc} = 10$, as in Fig. 3.12. We see that above $\log L \simeq 5.0$, the post Case B donors are not hotter than the hydrogen ZAMS stars. This is because of the large hydrogen envelope left after the Case B mass transfer phase, which makes the donor cooler. However, the surface hydrogen mass fraction of the donors is similar to the models with $\alpha_{sc} = 1$ (Fig. B.2). Hence, models with increased the semiconvective efficiency also cannot reproduce the observed properties of the apparently single WR stars in the SMC during their core helium burning phase. However, these models have the possibility to lose their remaining hydrogen envelope and get hotter after another mass transfer phase post core helium depletion, which may then resemble the apparently single WR stars in the SMC. We note however that the remaining lifetime of this phase is very short and may not be able to explain the entire population of the apparently single WR stars in the SMC.

3.7 Key assumptions and uncertainties

3.7.1 Envelope inflation

The study of envelope inflation is well documented in the literature starting from the study by Kato (1985) who found the existence of an extended radiative envelope above a convective core using the compton scattering opacity in very massive stars. Ishii et al. (1999) investigated the same phenomena using the updated OPAL opacities and found a metallicity dependent curving of the Zero Age main sequence to lower temperatures both in hydrogen and pure helium stars. These works were followed by Petrovic et al. (2006) and Grafener et al. (2012) who studied the effects of envelope inflation on the properties of WR stars and luminous blue variables. Sanyal et al. (2015) and Sanyal et al. (2017) did a comprehensive study of the effects of inflation on hydrogen rich massive main sequence stars in the LMC and other metallicities. Grassitelli et al. (2016) investigated the unstable envelopes of WR stars and found that they are unstable to radial pulsations in the mass range of 9-14 $M_\odot$.

Petrovic et al. (2006) investigated the inflation of massive helium stars at different metallicities and found that none of their SMC metallicity models inflate. However, with increase in metallicity they find that inflation sets in at lower initial mass helium stars. We find that our Case A stripped mass donors do not inflate. However, Case B donors have much more remaining hydrogen mass in their envelope and have larger radii and are cooler. Köhler et al. (2015) found that their SMC helium star models start to inflate at around $\log L = 6.0$. Even though the exact extent of the effect of inflation at SMC metallicity is model dependent in the literature, our post mass transfer donors generally agree quite well with the pure helium ZAMS studied in the literature.

3.7.2 Efficiency and stability of mass transfer

Observations of binary models have shown that a rich variety of constraints on mass transfer efficiency in models are needed. While some require a low mass transfer efficiency (Langer et al., 2003b), others require a substantially higher efficiency (Wellstein et al., 1999). Some studies have also found that mass transfer efficiency reduces with decreasing mass ratio of the system (Petrovic et al., 2005) and

increasing orbital periods (de Mink et al., 2007). Our mass transfer model does in principle reproduce some of these correlations observed in the massive binaries, and the distribution of Algol binaries in the LMC and Galaxy.

In our models, the efficiency of mass accretion decreases when a star reaches critical rotatio. Hence, long period systems that are not tidally locked reach critical rotation on accreting a very small percentage of their mass (Packet, 1981). These models show a low mass accretion efficiency. This assumption implies that we remove all the excess transferred material that cannot be accreted, via stellar winds. Such a mass transfer model is simple and probably has to be replaced with a more detailed model. However, our mass transfer model do indeed show some promising results in the sense that our binary models are able to reproduce the observed distribution of massive Algol binaries.

C. Wang et al. (2020) were able to show quantitatively that the luminosity range of the rapidly rotating stars that had undergone a mass transfer phase in their models is in good agreement with the observed Be star population in NGC 330 (A. P. Milone et al., 2018). However, they found that to accurately reproduce the relative number of Be stars to blue stragglers, the criteria for the stability of mass transfer, based on the combined luminosity of stars being able to remove the excess transferred mass, need to be relaxed. Accordingly, the number of WR+OB star binaries in our models will increase. Nevertheless, the properties of the additional systems will not be fundamentally different to the ones already studied in our grid.

3.8 Conclusions

In this work, we have studied the distribution of various classes of binary systems in a synthetic co-eval population of binary stars using detailed binary stellar evolution models at SMC metallicity. We have focussed on the properties of binary systems which are undergoing core hydrogen or helium burning. We compared our model predictions with the observed massive Algol binaries and WR stars. We outline our key results in the following paragraphs.

We predict to find of the order of 10 binaries in the Algol configuration at any time from ~1.5-30 Myrs in a typical co-eval binary population of ~10^5 $M_\odot$ at SMC metallicity. We do not expect this number to vary significantly with metallicity (c.f. Chapter 2). At very young ages of the co-eval population (2-7 Myrs), we predict to find ~10 WR+OB star binaries (Fig. 4.1).

The observable binary properties of our models in the semi-detached configuration such as the orbital period (Fig. 3.4) and the radius of the individual binary components matches well with observations. This implies that the physics of mass and angular momentum transfer used in our models are viable, as well as our implementation of convective mixing efficiencies. As already shown in Chapter 2, here we also demonstrate that the orbital period and mass ratio distribution of the most massive Algols are skewed towards higher periods and lower mass ratios. At the same time, we find that the surface enhancement of helium and nitrogen to be higher in more massive systems.

However, our models are not able to reproduce the ratio of effective temperatures (Fig. 3.7) and luminosity (Fig. 3.7) of the binary components of the observed Algol binaries. This implies two possibilities: 1) our models lack physics ingredients like the inclusion of energy transport between the binary components during the mass transfer phase, or 2) the derived temperatures of the observed Algol binaries are inaccurate since they are obtained from the respective spectral types and I-band flux ratios which are not sensitive to temperature differences for the case of massive OB type stars. Moreover, the mass ratio of the observed Algol binaries are lower than what is predicted by our models.

This implies that the observed sample is not complete as high mass ratio binaries are harder to observe, or our mass transfer efficiency model does not work for the massive Algol binaries in the SMC.

We find that our binary models that undergo Case AB mass transfer are able to reproduce the observed surface abundances, orbital period, luminosity and effective temperatures of the observed binary WR stars in the SMC. However, our Case A models are too stripped to match the relatively higher surface hydrogen mass fraction observed in the apparently single WR stars. On the other hand, our Case B models have too large of a hydrogen envelope to match the observed relatively hotter effective temperatures of the apparently single WR stars.

We find that an increased efficiency of internal semiconvective mixing in Case B mass donors lead to very steep hydrogen gradients that are needed to explain the apparently single WR stars (Schootemeijer et al., 2018). However, we find that these models also retain a large hydrogen envelope after the Case B mass transfer phase. We propose that another mass transfer phase in these models after core helium depletion can in principle remove the leftover hydrogen envelope and expose the steep hydrogen gradient to the surface, making the star hotter as well.

Our Case B donors show properties that can explain the peculiar O dwarfs found by Holgado (2018). These O dwarfs are found to have surface helium abundances of 0.6 or higher and show signs of binarity while their luminosity and effective temperatures correspond to stars in the main sequence. Our Case B models that are in the late stages of core helium burning (Fig. 3.12) have properties that are similar to the observed peculiar O dwarfs.

References

Abel, T., G. L. Bryan and M. L. Norman (2002), *The Formation of the First Star in the Universe*, Science **295** 93, arXiv: `astro-ph/0112088` [`astro-ph`] (cit. on p. 32).

Adamo, A. and N. Bastian (2018), "The Lifecycle of Clusters in Galaxies", *The Birth of Star Clusters*, ed. by S. Stahler, vol. 424 91 (cit. on p. 36).

Azzopardi, M. and J. Breysacher (1979), *New Wolf-Rayet stars in the Large Magellanic Cloud.*, Astronomy and Astrophysics **75** 243 (cit. on p. 58).

Banyard, G. et al. (2021), *The observed multiplicity properties of B-type stars in the Galactic young open cluster NGC 6231*, arXiv e-prints arXiv:2108.07814, arXiv: `2108.07814` [`astro-ph.SR`] (cit. on p. 32).

Bodensteiner, J., H. Sana, L. Mahy et al. (2020), *The young massive SMC cluster NGC 330 seen by MUSE. I. Observations and stellar content*, Astronomy and Astrophysics **634** A51, arXiv: `1911.03477` [`astro-ph.SR`] (cit. on pp. 32, 36).

Bodensteiner, J., H. Sana, C. Wang et al. (2021), *The young massive SMC cluster NGC 330 seen by MUSE II. Multiplicity properties of the massive-star population*, arXiv e-prints arXiv:2104.13409, arXiv: `2104.13409` [`astro-ph.SR`] (cit. on p. 39).

Böhm-Vitense, E. (1960), "Theory of the hydrogen convection zone", *Aerodynamic Phenomena in Stellar Atmospheres*, ed. by R. N. Thomas, vol. 12, IAU Symposium 338 (cit. on p. 34).

Braun, H. and N. Langer (1995), *Effects of accretion onto massive main sequence stars.*, Astronomy and Astrophysics **297** 483 (cit. on pp. 34, 47).

Breysacher, J. and B. E. Westerlund (1978), *Wolf-Rayet stars in the Small Magellanic Cloud.*, Astronomy and Astrophysics **67** 261 (cit. on p. 58).

Bromm, V. and R. B. Larson (2004), *The First Stars*, Annual Review of Astronomy and Astrophysics **42** 79, arXiv: `astro-ph/0311019` [`astro-ph`] (cit. on p. 32).

Brott, I. et al. (2011), *Rotating massive main-sequence stars. I. Grids of evolutionary models and isochrones*, Astronomy and Astrophysics **530** A115, arXiv: `1102.0530` [`astro-ph.SR`] (cit. on pp. 34, 35).

Cantiello, M. and N. Langer (2010), *Thermohaline mixing in evolved low-mass stars*, Astronomy and Astrophysics **521** A9, arXiv: `1006.1354` [`astro-ph.SR`] (cit. on p. 34).

Choi, J. et al. (2016), *Mesa Isochrones and Stellar Tracks (MIST). I. Solar-scaled Models*, The Astrophysical Journal **823** 102, arXiv: `1604.08592` [`astro-ph.SR`] (cit. on p. 35).

D'Antona, F. et al. (2017), *Stars caught in the braking stage in young Magellanic Cloud clusters*, Nature Astronomy **1** 0186, arXiv: `1707.07711` [`astro-ph.SR`] (cit. on p. 36).

de Mink, S. E., N. Langer, R. G. Izzard, H. Sana and A. de Koter (2013), *The Rotation Rates of Massive Stars: The Role of Binary Interaction through Tides, Mass Transfer, and Mergers*, The Astrophysical Journal **764** 166, arXiv: `1211.3742` [`astro-ph.SR`] (cit. on pp. 32, 35).

de Mink, S. E., O. R. Pols and R. W. Hilditch (2007), *Efficiency of mass transfer in massive close binaries. Tests from double-lined eclipsing binaries in the SMC*, Astronomy and Astrophysics **467** 1181, arXiv: `astro-ph/0703480` [`astro-ph`] (cit. on pp. 33, 35, 43, 56, 57, 60, 65).

Detmers, R. G., N. Langer, P. Podsiadlowski and R. G. Izzard (2008), *Gamma-ray bursts from tidally spun-up Wolf-Rayet stars?*, Astronomy and Astrophysics **484** 831, arXiv: `0804.0014` [`astro-ph`] (cit. on p. 35).

Eddington, A. S. (1916), *On the radiative equilibrium of the stars*, Monthly Notices of the Royal Astronomical Society **77** 16 (cit. on p. 36).

Eddington, A. S. (1920), *The Internal Constitution of the Stars*, The Scientific Monthly **11** 297 (cit. on p. 36).

Ferraro, F. R. et al. (2012), *Dynamical age differences among coeval star clusters as revealed by blue stragglers*, Nature **492** 393, arXiv: `1212.5071 [astro-ph.SR]` (cit. on p. 36).

Foellmi, C. (2004), *Another single hydrogen-rich Wolf-Rayet star in the SMC?*, Astronomy and Astrophysics **416** 291, arXiv: `astro-ph/0310153 [astro-ph]` (cit. on p. 58).

Foellmi, C., A. F. J. Moffat and M. A. Guerrero (2003), *Wolf-Rayet binaries in the Magellanic Clouds and implications for massive-star evolution - I. Small Magellanic Cloud*, Monthly Notices of the Royal Astronomical Society **338** 360 (cit. on p. 58).

Frebel, A. et al. (2005), *Nucleosynthetic signatures of the first stars*, Nature **434** 871, arXiv: `astro-ph/0503021 [astro-ph]` (cit. on p. 32).

Gerber, J. M., E. D. Friel and E. Vesperini (2021), *Light Element Abundances and Multiple Populations in M53*, The Astronomical Journal **161** 288, arXiv: `2103.10527 [astro-ph.SR]` (cit. on p. 36).

Gies, D., L. Wang and G. Peters (2019), "Detection of the progenitors of Be X-ray Binaries", *IAU Symposium*, ed. by L. M. Oskinova, E. Bozzo, T. Bulik and D. R. Gies, vol. 346, IAU Symposium 143 (cit. on p. 59).

Götberg, Y., S. E. de Mink and J. H. Groh (2017), *Ionizing spectra of stars that lose their envelope through interaction with a binary companion: role of metallicity*, Astronomy and Astrophysics **608** A11, arXiv: `1701.07439 [astro-ph.SR]` (cit. on p. 62).

Götberg, Y., S. E. de Mink, J. H. Groh et al. (2018), *Spectral models for binary products: Unifying subdwarfs and Wolf-Rayet stars as a sequence of stripped-envelope stars*, Astronomy and Astrophysics **615** A78, arXiv: `1802.03018 [astro-ph.SR]` (cit. on p. 62).

Götberg, Y., V. Korol et al. (2020), *Stars Stripped in Binaries: The Living Gravitational-wave Sources*, The Astrophysical Journal **904** 56, arXiv: `2006.07382 [astro-ph.SR]` (cit. on pp. 53, 59).

Grafener, G., S. P. Owocki and J. S. Vink (2012), *Stellar envelope inflation near the Eddington limit. Implications for the radii of Wolf-Rayet stars and luminous blue variables*, Astronomy and Astrophysics **538** A40, arXiv: `1112.1910 [astro-ph.SR]` (cit. on p. 64).

Grassitelli, L. et al. (2016), *Diagnostics of the unstable envelopes of Wolf-Rayet stars*, Astronomy and Astrophysics **590** A12, arXiv: `1603.08931 [astro-ph.SR]` (cit. on p. 64).

Hainich, R. et al. (2015), *Wolf-Rayet stars in the Small Magellanic Cloud. I. Analysis of the single WN stars*, Astronomy and Astrophysics **581** A21, arXiv: `1507.04000 [astro-ph.SR]` (cit. on pp. 33, 58, 59).

Harbeck, D., G. H. Smith and E. K. Grebel (2003), *CN Abundance Variations on the Main Sequence of 47 Tucanae*, The Astronomical Journal **125** 197, arXiv: `astro-ph/0210364 [astro-ph]` (cit. on p. 36).

Harries, T. J., R. W. Hilditch and I. D. Howarth (2003), *Ten eclipsing binaries in the Small Magellanic Cloud: fundamental parameters and Cloud distance*, Monthly Notices of the Royal Astronomical Society **339** 157, arXiv: `astro-ph/0210295 [astro-ph]` (cit. on pp. 33, 42, 56, 57).

Heger, A., N. Langer and S. E. Woosley (2000), *Presupernova Evolution of Rotating Massive Stars. I. Numerical Method and Evolution of the Internal Stellar Structure*, The Astrophysical Journal **528** 368, arXiv: `astro-ph/9904132 [astro-ph]` (cit. on p. 34).

Heger, A., S. E. Woosley and H. C. Spruit (2005), *Presupernova Evolution of Differentially Rotating Massive Stars Including Magnetic Fields*, The Astrophysical Journal **626** 350, arXiv: `astro-ph/0409422 [astro-ph]` (cit. on p. 34).

Hilditch, R. W., I. D. Howarth and T. J. Harries (2005), *Forty eclipsing binaries in the Small Magellanic Cloud: fundamental parameters and Cloud distance*, Monthly Notices of the Royal Astronomical Society **357** 304, arXiv: `astro-ph/0411672` `[astro-ph]` (cit. on pp. 33, 42, 56, 57).

Holgado, G. (2018), *Spectroscopic and physical characterization of the Galactic O-type stars targeted by the IACOB OWN surveys*, PhD thesis: Universidad de La Laguna (cit. on pp. 55, 59, 66).

Howarth, I. D. et al. (2015), *The VLT-FLAMES Tarantula Survey. XXIII. Two massive double-lined binaries in 30 Doradus*, Astronomy and Astrophysics **582** A73, arXiv: `1508.05791` `[astro-ph.SR]` (cit. on p. 51).

Hunter, I. et al. (2007), *The VLT-FLAMES survey of massive stars: surface chemical compositions of B-type stars in the Magellanic Clouds*, Astronomy and Astrophysics **466** 277, arXiv: `astro-ph/0609710` `[astro-ph]` (cit. on pp. 32, 33).

Ishii, M., M. Ueno and M. Kato (1999), *Core-Halo Structure of a Chemically Homogeneous Massive Star and Bending of the Zero-Age Main Sequence*, Publications of the Astronomical Society of Japan **51** 417, arXiv: `astro-ph/9907154` `[astro-ph]` (cit. on p. 64).

Jao, W.-C., T. J. Henry, D. R. Gies and N. C. Hambly (2018), *A Gap in the Lower Main Sequence Revealed by Gaia Data Release 2*, The Astrophysical Journal **861** L11, arXiv: `1806.07792` `[astro-ph.SR]` (cit. on p. 36).

Kato, M. (1985), *A new type of solution for very massive stars and the occurrence of steady mass loss*, Publications of the Astronomical Society of Japan **37** 311 (cit. on p. 64).

Kippenhahn, R., K. Kohl and A. Weigert (1967), *Entwicklung in engen Doppelstern systemen II.*, Zeitschrift for Astrophysik **66** 58 (cit. on p. 33).

Klencki, J., A. Istrate, G. Nelemans and O. Pols (2022), *Partial-envelope stripping and nuclear-timescale mass transfer from evolved supergiants at low metallicity*, Astronomy and Astrophysics **662** A56, arXiv: `2111.10271` `[astro-ph.SR]` (cit. on p. 62).

Kobulnicky, H. A. et al. (2014), *Toward Complete Statistics of Massive Binary Stars: Penultimate Results from the Cygnus OB2 Radial Velocity Survey*, The Astrophysical Journal Supplement Series **213** 34, arXiv: `1406.6655` `[astro-ph.SR]` (cit. on p. 32).

Koenigsberger, G. et al. (2014), *The HD 5980 Multiple System: Masses and Evolutionary Status*, The Astronomical Journal **148** 62, arXiv: `1408.0556` `[astro-ph.SR]` (cit. on p. 58).

Köhler, K. et al. (2015), *The evolution of rotating very massive stars with LMC composition*, Astronomy and Astrophysics **573** A71, arXiv: `1501.03794` `[astro-ph.SR]` (cit. on pp. 39, 64).

Kruckow, M. U., T. M. Tauris, N. Langer, M. Kramer and R. G. Izzard (2018), *Progenitors of gravitational wave mergers: binary evolution with the stellar grid-based code COMBINE*, Monthly Notices of the Royal Astronomical Society **481** 1908, arXiv: `1801.05433` `[astro-ph.SR]` (cit. on p. 33).

Krumholz, M. R. (2014), *The big problems in star formation: The star formation rate, stellar clustering, and the initial mass function*, Physics Reports **539** 49, arXiv: `1402.0867` `[astro-ph.GA]` (cit. on p. 36).

Krumholz, M. R., C. F. McKee and J. Bland -Hawthorn (2019), *Star Clusters Across Cosmic Time*, Annual Review of Astronomy and Astrophysics **57** 227, arXiv: `1812.01615` `[astro-ph.GA]` (cit. on p. 36).

Kudritzki, R. P., A. Pauldrach and J. Puls (1987), *Radiation driven winds of hot luminous stars. II. Wind models for O-stars in the Magellanic clouds.*, Astronomy and Astrophysics **173** 293 (cit. on p. 33).

Langer, N. (1991), *Evolution of massive stars in the Large Magellanic Cloud : models with semiconvection.*, Astronomy and Astrophysics **252** 669 (cit. on pp. 34, 45).

Langer, N., S. Wellstein and J. Petrovic (2003a), "On the evolution of massive close binaries", *A Massive Star Odyssey: From Main Sequence to Supernova*, ed. by K. van der Hucht, A. Herrero and C. Esteban, vol. 212, IAU Symposium 275 (cit. on p. 35).

– (2003b), "On the evolution of massive close binaries", *A Massive Star Odyssey: From Main Sequence to Supernova*, ed. by K. van der Hucht, A. Herrero and C. Esteban, vol. 212, IAU Symposium 275 (cit. on p. 64).

Lardo, C., E. Pancino, A. Mucciarelli and A. P. Milone (2012), *Carbon and nitrogen abundances of stellar populations in the globular cluster M 2*, Astronomy and Astrophysics **548** A107, arXiv: `1210.2566 [astro-ph.SR]` (cit. on p. 36).

Li, C. et al. (2019), *Extended Main-sequence Turnoffs in the Double Cluster h and chi Persei: The Complex Role of Stellar Rotation*, The Astrophysical Journal **876** 65, arXiv: `1904.02005 [astro-ph.SR]` (cit. on p. 36).

Lubow, S. H. and F. H. Shu (1975), *Gas dynamics of semidetached binaries.*, The Astrophysical Journal **198** 383 (cit. on p. 35).

Mahy, L., L. A. Almeida et al. (2020), *The Tarantula Massive Binary Monitoring. IV. Double-lined photometric binaries*, Astronomy and Astrophysics **634** A119, arXiv: `1912.06853 [astro-ph.SR]` (cit. on p. 33).

Mahy, L., C. Lanthermann et al. (2021), *Multiplicity of Galactic Luminous Blue Variable stars*, arXiv e-prints arXiv:2105.12380, arXiv: `2105.12380 [astro-ph.SR]` (cit. on p. 32).

Mahy, L., H. Sana et al. (2020), *The Tarantula Massive Binary Monitoring. III. Atmosphere analysis of double-lined spectroscopic systems*, Astronomy and Astrophysics **634** A118, arXiv: `1912.08107 [astro-ph.SR]` (cit. on p. 33).

Malkov, O. Y. (2020), *Semidetached double-lined eclipsing binaries: Stellar parameters and rare classes*, Monthly Notices of the Royal Astronomical Society **491** 5489 (cit. on p. 33).

Marchant, P. (2016), *The impact of tides and mass transfer on the evolution of metal-poor massive binary stars*, PhD thesis: University of Bonn (cit. on p. 34).

Marchant, P., N. Langer, P. Podsiadlowski, T. M. Tauris and T. J. Moriya (2016), *A new route towards merging massive black holes*, Astronomy and Astrophysics **588** A50, arXiv: `1601.03718 [astro-ph.SR]` (cit. on p. 35).

Massey, P., F. Bresolin, R. P. Kudritzki, J. Puls and A. W. A. Pauldrach (2004), *The Physical Properties and Effective Temperature Scale of O-Type Stars as a Function of Metallicity. I. A Sample of 20 Stars in the Magellanic Clouds*, The Astrophysical Journal **608** 1001, arXiv: `astro-ph/0402633 [astro-ph]` (cit. on p. 56).

Massey, P. and A. S. Duffy (2001), *A Search for Wolf-Rayet Stars in the Small Magellanic Cloud*, The Astrophysical Journal **550** 713, arXiv: `astro-ph/0010420 [astro-ph]` (cit. on p. 58).

Massey, P., K. A. G. Olsen and J. W. Parker (2003), *The Discovery of a 12th Wolf-Rayet Star in the Small Magellanic Cloud*, Publications of the Astronomical Society of the Pacific **115** 1265, arXiv: `astro-ph/0308237 [astro-ph]` (cit. on p. 58).

Mennekens, N. and D. Vanbeveren (2017), *A comparison between observed Algol-type double stars in the solar neighborhood and evolutionary computations of galactic case A binaries with a B-type primary at birth*, Astronomy and Astrophysics **599** A84, arXiv: `1611.08398 [astro-ph.SR]` (cit. on pp. 33, 60).

Milone, A. P. et al. (2018), *Multiple stellar populations in Magellanic Cloud clusters - VI. A survey of multiple sequences and Be stars in young clusters*, Monthly Notices of the Royal Astronomical Society **477** 2640, arXiv: `1802.10538` `[astro-ph.SR]` (cit. on pp. 32, 36, 65).

Moe, M. and R. Di Stefano (2017), *Mind Your Ps and Qs: The Interrelation between Period (P) and Mass-ratio (Q) Distributions of Binary Stars*, The Astrophysical Journal Supplement Series **230** 15, arXiv: `1606.05347` `[astro-ph.SR]` (cit. on p. 32).

Mokiem, M. R. et al. (2007), *The empirical metallicity dependence of the mass-loss rate of O- and early B-type stars*, Astronomy and Astrophysics **473** 603, arXiv: `0708.2042` `[astro-ph]` (cit. on p. 33).

Nelson, C. A. and P. P. Eggleton (2001), *A Complete Survey of Case A Binary Evolution with Comparison to Observed Algol-type Systems*, The Astrophysical Journal **552** 664, arXiv: `astro-ph/0009258` `[astro-ph]` (cit. on pp. 33, 53).

Niederhofer, F. et al. (2017), *The search for multiple populations in Magellanic Cloud clusters - I. Two stellar populations in the Small Magellanic Cloud globular cluster NGC 121*, Monthly Notices of the Royal Astronomical Society **464** 94, arXiv: `1609.01595` `[astro-ph.SR]` (cit. on p. 36).

Packet, W. (1981), *On the spin-up of the mass accreting component in a close binary system*, Astronomy and Astrophysics **102** 17 (cit. on pp. 55, 65).

Paczynski, B. (1966), *Evolution of Close Binaries. I.*, Acta Astronomica **16** 231 (cit. on p. 33).

– (1967a), *Evolution of Close Binaries. IV.*, Acta Astronomica **17** 193 (cit. on p. 33).

– (1967b), *Evolution of Close Binaries. V. The Evolution of Massive Binaries and the Formation of the Wolf-Rayet Stars*, Acta Astronomica **17** 355 (cit. on p. 33).

Paxton, B., L. Bildsten et al. (2011), *Modules for Experiments in Stellar Astrophysics (MESA)*, The Astrophysical Journal Supplement Series **192** 3, arXiv: `1009.1622` `[astro-ph.SR]` (cit. on p. 34).

Paxton, B., M. Cantiello et al. (2013), *Modules for Experiments in Stellar Astrophysics (MESA): Planets, Oscillations, Rotation, and Massive Stars*, The Astrophysical Journal Supplement Series **208** 4, arXiv: `1301.0319` `[astro-ph.SR]` (cit. on p. 34).

Paxton, B., P. Marchant et al. (2015), *Modules for Experiments in Stellar Astrophysics (MESA): Binaries, Pulsations, and Explosions*, The Astrophysical Journal Supplement Series **220** 15, arXiv: `1506.03146` `[astro-ph.SR]` (cit. on p. 34).

Paxton, B., J. Schwab et al. (2018), *Modules for Experiments in Stellar Astrophysics (MESA): Convective Boundaries, Element Diffusion, and Massive Star Explosions*, The Astrophysical Journal Supplement Series **234** 34, arXiv: `1710.08424` `[astro-ph.SR]` (cit. on p. 34).

Petrovic, J., N. Langer and K. A. van der Hucht (2005), *Constraining the mass transfer in massive binaries through progenitor evolution models of Wolf-Rayet+O binaries*, Astronomy and Astrophysics **435** 1013, arXiv: `astro-ph/0504242` `[astro-ph]` (cit. on pp. 35, 64).

Petrovic, J., O. Pols and N. Langer (2006), *Are luminous and metal-rich Wolf-Rayet stars inflated?*, Astronomy and Astrophysics **450** 219 (cit. on pp. 39, 64).

Pols, O. R. (1994), *Case A evolution of massive close binaries: formation of contact systems and possible reversal of the supernova order*, Astronomy and Astrophysics **290** 119 (cit. on p. 35).

Portegies Zwart, S. F., S. L. McMillan and M. Gieles (2010), *Young Massive Star Clusters*, Annual Review of Astronomy and Astrophysics **48** 431, eprint: `https://doi.org/10.1146/annurev-astro-081309-130834` (cit. on p. 36).

Renaud, F. (2018), *Star clusters in evolving galaxies*, New Astronomyr **81** 1, arXiv: `1801.04278` `[astro-ph.GA]` (cit. on p. 36).

Russell, H. N. (1914), *Relations Between the Spectra and Other Characteristics of the Stars*, Popular Astronomy **22** 275 (cit. on p. 36).

Salpeter, E. E. (1955), *The Luminosity Function and Stellar Evolution.*, The Astrophysical Journal **121** 161 (cit. on p. 34).

Sana, H. et al. (2012), *Binary Interaction Dominates the Evolution of Massive Stars*, Science **337** 444, arXiv: `1207.6397` `[astro-ph.SR]` (cit. on p. 32).

Sanyal, D., L. Grassitelli, N. Langer and J. M. Bestenlehner (2015), *Massive main-sequence stars evolving at the Eddington limit*, Astronomy and Astrophysics **580** A20, arXiv: `1506.02997` `[astro-ph.SR]` (cit. on pp. 33, 64).

Sanyal, D., N. Langer, D. Szécsi, S. -C Yoon and L. Grassitelli (2017), *Metallicity dependence of envelope inflation in massive stars*, Astronomy and Astrophysics **597** A71, arXiv: `1611.07280` `[astro-ph.SR]` (cit. on pp. 33, 64).

Schneider, F. R. N., P. Podsiadlowski, N. Langer, N. Castro and L. Fossati (2016), *Rejuvenation of stellar mergers and the origin of magnetic fields in massive stars*, Monthly Notices of the Royal Astronomical Society **457** 2355, arXiv: `1601.05084` `[astro-ph.SR]` (cit. on pp. 32, 35).

Schneider, F. R. N., S. T. Ohlmann et al. (2019), *Stellar mergers as the origin of magnetic massive stars*, Nature **574** 211, arXiv: `1910.14058` `[astro-ph.SR]` (cit. on pp. 32, 35).

Schootemeijer, A. and N. Langer (2018), *Wolf-Rayet stars in the Small Magellanic Cloud as testbed for massive star evolution*, Astronomy and Astrophysics **611** A75, arXiv: `1709.08727` `[astro-ph.SR]` (cit. on pp. 33, 43, 61, 62, 66).

Schootemeijer, A., N. Langer, N. J. Grin and C. Wang (2019), *Constraining mixing in massive stars in the Small Magellanic Cloud*, Astronomy and Astrophysics **625** A132, arXiv: `1903.10423` `[astro-ph.SR]` (cit. on pp. 33, 37, 54, 62).

Sen, K. et al. (2022), *Detailed models of interacting short-period massive binary stars*, Astronomy and Astrophysics **659** A98, arXiv: `2111.03329` `[astro-ph.SR]` (cit. on pp. 33, 35, 36).

Sen, K. (2020), *Evolution of binary stars on the HR diagram*, version 1 (cit. on pp. 33, 37).

Shenar, T., A. Gilkis, J. S. Vink, H. Sana and A. A. C. Sander (2020), *Why binary interaction does not necessarily dominate the formation of Wolf-Rayet stars at low metallicity*, Astronomy and Astrophysics **634** A79, arXiv: `2001.04476` `[astro-ph.SR]` (cit. on pp. 39, 41, 55, 61).

Shenar, T., R. Hainich, H. Todt, A. F. J. Moffat et al. (2018), *The shortest-period Wolf-Rayet binary in the Small Magellanic Cloud: Part of a high-order multiple system. Spectral and orbital analysis of SMC AB 6*, Astronomy and Astrophysics **616** A103, arXiv: `1805.00952` `[astro-ph.SR]` (cit. on pp. 58, 59).

Shenar, T., R. Hainich, H. Todt, A. Sander et al. (2016), *Wolf-Rayet stars in the Small Magellanic Cloud. II. Analysis of the binaries*, Astronomy and Astrophysics **591** A22, arXiv: `1604.01022` `[astro-ph.SR]` (cit. on pp. 33, 58, 59).

Song, Y.-Y. et al. (2021), *Dynamical masses and mass-to-light ratios of resolved massive star clusters - II. Results for 26 star clusters in the Magellanic Clouds*, Monthly Notices of the Royal Astronomical Society **504** 4160, arXiv: `2104.06882` `[astro-ph.GA]` (cit. on p. 36).

Sun, W., R. de Grijs, L. Deng and M. D. Albrow (2021), *Binary-driven stellar rotation evolution at the main-sequence turn-off in star clusters*, Monthly Notices of the Royal Astronomical Society **502** 4350, arXiv: `2102.02352` `[astro-ph.SR]` (cit. on p. 32).

Surkova, L. P. and M. A. Svechnikov (2004), *VizieR Online Data Catalog: Semi-detached eclipsing binaries (Surkova+, 2004)*, VizieR Online Data Catalog (cit. on p. 33).

Tolstoy, E., V. Hill and M. Tosi (2009), *Star-Formation Histories, Abundances, and Kinematics of Dwarf Galaxies in the Local Group*, Annual Review of Astronomy and Astrophysics **47** 371, arXiv: `0904.4505 [astro-ph.CO]` (cit. on p. 32).

Tutukov, A. V. and L. R. Yungelson (1971), *Evolution of close binaries with mass loss from system I*, Nauchnye Informatsii **20** 86 (cit. on p. 33).

– (1981), *Evolutionary Scenario for Close Binary Systems of Low and Moderate Masses*, Nauchnye Informatsii **49** 3 (cit. on p. 33).

Udalski, A. et al. (1998), *The Optical Gravitational Lensing Experiment. Eclipsing Binary Stars in the Small Magellanic Cloud*, Acta Astronomica **48** 563, arXiv: `astro-ph/9812348 [astro-ph]` (cit. on p. 56).

Ulrich, R. K. and H. L. Burger (1976), *The accreting component of mass-exchange binaries.*, The Astrophysical Journal **206** 509 (cit. on p. 35).

Van Rensbergen, W. and J. P. De Greve (2016), *Accretion disks in Algols: Progenitors and evolution*, Astronomy and Astrophysics **592** A151, arXiv: `1604.07589 [astro-ph.SR]` (cit. on p. 33).

van Rensbergen, W., J. P. De Greve, C. De Loore and N. Mennekens (2008), *Spin-up and hot spots can drive mass out of a binary*, Astronomy and Astrophysics **487** 1129, arXiv: `0804.1215 [astro-ph]` (cit. on p. 33).

van Rensbergen, W., J. P. De Greve, N. Mennekens, K. Jansen and C. De Loore (2010a), *Mass loss out of close binaries. Case A Roche lobe overflow*, Astronomy and Astrophysics **510** A13, arXiv: `0908.2021 [astro-ph.SR]` (cit. on p. 33).

– (2010b), *Mass loss out of close binaries. Case A Roche lobe overflow*, Astronomy and Astrophysics **510** A13, arXiv: `0908.2021 [astro-ph.SR]` (cit. on p. 60).

van Rensbergen, W., J. P. de Greve, N. Mennekens, K. Jansen and C. de Loore (2011), *Mass loss out of close binaries. The formation of Algol-type systems, completed with case B RLOF*, Astronomy and Astrophysics **528** A16, arXiv: `1008.2620 [astro-ph.SR]` (cit. on p. 33).

van Rensbergen, W. and J.-P. de Greve (2021), *On the Modeling of Algol-Type Binaries*, Galaxies **9** 19 (cit. on p. 33).

Vanbeveren, D., C. De Loore and W. Van Rensbergen (1998), *Massive stars*, Astronomy and Astrophysicsr **9** 63 (cit. on p. 35).

Venn, K. A. (1999), *A-Type Supergiant Abundances in the Small Magellanic Cloud: Probes of Evolution*, The Astrophysical Journal **518** 405, arXiv: `astro-ph/9901306 [astro-ph]` (cit. on pp. 32, 33).

Wang, C., N. Langer, A. Schootemeijer, N. Castro et al. (2020), *Effects of Close Binary Evolution on the Main-sequence Morphology of Young Star Clusters*, The Astrophysical Journal **888** L12, arXiv: `1912.07294 [astro-ph.SR]` (cit. on pp. 32, 34, 35, 37, 65).

Wang, C., N. Langer, A. Schootemeijer, A. Milone et al. (2022), *Stellar mergers as the origin of the blue main-sequence band in young star clusters*, Nature Astronomy, arXiv: `2202.05552 [astro-ph.SR]` (cit. on p. 32).

Wang, L., D. R. Gies and G. J. Peters (2018), *Detection of Additional Be+sdO Systems from IUE Spectroscopy*, The Astrophysical Journal **853** 156, arXiv: `1801.01066 [astro-ph.SR]` (cit. on p. 59).

Wang, L., D. R. Gies, G. J. Peters et al. (2021), *The Detection and Characterization of Be+sdO Binaries from HST/STIS FUV Spectroscopy*, The Astronomical Journal **161** 248, arXiv: `2103.13642 [astro-ph.SR]` (cit. on pp. 53, 59).

Weisz, D. R. et al. (2014), *The Star Formation Histories of Local Group Dwarf Galaxies. I. Hubble Space Telescope/Wide Field Planetary Camera 2 Observations*, The Astrophysical Journal **789** 147, arXiv: `1404.7144 [astro-ph.GA]` (cit. on p. 32).

Wellstein, S. and N. Langer (1999), *Implications of massive close binaries for black hole formation and supernovae*, Astronomy and Astrophysics **350** 148, arXiv: `astro-ph/9904256 [astro-ph]` (cit. on p. 64).

Wellstein, S., N. Langer and H. Braun (2001), *Formation of contact in massive close binaries*, Astronomy and Astrophysics **369** 939, arXiv: `astro-ph/0102244 [astro-ph]` (cit. on pp. 36, 43, 47, 53, 60).

Wyrzykowski, L. et al. (2004), *The Optical Gravitational Lensing Experiment. Eclipsing Binary Stars in the Small Magellanic Cloud*, Acta Astronomica **54** 1, arXiv: `astro-ph/0404523 [astro-ph]` (cit. on p. 56).

Yoon, S.-C., L. Dessart and A. Clocchiatti (2017), *Type Ib and IIb Supernova Progenitors in Interacting Binary Systems*, The Astrophysical Journal **840** 10, arXiv: `1701.02089 [astro-ph.SR]` (cit. on p. 53).

Compact object progenitors in the Hertzsprung–Russell diagram

Koushik Sen[a], David R. Aguilera-Dena[c,a], Norbert Langer[a,b], Chen Wang[a]

[a] Argelander-Institüt für Astronomie, Universität Bonn, Auf dem Hügel 71, 53121 Bonn, Germany
[b] Max-Planck-Institut für Radioastronomie, Auf dem Hügel 69, 53121 Bonn, Germany
[c] Institute of Astrophysics, FORTH, Dept. of Physics, University of Crete, Voutes, University Campus, GR-71003 Heraklion, Greece

In preparation for *Astronomy & Astrophysics*

ABSTRACT

Context: Recently, a large amount of observational data has been collected to study the photometric and spectroscopic properties of stripped-envelope supernovae (SE SNe). Identifying the position of the progenitors of SE SNe on the Hertzsprung-Russell (HR) diagram can reveal valuable information to understand these events and constrain our models.

Aims: We derive the observable properties of the progenitors of compact objects, neutron stars (NSs) and black holes (BHs), arising from the stable binary mass transfer channel (Case A and Case B) and non-interacting binaries.

Method: We use 2078 detailed binary evolution models with initial donor masses of 5-100 $M_{\odot}$, orbital periods of ∼1-3100 days and mass ratios of 0.3-0.95, at a metallicity of the Small Magellanic Cloud (SMC). The initial parameters are chosen via a Monte Carlo (MC) procedure that takes into consideration the emperical stellar and binary initial parameter distribution functions (donor masses, orbital periods and mass ratios). Our choice of initial binary parameters also enables us to use our models to emulate a coeval population of massive binaries in the SMC.

Results: We predict 10-40 BH+main sequence (MS) binaries at ages of 5-20 Myrs in a coeval population of binary stars, which is about 1-5% of the observable non-interacting binaries in our coeval population. In addition, we expect ∼10 NS+MS systems at ages between 10-30 Myrs. Our models

predict that the number of SE SNe are much higher than Type II supernova at ages below 20 Myrs, which corroborates the observed age dependence of their progenitors. We show the distribution of the compact object progenitors and their companions on the HR diagram at the onset of core collapse of the compact object progenitor. Our models predict no Type Ic supernova at SMC metallicity from the mass donors of the stable mass transfer channel, while only Case A donors can lead to a Type Ib supernova. Our Case A SE SNe progenitors are hotter than Case B ones, owing to a deeper stripping of their envelope. Most of the Case A accretors show surface helium enrichment and are not rotating critically while all our Case B accretors rotate critically and do not show any surface helium enrichment. One model in our grid also undergoes chemically homogeneous evolution. At the same pre-collapse helium core mass, NSs formed from stripped donor stars (with an associated SE SNe) are found to be lighter than ones formed from non-stripped stars (with an associated normal Type II SNe). *Conclusions:* We predict a population of hot SE SNe progenitors arising from the Case A binary mass transfer channel. The identification of Type Ib SNe at very low metallicity environments can likely constrain the stellar wind mass-loss rates implemented in our models.

Key words. binaries: general - stars: massive - stars: black holes - stars: neutron - supernovae: general

4.1 Introduction

Stars more massive than ~$8\,M_\odot$ are expected to end their lives with a supernova (SN) explosion when nuclear burning can no longer provide support against gravity and their cores collapse (Weiler et al., 1988; Bethe, 1990; Burrows et al., 1995; Hillebrandt et al., 2000; Burrows, 2000; Chan et al., 2018; Burrows et al., 2021). Since the first study by Baade et al. (1934), detailed theoretical studies have classified SN models based on their explosion mechanisms into- thermonuclear explosions (Hillebrandt et al., 2000; Mazzali et al., 2007), electron-capture (EC) SNe (ECSNe, Poelarends et al., 2008; Poelarends et al., 2017; Siess et al., 2018; Leung et al., 2019), core-collapse (CC) SNe (CCSNe, Woosley et al., 2002; Heger et al., 2003; Langer, 2012) and pulsational pair-instability (PPI) SNe (PPISNe, Fraley, 1968; Heger et al., 2002; Woosley, 2017; Marchant et al., 2019).

SNe explosions have also been classified from their observed spectral and photometric properties, in particular their optical spectra (Filippenko, 1997). The hydrogen rich Type II SNe are further divided into Type IIP (plateau light curve), IIL (linearly declining light curve) and IIn (having narrow emission lines). The hydrogen deficient SNe includes Type Ib (helium lines present), Ic (helium lines absent) and IIb (spectral properties transition from Type II to Type I). It is plausible that the evolutionary stage of the progenitor star in the Hertzsprung-Russell (HR) diagram (Russell, 1914) and the chemical composition of its envelope at the time of the SN explosion determine the mechanics of explosion and the observable characteristics (see, for e.g., reviews by Smartt, 2009; Langer, 2012).

A lot of work has already been done to understand the formation of hydrogen rich Type IIP, IIL and IIn supernova (for a review, see Smartt, 2009). One of the major goals in recent studies of SN explosions is to understand the progenitor stars that can produce the different types of stripped envelope (SE) SNe due to the different formation channels and the stripping mechanism, that allows for a large diversity within the progenitors. Detailed studies have been undertaken to understand the progenitors of hydrogen poor Type Ib, Ic and IIb SNe, collectively known as SE SNe (S.-C. Yoon et al., 2017; Aguilera-Dena et al., 2018; Sravan et al., 2019; Gilkis et al., 2019; Sravan et al., 2020; Schneider et al., 2021). Owing to the facts that massive stars preferentially form as binaries (Vanbeveren et al., 1998;

Sana et al., 2012; Sana et al., 2013; Kobulnicky et al., 2014; Moe et al., 2017; Banyard et al., 2021), and binary mass transfer is very efficient in stripping the hydrogen rich envelope of the donor star, it is plausible that stars in binaries are the major progenitors to the population of SE SNe (Podsiadlowski et al., 1993; Claeys et al., 2011; S.-C. Yoon, 2015; Soker, 2017), specially at low metallicity where stellar winds are too weak to remove the outer hydrogen envelope of the stars to the required extent (Heger et al., 2003; Sravan et al., 2019).

From the observational side, a direct way to determine the type of star that exploded is to search for progenitors in archival data of the host galaxies (Van Dyk et al., 2003; Smartt et al., 2004; Maund et al., 2005; W. Li et al., 2006). Compilations of progenitor stars have been made by Smartt et al. (2003), Gal-Yam et al. (2007), W. Li et al. (2007) and Kochanek et al. (2008), although incomplete and potentially biased due to undefined selection criterion (see discussion in Smartt, 2009). Following these compilations, Smartt (2009) and Eldridge et al. (2013) (see also, Smartt, 2015, for updated results) introduced a well-defined time- and volume-limited sample of 44 SNe in which they detected a dozen unambiguous progenitors. The position of these progenitors on the HR diagram can constrain various physics assumptions used in modelling their pre-supernova structure (Prentice et al., 2019; Farrell et al., 2020; Schneider et al., 2021).

Large-scale observational campaigns in recent years on SE SNe (Bianco et al., 2014; Taddia et al., 2016; Stritzinger et al., 2018) have enabled detailed studies of their photometric (Drout et al., 2011; Lyman et al., 2016; Prentice et al., 2016) and spectroscopic properties (Liu et al., 2016; Modjaz et al., 2016; Prentice et al., 2017; Fremling et al., 2018). For example, Taddia et al. (2018) (see also, Prentice et al., 2019) have analysed the light curves of 34 SE SNe with unparalleled photometric accuracy and wavelength range, from the Carnegie Supernova Project I (Hamuy et al., 2006). Observational evidence also points towards the binary channel being the major contributor to the population of SE SNe (Smith et al., 2011; Lyman et al., 2016; Taddia et al., 2018; Prentice et al., 2019).

In the last decade, several studies have shown that all stars above initial masses of $8\,M_\odot$ do not explode in a SN to form a neutron star (NS) remnant but may implode directly to form a black hole (BH) without an accompanying SN (Ertl et al., 2016; B. Müller et al., 2016; Sukhbold et al., 2018; Schneider et al., 2021). At low metallicity, chemically homogeneous evolution (Marchant et al., 2016; S. E. de Mink et al., 2016; Riley et al., 2021) can also produce stars that can be progenitors of hydrogen poor Type IIn/Ibn/Icn supernova via the PPISN channel (Woosley, 2017; Marchant et al., 2020; Woosley et al., 2021).

Despite the concerted efforts into studying each of the compact object formation channels in detail, an overall prediction of the relative populations of different types of compact object progenitors using detailed binary evolution models is lacking in the literature, partly because of the computational cost of calculating a large number of binary models to do such a statistical study. Moreover, the predictions from rapid binary evolution models have been shown to be unreliable (Laplace et al., 2020; Laplace et al., 2021), especially regarding the extent of envelope stripping of the donors.

Using a Monte Carlo approach that takes into account the initial mass and binary distribution functions (C. Wang et al., 2020), we model the evolution of a coeval population of massive binaries at a metallicity suitable for the Small Magellanic Cloud (SMC) and study the numbers of compact object binaries as a function of the population age. We then look at the pre-CC properties of the models on the HR diagram. Using simple differentiating conditions derived from the detailed studies on individual compact object formation channels, we predict the number and position of the different types of NS and direct collapse BH progenitors on the HR diagram.

Section 4.2 describes the model grid and the assumptions taken to study the properties of various

types of compact object progenitors. We study the number of compact object binaries as a function of the age of the coeval population and the position of compact object progenitors on the HR diagram in Sect. 4.3. In Sect. 4.4, we compare our predictions with observed progenitors of SE SNe and predict the properties of their observable companions. We compare our work with earlier work on different channels of compact object formation in Sect. 4.5. We discuss the important caveats in our work in Sect. 4.6 and summarise our main results in Sect. 4.7.

4.2 Method

For this study, based on Chapter 3, we use the same models of C. Wang et al. (2020) and described in Chapter 3. In what follows, we briefly summarise the assumptions relevant to this part of the study, that is, to understand the progenitors of NSs and BHs in a co-evolving population of binary stars in the SMC.

4.2.1 The binary grid

The grid consists of 2078 detailed binary evolution models evolved using MESA[1] (Modules for Experiments in Stellar Astrophysics, Paxton et al., 2011; Paxton et al., 2013; Paxton et al., 2015; Paxton et al., 2018, version 8845). The initial donor masses are between 5-100 $M_\odot$, initial orbital periods between 1 day - 8.6 years and initial mass ratios (ratio of initial mass of accretor to the initial mass of donor) between 0.3 and 0.95. The initial binary parameters of each model are chosen using a Monte Carlo method that assumes the Salpeter initial mass function for the initial donor masses (Salpeter, 1955), and a flat distribution of initial mass ratios and logarithm of initial orbital periods. This then amounts to the massive star population of a $\sim 10^5 \, M_\odot$ co-evolving population of binary stars that has stars between 0.1-100 $M_\odot$, assuming a binary fraction of 1.

The chemical composition and stellar physics assumptions of the individual components in a binary model are identical to the single rotating models of Brott et al. (2011). These include differential rotation and internal rotational mixing (Heger et al., 2000), magnetic angular momentum transport (Heger et al., 2005), non-equilibrium CNO nucleosynthesis and stellar mind mass loss. The binary physics follows that of Marchant et al. (2017). For more details, see Chapter 3.

The evolution of the models during the main sequence (MS) and post MS phases are described comprehensively in Chapter 3 and shown with the help of an animation[2] in the HR diagram (Sen, 2020). The evolution of the binary models are calculated until core carbon (helium) exhaustion of each binary component if the helium core mass at the end of core helium exhaustion is lesser (greater) than 13 $M_\odot$, or until the system merges. Models with helium core masses greater than 13 $M_\odot$ ran into convergence errors during their core carbon burning and hence were terminated at the end of core helium depletion. At the end of core carbon (or helium) burning of the first component, we compute the evolution of the remaining component as a single star.

---

[1] http://mesa.sourceforge.net/

[2] https://zenodo.org/record/4068428#.YPWZKHUzaV4

4.2.2 Formation of neutron stars and black holes

To determine whether a NS or a BH will be formed after a binary component completes core carbon burning (or helium burning- for models with helium cores greater than $13 \, M_\odot$), we look at their final core helium and carbon masses. To estimate the mass of the remnant for each pre-SN mass of the SE binary donors, we use table 2 of Woosley et al. (2020), which takes into account the explodability criterion (see also O'Connor et al., 2011; Ugliano et al., 2012; Ertl et al., 2016; B. Müller et al., 2016; Sukhbold et al., 2018). For doing this, we take the pre-SN mass of the donor to be equal to its core helium mass at the end of core carbon (or helium, for the most massive stars) burning. We assume that a progenitor star which has a final carbon core mass greater than $1.37 \, M_\odot$ and the resulting remnant mass less than $2.3 \, M_\odot$ to form a neutron star (Ertl et al., 2020; Woosley et al., 2020). Progenitors whose remnant masses are expected to be greater than $2.3 \, M_\odot$ are assumed to collapse directly into a BH without any associated SN.

This mapping of the pre-SN progenitor mass to the remnant mass was derived from a grid of helium stars with mass loss that was studied by Woosley (2019) and Ertl et al. (2020). Their models are expected to mimic the envelope-stripped donors in binaries. However, we note that non-stripped stars may be harder to explode than stripped stars (Laplace et al., 2021; Schneider et al., 2021), and as such, the explodability of our non-stripped accretor stars, at the same progenitor core mass, will be different. To determine the explodability of our non-stripped stars, we use the work of Sukhbold et al. (2016, table 2, 4 and 5) who investigated the properties of non-stripped CC progenitors having initial masses 9-120 $M_\odot$ using the same explosion engine (W18, Ertl et al., 2020) as in Woosley et al. (2020).

As in Woosley et al. (2020), we also assume that the remnant mass distribution is uniquely determined by the pre-SN mass of the helium cores of the binary stars. We also assume that the mapping is not sensitive to metallicity or internal composition. Furthermore. we differentiate between ECSN and CCSN during the formation of neutron stars. We assume that progenitors with carbon core masses between 1.37-1.43 $M_\odot$ to undergo ECSN and the rest to undergo CCSN (Kruckow et al., 2018, see also Poelarends et al., 2017; Siess et al., 2018). For a review, see Doherty et al. (2017).

We assume that the stellar surface parameters at CC to be approximately the same as the stellar surface parameters at the end of core carbon (or helium) burning. Stellar surface properties are not expected to change significantly in the ~ 1000 years between the end of core carbon burning and the onset of core collapse (Groh et al., 2013; S.-C. Yoon et al., 2017). For the BH progenitors that have helium core masses above $13 \, M_\odot$, depending on the presence of a hydrogen envelope above the core, the surface temperature and composition at the onset of CC may be altered by another mass transfer phase after the end of core helium burning, though the luminosity is expected to remain fairly similar (Laplace et al., 2020). For transparency, we demarcate the models that were terminated at the end of core helium depletion in our plots in Fig. 4.2.

We assume that stars with helium cores greater than $35 \, M_\odot$ at the end of core helium burning undergo PPISN (Marchant et al., 2019, see also Woosley et al., 2002; Chen et al., 2014; Yoshida et al., 2016; Woosley, 2017; Renzo et al., 2020; Powell et al., 2021). This boundary is shown to be quite robust to variations in metallicity (R. Farmer et al., 2019), internal mixing (Renzo et al., 2020; Umeda et al., 2020), stellar rotation (Marchant et al., 2020) and stellar wind mass loss (R. Farmer et al., 2019, see however Vink et al., 2021). On the other hand, nuclear reaction rates are expected to have a significant impact on this lower boundary (Takahashi, 2018; R. Farmer et al., 2019; Woosley et al., 2021).

At the onset of CC, we assume that progenitors of NSs that have total remaining hydrogen envelope
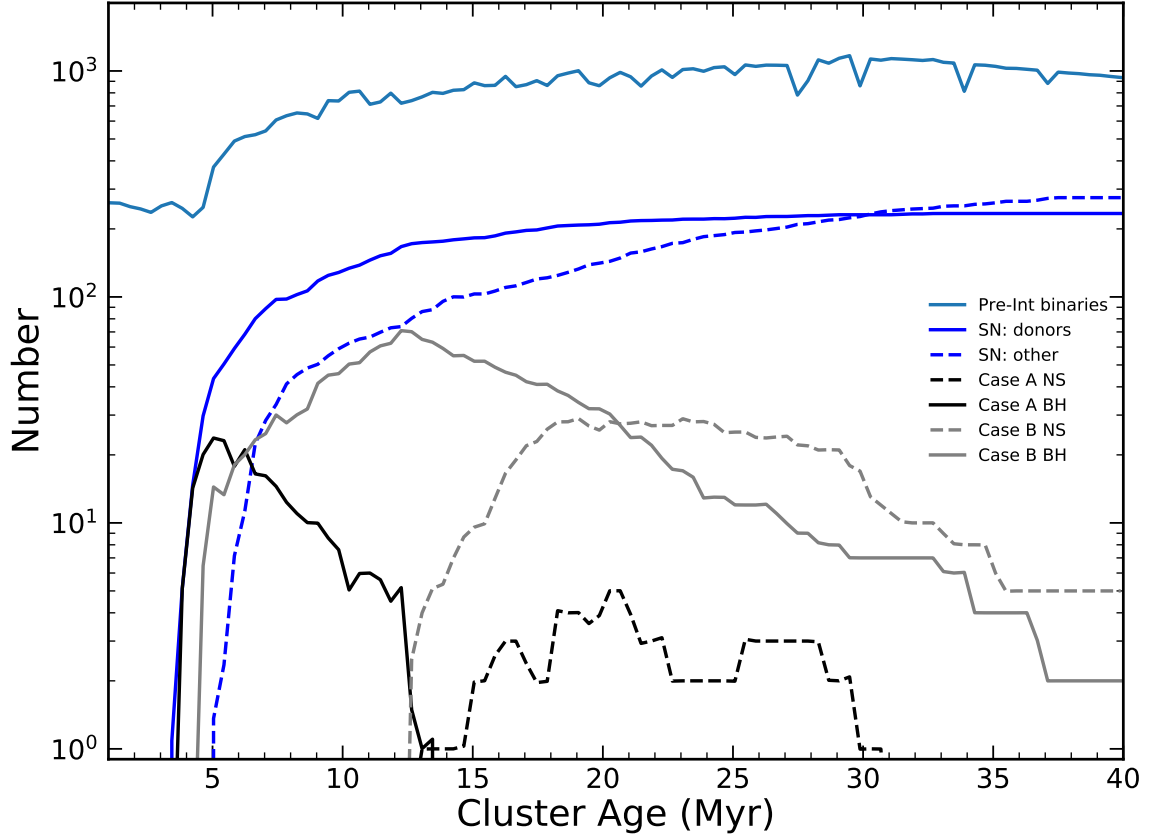
Figure 4.1: Number of compact object binaries and cumulative number of ECSN+CC events with cluster age. In this plot, we do not differentiate between ECSN, CC events and PPISN to improve readability. The solid black and grey lines indicate the number of BH+MS binaries at that cluster age, originating from the Case A and Case B mass transfer channel respectively. The dotted black and grey lines indicate the maximum number of NS+MS binaries (if no natal kick to disrupt the binary) that can originate from the Case A and Case B mass transfer channel at that cluster age, respectively. The blue solid line denotes the cumulative number of SNe events (except PPISNe) from Case A and Case B donors up to that cluster age. The blue dotted line indicates the cumulative number of SNe events (except PPISNe) from binary components other than Case A and Case B mass donors. The purple line shows the number of binaries that have not interacted and has luminosity lesser than the brightest non-interacted binary component by up to 1.5 dex at that cluster age.

mass less than 0.033 $M_\odot$, between 0.033-1 $M_\odot$ amd greater than 1 $M_\odot$ to give rise to spectral Type Ib, IIb and IIp of SNe respectively (Hachinger et al., 2012; Gilkis et al., 2022).

4.3 Results

4.3.1 Number of possible compact object binaries and transients as a function of the age of the coeval population

In order to quantify the temporal evolution of the number of transients and binaries that contain at least one compact object, we follow the evolution of the coeval population as a function of time, accounting

for systems in which at least one of their components has reached the end of its evolution. Figure 4.1 shows the number of different types of compact object binaries and the cumulative number of SN events as a function of the age of the coeval population. Our grid contains models with donor masses above $5\,M_\odot$. We see a slight decrease in the number of pre-interaction binaries (purple line) after $30\,\mathrm{Myrs}$ due to this incompleteness of models below $5\,M_\odot$. However, since stars below $5\,M_\odot$ are not expected to form NSs or BHs, the predicted numbers of compact object binaries and progenitors are meaningful up to $40\,\mathrm{Myrs}$. Since the BH+MS binaries typically originate from systems with an initially more massive primary than NS+MS binaries, we see that the number of BH+MS binaries begins to increase at an earlier age.

To provide a zeroth order estimate of the number of binaries that can have a compact object, we do not include natal kicks, which can disrupt the BH+MS or NS+MS binaries. While this assumption has been shown to be plausible for the BH+MS binaries (Belczynski et al., 2016; Sen et al., 2021), the kick velocities during the formation of NSs are found to be large enough to disrupt a significant fraction of systems (Hobbs et al., 2005). Hence, the number of NS+MS systems shown in this figure is a strict upper limit to the observable number of NS+MS binaries. Natal kicks will reduce the fraction of surviving compact NS+MS binaries, but we find that none of the systems that produce SNe after Case A or Case B stripping are disrupted by kicks due to mass loss from the system (Blaauw, 1961).

We see that the time at which BH+MS systems and NS+MS systems (arising from Case A mass transfer) are formed is fairly well separated at ~ 13 Myrs, while that is not so for the Case B systems. Inspection of our models reveals that very low initial mass ratio Case B systems can survive the mass transfer phase, while it is not so for Case A models (for e.g., see Fig. 2 of Langer et al., 2020). The efficiency of mass transfer for Case B systems is also very low, such that a very low mass accretor does not accrete much mass from its high mass donor (BH progenitor). Such a system usually lives longer as a BH+MS binary owing to the longer MS lifetime of the low mass companion. In the Case A mass transfer channel, low mass ratio binaries usually do not survive the mass transfer phase (leading to mergers instead) and hence there is a distinct gap in ages between BH and NS systems arising from Case A mass transfer.

If one accounts for a random Maxwellian SN kick velocity distribution (Hobbs et al., 2005; Wongwathanarat et al., 2012; B. Müller et al., 2020), about one-third of the NS+MS binaries are expected to survive the SN explosion. Hence, we expect a relatively larger number of BH+MS systems than NS+MS systems, even though the MS companions to the NSs are in general less massive and live longer than the companions to the BHs. During the first 20 Myrs of evolution of the cluster, we find that the number of SE SN originating from the donors of Case A and Case B mass transfer are higher than the number of ordinary Type II SNe that are expected from the accretors of interacting binaries and non-interacting binaries.

We attribute this to the following reasons. Firstly, accretors of interacting binaries are less massive than their donors and hence they live longer and undergo a SN after the donor. Secondly, components of non-interacting binaries essentially live their lives as a single star where they have a large hydrogen envelope. During core helium burning, the helium core mass of the non-interacting binaries grow due to the presence of a hydrogen burning shell, thereby adding more helium fuel and increasing the helium burning lifetime of the non-interacting systems. On the other hand, the helium cores of stripped donors shrink in mass due to the retreating convective core and the absence of a hydrogen burning shell (Laplace et al., 2021). Lastly, it has been shown that stripped stars are easier to explode than non-stripped stars (e.g. Schneider et al., 2021), such that envelope stripping due to mass transfer leads to relatively more massive stars undergoing SN explosions which would have otherwise collapsed

to form BHs. Hence, SN explosions from binary donors start to occur at an earlier epoch than SNe originating from non-interacting systems. This leads to a testable observational prediction that we expect the progenitors of SE SNe to be younger than those of Type IIp SNe. Evidence of such an age dependence has been found recently by Kankare et al. (2021), where they find that the progenitors of 14 hydrogen poor SNe to be younger than the progenitors of 15 hydrogen rich SNe at 3σ confidence level in the galaxy NGC 3256.

4.3.2 Properties of compact object progenitors in the HR diagram

Figure 4.2 shows the location in the HR diagram of the progenitors of NSs and BHs from the stable mass transfer channels and non-interacting binaries at CC. Using the criteria described in Sect. 4.2.2, we distinguish between four types of compact object progenitors; namely, the ECSN and CCSN progenitors that give rise to NSs, and the massive stars and PPISN progenitors that give rise to BHs. We see that the ECSN progenitors span a very narrow range of luminosities in our grid. This is because we assume a very small range of carbon core masses (1.37-1.43 $M_\odot$ Kruckow et al., 2018) that can give rise to ECSN in our models. Increasing this range of carbon core masses (1.37-1.52 $M_\odot$ Poelarends et al., 2017) will increase the corresponding range in luminosity and number of ECSN.

The most massive stars in our grid gives rise to PPISN (translucent grey shaded area). Here, the upper and lower limits on the luminosity range are determined by our assumption on the core helium mass cut-off and maximum donor mass in our model grid, respectively. Since our grid contains donors up to 100 $M_\odot$, we expect the upper luminosity limit to be extended to higher values if more massive donors are included. On the other hand, the lower luminosity limit is shown to be quite robust, except for changes in nuclear reaction rates (R. Farmer et al., 2019). Overall, the number of ECSN and PPISN progenitors are quite low compared to the core collapse progenitors (failed and successful SN).

We see that the Case A donor progenitors are much hotter than the Case B donor progenitors. Case A models have shorter orbital periods than Case B models, and their donors go through three envelope stripping episodes before the end of core helium burning compared to only one for the Case B donors. The extent of envelope stripping is also higher for shorter orbital period models (S.-C. Yoon et al., 2017). Accordingly, all our Case A donors have surface hydrogen mass fraction below 0.3 at the time of core collapse. The most luminous Case A donors become stripped of their entire hydrogen envelope during their second mass transfer episode (Case AB), which takes place during the Hertzsprung gap, and their stellar surface is composed almost purely of helium (blue asterisk marks with black frames). These stars can be the possible progenitors of Type Ibn SNe in the SMC via a PPI event (Foley et al., 2007; Pastorello et al., 2007). In agreement with previous works of binary and stripped-envelope star evolution at low metallicity (Laplace et al., 2020), we note that none of our donors gets stripped of their nitrogen rich helium envelope. Hence, our models predict the absence of WC type stars, that have helium envelopes enriched with the products of helium burning, as well as of possible Type Ic SN progenitors in the SMC (Dessart et al., 2020).

On the other hand, Case B donor progenitors are relatively cooler than the Case A progenitors and also have higher amounts of total hydrogen mass remaining in their stellar envelopes at the end of their evolution. Only the more luminous Case B donors have a surface hydrogen mass fraction lower than 0.3, but none of them are lower than 0.1. While the leftover hydrogen mass decreases monotonically with surface temperature (at a fixed luminosity, see Fig. 4.2) for most of the donor progenitors, it is not monotonic with respect to the luminosity (at a fixed temperature). Case A donors at $\log T_{\rm eff} \sim 4.45$ and $\log L/L_\odot \sim 4.8$ have smaller remaining total hydrogen mass than Case B donors at the same
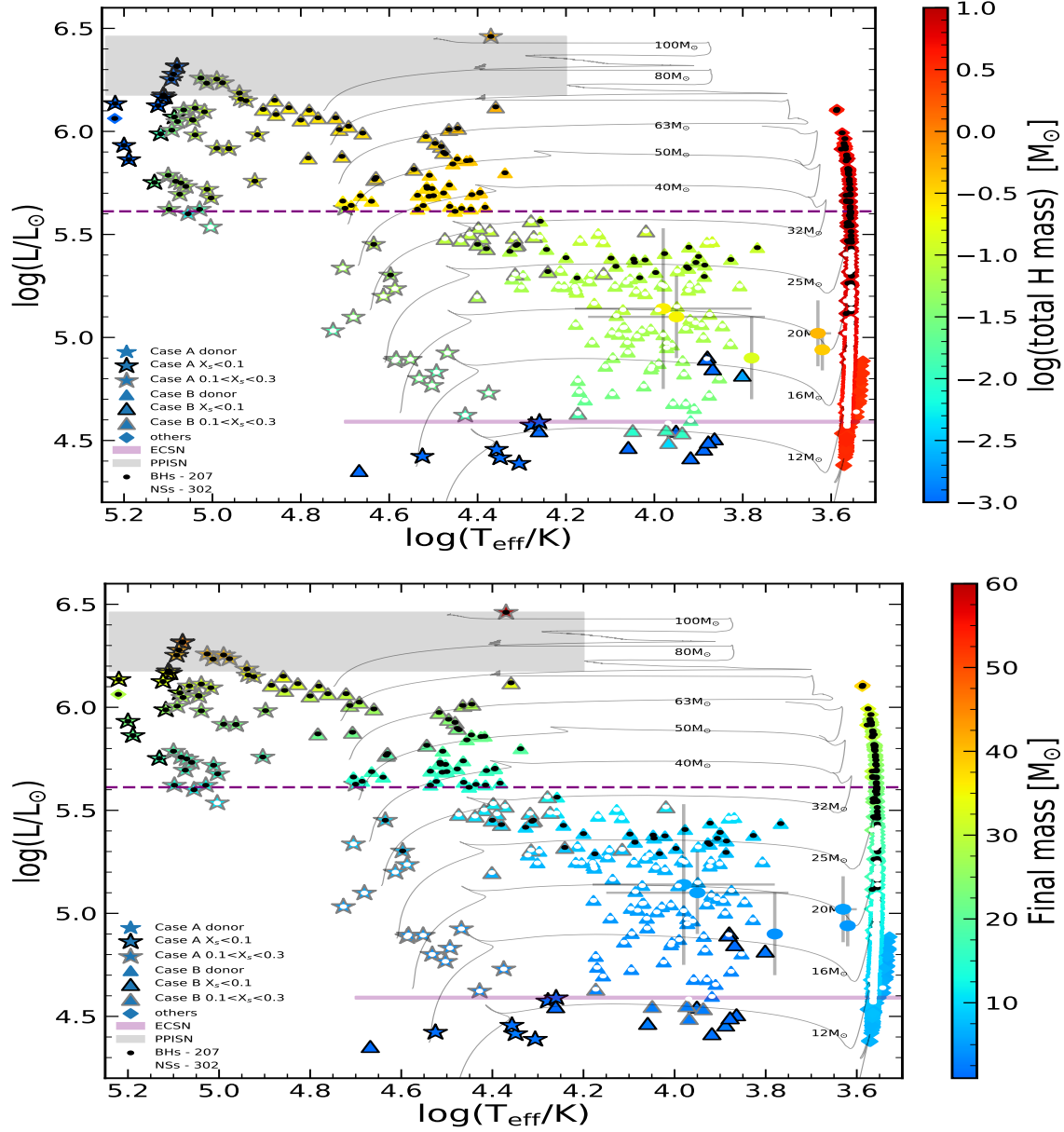
Figure 4.2: HR diagram showing the locations of the binary components from the stable mass transfer channels (Case A and Case B) and non-interacting binaries at CC. The colour-bar indicates the remaining hydrogen mass (top panel) or the total stellar mass (bottom panel) of the progenitor at the end of core carbon (or helium, depending on core helium mass) burning. Case A donor stars are shown with asterisk and Case B donors are shown with triangles. The symbols have a black or grey frame if the surface hydrogen mass fraction of the progenitor is less than 0.1 or between 0.1 to 0.3, respectively. All other progenitors (accretors of Case A and Case B binaries and both components of non-interacting binaries) are shown in diamonds. Small black and white dots over the symbols indicate the likely formation of a BH or NS respectively. The circles denote the five observed progenitors of Type IIb SN along with their error bars. The colour coding of the observed Type IIb progenitors in the left panel are taken from Farrell et al. (2020), while it is shown in black in the right panel and does not correspond to the colour-bar. The progenitors that give rise to ECSN and PPISN are highlighted in purple and grey patches, respectively (Kruckow et al., 2018; Marchant et al., 2019). The single star tracks (grey lines) in the background are taken from (Schootemeijer et al., 2019). Models below the horizontal, dashed, purple line were evolved until core carbon depletion, while those above the line are evolved until core helium depletion.
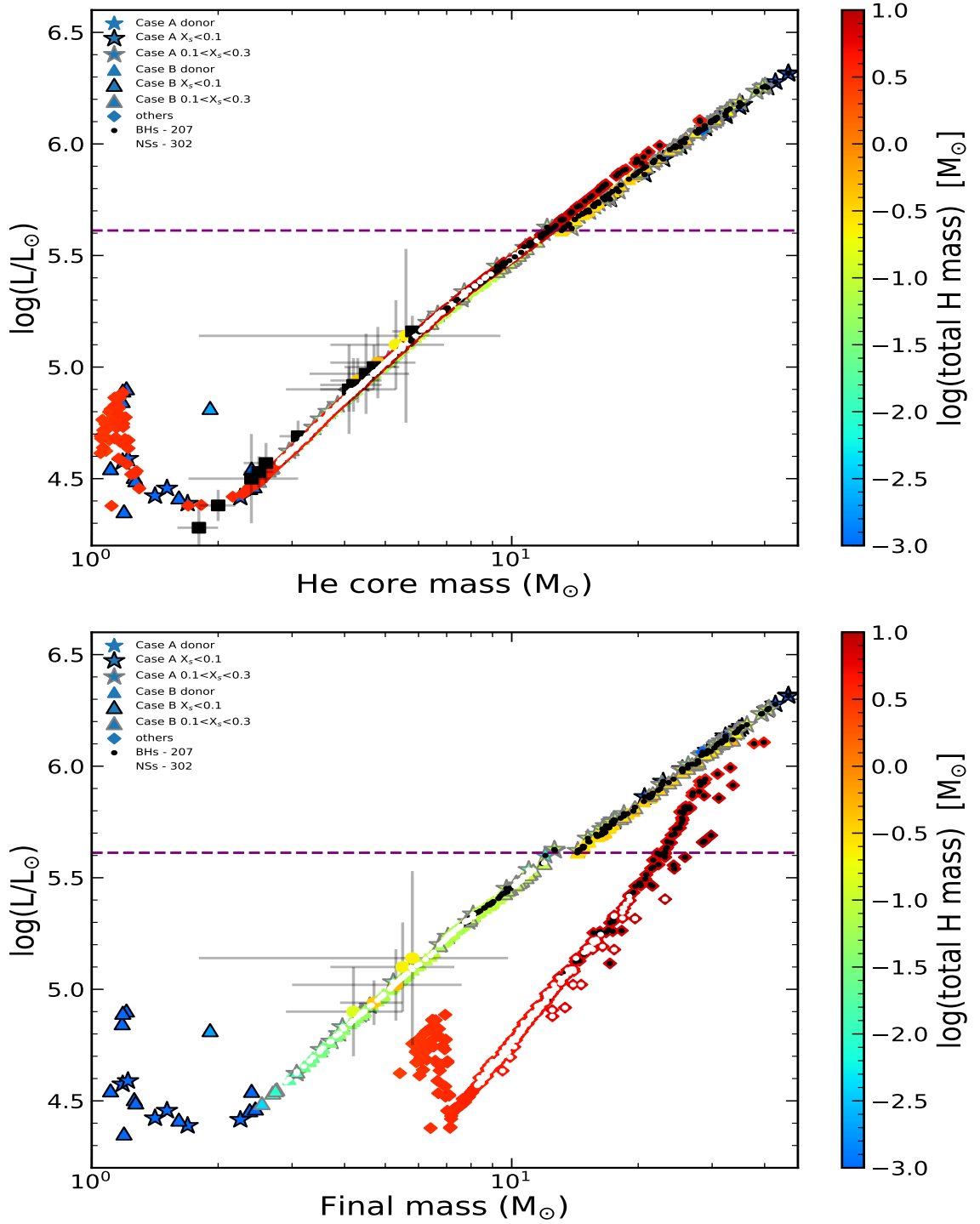
Figure 4.3: Luminosity of our model binary components as a function of their helium core mass (top panel) and star mass (bottom panel) at the end of core carbon burning (or helium burning for models above the dashed purple line). The symbols for the models are the same as in Fig. 4.2. Coloured (corresponding to the colourbar) and black circles show the parameters of the observed Type IIb and IIp supernovae analysed by Farrell et al. (2020) respectively.

effective temperature but $\log L/L_\odot \sim 5.4$. We also note that some of the least luminous donors, having $\log L/L_\odot < 4.6$, that are expected to end up as white dwarfs (carbon core mass less than $1.37\,M_\odot$) are completely stripped of their outer hydrogen envelope. These models undergo a Case ABB or Case BB mass transfer during their Asymptotic Giant Branch (AGB) phase that strips the remaining hydrogen envelope.

We note the presence of one compact, massive progenitor at $\log T_{eff} \sim 5.2$ and $\log L/L_\odot \sim 6.06$, which is not a Case A or Case B stripped donor star. We find that this binary component undergoes chemically homogeneous evolution which leads to an increase in the surface temperature during core hydrogen and helium burning. This binary component is the initially heavier component of the binary, and the initially less massive component fails to undergo chemically homogeneous evolution. Chemically homogeneously evolving stars lead to the formation of very fast rotating stellar cores, that may ultimately lead to the production of either a superlumonus SN or a gamma-ray burst, leaving behind either a fast-spinning magnetar or a fast-spinning BH after exploding (Aguilera-Dena et al., 2018; Aguilera-Dena et al., 2020).

The bottom panel of Fig. 4.2 shows the distribution of the progenitors in the HR diagram with their total stellar mass before CC (defined in Sect.4.2.2) in colour-coding, which serves as a proxy of the SN ejecta mass in the case of successful explosions. At a fixed luminosity, the masses of donor stars are lower than those of accretors and non-interacting stars due to envelope stripping. We note that the total mass of all the progenitors increase monotonically with luminosity, for any fixed temperature, as the luminosity is set by the core mass of the progenitor stars.

We also find that most of CC progenitors rotate very slowly (c.f. S. C. Yoon et al., 2010; Qin et al., 2019) by the time it reaches CC, except for a few Case A CC SN progenitors having $4.5 < \log L/L_\odot < 5.5$ (Fig. C.1, top panel). Since they originate from the shortest orbital period binaries (Fig. C.1, right panel), tidal interactions were strong enough (and stellar winds were weak enough at the relatively lower luminosity at this metallicity) to preserve some amount of rotational angular momentum in these donors.

From the maximum hydrogen mass in the envelope at core carbon depletion, we find that our Case A and Case B donor models are expected to be progenitors of Type Ib and Type IIb SN in the SMC respectively. The most luminous donors with low enough envelope hydrogen mass to be potential Type Ib SN progenitors have high final masses, corresponding to BH progenitors instead. All the accretors have hydrogen envelopes $\geq 10\,M_\odot$ and, together with the non-interacting binary components, comprise the population of ordinary Type IIp CC progenitors. We study the quantitative number of these predicted progenitor systems below.

Figure 4.3 shows the luminosity as a function of the helium core mass (top panel) and total star mass (bottom panel) at the end of core carbon burning (or helium burning, above the purple dashed line) of our binary models. We see that the helium core mass of the stripped donors (both Case A and Case B) are almost the same as those for the non-stripped accretors and non-interacting binary components. The luminosity of the NS and BH progenitors increase monotonically with the core helium mass. The WD progenitors on the other hand, having a helium core mass less than $1.37\,M_\odot$, originate from stars that undergo an AGB phase where the stars expand and increase in luminosity.

The total stellar mass of the Case A and Case B donors are nearly equal to the helium core mass (compare bottom panel with top panel) while the non-stripped models have a large hydrogen envelope and their core. The difference in mass of hydrogen envelope remaining at any given luminosity between stripped and non-stripped compact object progenitors decreases with the increase in luminosity because of the luminosity dependent wind mass-loss rates, where the wind mass-loss rate increases with

luminosity, thereby facilitating the partial removal of the outer hydrogen envelope in more massive accretors.

4.3.3 Numbers of NS and BH progenitors

The initial binary parameters in our grid are derived using a Monte Carlo approach that takes into account the initial mass function (Salpeter, 1955) and the empirical binary distribution functions (Sana et al., 2012). So, our model grid is expected to be mimic a $10^5 \, M_\odot$ coeval population of binary stars and we can predict the actual number of compact object progenitors expected from the stable mass transfer channel. The effect of including single stars is discussed later.

Figure 4.4 (top panel) shows the distribution of the various types of NS and BH progenitors as a function of the total remaining hydrogen mass in the star. The ratio of Case A donors to Case B donors is $63/171 \simeq 0.37$. Hence, Case A binaries are expected to significantly contribute to the population of compact objects arising from SE stars. Models that have leftover hydrogen mass less than $0.033 \, M_\odot$ can become progenitors of Type Ib SNe. On the other hand, the remaining stripped donors are expected to be progenitors of Type IIb SNe. The accretors of binaries that have interacted and both binary components of non-interacting binaries will give rise to ordinary Type IIp SNe.

The bottom panel of Fig. 4.4 shows the various types of outcomes expected from the CC of the progenitors, namely, we distinguish between models that might undergo ECSN to form a NS, CCSN to form a NS, directly form BHs, or experience PPI and form BHs. We find that a few of the most hydrogen poor Case A donors are expected to undergo PPISN. If the entire hydrogen or helium envelope of these progenitors can be lost via pulsations, these models can provide a channel for the formation of Type Ibn SN. Interestingly, none of our Case B models or accretors of interacting binaries or non-interacting binary components are expected to be progenitors of PPISN at the SMC metallicity. The donors of models with initial masses $\geq 80 \, M_\odot$, that are expected to be the progenitors of the PPISN, begin to expand to red supergiant proportions (see single star tracks in the background of Fig. 4.2) while on their main sequence, filling their Roche Lobe and undergoing Case A mass transfer.

As discussed in Sect. 4.3.2, the number of ECSN progenitors in our grid is very small, with none of our Case A models being in this category. This is however expected to be an artifact of the resolution of our grid that only contains 2078 models and not a result of any underlying physical difference between Case A and Case B models. In Fig. 4.5, we show the percentage fractions of the different types of NS and BH progenitors from the the Case A and Case B mass transfer channel. We see that the ECSN and PPISN account only for 2.6% and 2% of the compact object progenitors in the SMC from the stable mass transfer channel. Also, SE SNe are estimated to comprise of ~33% (Case A-CCSN + Case B-CCSN divided by others-CCSN) of the total number of supernova events in our binary population.

We have seen that very few of our binary donors undergo ECSN and no non-interacting binaries undergo PPISN. So, in stellar populations that also contain single stars, the single stars are also mostly expected to be progenitors of CCSN or failed CCSN that results in the formation of BHs. Hence, the number of ECSN and PPISN are expected to be similar to the number yield from binaries (see also, Willcox et al., 2021) and total number of the other two types of compact object progenitors are expected to become doubled, assuming a binary fraction of 0.5 (Sana et al., 2012; Banyard et al., 2021) in a stellar population having mass $2 \times 10^5 \, M_\odot$. We see that both the binary components of all non-interacting binaries in our grid are predicted to undergo Type IIp supernovae. Hence, if single stars do not have eruptive mass-loss, none of the single stars will be stripped by ordinary stellar winds
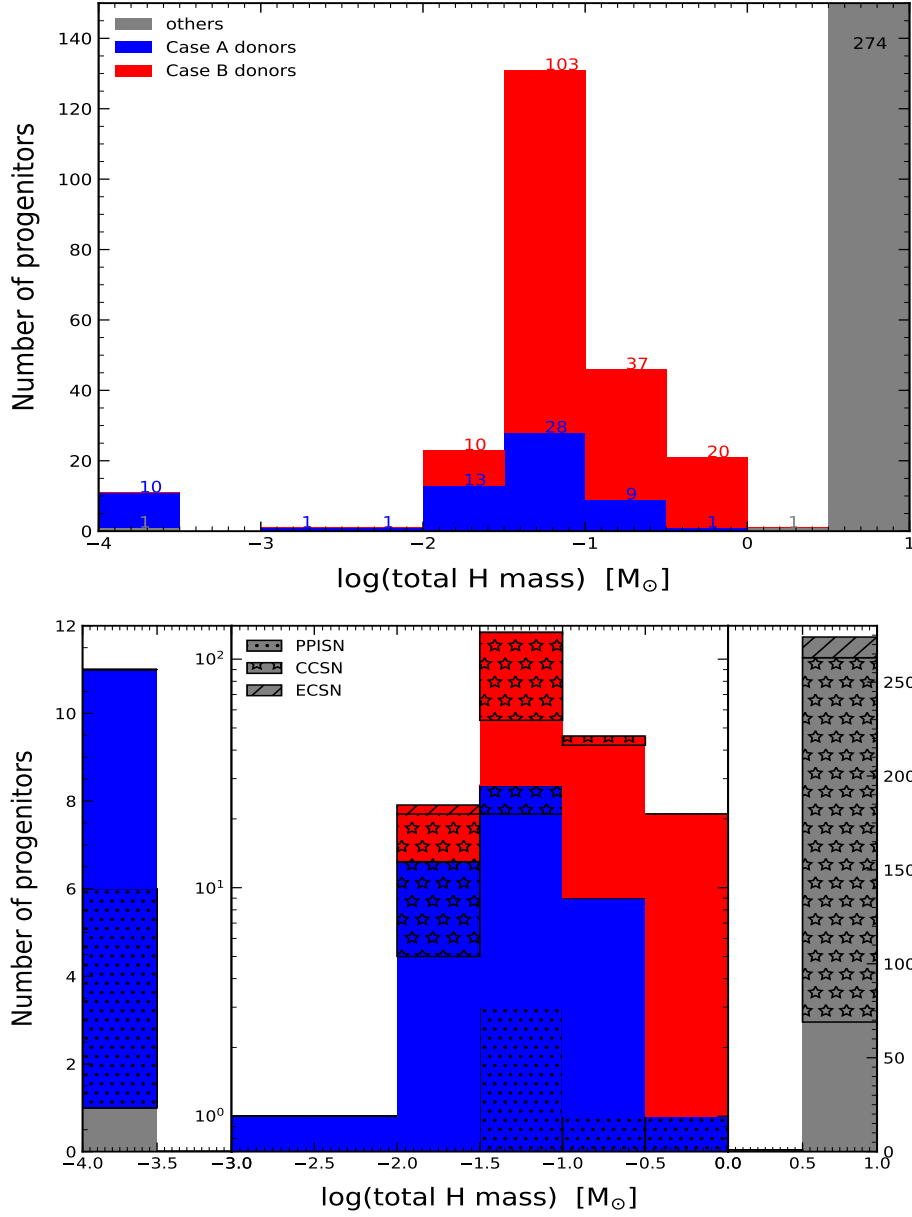
Figure 4.4: Histogram of numbers of NS or BH progenitors originating from our binary model grid as a function of the total hydrogen mass left at core carbon (or helium, depending on core helium mass) depletion of the progenitor. Case A donor stars are shown with blue and Case B donors are shown with red. All other progenitors are shown in grey. The dot, star and line hatching denote progenitors that are expected to undergo PPISN, CCSN and ECSN respectively. The unhatched portions denotes progenitors that are expected to directly collapse into a BH without a SN. *Top panel*: The total number of progenitors in the rightmost bin is 274, beyond the ordinate cut-off at 150. *Bottom panel*: The middle subplot of the bottom panel is in logarithmic axis to clearly show the different types of NS and BH progenitors, while the right hand side subplot is in linear scale and shows the division of progenitors that originate from binary accretors and non-interacting binary components. We note that models in the leftmost bin [-4,-3.5] of both panels have no hydrogen mass, but are included by hand to display and contrast them, on the same plot, from the models that have some hydrogen mass left.
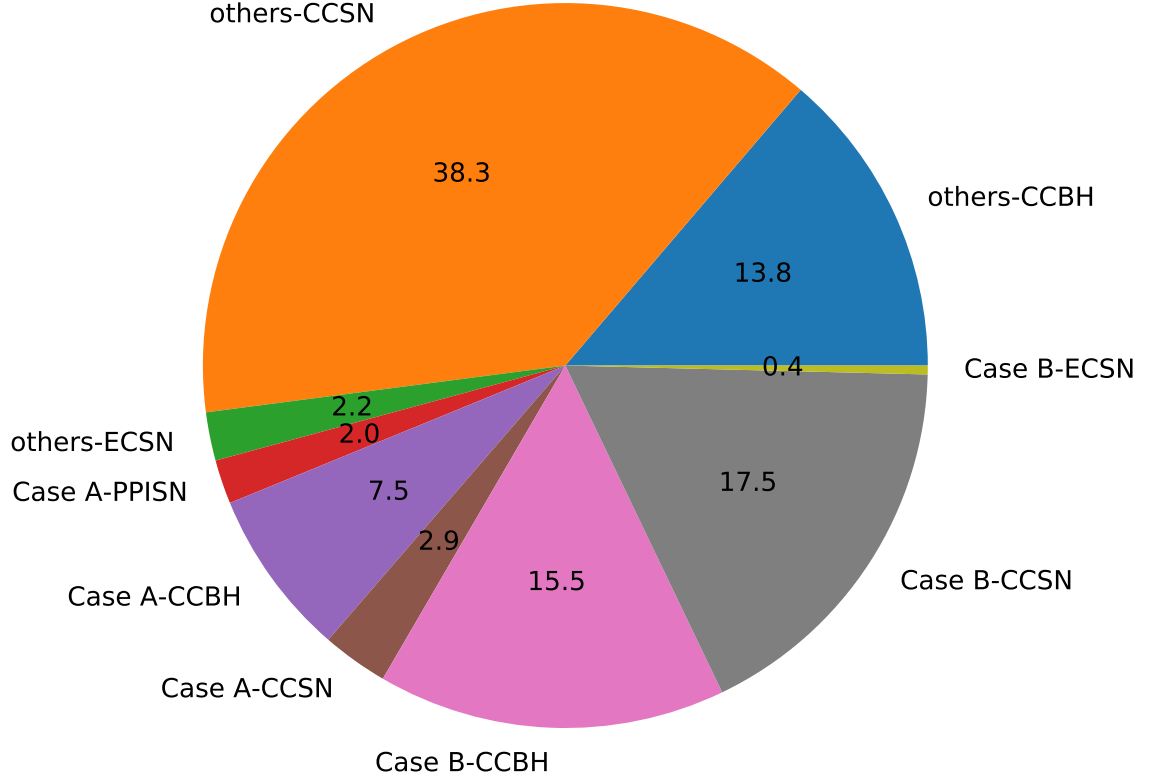
Figure 4.5: Fraction of different types of compact object progenitors expected from the stable binary mass transfer channels and non-interacting binaries in a $10^5 \, M_\odot$ coeval population of binary stars. 'Case A' and 'Case B' indicates the progenitors originating from Case A and Case B donor stars. Others indicate the progenitors originating from the accretors of interacting binaries and from both binary components of non-interacting binaries. 'ECSN', 'CCSN', 'CCBH' and 'PPISN' denote ECSN to form NSs, CCSN to form NSs, direct in-fall to form BHs and PPISN to form BHs, respectively.

at SMC metallicity, and all the single star progenitors are expected to undergo Type IIp SNe. Hence, the fractional number of SE SNe is expected to reduce by half to ∼16%.

Remnant mass distribution

Figure 4.6 (top panel) shows the distribution of compact object remnant masses as a function of their helium core mass. The remnant masses of stripped Case A and Case B donors are calculated using table 2 of Woosley et al. (2020). We interpolate between the helium core masses in table 2 of Woosley et al. (2020) using the nearest neighbour interpolation method. For the non-stripped progenitors, we
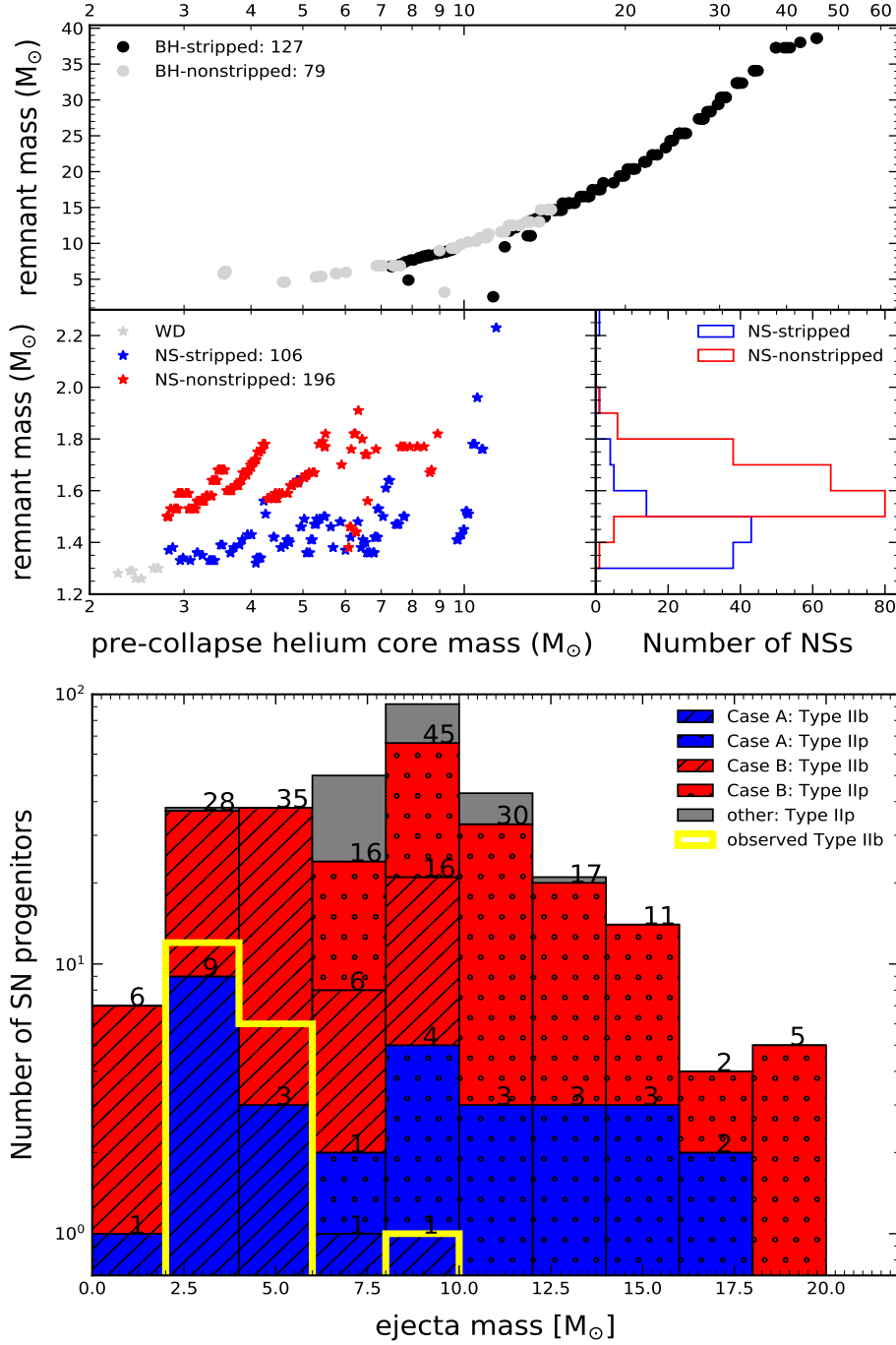
Figure 4.6: *Top panel:* Predicted remnant masses of BHs (top subplot) and NSs (bottom-left subplot) as a function of the progenitor helium core masses and the distribution of NS remnant masses (bottom-right subplot) arising from binary-stripped and non-stripped progenitors. The black and grey circles, red and blue asterisks represent BHs and NSs from binary-stripped and non-stripped progenitors, respectively. The light-grey markers show the progenitors that have carbon core masses less than $1.37\,M_\odot$ but are expected to undergo a SN from the criterion of Woosley et al. (2020). *Bottom panel:* Distribution of ejecta mass from SNe (except PPISNe) for different spectral types of SNe (Type IIb: hatched, Type IIp: dotted) with the color coding denoting the SNe originating from Case A (blue), Case B (red) binary components and non-interacting binaries (grey). The thick, yellow-coloured step-histogram show the estimated ejecta mass of the observed Type IIb SNe listed in Table 4.1.

use table 5 (the results from the W18 column) of Sukhbold et al. (2016).

The highest and lowest masses of neutron stars predicted from our models is ~2.25 $M_\odot$ and 1.32 $M_\odot$, respectively (bottom-left subplot). We see that there is a small mass gap between the maximum NS mass and the minimum BH mass (compare bottom and top subplots). We also see a small gap in the BH mass distribution around ~7-9 $M_\odot$ from the non-stripped progenitors and ~10-13 $M_\odot$ from the stripped progenitors (top subplot). This arises from the non-monotonicity of the explodability criterion (Sukhbold et al., 2016; Sukhbold et al., 2018; Woosley et al., 2020) used to determine the formation of a NS or BH. We note that the most massive NSs come from this island of explodability in the BH mass distribution. The highest mass of BHs formed from our grid is ~39 $M_\odot$.

Since we account for the islands of explodability in our prediction of the compact object remnants, we see that the total number of NSs (302) are much higher than the total number of BHs (207). Moreover, the islands of explodability for stripped and non-stripped progenitors are at different progenitor core masses and hence, at different luminosity on the HR diagram (Fig. 4.2). If we do not consider the islands of explodability and consider that all models having helium core masses above 6.6 $M_\odot$ collapses to form a BH, we find that the number of BHs predicted to form increases significantly to 252 and the number of NSs formed decreases to 257. Most notably, there is a drastic reduction in the number of stripped SNe progenitors from 106 to 65 in our models while the number of non-stripped SNe remains similar at 192. Accordingly, there is a significant increase in the number of stripped BH progenitors from 127 to 169.

Our models predict that stripped Case A and Case B donors form lighter NSs when compared to non-stripped progenitors having the same pre-collapse helium core mass. We attribute this systemic difference in mass to the amount of material above the core available for fallback onto the SN, increasing the final mass of the proto-neutron star (Sukhbold et al., 2016). The peak in neutron star masses predicted from our models is at 1.5-1.6 $M_\odot$. However, most of the stripped donors are expected to form NSs with masses below 1.5 $M_\odot$ while the non-stripped stars form NSs with masses $\geq$ 1.5 $M_\odot$.

The bottom panel of Fig. 4.6 shows the predicted ejecta masses from our models that are expected to undergo a SN explosion. We estimate the ejecta mass to be equal to the difference between the star mass prior to CC and the remnant mass estimated from Sukhbold et al. (2016) and Woosley et al. (2020) for non-stripped and stripped stars, respectively. Progenitors of Type IIb supernova (hatched), that come from stripped binary donor stars, have low ejecta masses from 0-10 $M_\odot$ with the lowest ejecta masses coming from the least massive stripped Case A donors. The ordinary Type II supernova are estimated to have ejecta masses between 6-20 $M_\odot$. We note that the maximum ejecta mass from binary accretors (blue and red dotted) is larger than that from non-interacting binaries (grey).

4.4 Comparison with observations

Modern dedicated transient surveys, such as the Zwicky Transient Facility (Bellm et al., 2019; Graham et al., 2019), the Palomar Transient Factory (Law et al., 2009; Rau et al., 2009), the Sloan Digital Sky Survey (Frieman et al., 2008; Sako et al., 2008) and the Lick Observatory Supernova Search (W. D. Li et al., 2000; Filippenko et al., 2001) have increased the wealth of high-quality photometric and spectroscopic observations of both Type II and SE SNe at an unprecedented pace. The number of observations is expected to increase in the coming decades with upcoming surveys such as the Large Synoptic Survey Telescope (LSST Science Collaboration et al., 2017).

In the last two decades, direct imaging of SN progenitors has advanced considerably (see, for e.g.,

Smartt, 2015; Van Dyk, 2017). A comparison of the observed properties of these SN progenitors with models on the HR diagram can help us understand the formation channels and rates of these events, as well as other transients, such as compact object mergers (Smartt, 2009). About ~17 progenitors of CCSNe have been identified, of which 5 of them are of Type IIb SE SNe: SN 1993J (Aldering et al., 1994), SN 2008ax (Crockett et al., 2008), SN 2011dh (Arcavi et al., 2011; Maund et al., 2011), SN 2013df (Van Dyk et al., 2014), and SN 2016gkg (Kilpatrick et al., 2017; Tartaglia et al., 2017).

Figure 4.2 show the position of the above five Type IIb SE SNe on the HR diagram. Their parameters (effective temperature, luminosity and its errorbar) are taken from table 1 of Farrell et al. (2020). The errorbars in effective temperature are taken from Smartt (2015, for 2008ax, 2011dh and 2013df), Aldering et al. (1994, for 1993J) and Kilpatrick et al. (2017, for 2016gkg). We see that the luminosity and effective temperatures of the observed progenitors indicate that, if they originated from binaries, they likely underwent a Case B mass transfer. Moreover, their envelope mass and total stellar mass (derived by Farrell et al., 2020, from stellar models) also matches well with our model predictions (see Fig. 4.3). Observational evidence for binarity has already been found for SN 1993J (Podsiadlowski et al., 1993; Nomoto et al., 1993; Woosley et al., 1994; Maund et al., 2004; Fox et al., 2014) and SN 2011dh (Van Dyk et al., 2013; Folatelli et al., 2014).

Table 4.1 lists the observed Type IIb SNe for which ejecta masses have been derived in the literature (see references in the table). We see from Fig. 4.6 (lower panel) that the predicted ejecta masses are in good agreement with the observations, giving credence to the binary origin of these Type IIb SNe (see also, Smith et al., 2011; Lyman et al., 2016; Taddia et al., 2018; Prentice et al., 2019).

Figure 4.7 show the distribution of different stellar properties of accretors of binaries that undergo Case A or Case B mass transfer, at the time of compact object formation of the donor. The top panel shows the distribution of luminosities. We see that the peak in the luminosity distribution of Case A accretors are higher than that of Case B accretors. Moreover, the number of Case A accretors show a decreasing trend with luminosity. This is due to a combination of two reasons: i) the parameter space for Case A mass transfer decreases with decrease in the mass (and hence the luminosity) of the donor. More models (to be precise, longer orbital period models) undergo Case A mass transfer at higher donor masses. Accordingly, there are more Case A accretors at higher luminosity. ii) The mass transfer in our Case A models is efficient compared to Case B models where the tides are not strong enough to halt the spin-up of the accretor to critical rotation. From the bottom panel we see that most of our Case A accretors are not rotating critically (see colour-bar), and hence they undergo efficient mass transfer. Due to this efficient mass transfer, the accretor masses increase and are also rejuvenated since we use efficient semi-convection (Braun et al., 1995). This rejuvenation process also increases the luminosity of the accretors of Case A binaries compared to Case B accretors. The decrease in the number of Case B accretors with $\log L < 4.0$ is because the number of donors that can form a compact object goes to zero below a certain core mass. However, we do not see a steep cut-off in the accretor luminosity but a gradual decline due to the effect of the binary mass ratio where a low mass accretor can be in a binary with a high mass donor that is massive enough to form a compact object upon CC.

We see that most of the accretors of the Case A binaries are tidally locked while those of the Case B models are critically rotating at the time of compact object formation. Owing to the low mass-loss rates at SMC metallicity, the critically rotating Case B accretors do not spin down during their remaining MS lifetime (Sen, 2020). Since single star evolution is unlikely to produce a large fraction of critically rotating stars (Hastings et al., 2020), critically rotating stars in low metallicity clusters are ideal candidates to search for compact objects. On the other hand, Case A accretors have much shorter orbital periods (Fig. C.1) and correspondingly larger orbital velocities. They also have
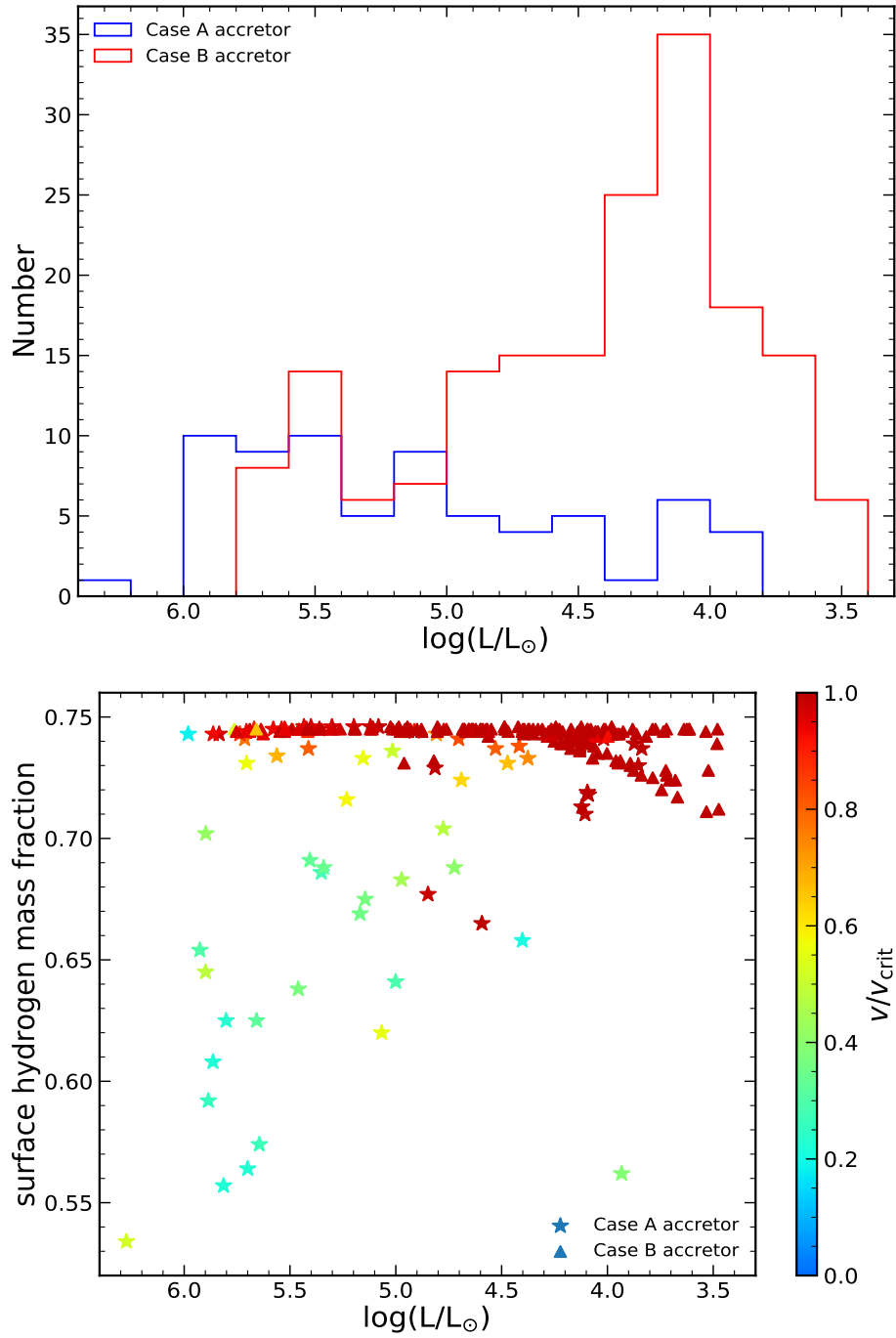
Figure 4.7: *Top panel:* Luminosity distribution of the accretors of Case A (blue) and Case B (red) binaries at the time of compact object formation of the donor. *Bottom panel:* Surface hydrogen mass fraction as a function of luminosity of the accretors of Case A and Case B binaries at the time of compact object formation of the donor. The colour-bar denotes the ratio of the rotational velocity of the accretor to its critical velocity.

Table 4.1: Ejecta mass of observed Type IIb SNe taken from the literature.

Name	M_{ej} ($M_\odot$)	Refs
2017gpn	2.00	1
2004ff	2.20	2
2006ba	2.60	2
2011dh4	2.80	3
2017hyh	3.00	1
2006bf	3.00	2
2004ex	3.20	2
2013df	3.30	3
2017ixz	3.50	1
2009Z	3.80	2
1993J	3.90	3
2005bj	3.90	2
2008ax	4.10	3
2008aq	4.30	2
2016gkg	4.40	3
2013bb	4.80	1
2005Q	4.90	2
2006T	5.50	2
2009K	9.10	2

(1) Prentice et al. (2019); (2) Taddia et al. (2018); (3) Farrell et al. (2020).

lower than primordial surface hydrogen mass fraction, signifying surface helium enrichment. The Case A compact object+MS binaries are more likely to be observed spectroscopically via periodic shifts in their radial velocity curves or from photometric variability of the MS star induced by the compact object companion in a tight orbit (Zucker et al., 2007; Masuda et al., 2019).

4.5 Comparison with earlier work

Sravan et al. (2019) and Sravan et al. (2020) investigated the properties of the progenitors of Type IIb SNe, focusing on the Case B channel. While we see that the Case B channel contributes to ~85% of the Type IIb progenitors in our grid (Fig. 4.5), we also find that the Case A donors form a distinctly separate population of hot SE stars prior to their CC (Fig. 4.2). The Type IIb progenitors from the Case B channel are expected to be mostly blue supergiants while the Case A donors may be as hot as main sequence stars prior to CC.

Assuming a binary fraction of 0.5, we discussed (in Sec. 4.3.3) that the percentage of SE SNe from the stable binary mass transfer channel in our population is ~16%. Around 70% of the binaries where the initially more massive primary undergoes a SNe are expected to disrupt and the accretor evolves as a effectively single star. For the binaries that do survive the SN explosion and form NSs, the mass ratio is generally too extreme for stable mass transfer to take place just after the accretor completes core hydrogen burning. As such, these systems are likely to merge. For the binaries where the donors

are massive enough such that they directly collapse into a BH, their accretors can fill their Roche lobe after core hydrogen depletion and survive a common envelope phase to form a SE SNe progenitor. However, we do not expect such a channel to significantly alter our predicted fraction of SE SNe at low metallicity.

Our prediction fraction of SE SNe (16%) is in good agreement with that predicted by Sravan et al. (2019, 15%). However, their work did not include the contribution from Case A binaries that are also expected to contribute to the population of SE SNe. At high metallicity, the observed Type IIb SNe rate is ~11% (W. Li et al., 2011; Smith et al., 2011; Graur et al., 2017). Evidence for a higher rate of Type IIb SNe has been found in lower metallicity galaxies (Arcavi et al., 2010; Graur et al., 2017), although these studies had a smaller sample size to derive their statistics from. We also note that the predicted number from Sravan et al. (2019) is true for their models with very low mass transfer efficiency, and we also implement accretor spin-up dependent mass accretion, which leads to very low transfer efficiency for most of our models (for more details, see Chapter 2.

We also note that if we do not account for the island of explodability in our progenitor mass space, the number of SE SNe reduces by ~40% (to 65, from 106, Sect. 4.3.3). This reduction would reduce the number of Type IIb supernova predicted from 16% to 10%. Hence, a bias-corrected sample of SNe progenitors at low metallicity might be able to give evidence towards the presence/absence of the island of explodability in nature.

Sravan et al. (2019) also find that to explain the observed Type IIb supernova rate at high metallicity, the wind mass-loss rates used in their work needs to be reduced, so that stars at higher metallicity do not lose their entire hydrogen envelope prior to core collapse. Our prescription for the wind mass loss rates are the same as that of Sravan et al. (2019) and we note that reducing the wind mass-loss rate further will reduce our predicted number of Type Ib SNe at a metallicity resembling that of the SMC.

Miyaji et al. (1980), Nomoto et al. (1984) and Poelarends et al. (2008) have shown that ECSNe from single stars are less common than initially thought. However, their rates could be enhanced in binaries because envelope stripping by Roche lobe overflow onto a companion suppresses second dredge-up (Podsiadlowski et al., 2004; Ibeling et al., 2013; Poelarends et al., 2017). More recently, Willcox et al. (2021) have argued that the observed pulsar speed distribution can be explained if ECSNe is assumed to only occur when the progenitor is stripped by binary. As such, the final conclusion on the number of ECSNe is very sensitive to our assumption on the range of core carbon masses that will result in an ECSNe. Overall however, the fraction of ECSNe are very small compared to CCSNe (Fig. 4.5).

4.6 Key assumptions and uncertainties

In this section, we discuss the effect of the various physics assumptions implemented in our models on our results.

4.6.1 Envelope inflation

Starting with the works of Kato (1985) and Ishii et al. (1999) who investigated the presence of an extended radiative envelope above the convective cores of very massive stars, envelope inflation in stars at different metallicities have been studied extensively (Petrovic et al., 2006; Grafener et al., 2012; Sanyal et al., 2015; Grassitelli et al., 2016; Sanyal et al., 2017), both for main sequence and pure helium stars. Petrovic et al. (2006) found that their models at SMC metallicity does not inflate. On the

other hand, the models of Köhler et al. (2015) at SMC metallicity are found to inflate above $\log L/L_\odot$ = 6. Hence, the inflation of very massive stars at SMC metallicity is model dependent in the literature.

Our binary donors are not found to inflate neither during the main sequence nor during their helium burning lifetime. The inflation of stripped envelope donors may lead to further mass transfer episodes during core helium burning, that can significantly change the surface properties of the donor stars (see also Laplace et al., 2020; Laplace et al., 2021), especially their surface temperatures and abundances prior to CC. This in turn will affect the spectral properties of the SN light curves. Petrovic et al. (2006) had derived an analytical relation for the upper limit to the mass-loss rate above which an inflated envelope of massive stars is not sustainable. The mass transfer rate from our donors during the Roche lobe overflow phase is much higher than this analytical value derived by (Petrovic et al., 2006). Hence, we expect that stripped envelope stars arising from the stable binary mass transfer channel to not inflate during core helium burning, as is also seen in our models.

4.6.2 Efficiency and stability of mass transfer

Observations of massive binary systems have revealed that a single binary mass transfer efficiency cannot explain their observable properties, such as the distribution of their mass ratios and orbital periods, or their surface abundances. Some systems indicate that they underwent an efficient mass transfer phase (Langer et al., 2003), while others require a highly inefficient mass transfer efficiency to be able to explain their observed properties (Wellstein et al., 1999). Further studies have also revealed hints on a binary parameter dependent mass transfer efficiency, where the mass transfer efficiency decreases with the decrease in mass ratio (Petrovic et al., 2005) and increase in orbital periods (S. E. de Mink et al., 2007).

In Chapter 2, we showed that the accretor spin-up dependent mass transfer efficiency is able to explain the orbital period-mass ratio distribution of massive Algol binaries in the LMC and the Galaxy. We adopt the same implementation of mass transfer efficiency in our models. Hence, the mass transfer efficiency of our Case B models is very low, owing to the longer orbital periods. Sravan et al. (2019) also found that the observed fraction of Type IIb SNe at low metallicity can be explained only by their low mass transfer efficiency models. An efficient mass transfer efficiency will lead to more models entering a contact configuration and end up merging (Menon et al., 2021), reducing the number of binary models that survive the mass transfer phase, and thereby the fraction of SE SNe (Sravan et al., 2019).

In our models, mass accretion is stopped when the accretor reaches critical rotation. Stars reach critical rotation on accreting a very small percentage of their own stellar mass (Packet, 1981). Hence, long period models, where tidal locking is absent, mass transfer efficiency is very low. This assumption also means that we have somehow remove all the excess transferred material that cannot be accreted. We choose to do it by artificially increasing the wind mass-loss rate of the accretor. We assume that the combined luminosity of both stars to power this mass loss. However, when this combined luminosity is unable to drive the excess mass loss, we assume the stars would enter a common envelope and merge.

C. Wang et al. (2020) found that to reproduce the relative number of Be stars to blue stragglers in NGC 330, the criteria for the stability of mass transfer, based on the combined luminosity of stars being able to remove the excess transferred mass, need to be relaxed. Accordingly, the number of binary models surviving the mass transfer phase and their donors becoming progenitors of SE SNe will increase. This will increase our predicted fraction of Type IIb SNe.

4.6.3 Wind mass-loss rates

In the SMC, the lowest luminosity of an observed Wolf-Rayet (WR) star is at $\log L/L_\odot = 5.6$. It is now believed that stars below this luminosity do not show the characteristic WR spectrum (Shenar et al., 2020) and their wind mass loss rates are orders of magnitude lower than WR stars (Vink, 2017). However, this reduced mass-loss rates are not considered in our models of the lower luminosity stripped stars, where we extrapolate the WR mass loss rates to lower luminosities. Hence, the amount of total hydrogen mass left in the stripped envelope stars might be higher than is predicted by our models. However, we do not expect the core evolution of these models to be affected as even our *higher* wind mass-loss rates do not strip the entire hydrogen envelope of the stars. Hence, the explodability of these models should not be affected as it mainly depends on the core structure of the star. Furthermore, lower luminosity stripped stars originate from lower initial masses where most stars are expected to explode.

Recently, it has been suggested (Beasor et al., 2021) that the red supergiant (RSG) mass-loss rates used in stellar evolution calculations are over-estimated. They showed that with their emperically calibrated RSG mass-loss rates, a larger hydrogen envelope is present on the compact object progenitor star prior to CC. We note that if this is indeed true, then the predicted distribution of ejecta masses of our Type IIp progenitors is expected to shift towards higher ejecta masses.

4.6.4 Uncertainties in the core structure

Even though we use detailed binary evolution models to determine the structure of our models, there are still numerical issues that affect the accuracy of simulations of massive star evolution. For example, numerical resolution and the nuclear network used can lead to differences in core structure prior to CC. This in turn affects the explodability of the massive stars (R. Farmer et al., 2016). Moreover, we do not calculate our models up to CC but use the core helium mass of our models at the end of core carbon burning to determine their explodability. As such, we cannot be certain as to exactly which model would explode or not if we applied the explodability criterion on each of our models explicitly. Moreover, we use one dimensional models of massive stars while it has recently been found that three dimensional models are more prone to explosion due to turbulence arising in them that promotes shock revival (Vartanyan et al., 2021).

Another major uncertainty in the evolution of stripped envelope stars is the reaction rate of the $^{12}C(\alpha, \gamma)^{16}O$ reaction (deBoer et al., 2017). It influences the amount of carbon left after core helium burning, and hence can determine whether the following core carbon burning phase proceeds radiatively or convectively (Imbriani et al., 2001). Several studies have found that this has a major effect on the explodability of massive stars (Sukhbold et al., 2014; R. Farmer et al., 2019; Patton et al., 2020; Schneider et al., 2021). Exploring the effect of such uncertainties are well beyond the scope of this work, as it may affect the individual outcomes of each of our model binary components. However, since our models cover a large range of the binary parameter space, we expect that this uncertainty will not affect the overall conclusions we derive from this work.

The extent of convective core overshooting during the helium burning phase is also ill-constrained. A change in the assumed overshooting parameter will result in a different core mass, affecting the lifetime of the core helium burning and subsequent burning phases, as well as the final structure of the star prior to CC. Most importantly, overshooting in low mass helium stars will affect the lower limit of the initial mass of stars that can undergo a CCSNe (Chanlaridis et al., 2021).

4.6.5 Islands of explodability in the context of compact object formation

Recently, detailed studies have revealed that the structure of the star plays a complex role in determining the outcome of a CC event in massive stars (see, for e.g., O'Connor et al., 2011; Ertl et al., 2016; Sukhbold et al., 2016; Patton et al., 2020; Woosley et al., 2020; Ertl et al., 2020). The general consensus on the continuity of the progenitor mass space and the remnant mass space (for e.g., Fryer et al., 2012) is changing, with the most recent discovery of "islands of explodability" in the progenitor mass space. It has been shown that two progenitors stars of very similar total mass can have very different outcomes (NS or BH) from a CC event, based on minute differences in the structure of their core. The situation may be further complicated by the presence of fallback SNe from very massive stars that produce light remnants (NSs). If these islands of explodability are not a numerical artifact, this would decrease the predicted rates of binary BH mergers and increase the likelihood of observing extreme mass ratio NS-BH mergers (for e.g., GW 190814, Abbott et al., 2020).

4.6.6 SNe from binary mergers

Recently, it has been found that very short period binaries (initial orbital periods less than 2 days) enter into a contact configuration during their Case A mass transfer phase and eventually merge while both stars are on their main sequence (Menon et al., 2021). We model the subsequent evolution of these main sequence mergers following the treatment of Schneider et al. (2016) and Schneider et al. (2019), adopting an appropriate stellar mass, age and central hydrogen abundance for the initial single stellar model after the merger happens. With this assumption, we find that our models predict that all mergers lead to Type IIp SNe. However, earlier work has shown that binary mergers can form fast rotating single stars that lead to long duration gamma ray bursts (S. .-.-C. Yoon et al., 2005; Woosley et al., 2006; Dessart et al., 2008), SN progenitors that explode as blue supergiants (Menon et al., 2019) and luminous blue variables that explode as superluminous SNe (Justham et al., 2014).

4.7 Conclusions

Using a grid of 2078 detailed binary evolution models, with their initial binary parameters derived using a Monte Carlo procedure that takes into account the binary distribution functions, we study the number of compact object+main sequence binaries in a coeval population of binary stars in the SMC. Since our initial binary parameters are weighted by the initial mass function, binary period and mass ratio distribution, we also look at the distribution of compact object progenitors on the HR diagram and as function of various relevant stellar parameters.

We predict 10-40 BH+OB binaries in a $10^5 \, M_\odot$ population of binary stars at ages of 5-20 Myrs, along with ~10 NS+OB binaries at ages of 10-30 Myrs. We find that the companions to Case A SE SNe progenitors to be mostly tidally locked to the orbit and showing surface helium enrichment, while the companions to Case B SE SNe progenitors are critically rotating and has almost no surface helium enrichment. We find the existence of a time delay between the occurrence of SE SNe and ordinary Type IIp SNe during the first 20 Myrs of the evolution of the cluster (Fig. 4.1).

We show the position of the compact object progenitors on the HR diagram prior to core collapse (Fig. 4.2) to guide the upcoming photometric and spectroscopic surveys on SE SNe and their progenitors that are expected to start in the upcoming years. We predict the presence of a population of hot SE

SNe progenitors arising from the Case A binary mass transfer channel along with the relatively cooler SE SNe progenitors originating from the Case B channel.

We predict the distribution of ejecta masses and remnant masses for our compact object progenitors, using the result of Sukhbold et al. (2016) for the non-stripped stars and the results of Woosley et al. (2020) for our stripped stars. The observed ejecta masses of Type IIb SNe are in good agreement with our model predictions 4.3.3. We also find that NSs formed from SE binary stars having same core helium mass to be generally less massive than those formed from non-stripped stars.

References

Abbott, R. et al. (2020), *GW190814: Gravitational Waves from the Coalescence of a 23 Solar Mass Black Hole with a 2.6 Solar Mass Compact Object*, The Astrophysical Journal **896** L44, arXiv: `2006.12611 [astro-ph.HE]` (cit. on p. 97).

Aguilera-Dena, D. R., N. Langer, J. Antoniadis and B. Müller (2020), *Precollapse Properties of Superluminous Supernovae and Long Gamma-Ray Burst Progenitor Models*, The Astrophysical Journal **901** 114, arXiv: `2008.09132 [astro-ph.SR]` (cit. on p. 85).

Aguilera-Dena, D. R., N. Langer, T. J. Moriya and A. Schootemeijer (2018), *Related Progenitor Models for Long-duration Gamma-Ray Bursts and Type Ic Superluminous Supernovae*, The Astrophysical Journal **858** 115, arXiv: `1804.07317 [astro-ph.SR]` (cit. on pp. 76, 85).

Aldering, G., R. M. Humphreys and M. Richmond (1994), *SN 1993J: The Optical Properties of its Progenitor*, The Astronomical Journal **107** 662 (cit. on p. 91).

Arcavi, I., A. Gal-Yam, M. M. Kasliwal et al. (2010), *Core-collapse Supernovae from the Palomar Transient Factory: Indications for a Different Population in Dwarf Galaxies*, The Astrophysical Journal **721** 777, arXiv: `1004.0615 [astro-ph.CO]` (cit. on p. 94).

Arcavi, I., A. Gal-Yam, O. Yaron et al. (2011), *SN 2011dh: Discovery of a Type IIb Supernova from a Compact Progenitor in the Nearby Galaxy M51*, The Astrophysical Journal **742** L18, arXiv: `1106.3551 [astro-ph.CO]` (cit. on p. 91).

Baade, W. and F. Zwicky (1934), *Remarks on Super-Novae and Cosmic Rays*, Physical Review **46** 76 (cit. on p. 76).

Banyard, G. et al. (2021), *The observed multiplicity properties of B-type stars in the Galactic young open cluster NGC 6231*, arXiv e-prints arXiv:2108.07814, arXiv: `2108.07814 [astro-ph.SR]` (cit. on pp. 77, 86).

Beasor, E. R., B. Davies and N. Smith (2021), *The impact of realistic red supergiant mass-loss on stellar evolution*, arXiv e-prints arXiv:2109.03239, arXiv: `2109.03239 [astro-ph.SR]` (cit. on p. 96).

Belczynski, K., D. E. Holz, T. Bulik and R. O'Shaughnessy (2016), *The first gravitational-wave source from the isolated evolution of two stars in the 40-100 solar mass range*, Nature **534** 512, arXiv: `1602.04531 [astro-ph.HE]` (cit. on p. 81).

Bellm, E. C. et al. (2019), *The Zwicky Transient Facility: System Overview, Performance, and First Results*, Publications of the Astronomical Society of the Pacific **131** 018002, arXiv: `1902.01932 [astro-ph.IM]` (cit. on p. 90).

Bethe, H. A. (1990), *Supernova mechanisms*, Reviews of Modern Physics **62** 801 (cit. on p. 76).

Bianco, F. B. et al. (2014), *Multi-color Optical and Near-infrared Light Curves of 64 Stripped-envelope Core-Collapse Supernovae*, The Astrophysical Journal Supplement Series **213** 19, arXiv: `1405.1428 [astro-ph.SR]` (cit. on p. 77).

Blaauw, A. (1961), *On the origin of the O- and B-type stars with high velocities (the "run-away" stars), and some related problems*, Bulletin of the Astronomical Institutes of the Netherlands **15** 265 (cit. on p. 81).

Braun, H. and N. Langer (1995), *Effects of accretion onto massive main sequence stars.*, Astronomy and Astrophysics **297** 483 (cit. on p. 91).

Brott, I. et al. (2011), *Rotating massive main-sequence stars. I. Grids of evolutionary models and isochrones*, Astronomy and Astrophysics **530** A115, arXiv: `1102.0530 [astro-ph.SR]` (cit. on p. 78).

Burrows, A. and D. Vartanyan (2021), *Core-collapse supernova explosion theory*, Nature **589** 29, arXiv: `2009.14157` `[astro-ph.SR]` (cit. on p. 76).

Burrows, A. (2000), *Supernova explosions in the Universe*, Nature **403** 727 (cit. on p. 76).

Burrows, A., J. Hayes and B. A. Fryxell (1995), *On the Nature of Core-Collapse Supernova Explosions*, The Astrophysical Journal **450** 830, arXiv: `astro-ph/9506061` `[astro-ph]` (cit. on p. 76).

Chan, C., B. Müller, A. Heger, R. Pakmor and V. Springel (2018), *Black Hole Formation and Fallback during the Supernova Explosion of a 40 M $_\odot$ Star*, The Astrophysical Journal **852** L19, arXiv: `1710.00838` `[astro-ph.SR]` (cit. on p. 76).

Chanlaridis, S. et al. (2021), *Stripped stars as progenitors of thermonuclear supernovae. Metallicity dependence and pre-explosion properties*, Astronomy & Astrophysics, submitted (cit. on p. 96).

Chen, K.-J., A. Heger, S. Woosley, A. Almgren and D. J. Whalen (2014), *Pair Instability Supernovae of Very Massive Population III Stars*, The Astrophysical Journal **792** 44, arXiv: `1402.5960` `[astro-ph.HE]` (cit. on p. 79).

Claeys, J. S. W., S. E. de Mink, O. R. Pols, J. J. Eldridge and M. Baes (2011), *Binary progenitor models of type IIb supernovae*, Astronomy and Astrophysics **528** A131, arXiv: `1102.1732` `[astro-ph.SR]` (cit. on p. 77).

Crockett, R. M. et al. (2008), *The type IIb SN 2008ax: the nature of the progenitor*, Monthly Notices of the Royal Astronomical Society **391** L5, arXiv: `0805.1913` `[astro-ph]` (cit. on p. 91).

de Mink, S. E. and I. Mandel (2016), *The chemically homogeneous evolutionary channel for binary black hole mergers: rates and properties of gravitational-wave events detectable by advanced LIGO*, Monthly Notices of the Royal Astronomical Society **460** 3545, arXiv: `1603.02291` `[astro-ph.HE]` (cit. on p. 77).

de Mink, S. E., O. R. Pols and R. W. Hilditch (2007), *Efficiency of mass transfer in massive close binaries. Tests from double-lined eclipsing binaries in the SMC*, Astronomy and Astrophysics **467** 1181, arXiv: `astro-ph/0703480` `[astro-ph]` (cit. on p. 95).

deBoer, R. J. et al. (2017), *The $^{12}C(\alpha,\gamma)^{16}O$ reaction and its implications for stellar helium burning*, Reviews of Modern Physics **89** 035007, arXiv: `1709.03144` `[nucl-ex]` (cit. on p. 96).

Dessart, L., A. Burrows, E. Livne and C. D. Ott (2008), *The Proto-Neutron Star Phase of the Collapsar Model and the Route to Long-Soft Gamma-Ray Bursts and Hypernovae*, The Astrophysical Journal **673** L43, arXiv: `0710.5789` `[astro-ph]` (cit. on p. 97).

Dessart, L., S.-C. Yoon, D. R. Aguilera-Dena and N. Langer (2020), *Supernovae Ib and Ic from the explosion of helium stars*, Astronomy and Astrophysics **642** A106, arXiv: `2008.07601` `[astro-ph.SR]` (cit. on p. 82).

Doherty, C. L., P. Gil-Pons, L. Siess and J. C. Lattanzio (2017), *Super-AGB Stars and their Role as Electron Capture Supernova Progenitors*, Publications of the Astronomical Society of Australia **34** e056, arXiv: `1703.06895` `[astro-ph.SR]` (cit. on p. 79).

Drout, M. R. et al. (2011), *The First Systematic Study of Type Ibc Supernova Multi-band Light Curves*, The Astrophysical Journal **741** 97, arXiv: `1011.4959` `[astro-ph.CO]` (cit. on p. 77).

Eldridge, J. J., M. Fraser, S. J. Smartt, J. R. Maund and R. M. Crockett (2013), *The death of massive stars - II. Observational constraints on the progenitors of Type Ibc supernovae*, Monthly Notices of the Royal Astronomical Society **436** 774, arXiv: `1301.1975` `[astro-ph.SR]` (cit. on p. 77).

Ertl, T., H. .-.-T. Janka, S. E. Woosley, T. Sukhbold and M. Ugliano (2016), *A Two-parameter Criterion for Classifying the Explodability of Massive Stars by the Neutrino-driven Mechanism*, The Astrophysical Journal **818** 124, arXiv: `1503.07522` `[astro-ph.SR]` (cit. on pp. 77, 79, 97).

Ertl, T., S. E. Woosley, T. Sukhbold and H. .-.-T. Janka (2020), *The Explosion of Helium Stars Evolved with Mass Loss*, The Astrophysical Journal **890** 51, arXiv: `1910.01641` `[astro-ph.HE]` (cit. on pp. 79, 97).

Farmer, R., C. E. Fields et al. (2016), *On Variations Of Pre-supernova Model Properties*, The Astrophysical Journal Supplement Series **227** 22, arXiv: `1611.01207` `[astro-ph.SR]` (cit. on p. 96).

Farmer, R., M. Renzo, S. E. de Mink, P. Marchant and S. Justham (2019), *Mind the Gap: The Location of the Lower Edge of the Pair-instability Supernova Black Hole Mass Gap*, The Astrophysical Journal **887** 53, arXiv: `1910.12874` `[astro-ph.SR]` (cit. on pp. 79, 82, 96).

Farrell, E. J., J. H. Groh, G. Meynet and J. J. Eldridge (2020), *The uncertain masses of progenitors of core-collapse supernovae and direct-collapse black holes*, Monthly Notices of the Royal Astronomical Society **494** L53, arXiv: `2001.08711` `[astro-ph.SR]` (cit. on pp. 77, 83, 84, 91, 93).

Filippenko, A. V. (1997), *Optical Spectra of Supernovae*, Annual Review of Astronomy and Astrophysics **35** 309 (cit. on p. 76).

Filippenko, A. V., W. D. Li, R. R. Treffers and M. Modjaz (2001), "The Lick Observatory Supernova Search with the Katzman Automatic Imaging Telescope", *IAU Colloq. 183: Small Telescope Astronomy on Global Scales*, ed. by B. Paczynski, W.-P. Chen and C. Lemme, vol. 246, Astronomical Society of the Pacific Conference Series 121 (cit. on p. 90).

Folatelli, G. et al. (2014), *A Blue Point Source at the Location of Supernova 2011dh*, The Astrophysical Journal **793** L22, arXiv: `1409.0700` `[astro-ph.SR]` (cit. on p. 91).

Foley, R. J. et al. (2007), *SN 2006jc: A Wolf-Rayet Star Exploding in a Dense He-rich Circumstellar Medium*, The Astrophysical Journal **657** L105, arXiv: `astro-ph/0612711` `[astro-ph]` (cit. on p. 82).

Fox, O. D. et al. (2014), *Uncovering the Putative B-star Binary Companion of the SN 1993J Progenitor*, The Astrophysical Journal **790** 17, arXiv: `1405.4863` `[astro-ph.HE]` (cit. on p. 91).

Fraley, G. S. (1968), *Supernovae Explosions Induced by Pair-Production Instability*, Astrophysics and Space Science **2** 96 (cit. on p. 76).

Fremling, C. et al. (2018), *Oxygen and helium in stripped-envelope supernovae*, Astronomy and Astrophysics **618** A37, arXiv: `1807.00100` `[astro-ph.HE]` (cit. on p. 77).

Frieman, J. A. et al. (2008), *The Sloan Digital Sky Survey-II Supernova Survey: Technical Summary*, The Astronomical Journal **135** 338, arXiv: `0708.2749` `[astro-ph]` (cit. on p. 90).

Fryer, C. L. et al. (2012), *Compact Remnant Mass Function: Dependence on the Explosion Mechanism and Metallicity*, The Astrophysical Journal **749** 91, arXiv: `1110.1726` `[astro-ph.SR]` (cit. on p. 97).

Gal-Yam, A. et al. (2007), "Preliminary Results from the Caltech Core-Collapse Project (CCCP)", *The Multicolored Landscape of Compact Objects and Their Explosive Origins*, ed. by T. di Salvo et al., vol. 924, American Institute of Physics Conference Series 297, arXiv: `astro-ph/0611919` `[astro-ph]` (cit. on p. 77).

Gilkis, A. and I. Arcavi (2022), *How much hydrogen is in Type Ib and IIb supernova progenitors?*, Monthly Notices of the Royal Astronomical Society **511** 691, arXiv: `2111.04432` `[astro-ph.SR]` (cit. on p. 80).

Gilkis, A., J. S. Vink, J. J. Eldridge and C. A. Tout (2019), *Effects of winds on the leftover hydrogen in massive stars following Roche lobe overflow*, Monthly Notices of the Royal Astronomical Society **486** 4451, arXiv: `1904.09221` `[astro-ph.SR]` (cit. on p. 76).

Grafener, G., S. P. Owocki and J. S. Vink (2012), *Stellar envelope inflation near the Eddington limit. Implications for the radii of Wolf-Rayet stars and luminous blue variables*, Astronomy and Astrophysics **538** A40, arXiv: `1112.1910` [`astro-ph.SR`] (cit. on p. 94).

Graham, M. J. et al. (2019), *The Zwicky Transient Facility: Science Objectives*, Publications of the Astronomical Society of the Pacific **131** 078001, arXiv: `1902.01945` [`astro-ph.IM`] (cit. on p. 90).

Grassitelli, L. et al. (2016), *Diagnostics of the unstable envelopes of Wolf-Rayet stars*, Astronomy and Astrophysics **590** A12, arXiv: `1603.08931` [`astro-ph.SR`] (cit. on p. 94).

Graur, O., F. B. Bianco, S. Huang et al. (2017), *LOSS Revisited. I. Unraveling Correlations Between Supernova Rates and Galaxy Properties, as Measured in a Reanalysis of the Lick Observatory Supernova Search*, The Astrophysical Journal **837** 120, arXiv: `1609.02921` [`astro-ph.HE`] (cit. on p. 94).

Graur, O., F. B. Bianco, M. Modjaz et al. (2017), *LOSS Revisited. II. The Relative Rates of Different Types of Supernovae Vary between Low- and High-mass Galaxies*, The Astrophysical Journal **837** 121, arXiv: `1609.02923` [`astro-ph.HE`] (cit. on p. 94).

Groh, J. H., G. Meynet, C. Georgy and S. Ekström (2013), *Fundamental properties of core-collapse supernova and GRB progenitors: predicting the look of massive stars before death*, Astronomy and Astrophysics **558** A131, arXiv: `1308.4681` [`astro-ph.SR`] (cit. on p. 79).

Hachinger, S. et al. (2012), *How much H and He is 'hidden' in SNe Ib/c? - I. Low-mass objects*, Monthly Notices of the Royal Astronomical Society **422** 70, arXiv: `1201.1506` [`astro-ph.SR`] (cit. on p. 80).

Hamuy, M. et al. (2006), *The Carnegie Supernova Project: The Low-Redshift Survey*, Publications of the Astronomical Society of the Pacific **118** 2, arXiv: `astro-ph/0512039` [`astro-ph`] (cit. on p. 77).

Hastings, B., C. Wang and N. Langer (2020), *The single star path to Be stars*, Astronomy and Astrophysics **633** A165, arXiv: `1912.05290` [`astro-ph.SR`] (cit. on p. 91).

Heger, A., C. L. Fryer, S. E. Woosley, N. Langer and D. H. Hartmann (2003), *How Massive Single Stars End Their Life*, The Astrophysical Journal **591** 288, arXiv: `astro-ph/0212469` [`astro-ph`] (cit. on pp. 76, 77).

Heger, A., N. Langer and S. E. Woosley (2000), *Presupernova Evolution of Rotating Massive Stars. I. Numerical Method and Evolution of the Internal Stellar Structure*, The Astrophysical Journal **528** 368, arXiv: `astro-ph/9904132` [`astro-ph`] (cit. on p. 78).

Heger, A. and S. E. Woosley (2002), *The Nucleosynthetic Signature of Population III*, The Astrophysical Journal **567** 532, arXiv: `astro-ph/0107037` [`astro-ph`] (cit. on p. 76).

Heger, A., S. E. Woosley and H. C. Spruit (2005), *Presupernova Evolution of Differentially Rotating Massive Stars Including Magnetic Fields*, The Astrophysical Journal **626** 350, arXiv: `astro-ph/0409422` [`astro-ph`] (cit. on p. 78).

Hillebrandt, W. and J. C. Niemeyer (2000), *Type IA Supernova Explosion Models*, Annual Review of Astronomy and Astrophysics **38** 191, arXiv: `astro-ph/0006305` [`astro-ph`] (cit. on p. 76).

Hobbs, G., D. R. Lorimer, A. G. Lyne and M. Kramer (2005), *A statistical study of 233 pulsar proper motions*, Monthly Notices of the Royal Astronomical Society **360** 974, arXiv: `astro-ph/0504584` [`astro-ph`] (cit. on p. 81).

Ibeling, D. and A. Heger (2013), *The Metallicity Dependence of the Minimum Mass for Core-collapse Supernovae*, The Astrophysical Journal **765** L43, arXiv: `1301.5783` [`astro-ph.SR`] (cit. on p. 94).

Imbriani, G. et al. (2001), *The $^{12}C(\alpha, \gamma)^{16}O$ Reaction Rate and the Evolution of Stars in the Mass Range 0.8<=M/M$_{solar}$<=25*, The Astrophysical Journal **558** 903, arXiv: `astro-ph/0107172` `[astro-ph]` (cit. on p. 96).

Ishii, M., M. Ueno and M. Kato (1999), *Core-Halo Structure of a Chemically Homogeneous Massive Star and Bending of the Zero-Age Main Sequence*, Publications of the Astronomical Society of Japan **51** 417, arXiv: `astro-ph/9907154 [astro-ph]` (cit. on p. 94).

Justham, S., P. Podsiadlowski and J. S. Vink (2014), *Luminous Blue Variables and Superluminous Supernovae from Binary Mergers*, The Astrophysical Journal **796** 121, arXiv: `1410.2426` `[astro-ph.SR]` (cit. on p. 97).

Kankare, E. et al. (2021), *Core-collapse supernova subtypes in luminous infrared galaxies*, Astronomy and Astrophysics **649** A134, arXiv: `2102.13512 [astro-ph.SR]` (cit. on p. 82).

Kato, M. (1985), *A new type of solution for very massive stars and the occurrence of steady mass loss*, Publications of the Astronomical Society of Japan **37** 311 (cit. on p. 94).

Kilpatrick, C. D. et al. (2017), *On the progenitor of the Type IIb supernova 2016gkg*, Monthly Notices of the Royal Astronomical Society **465** 4650, arXiv: `1610.04587 [astro-ph.SR]` (cit. on p. 91).

Kobulnicky, H. A. et al. (2014), *Toward Complete Statistics of Massive Binary Stars: Penultimate Results from the Cygnus OB2 Radial Velocity Survey*, The Astrophysical Journal Supplement Series **213** 34, arXiv: `1406.6655 [astro-ph.SR]` (cit. on p. 77).

Kochanek, C. S. et al. (2008), *A Survey About Nothing: Monitoring a Million Supergiants for Failed Supernovae*, The Astrophysical Journal **684** 1336, arXiv: `0802.0456` `[astro-ph]` (cit. on p. 77).

Köhler, K. et al. (2015), *The evolution of rotating very massive stars with LMC composition*, Astronomy and Astrophysics **573** A71, arXiv: `1501.03794 [astro-ph.SR]` (cit. on p. 95).

Kruckow, M. U., T. M. Tauris, N. Langer, M. Kramer and R. G. Izzard (2018), *Progenitors of gravitational wave mergers: binary evolution with the stellar grid-based code COMBINE*, Monthly Notices of the Royal Astronomical Society **481** 1908, arXiv: `1801.05433 [astro-ph.SR]` (cit. on pp. 79, 82, 83).

Langer, N. (2012), *Presupernova Evolution of Massive Single and Binary Stars*, Annual Review of Astronomy and Astrophysics **50** 107, arXiv: `1206.5443 [astro-ph.SR]` (cit. on p. 76).

Langer, N., C. Schurmann et al. (2020), *Properties of OB star-black hole systems derived from detailed binary evolution models*, Astronomy and Astrophysics **638** A39, arXiv: `1912.09826` `[astro-ph.SR]` (cit. on p. 81).

Langer, N., S. Wellstein and J. Petrovic (2003), "On the evolution of massive close binaries", *A Massive Star Odyssey: From Main Sequence to Supernova*, ed. by K. van der Hucht, A. Herrero and C. Esteban, vol. 212, IAU Symposium 275 (cit. on p. 95).

Laplace, E., Y. Gotberg, S. E. de Mink, S. Justham and R. Farmer (2020), *The expansion of stripped-envelope stars: Consequences for supernovae and gravitational-wave progenitors*, Astronomy and Astrophysics **637** A6, arXiv: `2003.01120 [astro-ph.SR]` (cit. on pp. 77, 79, 82, 95).

Laplace, E., S. Justham et al. (2021), *Different to the core: the pre-supernova structures of massive single and binary-stripped stars*, arXiv e-prints arXiv:2102.05036, arXiv: `2102.05036 [astro-ph.SR]` (cit. on pp. 77, 79, 81, 95).

Law, N. M. et al. (2009), *The Palomar Transient Factory: System Overview, Performance, and First Results*, Publications of the Astronomical Society of the Pacific **121** 1395, arXiv: `0906.5350` `[astro-ph.IM]` (cit. on p. 90).

Leung, S.-C. and K. Nomoto (2019), *Final evolution of super-AGB stars and supernovae triggered by electron capture*, Publications of the Astronomical Society of Australia **36** e006 (cit. on p. 76).

Li, W. D. et al. (2000), "The Lick Observatory Supernova Search", *Cosmic Explosions: Tenth AstroPhysics Conference*, ed. by S. S. Holt and W. W. Zhang, vol. 522, American Institute of Physics Conference Series 103, arXiv: `astro-ph/9912336 [astro-ph]` (cit. on p. 90).

Li, W., J. Leaman et al. (2011), *Nearby supernova rates from the Lick Observatory Supernova Search - II. The observed luminosity functions and fractions of supernovae in a complete sample*, Monthly Notices of the Royal Astronomical Society **412** 1441, arXiv: `1006.4612 [astro-ph.SR]` (cit. on p. 94).

Li, W., S. D. Van Dyk et al. (2006), *Identification of the Red Supergiant Progenitor of Supernova 2005cs: Do the Progenitors of Type II-P Supernovae Have Low Mass?*, The Astrophysical Journal **641** 1060, arXiv: `astro-ph/0507394 [astro-ph]` (cit. on p. 77).

Li, W., X. Wang et al. (2007), *On the Progenitors of Two Type II-P Supernovae in the Virgo Cluster*, The Astrophysical Journal **661** 1013, arXiv: `astro-ph/0701049 [astro-ph]` (cit. on p. 77).

Liu, Y.-Q., M. Modjaz, F. B. Bianco and O. Graur (2016), *Analyzing the Largest Spectroscopic Data Set of Stripped Supernovae to Improve Their Identifications and Constrain Their Progenitors*, The Astrophysical Journal **827** 90, arXiv: `1510.08049 [astro-ph.HE]` (cit. on p. 77).

LSST Science Collaboration et al. (2017), *Science-Driven Optimization of the LSST Observing Strategy*, arXiv e-prints arXiv:1708.04058, arXiv: `1708.04058 [astro-ph.IM]` (cit. on p. 90).

Lyman, J. D. et al. (2016), *Bolometric light curves and explosion parameters of 38 stripped-envelope core-collapse supernovae*, Monthly Notices of the Royal Astronomical Society **457** 328, arXiv: `1406.3667 [astro-ph.SR]` (cit. on pp. 77, 91).

Marchant, P., N. Langer, P. Podsiadlowski, T. M. Tauris, S. de Mink et al. (2017), *Ultra-luminous X-ray sources and neutron-star-black-hole mergers from very massive close binaries at low metallicity*, Astronomy and Astrophysics **604** A55, arXiv: `1705.04734 [astro-ph.HE]` (cit. on p. 78).

Marchant, P., N. Langer, P. Podsiadlowski, T. M. Tauris and T. J. Moriya (2016), *A new route towards merging massive black holes*, Astronomy and Astrophysics **588** A50, arXiv: `1601.03718 [astro-ph.SR]` (cit. on p. 77).

Marchant, P. and T. J. Moriya (2020), *The impact of stellar rotation on the black hole mass-gap from pair-instability supernovae*, Astronomy and Astrophysics **640** L18, arXiv: `2007.06220 [astro-ph.HE]` (cit. on pp. 77, 79).

Marchant, P., M. Renzo et al. (2019), *Pulsational Pair-instability Supernovae in Very Close Binaries*, The Astrophysical Journal **882** 36, arXiv: `1810.13412 [astro-ph.HE]` (cit. on pp. 76, 79, 83).

Masuda, K. and K. Hotokezaka (2019), *Prospects of Finding Detached Black Hole-Star Binaries with TESS*, The Astrophysical Journal **883** 169, arXiv: `1808.10856 [astro-ph.HE]` (cit. on p. 93).

Maund, J. R., M. Fraser et al. (2011), *The Yellow Supergiant Progenitor of the Type II Supernova 2011dh in M51*, The Astrophysical Journal **739** L37, arXiv: `1106.2565 [astro-ph.SR]` (cit. on p. 91).

Maund, J. R., S. J. Smartt and I. J. Danziger (2005), *The progenitor of SN 2005cs in the Whirlpool Galaxy*, Monthly Notices of the Royal Astronomical Society **364** L33, arXiv: `astro-ph/0507502 [astro-ph]` (cit. on p. 77).

Maund, J. R., S. J. Smartt, R. P. Kudritzki, P. Podsiadlowski and G. F. Gilmore (2004), *The massive binary companion star to the progenitor of supernova 1993J*, Nature **427** 129, arXiv: `astro-ph/0401090 [astro-ph]` (cit. on p. 91).

Mazzali, P. A., F. K. Röpke, S. Benetti and W. Hillebrandt (2007), *A Common Explosion Mechanism for Type Ia Supernovae*, Science **315** 825, arXiv: `astro-ph/0702351 [astro-ph]` (cit. on p. 76).

Menon, A., N. Langer et al. (2021), *Detailed evolutionary models of massive contact binaries I. Model grids and synthetic populations for the Magellanic Clouds*, Monthly Notices of the Royal Astronomical Society, arXiv: `2011.13459` [`astro-ph.SR`] (cit. on pp. 95, 97).

Menon, A., V. Utrobin and A. Heger (2019), *Explosions of blue supergiants from binary mergers for SN 1987A*, Monthly Notices of the Royal Astronomical Society **482** 438, arXiv: `1806.08072` [`astro-ph.SR`] (cit. on p. 97).

Miyaji, S., K. Nomoto, K. Yokoi and D. Sugimoto (1980), *Supernova triggered by electron captures.*, Publications of the Astronomical Society of Japan **32** 303 (cit. on p. 94).

Modjaz, M., Y. Q. Liu, F. B. Bianco and O. Graur (2016), *The Spectral SN-GRB Connection: Systematic Spectral Comparisons between Type Ic Supernovae and Broad-lined Type Ic Supernovae with and without Gamma-Ray Bursts*, The Astrophysical Journal **832** 108, arXiv: `1509.07124` [`astro-ph.HE`] (cit. on p. 77).

Moe, M. and R. Di Stefano (2017), *Mind Your Ps and Qs: The Interrelation between Period (P) and Mass-ratio (Q) Distributions of Binary Stars*, The Astrophysical Journal Supplement Series **230** 15, arXiv: `1606.05347` [`astro-ph.SR`] (cit. on p. 77).

Müller, B., A. Heger, D. Liptai and J. B. Cameron (2016), *A simple approach to the supernova progenitor-explosion connection*, Monthly Notices of the Royal Astronomical Society **460** 742, arXiv: `1602.05956` [`astro-ph.SR`] (cit. on pp. 77, 79).

Müller, B. and V. Varma (2020), *A 3D simulation of a neutrino-driven supernova explosion aided by convection and magnetic fields*, Monthly Notices of the Royal Astronomical Society **498** L109, arXiv: `2007.04775` [`astro-ph.HE`] (cit. on p. 81).

Nomoto, K., T. Suzuki et al. (1993), *A type IIb model for supernova 1993J*, Nature **364** 507 (cit. on p. 91).

Nomoto, K., F. .-.-K. Thielemann and K. Yokoi (1984), *Accreting white dwarf models for type I supern. III. Carbon deflagration supernovae.*, The Astrophysical Journal **286** 644 (cit. on p. 94).

O'Connor, E. and C. D. Ott (2011), *Black Hole Formation in Failing Core-Collapse Supernovae*, The Astrophysical Journal **730** 70, arXiv: `1010.5550` [`astro-ph.HE`] (cit. on pp. 79, 97).

Packet, W. (1981), *On the spin-up of the mass accreting component in a close binary system*, Astronomy and Astrophysics **102** 17 (cit. on p. 95).

Pastorello, A. et al. (2007), *A giant outburst two years before the core-collapse of a massive star*, Nature **447** 829, arXiv: `astro-ph/0703663` [`astro-ph`] (cit. on p. 82).

Patton, R. A. and T. Sukhbold (2020), *Towards a realistic explosion landscape for binary population synthesis*, Monthly Notices of the Royal Astronomical Society **499** 2803, arXiv: `2005.03055` [`astro-ph.SR`] (cit. on pp. 96, 97).

Paxton, B., L. Bildsten et al. (2011), *Modules for Experiments in Stellar Astrophysics (MESA)*, The Astrophysical Journal Supplement Series **192** 3, arXiv: `1009.1622` [`astro-ph.SR`] (cit. on p. 78).

Paxton, B., M. Cantiello et al. (2013), *Modules for Experiments in Stellar Astrophysics (MESA): Planets, Oscillations, Rotation, and Massive Stars*, The Astrophysical Journal Supplement Series **208** 4, arXiv: `1301.0319` [`astro-ph.SR`] (cit. on p. 78).

Paxton, B., P. Marchant et al. (2015), *Modules for Experiments in Stellar Astrophysics (MESA): Binaries, Pulsations, and Explosions*, The Astrophysical Journal Supplement Series **220** 15, arXiv: `1506.03146` [`astro-ph.SR`] (cit. on p. 78).

Paxton, B., J. Schwab et al. (2018), *Modules for Experiments in Stellar Astrophysics (MESA): Convective Boundaries, Element Diffusion, and Massive Star Explosions*, The Astrophysical Journal Supplement Series **234** 34, arXiv: `1710.08424` [`astro-ph.SR`] (cit. on p. 78).

Petrovic, J., N. Langer and K. A. van der Hucht (2005), *Constraining the mass transfer in massive binaries through progenitor evolution models of Wolf-Rayet+O binaries*, Astronomy and Astrophysics **435** 1013, arXiv: `astro-ph/0504242 [astro-ph]` (cit. on p. 95).

Petrovic, J., O. Pols and N. Langer (2006), *Are luminous and metal-rich Wolf-Rayet stars inflated?*, Astronomy and Astrophysics **450** 219 (cit. on pp. 94, 95).

Podsiadlowski, P., J. J. L. Hsu, P. C. Joss and R. R. Ross (1993), *The progenitor of supernova 1993J: a stripped supergiant in a binary system?*, Nature **364** 509 (cit. on pp. 77, 91).

Podsiadlowski, P., N. Langer et al. (2004), *The Effects of Binary Evolution on the Dynamics of Core Collapse and Neutron Star Kicks*, The Astrophysical Journal **612** 1044, arXiv: `astro-ph/0309588 [astro-ph]` (cit. on p. 94).

Poelarends, A. J. T., F. Herwig, N. Langer and A. Heger (2008), *The Supernova Channel of Super-AGB Stars*, The Astrophysical Journal **675** 614, arXiv: `0705.4643 [astro-ph]` (cit. on pp. 76, 94).

Poelarends, A. J. T., S. Wurtz, J. Tarka, L. Cole Adams and S. T. Hills (2017), *Electron Capture Supernovae from Close Binary Systems*, The Astrophysical Journal **850** 197, arXiv: `1710.11143 [astro-ph.HE]` (cit. on pp. 76, 79, 82, 94).

Powell, J., B. Müller and A. Heger (2021), *The final core collapse of pulsational pair instability supernovae*, Monthly Notices of the Royal Astronomical Society **503** 2108, arXiv: `2101.06889 [astro-ph.HE]` (cit. on p. 79).

Prentice, S. J., C. Ashall et al. (2019), *Investigating the properties of stripped-envelope supernovae; what are the implications for their progenitors?*, Monthly Notices of the Royal Astronomical Society **485** 1559, arXiv: `1812.03716 [astro-ph.HE]` (cit. on pp. 77, 91, 93).

Prentice, S. J. and P. A. Mazzali (2017), *A physically motivated classification of stripped-envelope supernovae*, Monthly Notices of the Royal Astronomical Society **469** 2672, arXiv: `1704.06635 [astro-ph.HE]` (cit. on p. 77).

Prentice, S. J., P. A. Mazzali et al. (2016), *The bolometric light curves and physical parameters of stripped-envelope supernovae*, Monthly Notices of the Royal Astronomical Society **458** 2973, arXiv: `1602.01736 [astro-ph.HE]` (cit. on p. 77).

Qin, Y., P. Marchant, T. Fragos, G. Meynet and V. Kalogera (2019), *On the Origin of Black Hole Spin in High-mass X-Ray Binaries*, The Astrophysical Journal **870** L18, arXiv: `1810.13016 [astro-ph.SR]` (cit. on p. 85).

Rau, A. et al. (2009), *Exploring the Optical Transient Sky with the Palomar Transient Factory*, Publications of the Astronomical Society of the Pacific **121** 1334, arXiv: `0906.5355 [astro-ph.CO]` (cit. on p. 90).

Renzo, M., R. J. Farmer et al. (2020), *Sensitivity of the lower edge of the pair-instability black hole mass gap to the treatment of time-dependent convection*, Monthly Notices of the Royal Astronomical Society **493** 4333, arXiv: `2002.08200 [astro-ph.SR]` (cit. on p. 79).

Renzo, M., R. Farmer et al. (2020), *Predictions for the hydrogen-free ejecta of pulsational pair-instability supernovae*, Astronomy and Astrophysics **640** A56, arXiv: `2002.05077 [astro-ph.SR]` (cit. on p. 79).

Riley, J. et al. (2021), *Chemically homogeneous evolution: a rapid population synthesis approach*, Monthly Notices of the Royal Astronomical Society **505** 663, arXiv: `2010.00002 [astro-ph.SR]` (cit. on p. 77).

Russell, H. N. (1914), *Relations Between the Spectra and Other Characteristics of the Stars*, Popular Astronomy **22** 275 (cit. on p. 76).

Sako, M. et al. (2008), *The Sloan Digital Sky Survey-II Supernova Survey: Search Algorithm and Follow-up Observations*, The Astronomical Journal **135** 348, arXiv: `0708.2750` `[astro-ph]` (cit. on p. 90).

Salpeter, E. E. (1955), *The Luminosity Function and Stellar Evolution.*, The Astrophysical Journal **121** 161 (cit. on pp. 78, 86).

Sana, H., A. de Koter et al. (2013), *The VLT-FLAMES Tarantula Survey. VIII. Multiplicity properties of the O-type star population*, Astronomy and Astrophysics **550** A107, arXiv: `1209.4638` `[astro-ph.SR]` (cit. on p. 77).

Sana, H., S. E. de Mink et al. (2012), *Binary Interaction Dominates the Evolution of Massive Stars*, Science **337** 444, arXiv: `1207.6397` `[astro-ph.SR]` (cit. on pp. 77, 86).

Sanyal, D., L. Grassitelli, N. Langer and J. M. Bestenlehner (2015), *Massive main-sequence stars evolving at the Eddington limit*, Astronomy and Astrophysics **580** A20, arXiv: `1506.02997` `[astro-ph.SR]` (cit. on p. 94).

Sanyal, D., N. Langer, D. Szécsi, S. -C Yoon and L. Grassitelli (2017), *Metallicity dependence of envelope inflation in massive stars*, Astronomy and Astrophysics **597** A71, arXiv: `1611.07280` `[astro-ph.SR]` (cit. on p. 94).

Schneider, F. R. N., P. Podsiadlowski, N. Langer, N. Castro and L. Fossati (2016), *Rejuvenation of stellar mergers and the origin of magnetic fields in massive stars*, Monthly Notices of the Royal Astronomical Society **457** 2355, arXiv: `1601.05084` `[astro-ph.SR]` (cit. on p. 97).

Schneider, F. R. N., P. Podsiadlowski and B. Müller (2021), *Pre-supernova evolution, compact-object masses, and explosion properties of stripped binary stars*, Astronomy and Astrophysics **645** A5, arXiv: `2008.08599` `[astro-ph.SR]` (cit. on pp. 76, 77, 79, 81, 96).

Schneider, F. R. N., S. T. Ohlmann et al. (2019), *Stellar mergers as the origin of magnetic massive stars*, Nature **574** 211, arXiv: `1910.14058` `[astro-ph.SR]` (cit. on p. 97).

Schootemeijer, A., N. Langer, N. J. Grin and C. Wang (2019), *Constraining mixing in massive stars in the Small Magellanic Cloud*, Astronomy and Astrophysics **625** A132, arXiv: `1903.10423` `[astro-ph.SR]` (cit. on p. 83).

Sen, K. et al. (2021), *X-ray emission from BH+O star binaries expected to descend from the observed galactic WR+O binaries*, arXiv e-prints arXiv:2106.01395, arXiv: `2106.01395` `[astro-ph.SR]` (cit. on p. 81).

Sen, K. (2020), *Evolution of binary stars on the HR diagram*, version 1 (cit. on pp. 78, 91).

Shenar, T., A. Gilkis, J. S. Vink, H. Sana and A. A. C. Sander (2020), *Why binary interaction does not necessarily dominate the formation of Wolf-Rayet stars at low metallicity*, Astronomy and Astrophysics **634** A79, arXiv: `2001.04476` `[astro-ph.SR]` (cit. on p. 96).

Siess, L. and U. Lebreuilly (2018), *Case A and B evolution towards electron capture supernova*, Astronomy and Astrophysics **614** A99, arXiv: `1807.04008` `[astro-ph.SR]` (cit. on pp. 76, 79).

Smartt, S. J. (2015), *Observational Constraints on the Progenitors of Core-Collapse Supernovae: The Case for Missing High-Mass Stars*, Publications of the Astronomical Society of Australia **32** e016, arXiv: `1504.02635` `[astro-ph.SR]` (cit. on pp. 77, 90, 91).

Smartt, S. J., J. R. Maund, G. F. Gilmore et al. (2003), *Mass limits for the progenitor star of supernova 2001du and other Type II-P supernovae*, Monthly Notices of the Royal Astronomical Society **343** 735, arXiv: `astro-ph/0301324` `[astro-ph]` (cit. on p. 77).

Smartt, S. J. (2009), *Progenitors of Core-Collapse Supernovae*, Annual Review of Astronomy and Astrophysics **47** 63, arXiv: `0908.0700` `[astro-ph.SR]` (cit. on pp. 76, 77, 91).

Smartt, S. J., J. R. Maund, M. A. Hendry et al. (2004), *Detection of a Red Supergiant Progenitor Star of a Type II-Plateau Supernova*, Science **303** 499, arXiv: `astro-ph/0401235` `[astro-ph]` (cit. on p. 77).

Smith, N., W. Li, A. V. Filippenko and R. Chornock (2011), *Observed fractions of core-collapse supernova types and initial masses of their single and binary progenitor stars*, Monthly Notices of the Royal Astronomical Society **412** 1522, arXiv: `1006.3899` `[astro-ph.HE]` (cit. on pp. 77, 91, 94).

Soker, N. (2017), *Grazing envelope evolution towards Type IIb supernovae*, Monthly Notices of the Royal Astronomical Society **470** L102, arXiv: `1703.09128` `[astro-ph.HE]` (cit. on p. 77).

Sravan, N., P. Marchant and V. Kalogera (2019), *Progenitors of Type IIb Supernovae. I. Evolutionary Pathways and Rates*, The Astrophysical Journal **885** 130, arXiv: `1808.07580` `[astro-ph.SR]` (cit. on pp. 76, 77, 93–95).

Sravan, N., P. Marchant, V. Kalogera, D. Milisavljevic and R. Margutti (2020), *Progenitors of Type IIb Supernovae. II. Observable Properties*, The Astrophysical Journal **903** 70, arXiv: `2009.06405` `[astro-ph.HE]` (cit. on pp. 76, 93).

Stritzinger, M. D. et al. (2018), *The Carnegie Supernova Project I. Photometry data release of low-redshift stripped-envelope supernovae*, Astronomy and Astrophysics **609** A134, arXiv: `1707.07616` `[astro-ph.HE]` (cit. on p. 77).

Sukhbold, T., T. Ertl, S. E. Woosley, J. M. Brown and H. .-.-T. Janka (2016), *Core-collapse Supernovae from 9 to 120 Solar Masses Based on Neutrino-powered Explosions*, The Astrophysical Journal **821** 38, arXiv: `1510.04643` `[astro-ph.HE]` (cit. on pp. 79, 90, 97, 98).

Sukhbold, T. and S. E. Woosley (2014), *The Compactness of Presupernova Stellar Cores*, The Astrophysical Journal **783** 10, arXiv: `1311.6546` `[astro-ph.SR]` (cit. on p. 96).

Sukhbold, T., S. E. Woosley and A. Heger (2018), *A High-resolution Study of Presupernova Core Structure*, The Astrophysical Journal **860** 93, arXiv: `1710.03243` `[astro-ph.HE]` (cit. on pp. 77, 79, 90).

Taddia, F., J. Sollerman et al. (2016), *Long-rising Type II supernovae from Palomar Transient Factory and Caltech Core-Collapse Project*, Astronomy and Astrophysics **588** A5 (cit. on p. 77).

Taddia, F., M. D. Stritzinger et al. (2018), *The Carnegie Supernova Project I. Analysis of stripped-envelope supernova light curves*, Astronomy and Astrophysics **609** A136, arXiv: `1707.07614` `[astro-ph.HE]` (cit. on pp. 77, 91, 93).

Takahashi, K. (2018), *The Low Detection Rate of Pair-instability Supernovae and the Effect of the Core Carbon Fraction*, The Astrophysical Journal **863** 153, arXiv: `1807.05373` `[astro-ph.HE]` (cit. on p. 79).

Tartaglia, L. et al. (2017), *The Progenitor and Early Evolution of the Type IIb SN 2016gkg*, The Astrophysical Journal **836** L12, arXiv: `1611.00419` `[astro-ph.HE]` (cit. on p. 91).

Ugliano, M., H.-T. Janka, A. Marek and A. Arcones (2012), *Progenitor-explosion Connection and Remnant Birth Masses for Neutrino-driven Supernovae of Iron-core Progenitors*, The Astrophysical Journal **757** 69, arXiv: `1205.3657` `[astro-ph.SR]` (cit. on p. 79).

Umeda, H., T. Yoshida, C. Nagele and K. Takahashi (2020), *Pulsational Pair-instability and the Mass Gap of Population III Black Holes: Effects of Overshooting*, The Astrophysical Journal **905** L21, arXiv: `2010.16032` `[astro-ph.HE]` (cit. on p. 79).

Van Dyk, S. D. (2017), *The direct identification of core-collapse supernova progenitors*, Philosophical Transactions of the Royal Society of London Series A **375** 20160277 (cit. on p. 91).

Van Dyk, S. D., W. Li and A. V. Filippenko (2003), *On the Progenitor of Supernova 2001du in NGC 1365*, Publications of the Astronomical Society of the Pacific **115** 448, arXiv: `astro-ph/0301346` `[astro-ph]` (cit. on p. 77).

Van Dyk, S. D., W. Zheng, K. I. Clubb et al. (2013), *The Progenitor of Supernova 2011dh has Vanished*, The Astrophysical Journal **772** L32, arXiv: `1305.3436` `[astro-ph.SR]` (cit. on p. 91).

Van Dyk, S. D., W. Zheng, O. D. Fox et al. (2014), *The Type IIb Supernova 2013df and its Cool Supergiant Progenitor*, The Astronomical Journal **147** 37, arXiv: `1312.3984` `[astro-ph.SR]` (cit. on p. 91).

Vanbeveren, D., C. De Loore and W. Van Rensbergen (1998), *Massive stars*, Astronomy and Astrophysicsr **9** 63 (cit. on p. 76).

Vartanyan, D. and M. S. B. Coleman (2021), *The Collapse and Three-Dimensional Explosion of Three-Dimensional, vis à vis One-Dimensional, Massive-star Supernova Progenitor Models*, arXiv e-prints arXiv:2109.10920, arXiv: `2109.10920` `[astro-ph.SR]` (cit. on p. 96).

Vink, J. S. (2017), *Winds from stripped low-mass helium stars and Wolf-Rayet stars*, Astronomy and Astrophysics **607** L8, arXiv: `1710.02010` `[astro-ph.SR]` (cit. on p. 96).

Vink, J. S., E. R. Higgins, A. A. C. Sander and G. N. Sabhahit (2021), *Maximum black hole mass across cosmic time*, Monthly Notices of the Royal Astronomical Society **504** 146, arXiv: `2010.11730` `[astro-ph.HE]` (cit. on p. 79).

Wang, C. et al. (2020), *Effects of Close Binary Evolution on the Main-sequence Morphology of Young Star Clusters*, The Astrophysical Journal **888** L12, arXiv: `1912.07294` `[astro-ph.SR]` (cit. on pp. 77, 78, 95).

Weiler, K. W. and R. A. Sramek (1988), *Supernovae and supernova remnants.*, Annual Review of Astronomy and Astrophysics **26** 295 (cit. on p. 76).

Wellstein, S. and N. Langer (1999), *Implications of massive close binaries for black hole formation and supernovae*, Astronomy and Astrophysics **350** 148, arXiv: `astro-ph/9904256` `[astro-ph]` (cit. on p. 95).

Willcox, R. et al. (2021), *Constraints on Weak Supernova Kicks from Observed Pulsar Velocities*, arXiv e-prints arXiv:2107.04251, arXiv: `2107.04251` `[astro-ph.HE]` (cit. on pp. 86, 94).

Wongwathanarat, A., H.-T. Janka and E. Müller (2012), "3D Core-Collapse Supernova Simulations: Neutron Star Kicks and Nickel Distribution", *Death of Massive Stars: Supernovae and Gamma-Ray Bursts*, ed. by P. Roming, N. Kawai and E. Pian, vol. 279 150 (cit. on p. 81).

Woosley, S. E. (2017), *Pulsational Pair-instability Supernovae*, The Astrophysical Journal **836** 244, arXiv: `1608.08939` `[astro-ph.HE]` (cit. on pp. 76, 77, 79).

– (2019), *The Evolution of Massive Helium Stars, Including Mass Loss*, The Astrophysical Journal **878** 49, arXiv: `1901.00215` `[astro-ph.SR]` (cit. on p. 79).

Woosley, S. E. and J. S. Bloom (2006), *The Supernova Gamma-Ray Burst Connection*, Annual Review of Astronomy and Astrophysics **44** 507, arXiv: `astro-ph/0609142` `[astro-ph]` (cit. on p. 97).

Woosley, S. E., R. G. Eastman, T. A. Weaver and P. A. Pinto (1994), *SN 1993J: A Type IIb Supernova*, The Astrophysical Journal **429** 300 (cit. on p. 91).

Woosley, S. E., A. Heger and T. A. Weaver (2002), *The evolution and explosion of massive stars*, Reviews of Modern Physics **74** 1015 (cit. on pp. 76, 79).

Woosley, S. E. and A. Heger (2021), *The Pair-instability Mass Gap for Black Holes*, The Astrophysical Journal **912** L31, arXiv: `2103.07933` `[astro-ph.SR]` (cit. on pp. 77, 79).

Woosley, S. E., T. Sukhbold and H. .-.-T. Janka (2020), *The Birth Function for Black Holes and Neutron Stars in Close Binaries*, The Astrophysical Journal **896** 56, arXiv: `2001.10492` `[astro-ph.HE]` (cit. on pp. 79, 88–90, 97, 98).

Yoon, S. .-.-C. and N. Langer (2005), *Evolution of rapidly rotating metal-poor massive stars towards gamma-ray bursts*, Astronomy and Astrophysics **443** 643, arXiv: `astro-ph/0508242` `[astro-ph]` (cit. on p. 97).

Yoon, S. C., S. E. Woosley and N. Langer (2010), *Type Ib/c Supernovae in Binary Systems. I. Evolution and Properties of the Progenitor Stars*, The Astrophysical Journal **725** 940, arXiv: `1004.0843` `[astro-ph.SR]` (cit. on p. 85).

Yoon, S.-C. (2015), *Evolutionary Models for Type Ib/c Supernova Progenitors*, Publications of the Astronomical Society of Australia **32** e015, arXiv: `1504.01205` `[astro-ph.SR]` (cit. on p. 77).

Yoon, S.-C., L. Dessart and A. Clocchiatti (2017), *Type Ib and IIb Supernova Progenitors in Interacting Binary Systems*, The Astrophysical Journal **840** 10, arXiv: `1701.02089` `[astro-ph.SR]` (cit. on pp. 76, 79, 82).

Yoshida, T., H. Umeda, K. Maeda and T. Ishii (2016), *Mass ejection by pulsational pair instability in very massive stars and implications for luminous supernovae*, Monthly Notices of the Royal Astronomical Society **457** 351, arXiv: `1511.01695` `[astro-ph.SR]` (cit. on p. 79).

Zucker, S., T. Mazeh and T. Alexander (2007), *Beaming Binaries: A New Observational Category of Photometric Binary Stars*, The Astrophysical Journal **670** 1326, arXiv: `0708.2100` `[astro-ph]` (cit. on p. 93).

X-ray emission from BH+O star binaries expected to descend from the observed galactic WR+O binaries

Koushik Sen^a, Xiao-Tian Xu^{a,b}, Norbert Langer^{a,b}, Ileyk El Mellah^c,
C. Schürmann^{a,b} & Martin Quast^a

^{a} Argelander-Institüt für Astronomie, Universität Bonn, Auf dem Hügel 71, 53121 Bonn, Germany
^{b} Max-Planck-Institut für Radioastronomie, Auf dem Hügel 69, 53121 Bonn, Germany
^{c} Univ. Grenoble Alpes, CNRS, IPAG, 414 Rue de la Piscine, 38400 Saint-Martin-d'Hères, France

Summary: In the isolated binary evolution channel, black hole+O (BH+O) star binaries are expected to form from Wolf-Rayet+O (WR+O) star binaries. In the Milky Way, based on reasonable assumptions on the star formation history, millions of BHs are expected to be present. While ~80 WR+O star binaries have been found, observations of BH+O star binaries are very rare, with Cyg X-1 being the only high-mass X-ray binary (HMXB) confirmed to host a stellar-mass BH. Taking into consideration that BH+O star systems have a longer life than their progenitor WR+O star systems, we arrive at a number discrepancy because there are far fewer observed BH+O star systems in our galaxy. To alleviate this tension, it has been suggested that WR stars collapse to form BHs with an associated high kick velocity that disrupts the binary at the time of BH formation.

An alternative explanation is that observing BHs is challenging because they do not emit electromagnetic radiation on their own at a detectable level. Instead, we rely on the emission from an accretion disk around the BH, or on single-lined spectroscopic binaries to constrain the minimum mass of an unseen companion, or astrometry. In this work, we look at the likelihood of the formation of an accretion disk around a BH in BH+O star systems that are expected to be descendants of observed

WR+O star systems. We look at the effect of varying the BH spin parameter, the efficiency of angular momentum accretion onto the BH and the wind velocity of the O star companion on the probability of formation of the accretion disk.

For this exercise, we assume spherically symmetric Bondi-Hoyle accretion from the stellar wind of the O star. The accretion radius of a BH is defined as the radius around the BH where the wind streamlines of the O star can get bound to the BH due to its strong gravitational field. The specific angular momentum carried by the wind matter at the accretion radius can be transformed into an equivalent circularisation radius, where the wind matter will revolve around the BH in a circle. If this circularisation radius is larger than the radius of the innermost stable circular orbit (ISCO) of the BH, an accretion disk can form. The circularisation radius depends on the efficiency of angular momentum accretion and the wind speed of the O star. The ISCO radius depends on the spin of the BH, and the orientation of the accretion disk angular momentum with respect to the spin of the BH. It is the lowest for a maximally spinning BH with a prograde accretion disk and the highest for a maximally spinning BH with a retrograde accretion disk. The ISCO radius of a non-rotating BH is between the above two. Accretion disks formed in this way are expected to be geometrically thin, but optically-thick, centrifugally maintained structures mostly radiating in X-rays. When the X-ray flux at Earth is larger than the minimum flux cut-off of non-focussing X-ray telescopes, we can observe the BH+O star binary as an HMXB.

From detailed stellar and binary evolution modelling, we expect that the spin of the first formed BH in a binary is very low, due to efficient angular momentum transport inside the progenitor star. Detailed hydrodynamical simulations have shown that the efficiency of specific angular momentum accretion in these models is around one-third of the specific angular momentum available at the accretion radius. With these assumptions and a beta law for the wind velocity of the O star, we find that an accretion disk will not form in the BH+O star binaries that are expected to form from most of the observed WR+O star binaries in the Milky Way, making them X-ray quiet and unobservable as an HMXB. We show that previous works in the literature underestimated the wind velocity from O stars significantly, which lead to the prediction of X-ray emission from most BH+O star binaries. We also show that the presence of a maximally spinning BH greatly increases the probability of forming a prograde accretion disk, which is corroborated by the measured high spins of three observed BH HMXBs: Cyg X-1, LMC X-1 and M33 X-7. Our results reveal that a high natal kick during the formation of a BH is not necessary to understand the discrepancy in the number of BH+O star systems and WR+O star systems in the Milky Way. Observations of X-ray quiescent BH+O binaries via alternative methods are expected to reveal more information about these systems.

Outlook

This thesis was aimed at understanding the evolution of short-period massive binaries that undergo mass transfer while both the binary components are burning hydrogen at their core. This is very important in our current understanding of stellar evolution (for a review, see Langer, 2012; Crowther, 2019) as most massive stars preferentially form in binaries (Sana et al., 2012; Sana et al., 2013; Moe et al., 2017) and the majority of observable post-interaction binaries are expected to originate from short-period binaries (de Mink et al., 2014). Moreover, the predicted rate of compact object mergers can vary by over an order of magnitude depending on the physics assumptions used (Mink et al., 2015). Hence, it is essential to constrain the uncertainties in early stages of binary evolution so that they do not propagate into our predictions of the merger rates. With new observatories to detect gravitational waves being set up in different parts of the world (e.g. LIGO-India), and in space (Laser Interferometer Space Antenna and the Einstein Telescope), having improved detection thresholds, the field of gravitational wave astronomy is expected to blossom in this decade.

Recent, ongoing and future observational programmes such as the Zwicky Transient Facility (Bellm et al., 2019; Graham et al., 2019), the Palomar Transient Factory (Law et al., 2009; Rau et al., 2009), the Sloan Digital Sky Survey (Frieman et al., 2008; Sako et al., 2008) the Lick Observatory Supernova Search (Li et al., 2000; Filippenko et al., 2001), the Large Synoptic Survey Telescope (LSST Science Collaboration et al., 2017), the Vera C. Rubin Observatory, James Webb Space Telescope and several others are revolutionizing the field by observing and classifying new types of transients every day. A lot of observing time is being dedicated to stripped envelope supernova, which are thought to originate mostly from massive binaries. Understanding the properties of these events will enable us put accurate constraints on many aspects of binary evolution theory. Even the most common types of supernovae still pose questions about various aspects of stellar evolution such as mass loss rates, rotation rates, angular momentum transport and internal mixing.

One of the most crucial aspects of massive binary evolution this thesis has been able to put a handle on is the binary mass transfer efficiency (de Mink et al., 2007). In most binary population synthesis codes, mass transfer efficiency was parametrized by a constant. This thesis has shown that this might not be an accurate description, and a mass transfer efficiency that depends on the interaction between tidal forces and spin-up due to accretion is able to better explain the orbital period and mass ratio distribution of massive Algol binaries simultaneously. The fact that our mass transfer efficiency prescription is able to reproduce many observed Algol binaries in the Galaxy as well as the Magellanic Clouds, gives concrete evidence for its applicability in different metallicity environments.

Langer et al. (2020) predicted that 3% of massive OB binaries harbour a black hole as its companion. In Chapter 5, we found that most of these black hole binaries will not be observable in X-rays due to the lack of an accretion disk around the black hole. This means that we need to rely on indirect methods to identify the majority of this population of black hole binaries in our Galaxy. To this end the GAIA satellite offers an unique opportunity to identify such systems via periodic astrometric variations (Breivik et al., 2017; Mashian et al., 2017; Yalinewich et al., 2018; Yamaguchi et al., 2018; Andrews et al., 2019; Janssens et al., 2022). Furthermore, BH+O binaries can also be detected from photometric variability of the O star induced by the BH companion (Zucker et al., 2007; Masuda et al., 2019), or spectroscopically via the periodic shift in radial velocity of the O star.

Furthermore, 2D and 3D simulations have shown that hydrodynamic effects (e.g. Janka et al., 1996; Blondin et al., 2003; Hanke et al., 2013), magnetic effects (e.g. Kotake et al., 2004; Obergaulinger et al., 2006; Obergaulinger et al., 2018) and rotation (e.g. Ott et al., 2005; Takiwaki et al., 2016) can influence the observable properties of supernova explosions. Our models in Chapter 4 can be used as a realistic initial condition to study the observable properties of a population of stripped envelope supernovae and characterise the amount of ejecta masses, nickel masses and explosion energies that can be injected into the intracluster medium. To further understand the properties of high-mass X-ray binaries, we can use the models introduced in Chapter 2 and the knowledge we have gained in Chapter 5 to derive the population of high-mass X-ray binaries expected in the Large Magellanic Cloud. Studying the properties of the O star companions to these black holes can help identify OB stars, that might host a black hole but are presently X-ray quiet, for follow-up radial velocity observations.

Our models predict that only the donors of short-period binaries that undergo Case A mass transfer may undergo Type Ib supernova in the Small Magellanic Cloud from the stable massive binary evolution channel. This indirectly implies that most stars at low metallicity are unable to get rid of their entire hydrogen envelope neither via stellar winds as they are very weak at low metallicity nor via binary interactions. This has large consequences for the source of ionizing radiation in the early universe (Bromm et al., 2011; Götberg et al., 2017). In this situation, identification of binary companions to hydrogen-rich Wolf-Rayet stars becomes pivotal at low metallicity. The absence of binary companions means either that stars at low metallicity can shed their envelope, implying our mass-loss rates are underestimated, or the detection of binary companions will be able to give zeroth order constraints on the subsequent common envelope phase that still needs to be understood properly.

We have shown that mass transfer in very massive binary evolution models defy conventional knowledge of binary evolution (Chapter **??**). For example, we showed that nuclear timescale mass transfer can occur from a more massive to a less massive star. We have found evidence for the existence of this 'reverse Algol' evolution channel in binary systems such as VFTS 094 and VFTS 176 (Mahy et al., 2020; Mahy et al., 2020) and observations of hydrogen-rich Wolf-Rayet stars. Detailed population synthesis studies and comparison of model predictions to observed properties of hydrogen-rich Wolf-Rayet stars in the Galaxy and Magellanic Clouds are expected to lead to a new way to explain these objects as a part of binary systems.

The European Extremely Large Telescope is slated to start observing the sky in 2027. This is touted to be a major leap in observational stellar astronomy as it is expected to be able to observe individual massive stars in galaxies beyond the Milky Way and the Magellanic Clouds. This will hugely increase the volume of the Universe we can use to study massive star evolution, as well as probe deeper into the high redshift regime i.e. the Early Universe. In a nutshell, there is a very fascinating future ahead of us stellar astronomers, both from the theoretical modelling side as well as the observational side, with loads of observational data and theoretical computing power becoming accessible everyday.

References

Andrews, J. J., K. Breivik and S. Chatterjee (2019), *Weighing the Darkness: Astrometric Mass Measurement of Hidden Stellar Companions Using Gaia*, The Astrophysical Journal **886** 68, arXiv: `1909.05606` `[astro-ph.SR]` (cit. on p. 114).

Bellm, E. C. et al. (2019), *The Zwicky Transient Facility: System Overview, Performance, and First Results*, Publications of the Astronomical Society of the Pacific **131** 018002, arXiv: `1902.01932` `[astro-ph.IM]` (cit. on p. 113).

Blondin, J. M., A. Mezzacappa and C. DeMarino (2003), *Stability of Standing Accretion Shocks, with an Eye toward Core-Collapse Supernovae*, Astrophysical Journal **584** 971, arXiv: `astro-ph/0210634` `[astro-ph]` (cit. on p. 114).

Breivik, K., S. Chatterjee and S. L. Larson (2017), *Revealing Black Holes with Gaia*, The Astrophysical Journal **850** L13, arXiv: `1710.04657` `[astro-ph.SR]` (cit. on p. 114).

Bromm, V. and N. Yoshida (2011), *The First Galaxies*, Annual Review of Astronomy and Astrophysics **49** 373, arXiv: `1102.4638` `[astro-ph.CO]` (cit. on p. 114).

Crowther, P. A. (2019), *Massive Stars in the Tarantula Nebula: A Rosetta Stone for Extragalactic Supergiant HII Regions*, Galaxies **7** 88, arXiv: `1911.02047` `[astro-ph.SR]` (cit. on p. 113).

de Mink, S. E., O. R. Pols and R. W. Hilditch (2007), *Efficiency of mass transfer in massive close binaries. Tests from double-lined eclipsing binaries in the SMC*, Astronomy and Astrophysics **467** 1181, arXiv: `astro-ph/0703480` `[astro-ph]` (cit. on p. 113).

de Mink, S. E., H. Sana, N. Langer, R. G. Izzard and F. R. N. Schneider (2014), *The Incidence of Stellar Mergers and Mass Gainers among Massive Stars*, The Astrophysical Journal **782** 7, arXiv: `1312.3650` `[astro-ph.SR]` (cit. on p. 113).

Filippenko, A. V., W. D. Li, R. R. Treffers and M. Modjaz (2001), "The Lick Observatory Supernova Search with the Katzman Automatic Imaging Telescope", *IAU Colloq. 183: Small Telescope Astronomy on Global Scales*, ed. by B. Paczynski, W.-P. Chen and C. Lemme, vol. 246, Astronomical Society of the Pacific Conference Series 121 (cit. on p. 113).

Frieman, J. A. et al. (2008), *The Sloan Digital Sky Survey-II Supernova Survey: Technical Summary*, The Astronomical Journal **135** 338, arXiv: `0708.2749` `[astro-ph]` (cit. on p. 113).

Götberg, Y., S. E. de Mink and J. H. Groh (2017), *Ionizing spectra of stars that lose their envelope through interaction with a binary companion: role of metallicity*, Astronomy and Astrophysics **608** A11, arXiv: `1701.07439` `[astro-ph.SR]` (cit. on p. 114).

Graham, M. J. et al. (2019), *The Zwicky Transient Facility: Science Objectives*, Publications of the Astronomical Society of the Pacific **131** 078001, arXiv: `1902.01945` `[astro-ph.IM]` (cit. on p. 113).

Hanke, F., B. Müller, A. Wongwathanarat, A. Marek and H.-T. Janka (2013), *SASI Activity in Three-dimensional Neutrino-hydrodynamics Simulations of Supernova Cores*, Astrophysical Journal **770** 66, arXiv: `1303.6269` `[astro-ph.SR]` (cit. on p. 114).

Janka, H. .-.-T. and E. Mueller (1996), *Neutrino heating, convection, and the mechanism of Type-II supernova explosions.*, Astronomy and Astrophysics **306** 167 (cit. on p. 114).

Janssens, S. et al. (2022), *Uncovering astrometric black hole binaries with massive main-sequence companions with Gaia*, Astronomy and Astrophysics **658** A129, arXiv: `2111.06427` `[astro-ph.SR]` (cit. on p. 114).

Kotake, K., H. Sawai, S. Yamada and K. Sato (2004), *Magnetorotational Effects on Anisotropic Neutrino Emission and Convection in Core-Collapse Supernovae*, Astrophysical Journal **608** 391 (cit. on p. 114).

Langer, N. (2012), *Presupernova Evolution of Massive Single and Binary Stars*, Annual Review of Astronomy and Astrophysics **50** 107, arXiv: `1206.5443` `[astro-ph.SR]` (cit. on p. 113).

Langer, N. et al. (2020), *Properties of OB star-black hole systems derived from detailed binary evolution models*, Astronomy and Astrophysics **638** A39, arXiv: `1912.09826` `[astro-ph.SR]` (cit. on p. 114).

Law, N. M. et al. (2009), *The Palomar Transient Factory: System Overview, Performance, and First Results*, Publications of the Astronomical Society of the Pacific **121** 1395, arXiv: `0906.5350` `[astro-ph.IM]` (cit. on p. 113).

Li, W. D. et al. (2000), "The Lick Observatory Supernova Search", *Cosmic Explosions: Tenth AstroPhysics Conference*, ed. by S. S. Holt and W. W. Zhang, vol. 522, American Institute of Physics Conference Series 103, arXiv: `astro-ph/9912336` `[astro-ph]` (cit. on p. 113).

LSST Science Collaboration et al. (2017), *Science-Driven Optimization of the LSST Observing Strategy*, arXiv e-prints arXiv:1708.04058, arXiv: `1708.04058` `[astro-ph.IM]` (cit. on p. 113).

Mahy, L., L. A. Almeida et al. (2020), *The Tarantula Massive Binary Monitoring. IV. Double-lined photometric binaries*, Astronomy and Astrophysics **634** A119, arXiv: `1912.06853` `[astro-ph.SR]` (cit. on p. 114).

Mahy, L., H. Sana et al. (2020), *The Tarantula Massive Binary Monitoring. III. Atmosphere analysis of double-lined spectroscopic systems*, Astronomy and Astrophysics **634** A118, arXiv: `1912.08107` `[astro-ph.SR]` (cit. on p. 114).

Mashian, N. and A. Loeb (2017), *Hunting black holes with Gaia*, Monthly Notices of the Royal Astronomical Society **470** 2611, arXiv: `1704.03455` `[astro-ph.HE]` (cit. on p. 114).

Masuda, K. and K. Hotokezaka (2019), *Prospects of Finding Detached Black Hole-Star Binaries with TESS*, The Astrophysical Journal **883** 169, arXiv: `1808.10856` `[astro-ph.HE]` (cit. on p. 114).

Mink, S. E. de and K. Belczynski (2015), *Merger rates of double neutron stars and stellar origin black holes: The Impact of Initial Conditions on Binary Evolution Predictions*, arXiv: High Energy Astrophysical Phenomena (cit. on p. 113).

Moe, M. and R. Di Stefano (2017), *Mind Your Ps and Qs: The Interrelation between Period (P) and Mass-ratio (Q) Distributions of Binary Stars*, The Astrophysical Journal Supplement Series **230** 15, arXiv: `1606.05347` `[astro-ph.SR]` (cit. on p. 113).

Obergaulinger, M., M. A. Aloy, H. Dimmelmeier and E. Müller (2006), *Axisymmetric simulations of magnetorotational core collapse: approximate inclusion of general relativistic effects*, Astronomy and Astrophysics **457** 209, arXiv: `astro-ph/0602187` `[astro-ph]` (cit. on p. 114).

Obergaulinger, M., O. Just and M. A. Aloy (2018), *Core collapse with magnetic fields and rotation*, Journal of Physics G Nuclear Physics **45** 084001, arXiv: `1806.00393` `[astro-ph.HE]` (cit. on p. 114).

Ott, C. D., S. Ou, J. E. Tohline and A. Burrows (2005), *One-armed Spiral Instability in a Low-T/|W| Postbounce Supernova Core*, Astrophysical Journal, Letters **625** L119, arXiv: `astro-ph/0503187` `[astro-ph]` (cit. on p. 114).

Rau, A. et al. (2009), *Exploring the Optical Transient Sky with the Palomar Transient Factory*, Publications of the Astronomical Society of the Pacific **121** 1334, arXiv: `0906.5355` `[astro-ph.CO]` (cit. on p. 113).

Sako, M. et al. (2008), *The Sloan Digital Sky Survey-II Supernova Survey: Search Algorithm and Follow-up Observations*, The Astronomical Journal **135** 348, arXiv: `0708.2750` [`astro-ph`] (cit. on p. 113).

Sana, H., A. de Koter et al. (2013), *The VLT-FLAMES Tarantula Survey. VIII. Multiplicity properties of the O-type star population*, Astronomy and Astrophysics **550** A107, arXiv: `1209.4638` [`astro-ph.SR`] (cit. on p. 113).

Sana, H., S. E. de Mink et al. (2012), *Binary Interaction Dominates the Evolution of Massive Stars*, Science **337** 444, arXiv: `1207.6397` [`astro-ph.SR`] (cit. on p. 113).

Takiwaki, T., K. Kotake and Y. Suwa (2016), *Three-dimensional simulations of rapidly rotating core-collapse supernovae: finding a neutrino-powered explosion aided by non-axisymmetric flows*, Monthly Notices of the Royal Astronomical Society **461** L112, arXiv: `1602.06759` [`astro-ph.HE`] (cit. on p. 114).

Yalinewich, A., P. Beniamini, K. Hotokezaka and W. Zhu (2018), *Dark passengers in stellar surveys*, Monthly Notices of the Royal Astronomical Society **481** 930, arXiv: `1807.00835` [`astro-ph.SR`] (cit. on p. 114).

Yamaguchi, M. S., N. Kawanaka, T. Bulik and T. Piran (2018), *Detecting Black Hole Binaries by Gaia*, The Astrophysical Journal **861** 21, arXiv: `1710.09839` [`astro-ph.SR`] (cit. on p. 114).

Zucker, S., T. Mazeh and T. Alexander (2007), *Beaming Binaries: A New Observational Category of Photometric Binary Stars*, The Astrophysical Journal **670** 1326, arXiv: `0708.2100` [`astro-ph`] (cit. on p. 114).

Appendix to Chapter 2

Astronomy
&
Astrophysics

Detailed models of interacting short-period massive binary stars

K. Sen[1,2] , N. Langer[1,2], P. Marchant[3], A. Menon[1,4], S. E. de Mink[5,4,6], A. Schootemeijer[1], C. Schürmann[1,2],
L. Mahy[7], B. Hastings[1,2], K. Nathaniel[1], H. Sana[3], C. Wang[1,2], and X. T. Xu[1,2]

[1] Argelander-Institut für Astronomie, Universität Bonn, Auf dem Hügel 71, 53121 Bonn, Germany
  e-mail: ksen@astro.uni-bonn.de
[2] Max-Planck-Institut für Radioastronomie, Auf dem Hügel 69, 53121 Bonn, Germany
[3] Institute of Astronomy, KU Leuven, Celestijnenlaan 200D, 3001 Leuven, Belgium
[4] Astronomical Institute "Anton Pannekoek", University of Amsterdam, Science Park 904, 1098 XH Amsterdam, The Netherlands
[5] Max Planck Institute for Astrophysics, Karl-Schwarzschild-Strasse 1, 85748 Garching, Germany
[6] Center for Astrophysics, Harvard-Smithsonian, 60 Garden Street, Cambridge, MA 02138, USA
[7] Royal Observatory of Belgium, Avenue Circulaire/Ringlaan 3, 1180 Brussels, Belgium

ABSTRACT

Context. The majority of massive stars are part of binary systems. In about a quarter of these, the companions are so close that mass transfer occurs while they undergo core hydrogen burning, first on the thermal and then on the nuclear timescale. The nuclear timescale mass transfer leads to observational counterparts: the semi-detached so-called massive Algol binaries. These systems may provide urgently needed tests of the physics of mass transfer. However, comprehensive model predictions for these systems are sparse.
Aims. We use a large grid of detailed evolutionary models of short-period massive binaries and follow-up population synthesis calculations to derive probability distributions of the observable properties of massive Algols and their descendants.
Methods. Our results are based on ~10 000 binary model sequences calculated with the stellar evolution code MESA, using a metallicity suitable for the Large Magellanic Cloud (LMC), covering initial donor masses between $10\,M_\odot$ and $40\,M_\odot$ and initial orbital periods above 1.4 d. These models include internal differential rotation and magnetic angular momentum transport, non-conservative mass and angular momentum transfer between the binary components, and time-dependent tidal coupling.
Results. Our models imply ~30, or ~3% of the ~1000, core hydrogen burning O-star binaries in the LMC to be currently in the semi-detached phase. Our donor models are up to 25 times more luminous than single stars of an identical mass and effective temperature, which agrees with the observed Algols. A comparison of our models with the observed orbital periods and mass ratios implies rather conservative mass transfer in some systems, while a very inefficient one in others. This is generally well reproduced by our spin-dependent mass transfer algorithm, except for the lowest considered masses. The observations reflect the slow increase of the surface nitrogen enrichment of the donors during the semi-detached phase all the way to CNO equilibrium. We also investigate the properties of our models after core hydrogen depletion of the donor star, when these models correspond to Wolf-Rayet or helium+OB star binaries.
Conclusions. A dedicated spectroscopic survey of massive Algol systems may allow to derive the dependence of the efficiency of thermal timescale mass transfer on the binary parameters, as well as the efficiency of semiconvective mixing in the stellar interior. This would be a crucial step towards reliable binary models up to the formation of supernovae and compact objects.

Key words. stars: massive – stars: evolution – binaries: close – stars: abundances – stars: statistics

1. Introduction

In the last two decades, it has been well established that massive stars are preferentially born as members of binary or multiple systems (Vanbeveren et al. 1998; Sana et al. 2012, 2013; Kobulnicky et al. 2014; Moe & Di Stefano 2017; Banyard et al. 2022). Hence, the study of their evolution is complicated by the fact that they can interact with their companion, which can significantly alter their properties and lead to observable characteristics that differ largely from those obtained from single stars (Podsiadlowski et al. 1992; de Mink et al. 2013; Wang et al. 2020). This complexity makes the modelling of massive binary star evolution challenging, and many aspects of it are not yet well understood (Langer 2012; Crowther 2019).

Since stars tend to expand with age, mass transfer via a Roche-lobe overflow occurs naturally in many close binaries. In the tightest binaries, mass transfer may occur while both stars are still undergoing core hydrogen burning (Pols 1994; Vanbeveren et al. 1998; Wellstein et al. 2001; de Mink et al. 2007), initiating

the so-called Case A mass transfer phase. Case A mass transfer is unique in the sense that it comprises a nuclear timescale mass transfer stage, and it has the massive Algol systems (or contact systems, see Menon et al. 2021) as observational counterparts, where the currently less massive, Roche-lobe filling star is transferring mass to a more massive star in a semi-detached configuration. Mass transfer in massive binaries otherwise (with rare exceptions, such as in Quast et al. 2019) occurs on the much shorter thermal or even dynamical timescale, and it is much less likely to be observed.

In Case A binaries, mass transfer first occurs on the thermal timescale of the donor star in a shrinking binary orbit. After the mass ratio is inverted, the orbit widens as a consequence of mass and angular momentum transfer. Thence, the mass transfer is driven by the slow expansion of the donor star due to core hydrogen burning. This gives rise to the nuclear timescale semi-detached phase, known as the slow Case A mass transfer, with a duration of a considerable fraction of the lifetime of the binary. Since all binaries in this phase previously experienced an intense

phase of thermal timescale mass transfer (fast Case A), comparing models with observed semi-detached massive binaries is not only constraining the observable slow mass transfer phase, but also the much less understood thermal timescale mass transfer.

Case A evolution has likely preceded most of the observed short period massive Wolf-Rayet+OB star binaries (Massey 1981; Niemela & Moffat 1982; van der Hucht 2001; Petrovic et al. 2005) and massive black hole binaries such as Cygnus X-1, LMC-X1, and M 33 X-7 (Valsecchi et al. 2010; Qin et al. 2019; Langer et al. 2020). Recently, Quast et al. (2019) have shown that nuclear timescale mass transfer can also occur in supergiant X-ray binaries (see also Pavlovskii et al. 2017; Marchant et al. 2021). The short period of many of these post main sequence systems (Walter et al. 2015) implies that many of them evolved previously through Case A mass transfer.

Massive Case A binaries are also thought to contribute to the double neutron star and double black hole binaries population in the Universe (e.g. Kruckow et al. 2018). At low metallicity (less than one-tenth of Solar) and high mass (above $40\,M_\odot$) however, chemically homogeneous evolution may prevent expansion and mass transfer in short period binaries (de Mink et al. 2009; Marchant et al. 2016; Mandel & de Mink 2016; Hastings et al. 2020), potentially leading to BH mergers observable by gravitational waves (Abbott et al. 2019).

Modern observations of massive star binaries allow to determine the binary and stellar properties of individual systems in great detail (Hilditch et al. 2005; Torres et al. 2010; Martins et al. 2017; Pavlovski et al. 2018; Johnston et al. 2019; Mahy et al. 2020a,b; Janssens et al. 2021). This provides ideal conditions to constrain the uncertain physics assumptions in binary evolution models (Ritchie et al. 2010; Clark et al. 2014; Abdul-Masih et al. 2019). In particular, semi-detached double-lined systems provide a unique opportunity to derive the basic stellar properties of binaries with unprecedented precision, which can be used to test our models of stellar and binary evolution (Pols et al. 1997; Nelson & Eggleton 2001; de Mink et al. 2007, 2009).

Massive binaries with initial orbital periods below roughly 10 d undergo Case A evolution. Based on the period distribution of massive binaries obtained by Sana et al. (2012), this implies that about one quarter of all massive binaries will follow this path. Unfortunately, rapid binary evolutionary codes such as BSE (Binary Star Evolution, Hurley et al. 2002), Binary_C (Izzard et al. 2006), StarTrack (Belczynski et al. 2008), COM-PAS (Compact Object Mergers: Population Astrophysics and Statistics, Stevenson et al. 2017), ComBinE (Kruckow et al. 2018), MOBSE (Massive Objects in Binary Stellar Evolution, Giacobbo et al. 2018), SEVN (Stellar EVolution for *N*-body, Spera et al. 2019) and COSMIC (Compact Object Synthesis and Monte Carlo Investigation Code, Breivik et al. 2020) can treat Case A evolution only rudimentarily, since the above codes are based on single stars models, and on models of helium stars. However, the internal structure of mass donors in Case A binary models differs largely from both. Our detailed binary models include internal differential rotation and magnetic angular momentum transport in the individual stars, non-conservative mass and angular momentum transfer between the binary components, and time-dependent tidal coupling.

Previous studies of the Case A mass transfer phase of massive binaries based on detailed binary evolution grids identified stellar binary models that can provide a good fit to the individual observed Algol binary systems (Nelson & Eggleton 2001), and constrain the underlying physics such as mass transfer efficiency as a function of the initial binary parameters (de Mink et al. 2007). The binary models of Eldridge et al. (2017, BPASS-

Binary Population and Spectral Synthesis) also include Case A evolution. However, in their models the mass gainers are computed after the calculation of the evolution of the donor stars. Details of the Case A phase are not discussed.

A detailed study of the expected observable characteristics of this phase is lacking in the literature. Others studies on the Case A mass transfer phase focussed on low and intermediate mass stars (Mennekens & Vanbeveren 2017; Negu & Tessema 2018), where evidence for non-conservative mass transfer was found. In this work, we aim to provide a bridge between theory and observations by studying a grid of detailed binary evolution models and providing distributions of observable properties of massive binaries in this stage, that is, the slow Case A mass transfer phase.

For binaries having shorter initial orbital periods, the accretors can also fill their Roche lobes during the slow Case A mass transfer phase, and reach a contact configuration (Pols 1994; Wellstein et al. 2001), with the possibility of starting inverse mass transfer back to the donor while both components are burning hydrogen at their cores. Evolution during the contact phase is investigated in Menon et al. (2021). Our study focusses on the semi-detached configuration during the Case A mass transfer phase.

Section 2 gives a brief overview of the grid of detailed stellar evolution models and important physics assumptions. Section 3 describes the typical evolution of a Case A model and the mass transfer efficiency in our grid of models. Section 4 describes the observable distributions of stellar parameters during the slow Case A mass transfer phase obtained from the binary model grid. The properties of our Case A models after core hydrogen depletion is reported in Sect. 5. We compare our model predictions with the observed massive Algol binaries in the Large Magellanic Cloud (LMC) and the Milky Way in Sect. 6. In Sect. 7, we compare our work with relevant studies in the literature. We then briefly summarise our results and present our take-home messages in Sect. 8.

2. Method

2.1. The detailed binary evolution grid

To study the properties of Case A mass transfer, we use a dense grid of detailed massive binary evolution models (Marchant 2017) with an initial metallicity and composition representative of young star-forming regions in the LMC. The models were calculated using the 1D stellar evolution code MESA[1] (Modules for Experiments in Stellar Astrophysics, Paxton et al. 2011, 2013, 2015, 2018, version 8845[2]). The stellar and binary physics assumptions are described in detail by Paxton et al. (2015) and Marchant (2017). The most important and relevant ones are discussed in the following paragraphs.

The chemical composition and wind mass loss rates are set as in Brott et al. (2011a): the hydrogen, helium and metal mass fractions used in our models are 0.7391, 0.2562 and 0.0047 respectively. The initial abundances (in units of $12 + \log$ [element/H]) for C, N, O, Mg, Si, Fe adopted are 7.75, 6.90, 8.35, 7.05, 7.20 and 7.05 respectively. All other elements are solar abundances (Asplund et al. 2005) scaled down by 0.4 dex. The physics of differential rotation and rotational mixing follows that of Heger et al. (2000) while the magnetic angular momentum transport is

---

[1] http://mesa.sourceforge.net/
[2] Inlists to reproduce the models used in this work can be downloaded from github.com/orlox/mesa_input_data/tree/master/2016_binary_models.

as in Heger et al. (2005). The mass transfer rates are calculated following Marchant et al. (2016). When only one component of the binary overflows its Roche lobe, the mass transfer rate from the Roche lobe filling star is implicitly calculated so as to make the star just fill its Roche lobe. When both components of the binary fill their Roche lobes, the contact phase is calculated as described in Sect. 2.2 of the same work.

The accretion of angular momentum from the transferred matter follows the implementation of de Mink et al. (2013), which is based on the results of Lubow & Shu (1975) and Ulrich & Burger (1976). A differentiation between disc and ballistic modes of accretion during the mass transfer phases is considered. To determine which mode of accretion occurs, we compare the minimum distance of approach of the accretion stream (Lubow & Shu 1975; Ulrich & Burger 1976)

$$R_{\min} = 0.0425a \left(\frac{M_a}{M_d} + \frac{M_a^2}{M_d^2} \right)^{1/4} \qquad (1)$$

to the radius of the accretor star (R_a). Here, a is the orbital separation, M_d and M_a are the masses of the initially more massive donor star and initially less massive accretor star respectively. Accretion is assumed to be ballistic when $R_a > R_{\min}$, with a specific angular momentum of $(1.7GM_aR_{\min})^{1/2}$. Otherwise, accretion is assumed via a Keplerian disc with a specific angular momentum of $(GM_aR_a)^{1/2}$.

Equation (1) can be written in terms of orbital period, mass ratio and the mass of the accretor. We find that for an accretion disc to form, the orbital period of the binary during the mass transfer phase has to be longer than 20 d, for a $10\,M_\odot$ accretor when assuming a typical mass-radius relation (Gorda & Svechnikov 1998) to estimate the accretor radius. Hence, our Case A models are not expected to form an accretion disc during the slow Case A mass transfer phase. On the other hand, there are some observed Algol binaries that have an accretion disc (Table 2). Investigation into this discrepancy will be interesting, though beyond the scope of our present work.

The rotation periods of both components of the binary are assumed to be synchronised to the orbital period at their zero-age main sequence (ZAMS). Tidal interactions are modelled in a time-dependent fashion following the implementation by Detmers et al. (2008), using a synchronization timescale associated with the dynamical tide model of Zahn (1977), as appropriate for main sequence stars with radiative envelopes.

We use the standard Mixing Length Theory (Böhm-Vitense 1960) to model convection, with a mixing length parameter of $\alpha_{MLT} = 1.5$. The treatment of semiconvection follows Langer (1991) using $\alpha_{SC} = 0.01$ and the physics of thermohaline mixing is as in Cantiello & Langer (2010). We implement overshooting as a step function only to the top of the convective core up to 0.335 times the pressure scale height (Brott et al. 2011a). However, overshooting is applied only to layers inside a star which have a near-constant composition (Marchant 2017), implying that composition gradients are taken into account during the rejuvenation process of mass gaining stars (Braun & Langer 1995). The initial composition of the binary models also takes into account the nonsolar abundance ratios of the LMC, as in Brott et al. (2011a). Unlike Brott et al. (2011a) however, we use custom made OPAL opacity tables (Iglesias & Rogers 1996) in agreement with the initial abundance ratios of the LMC.

The initial donor mass (M_d) of the binary models range from 10.0 to 39.8 $M_\odot$ in steps of $\log(M_d/M_\odot) = 0.05$, where the donor star in a binary model is the initially more massive star. The accretor (M_a) is the initially less massive star of the model.

For every initial mass of the donor, models with different initial mass ratio (defined as $q = M_a/M_d$) ranging from 0.275 to 0.975 (in steps of 0.025) and initial orbital period (P_i) from ~1.41 d (log $P/d = 0.150$) to ~3165 d (log $P/d = 3.500$), in steps of $\Delta \log P_i/d = 0.025$, are calculated. This current work deals with the properties of models in the grid undergoing Case A mass transfer.

The models are evolved from the start of hydrogen burning and the orbit is assumed to be circular. The spin axes are assumed to be aligned to the orbital axis. This avoids the introduction of six free parameters at ZAMS, namely the initial rotation rates of each component. Admittedly, this assumption has no physical justification in nature, but it has been shown that moderate rotation does not significantly affect the evolution of individual stars (Brott et al. 2011a; Choi et al. 2016) while the fastest rotating stars may be products of binary evolution (de Mink et al. 2013; Wang et al. 2020). More importantly, the initially short-period binary models, that is, most of the Case A models we are dealing with in our study, get tidally locked soon after the beginning of the evolution from ZAMS (de Mink et al. 2009), irrespective of their initial individual stellar spin and direction. The spins of the post Case A models investigated here are influenced by the mass transfer episode where the mass donor fills its Roche volume and the mass gainer is typically spun up due to mass accretion. For similar reasons, the assumption of a circular orbit is not expected to affect our results significantly as our work is focussed on the properties of short-period binaries.

Mass transfer in the binary models is assumed to be conservative except for stellar winds until the accreting star spins up to critical rotation during the mass transfer process. However, Packet (1981) showed that stars only need to accrete a few percent of their total mass to spin up to critical rotation. Further accretion of matter is not possible unless angular momentum is lost by some mechanism. To model this loss of angular momentum when accretors reach critical rotation, the wind mass-loss rate of the accretor is increased to keep v_{rot}/v_{crit} near ~0.99, facilitating mass and angular momentum loss through the increased wind mass loss as described in Langer et al. (2003) and Petrovic et al. (2005). The amount of specific angular momentum removed from the orbit by the enhanced wind is equal to the specific orbital angular momentum of the accretor. At the same time, we remove the product of the specific spin angular momentum of the accretor at its surface times the mass removed from the system from the spin angular momentum of the accretor (Paxton et al. 2015). Here, v_{rot} and v_{crit} are the rotational and critical rotational velocities of the star as defined in Langer (1997).

Typically, the models where tidal effects can prevent the rapid spin-up of the accreting star lead to efficient mass transfer (i.e. very short orbital period models). In contrast, longer period models have comparatively much lower mass transfer efficiency. The efficiency of mass transfer is still an unsolved problem in binary evolution, with studies hinting at a decreasing efficiency with increasing orbital period (de Mink et al. 2007).

The assumption of increased mass-loss rates at close to critical rotation leads to a self-consistent way of determining the mass transfer efficiency, although it leads to very high mass-loss rates in models where tidal effects are unable to halt the rapid spin-up to critical rotation. To assess the feasibility of such high mass-loss rates in a model, an upper limit to the mass-loss rate ($\dot{M}_{upper}$) is calculated. For a radiation-driven wind, the upper limit is found by assuming that the mass that has to be lost is removed from a Keplerian disc whose radius is at most equal to that of the Roche lobe radius of the mass accreting star (with

mass M_a). Ignoring the donor (with mass M_d), the energy per unit mass (or gravitational potential) required to remove mass from the Roche lobe radius of the accretor is $GM_a/R_{RL,a}$. Assuming that the luminosity of both stars (L_d and L_a) is used to drive this mass loss, the resulting mass-loss rate is

$$\log \frac{\dot{M}_{upper}}{M_\odot/yr} = -7.19 + \log \frac{L_d + L_a}{L_\odot} - \log \frac{M_a}{M_\odot} + \log \frac{R_{RL,a}}{R_\odot}. \qquad (2)$$

For a typical model in our grid, having L_d, L_a, M_a and $R_{RL,a}$ of $4570\,L_\odot$, $3631\,L_\odot$, $6.25\,M_\odot$ and $10\,R_\odot$ respectively, the maximum mass loss rate ($\dot{M}_{upper}$) is $\sim 10^{-3}\,M_\odot\,yr^{-1}$.

When the mass-loss rate required in the model exceeds this maximum value that can be powered by the photon energy of both stars, the evolution of the model is stopped. The evolution of contact binaries are modelled as in Marchant et al. (2016) and they are stopped if mass overflow occurs from the L2 Lagrangian point during the contact phase. We also stop the evolution of a model if inverse mass transfer occurs in a binary model with a post main sequence component. We assume that the mass transfer in such models will not be stable and will lead to a common envelope evolution and merge. Otherwise, models are evolved till core carbon exhaustion if they have helium core masses less than $13\,M_\odot$ at the end of core helium burning, and till core helium depletion for models that have helium core mass greater than $13\,M_\odot$ (due to numerical issues faced in modelling the more massive stars all the way to core carbon depletion). Our study deals with the properties of binaries where both components are on the main sequence.

2.2. Initial binary distribution function

For our population synthesis predictions, each binary model m in our grid is assigned a weight factor W_m that depends on the initial donor mass M_d, the initial mass ratio q_i and the initial orbital period $\log P_i$. For the initial donor mass distribution, we use the Salpeter initial mass function (Salpeter 1955), and the Sana et al. (2012) exponents for the initial mass ratio and orbital period. While the latter have been derived using a modest sample of ~ 40 O-type binaries in the Milky Way, more recent studies of O and B type stars both in the Milky Way and the LMC have failed to reveal any statistically significant differences (Sana et al. 2013; Dunstall et al. 2015; Villaseñor et al. 2021; Banyard et al. 2022). Hence, our adopted values can also be taken as representative of the OB star population at LMC metallicity. As such, we define W_m as

$$W_m = (\log M_{d,i}/M_\odot)^{-1.35} * q_i^{-0.10} * (\log P_i/d)^{-0.55}. \qquad (3)$$

We obtain histograms for the distribution of an observable O_{obs}, defined as the value of the stellar parameter during the contact (cnt) or semi-detached (SD) phase, weighing with the amount of time spent in the cnt or SD phase and the initial binary distribution functions. The number fraction ($f_{obs,cnt\,or\,SD}$) of an observable stellar parameter in a given bin with bin edges $[O_1, O_2]$ is given by,

$$f_{obs,cnt\,or\,SD}\,(O_1 < O_{obs} < O_2) = \frac{\sum_{m=1}^{N} \delta_{O_1 O_2,m}\,W_m\,\Delta t_{cnt\,or\,SD,m}}{\sum_{m=1}^{N}\,W_m\,\Delta t_{cnt\,or\,SD,m}}, \qquad (4)$$

where m is the model number of a particular model in our grid and N is the total number of models that undergo Case A mass transfer (Case A models). $\Delta t_{cnt\,or\,SD,m}$ is the total time spent in the contact or semi-detached configuration by model m. $\delta_{O_1 O_2,m}$ is equal to 1 when the value of the observable for the model m is between O_1 and O_2 during the contact or semi-detached phase and zero otherwise.

2.3. Binary parameter space

To help understand the general properties of the models undergoing Case A mass transfer and aid in the interpretation of the results of our population synthesis, we briefly describe a slice of our parameter space. Figure 1 shows the evolutionary outcomes up to core hydrogen depletion for models with an initial donor mass of $22.4\,M_\odot$ and different initial orbital periods and mass ratios. Models with $\log (P_i/d) \lesssim 0.9$ undergo Case A mass transfer. The orbital period cut-off below which models undergo Case A mass transfer depends on the initial donor mass, with longer periods binaries able to undergo Case A mass transfer for higher initial donor masses (cf., Fig. F.1).

Notably, we find by inspection that all our Case A accretors undergo ballistic mass accretion from the donors (see discussion of Eq. (1)). We see that only a part of the parameter space survives the Case A mass transfer phase (marked by the lightblue colour). Models with low mass ratios (green) are terminated (and assumed to merge) during the fast Case A mass transfer phase because the combined luminosity of both of stars is insufficient to drive the excess mass-loss rate required to hinder over-critical rotation of the mass accretor, that is, the mass transfer rate in the model exceeds $\dot{M}_{upper}$ (given by Eq. (2)). They spend ~ 5000 yr in the fast Case A mass transfer phase before terminating and hence are not expected to significantly change the distribution of the observable properties of semi-detached binaries.

Models with very short orbital periods (purple) enter into a contact configuration during the slow Case A mass transfer and eventually experience L2 overflow. Such binaries are assumed to merge, due to the very low orbital periods. In the orange models, the initially less massive star overtakes the evolution of the mass donor during the slow Case A mass transfer phase and completes core hydrogen burning before the initially more massive star (Pols 1994; Wellstein et al. 2001). As such, a reverse mass transfer is initiated from initially less massive star (that is expanding rapidly after core hydrogen burning), on to the initially more massive Roche-lobe filling star that is still in its main sequence. This inverse mass transfer will likely be unstable and the binary is assumed to merge.

However, the above two types of models (purple and orange) spend up to ~ 10 Myr in the slow Case A mass transfer phase before they undergo L2 overflow. Hence, the contribution from these short period binaries to the observable properties of Algol binaries cannot be neglected. Similar figures for other initial donor masses are provided in (Fig. F.1). Since the radii of more massive donor stars are larger, binaries can undergo Case A mass transfer at longer orbital periods for greater initial donor masses. Moreover, since the luminosity of stars rises steeply with mass, the upper limit to the maximum mass transfer rate (Eq. (2)) also increases for higher initial donor masses. Since this upper limit to the maximum mass transfer rate determines the boundary between systems that merge vs systems that survive the fast Case A mass transfer, more systems survive the Case A mass transfer at higher initial donor masses.

3. Case A mass transfer

3.1. A Typical example

Figure 2 shows the typical evolution of a short period (~ 2.7 d) massive binary with initial donor and accretor mass of $17.80\,M_\odot$ and $14.24\,M_\odot$, respectively. It encounters mass transfer while both stars are burning hydrogen in their cores (panel a). The initially more massive star fills its Roche lobe at ~ 9.4 Myr which initiates mass transfer via Roche-lobe overflow (panel b). The
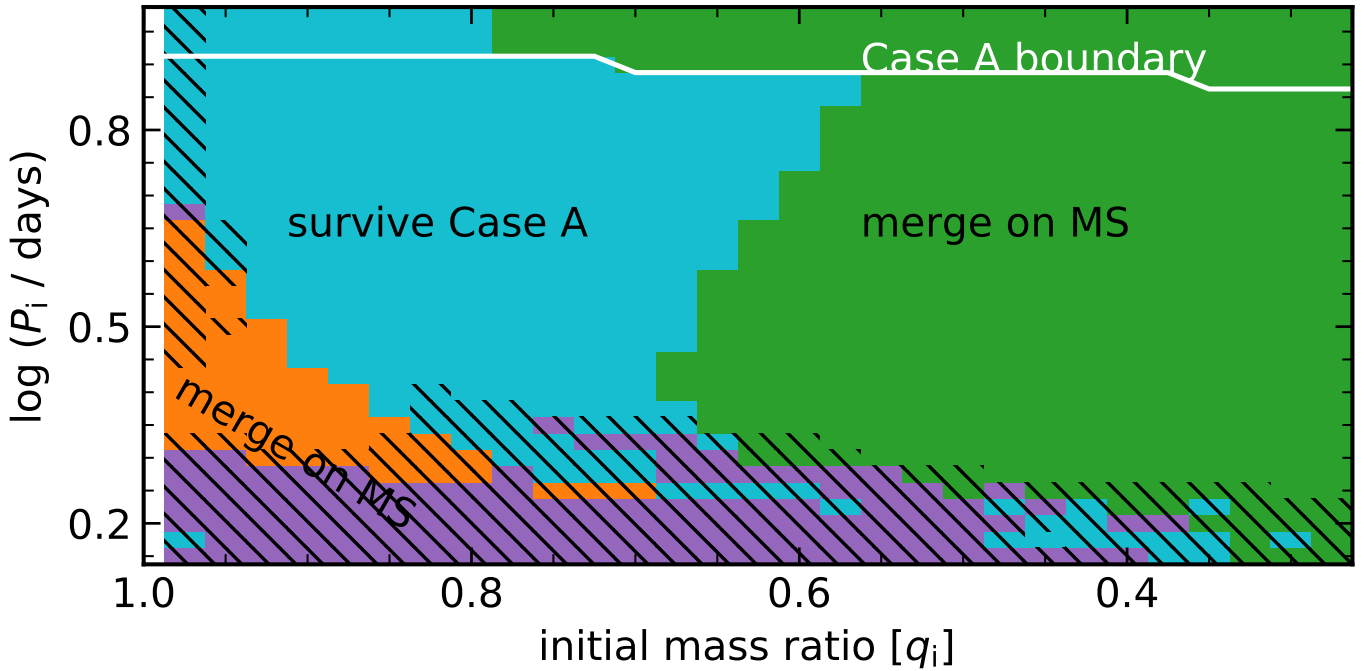
Fig. 1. Summary plot of binary models with an initial donor mass of $22.4\,M_\odot$, as a function of the initial binary orbital period and mass ratio. Each pixel in the plot represent the outcome of one binary model with the corresponding orbital period and mass ratio. The white line shows the maximum initial orbital period below which models undergo Case A mass transfer. The light blue coloured models survive the Case A mass transfer phase. The models marked in green are terminated during the fast Case A mass transfer phase. The purple models undergo mass overflow from the L2 Lagrangian point during core hydrogen burning. The orange models undergo inverse mass transfer onto the initially more massive Roche-lobe filling star while it is burning hydrogen, from the initially less massive component that has completed core hydrogen burning. Models that enter into a contact configuration, at any point of time during their main sequence evolution, are marked with hatching.

mass transfer rate rises above $10^{-4}\,M_\odot\,\mathrm{yr}^{-1}$ (panel d) during the so-called fast Case A mass transfer phase which occurs at the thermal timescale of the donor. We see that in this model, the fast Case A mass transfer is not purely conservative as the accretor quickly spins up to critical rotation (evidenced by the sharp increase in the ratio of rotational velocity to synchronous velocity in panel g). Only about 20% of the mass lost by the donor is accreted by the companion (panel c). The orbital period (solid black line, panel h), and in turn the orbital separation, first decreases and then increases as the mass ratio gets inverted and keeps diverging from unity.

For comparison, we also show the evolution of the orbital period if the mass transfer was fully conservative (black dashed line). We compute the orbital period (P) evolution in the conservative case following (Soberman et al. 1997)

$$\frac{P}{P_\mathrm{i}} = \left(\frac{M_\mathrm{d,i} M_\mathrm{a,i}}{M_\mathrm{d} M_\mathrm{a}}\right)^3,\tag{5}$$

where P_i, $M_\mathrm{d,i}$ and $M_\mathrm{a,i}$ are the initial orbital period of the binary, donor mass and accretor mass respectively. M_d, M_a and P are the masses of the donor, the accretor, and the orbital period at any stage during the conservative mass transfer process. To compute the orbital period under the assumption of conservative mass transfer, we take M_d from our simulations and compute M_a assuming the mass transfer process was conservative. Since the mass transfer is non-conservative during the fast Case A phase in this model, the increase in orbital period due to the fast Case A mass transfer is lower than for the conservative mass transfer case.

Following the fast Case A mass transfer episode, the binary enters into a nuclear timescale mass transfer phase where the

mass transfer rate is of the order of the nuclear timescale. This phase is known as the slow Case A phase, or the Algol phase (for a more detailed discussion, see Wellstein et al. 2001). In our work, we distinguish between the fast and slow Case A mass transfer phase based on the mass transfer rate in the binary, with the boundary at $10^{-5}\,M_\odot\,\mathrm{yr}^{-1}$.

There is a gradual increase in the surface abundances of helium and nitrogen during the slow Case A phase (panels e and f) as the mass transfer exposes the deeper layers of hydrogen burning processed material of the donor. We also note that most of the mass from the donor is lost during the fast Case A phase (panel c) and there is a slow loss and gain in mass of the donor and accretor respectively during the slow Case A phase. The amount of mass accreted depends on, amongst other factors, the spin-up of the accretor star in response to the mass accretion.

At the end of core hydrogen exhaustion, the remaining hydrogen envelope in the mass donor starts to expand and refill its Roche lobe. This leads to the onset of another thermal timescale mass transfer phase, that is, the Case AB phase, where most of the remaining hydrogen envelope is removed from the mass donor and the surface nitrogen abundance reaches the CNO equilibrium value and the surface helium mass fraction reaches ~0.77. Since the mass ratio increasingly diverges away from unity to higher values, the orbital period of the binary also increases during this mass transfer phase.

We define Case A mass transfer to be occurring in our binary models when there is a non-zero mass transfer rate in the binary model and the Roche lobe filling star is still burning hydrogen at its centre. This means that, in addition to the fast and slow Case A phases, main sequence contact models and inverse mass transfer during core hydrogen burning from the initially less massive component to the initially more massive star will
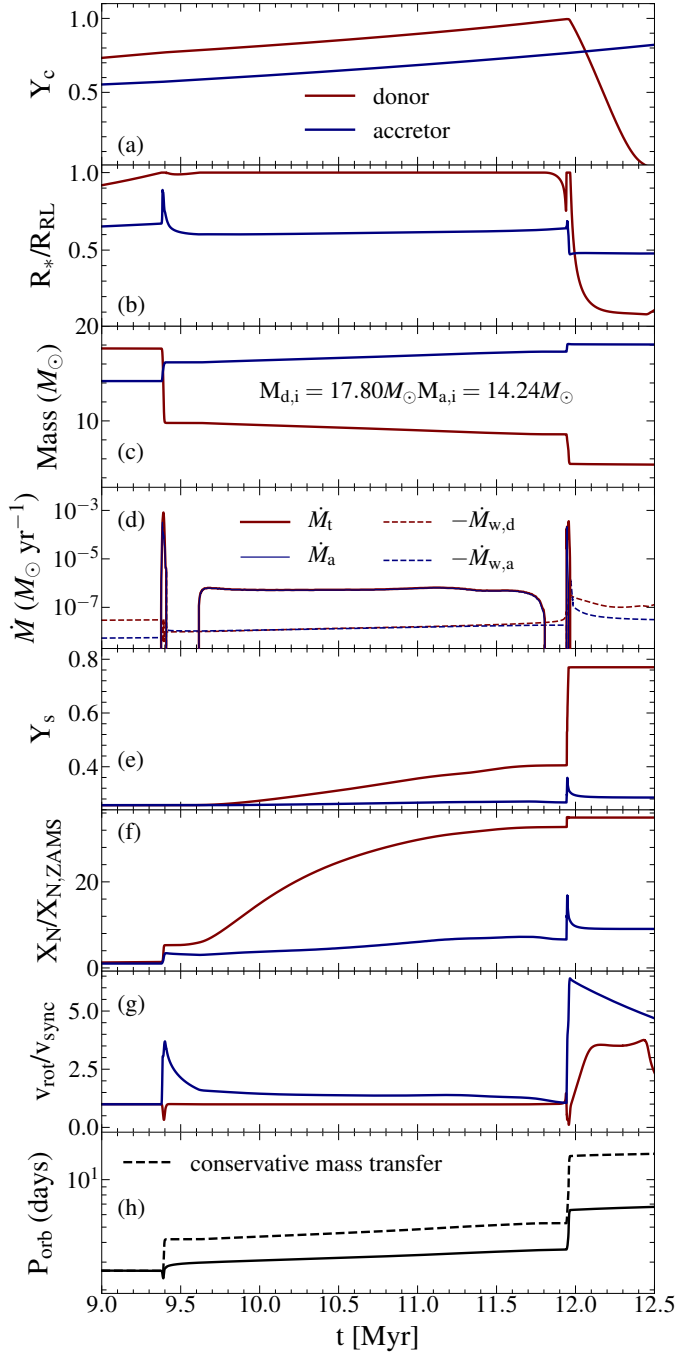
Fig. 2. Example of a Case A and Case AB mass transfer episode for a typical binary model in our grid. The initial donor mass, mass ratio and orbital period of the model are 17.8 $M_\odot$, 0.8 and ~2.7 d respectively. Various quantities are plotted as function of time, with $t = 0$ corresponding to the ZAMS stage of both stars. (a) central helium mass fraction of donor (red) and accretor (blue). (b) ratio of donor and accretor radius to their Roche lobe radii. (c) donor and accretor mass. (d) mass transfer rate $\dot{M}_t$ (red solid line), effective mass accretion rate $\dot{M}_a$ (blue solid line), and wind mass loss rates of donor ($-\dot{M}_{w,d}$, red dotted line) and accretor ($-\dot{M}_{w,a}$, blue dotted line), respectively. (e) surface helium mass fraction. (f) surface nitrogen enhancement factor. (g) ratio of rotational to orbital angular velocity. (h) orbital period (solid black line), and the orbital period our model would have obtained if the mass transfer would have been fully conservative (dashed black line).

also be part of the Case A mass transfer phase. The corresponding configuration of a binary model where one star (both stars)

fills its (their) Roche lobe(s) is called the semi-detached (contact) configuration.

One important point to keep in mind, however, is that for inverse slow Case A mass transfer from an initially less massive accretor, we do not change the notation of 'donor' and 'accretor' in our results. As such, we use the word 'donor' to denote the initially more massive star that fills its Roche lobe first, and 'accretor' to denote the initially less massive accretor star. Nevertheless, we point out whenever the contribution from inverse mass transfer binaries to the general population of slow Case A binaries is present.

3.2. Mass transfer efficiency in our models

Here, we define and analyse the mass transfer efficiency during the fast and slow Case A mass transfer in our binary models. To avoid misunderstandings, it needs to be carefully defined, since both binary components may also lose mass to a stellar wind. Notably, the mass transfer efficiency in our models is a function of time, and below, we evaluate their time-averaged mass transfer efficiency during fast and slow Case A mass transfer.

When we designate the donor's wind mass-loss rate as $\dot{M}_{w,d}$, and the rate of mass transfer via Roche-lobe overflow as $\dot{M}_t$, the total mass-loss rate from the donor stars is

$$\dot{M}_d = \dot{M}_{w,d} - \dot{M}_t, \tag{6}$$

where we define the mass transfer rate as a positive quantity and wind mass loss rate as a negative quantity. During fast Case A mass transfer, it is $\dot{M}_t \gg -\dot{M}_{w,d}$, such that the wind mass-loss rate from the donor is insignificant (cf., panel d of Fig. 2). During the slow Case A mass transfer phase however, wind mass loss and mass transfer rate can become comparable for the most massive donors in our grid. For a model with $(M_{d,i}, P_i, q_i) = (39.8\ M_\odot, 6.3\ d, 0.800)$, we find that ~0.5 $M_\odot$ of mass are lost from the donor via its stellar wind during the slow Case A mass transfer phase, while ~2 $M_\odot$ of mass are transferred via the first Lagrangian point during the same time.

The mass change of the accretor is obtained by subtracting its wind mass loss from the amount transferred, that is, $\dot{M}_a = \dot{M}_t + \dot{M}_{w,a}$, where $\dot{M}_a$ is the total rate of change of mass of the accretor and $\dot{M}_{w,a}$ is the wind mass-loss rate of the accretor. Here, the steep increase in wind mass loss for accretors rotating near critical rotation can become important. As explained in Sect. 2.1, this effect can lead to highly non-conservative mass transfer in our models, such that the term $\dot{M}_{w,a}$ can exceed the wind mass-loss rate of slowly rotating models by orders of magnitude. This happens for spun-up mass gainers near critical rotation, where the mass loss which prevents it from rotating faster than critical. For fully spun-up accretors, it is $\dot{M}_{w,a} \simeq -\dot{M}_t$.

As we model inefficient accretion like a stellar wind, we do not differentiate between the ordinary stellar wind and the mass loss required to prevent over-critical rotation in defining our mass transfer efficiency η, and set

$$\eta = \frac{\dot{M}_a}{\dot{M}_t}. \tag{7}$$

In this way, the mass transfer efficiency can range from 0 for critically rotating accretors to ~1 for tidally locked and/or slowly rotating accretors.

Figure 3 shows the time-averaged mass transfer efficiencies during fast (top and middle panel) and slow Case A (bottom panel). The top panel shows the mass transfer efficiencies of all our systems that survive fast Case A mass transfer as a binary.
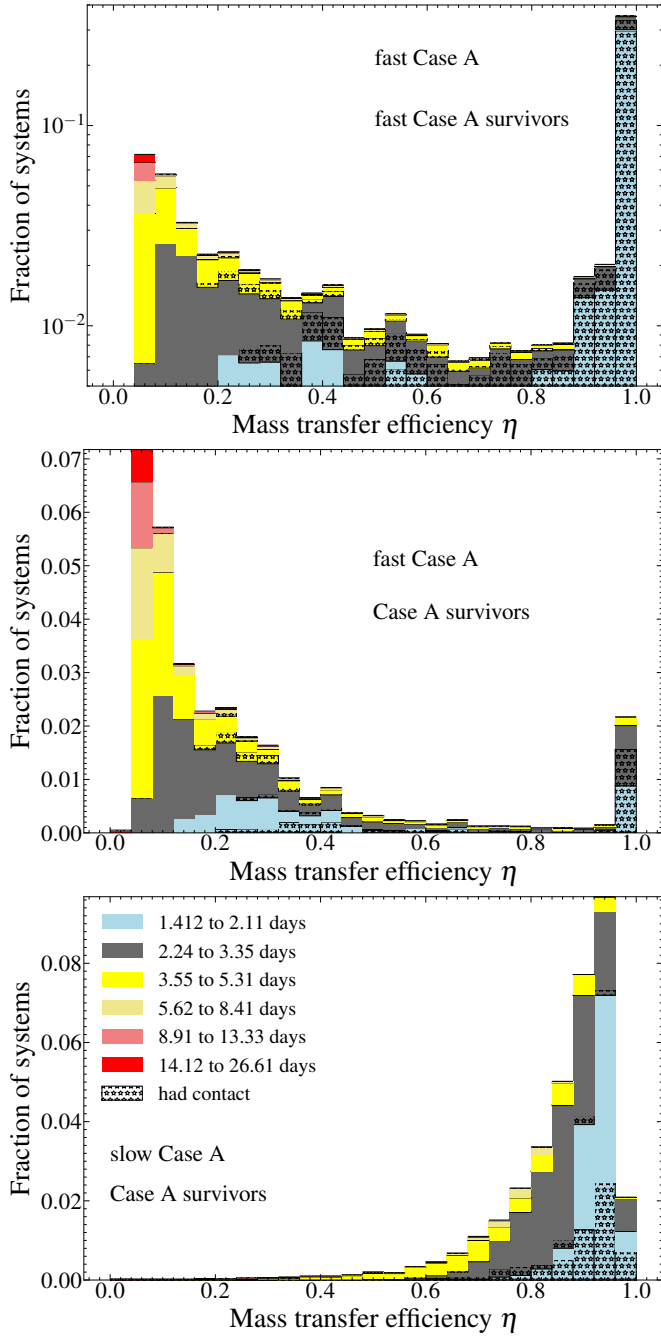
Fig. 3. Distribution of the time-averaged mass transfer efficiency during fast (*top two panels*) and slow (*bottom panel*) Case A mass transfer. The top plot includes all models that survive fast Case A mass transfer phase (i.e. light blue, orange and purple models in Fig. 1), while the middle panel includes only those models that survive also the slow Case A mass transfer phase (light blue models in Fig. 1). The colour coding is with respect to the initial orbital period of the binary model. The histograms are weighted with the birth probability of the binaries, and with the amount of time spent in the respective Case A mass transfer phase. The ordinate values are normalised to unity such that the value for each bin gives the weighted fraction of models that have their mass transfer efficiency between those bin edges during fast/slow Case A mass transfer. The fraction of models in any bin that undergo a contact phase are marked with star hatching.

It excludes models that we expect to merge very soon after the onset of the fast mass transfer (models marked in green in Fig. 1). We see that mass transfer efficiencies, from fully conservative

to fully non-conservative are realised by our models. While the distribution is rather flat for most of the mass transfer efficiency range, it shows distinct peaks near $\eta = 1$ and $\eta = 0.05$.

About ~35% of our models undergo nearly conservative fast Case A mass transfer. The initial period information (colour coding in Fig. 3) reveals that this happens for the shortest period binaries in our model grid. These systems remain effectively tidally locked at all times, such that their accretors are not spun up. On the other hand, models with initial orbital periods larger than ~4 d show mass transfer efficiencies below 40%, and the initially widest binaries evolve with accretion efficiencies below ~15%. This reflects the decreasing strength of the tidal interaction for larger orbital separations.

The middle panel of Fig. 3 shows the mass transfer efficiency during fast Case A for models that also survive the slow Case A mass transfer phase without merging. Of these, we find that 99.2% also survive the ensuing Case AB mass transfer. Models in our grid that survive the entire Case A mass transfer typically have low average fast Case A mass transfer efficiencies. Comparing the top and middle panels, we see that a large number of models that undergo conservative fast Case A mass transfer merge during the slow Case A mass transfer phase. These models, originating from very short initial periods that eventually undergo L2 overflow, actually spend a considerable amount of time in the slow Case A mass transfer phase before merging (compare peak at mass transfer efficiency near unity between the left and right panel). We find that some of these models also go through a nuclear-timescale contact phase before merging (see also Menon et al. 2021). Quantitatively, the weighted fraction of Case A models contributing to the middle panel is ~63% smaller than that in the top panel.

The time-averaged mass transfer efficiency during slow Case A mass transfer, for the models which survive the slow Case A (bottom panel of Fig. 3), is generally high. The slow Case A mass transfer occurs at the nuclear timescale and the mass transfer rate is also much lower, of the order of $10^{-7}\ M_\odot\ \mathrm{yr}^{-1}$. For the model with $(M_{\mathrm{d,i}}, P_i, q_i) = (39.8\ M_\odot, 6.3\ \mathrm{d}, 0.800)$, we find that ~0.3 $M_\odot$ of mass are lost from the accretor via stellar winds during the slow Case A mass transfer phase. Hence, the mass accreted by the mass gainer during the slow Case A mass transfer phase in this model is ~1.7 $M_\odot$. The mass transfer efficiency of this binary during slow Case A is about 85%. We show later that the majority of the accretors in the slow Case A phase are tidally synchronised. A comparison of time spent in the slow Case A phase between models that merge during the slow Case A phase vs models that survive the slow Case A phase reveals that our models predict ~70% of Algols binaries are expected to merge during their main sequence.

Figure F.2 shows the mass transfer efficiency of individual models in our grid for an initial donor mass of ~16 $M_\odot$ and ~40 $M_\odot$. We see that the mass transfer efficiency of the thermal timescale fast Case A and Case AB phase is low for the most of the 16 $M_\odot$ models. Owing to the increased tidal strength of higher mass donors, the mass transfer efficiency is near unity for the shortest period models of the 40 $M_\odot$ slice. We also see the dividing boundary as a function of orbital period and mass ratio at which the tidal strength is unable to counteract the spin-up of the accretor star. A lot more number of models undergo conservative slow Case A mass transfer, owing to the nuclear timescale mass transfer rate. Nevertheless, we again see a reasonably clear boundary between efficient and nonefficient mass transfer in the slow Case A mass transfer phase too.

We note that the amount of mass lost and gained during the slow Case A phase can be up to ~6 $M_\odot$ for the models (Fig. F.4)
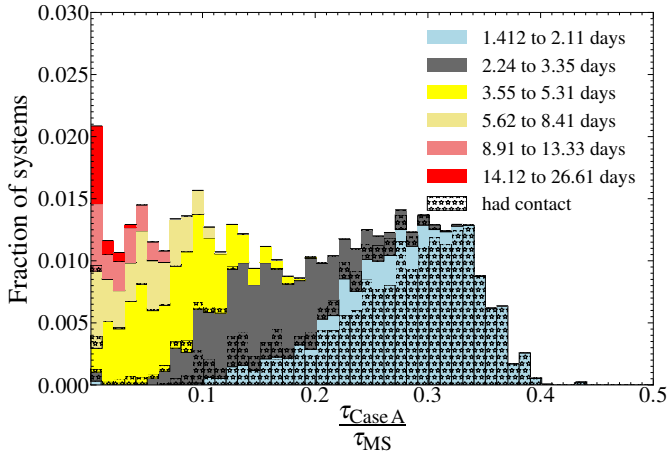
Fig. 4. Distribution of the fractional main sequence lifetime spent in the Case A mass transfer phase ($\tau_{\mathrm{Case\,A}}/\tau_{\mathrm{MS}}$; see text for the exact definition) of models with $\tau_{\mathrm{Case\,A}}/\tau_{\mathrm{MS}} > 0.001$. The colour coding differentiates between models arising from different ranges of initial orbital periods. The star hatching in each fractional main sequence lifetime bin denotes the relative number fraction of models in that bin that go through a contact phase during Case A mass transfer.

with an initial donor mass of 40 $M_\odot$, due to efficient mass accretion during the slow Case A phase. Another $\sim$4 $M_\odot$ of mass can be lost during the Case AB mass transfer phase (Fig. F.5) in our models. Also, a very small number of models with highest initial donor masses can undergo efficient Case AB mass transfer.

3.3. Life-time of Case A mass transfer

Here, we look at the amount of time spent by the binary models in the Case A mass transfer phase. Figure 4 assesses the fraction of the main sequence lifetime our models spent in the Case A mass transfer phase, $\tau_{\mathrm{Case\,A}}$, with the Case A mass transfer phase as defined in Sect. 3.1. Here, we define the main sequence lifetime (τ_{MS}) of a binary model as the hydrogen burning lifetime of the binary component which completes hydrogen burning first, or, for those binary models which merge during Case A evolution, the main sequence lifetime of a single star with half the total mass of the binary model. The number fraction f in each fractional main sequence ($\tau_{\mathrm{Case\,A}}/\tau_{\mathrm{MS}}$) bin $[a, b]$ is given as

$$f(a < \tau_{\mathrm{Case\,A}}/\tau_{\mathrm{MS}} < b) = \frac{\sum_{m=1}^{N} \delta_{ab,m} W_m}{\sum_{m=1}^{N} W_m}, \qquad (8)$$

where $\delta_{ab,m} = 1$ if the fraction of the main sequence lifetime spent by the model in Case A mass transfer phase is between a and b, and $\delta_{ab,m} = 0$ otherwise.

Figure 4 only includes models that spend more than 0.1% of their main sequence lifetime in the Case A mass transfer phase, which is of the order of the thermal timescale of the mass donors. This removes about 60% of all models that undergo Case A mass transfer, whose fate is to merge during fast mass transfer (green models in Fig. 1). Figure 4 shows that the shorter period binaries spend more time in the Case A mass transfer phase. Many of these models also go through a contact phase as denoted by the star hatching. The hatched versus unhatched part of each bin in this figure indicates the fraction of the models in any bin go through a contact phase, but is not indicative of the time spent in the respective phases.

We find that Case A models can spend up to a third of their main sequence lifetime in the semi-detached configuration. Usually, once Roche-lobe overflow occurs during core hydrogen

burning in binary, the binary spends most of the remaining main sequence lifetime of the donor in the semi-detached configuration (Fig. 2). However, we find that binaries in which Roche-lobe overflow occurs very early in their main sequence lifetime, the binary enters into a contact configuration and eventually merges via L2 overflow. This is why we do not find our Case A models to spend more than 40% of their main sequence lifetimes in the slow Case A phase. We assess the number of semi-detached massive binaries in the LMC which is expected from our models in Sect. 6.3.

4. Observable properties of semi-detached models

Here, we evaluate the distributions of observable properties of our binary models while they are in a semi-detached configuration. Besides our theoretical predictions, many of the plots in this section already include information about observed semi-detached binaries. However, we perform a comparison of our results with observations separately, in Sect. 6.
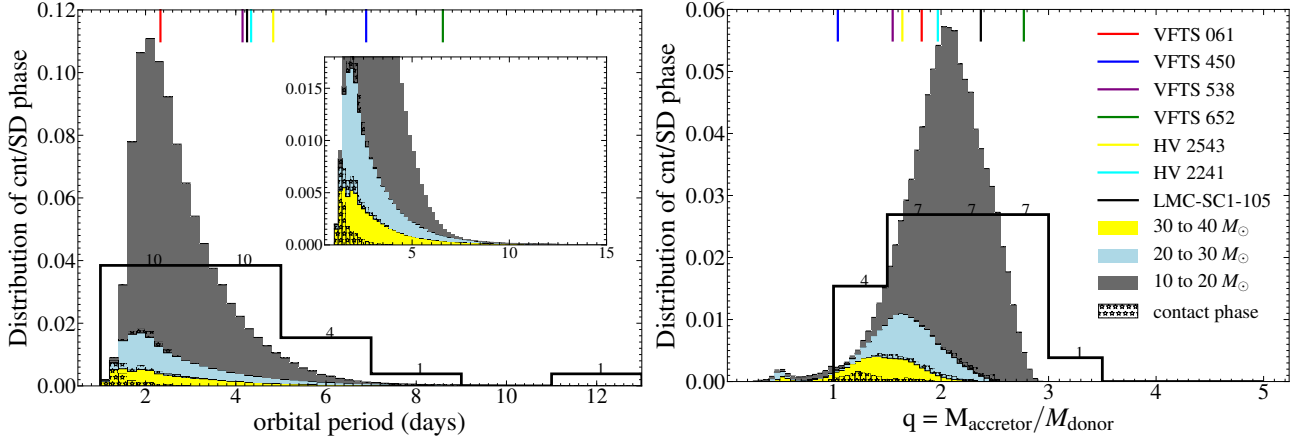
4.1. Orbital period and mass ratio distribution

Figure 5 shows the predicted orbital period distribution of our Case A binary models during the semi-detached (unhatched) and contact (hatched with stars) phases of their evolution. The histogram is weighted by the binary birth probability (see Sect. 2.2), and their time spent in each orbital period bin during their semi-detached or contact phase. Comparing the contributions from the semi-detached phase and the contact phase shows that $\sim$96% of the interacting Case A binaries in our grid are in the semi-detached configuration. However, our assessment of the contact binary parameter space is incomplete as our lowest initial orbital period is $\sim$1.4 d. Including models with shorter initial periods leads to a larger predicted fraction of contact systems (see Sect. 6.3 and Menon et al. 2021).

The drop in the period distribution of the semi-detached systems towards the shortest periods in Fig. 5 is, however, not due to our lower initial period cut-off. We see from Fig. 1 that the shortest period models in our grid do not survive the Case A mass transfer phase as binaries. Amongst these presumable mergers, the models with shortest orbital periods spend increasingly more time in the contact than in the semi-detached configuration. Consequently, our semi-detached model population is essentially complete, for the investigated mass range.

For models with longer orbital periods, Case A mass transfer starts comparatively later during the main sequence evolution of the donor. Once the slow Case A mass transfer starts, it continues until the end of the main sequence evolution of the donor. Since the histogram is weighted by the lifetime of the models in the Case A mass transfer phase, the longer period models do not contribute to the same extent as the shorter period models. Moreover, fewer long orbital period models undergo Case A mass transfer (depending on the initial donor mass, cf., Fig. F.1). Hence, the distribution drops off at higher orbital periods. The contribution from models in the contact phase keep increasing towards shorter periods and our grid is not ideal to investigate this phase. We predict to find most semi-detached systems around an orbital period of $\sim$1.5−4 d.

Figure 5 (right panel) shows the predicted distribution of the mass ratios of our Case A models during the semi-detached and contact phases. Since the mass ratio is inverted during fast Case A, the models do not spend much time at mass ratios below unity. A significant fraction of time is spent in the slow Case A mass transfer phase, where the mass ratio has already inverted.

Fig. 5. Distribution of orbital periods (*left panel*) and mass ratios (*right panel*) of our models during the semi-detached phase (unhatched) or contact phase (hatched with stars) of Case A mass transfer. Colour coding marks three different initial mass ranges, as indicated. The ordinate values are normalised such that the sum of the number fractions in all bins equals unity. Vertical lines at the top of the plots denote the orbital periods and mass ratios of observed Algol systems in the LMC (Table 1), identified through their colour (see legend, same for both panels). The inset in the *left panel* shows a zoomed-in distribution of the yellow and blue models. The black step-histogram denotes the distribution of orbital periods and mass ratios of 26 observed massive Algol systems in the Milky Way (Table 2). It is normalised such that the area under both the histograms is same. The number of stars contributing to each bin is given on top of each bin.

Hence, we see a large peak at mass ratios of ∼2. For more massive systems, the peak moves to smaller mass ratios due to the larger core mass fraction at higher mass.

The smaller peak near $q = 0.5$ arises from the shortest period models where a thermal timescale contact occurs, followed by a nuclear timescale inverse slow Case A mass transfer. For example, a system with parameters $(M_{1,i}, q_i, P_{orb,i}) = (28.3\,M_\odot, 0.800, 1.41\,\mathrm{d})$ evolves as follows. The initially more massive star undergoes fast Case A mass transfer, followed by slow Case A. During the slow Case A mass transfer episode, the then more massive accretor fills its Roche lobe and contact occurs, which initiates inverse mass transfer. Shortly after the onset of contact, the initially more massive star shrinks below its Roche lobe radius, and the inverse slow Case A mass transfer occurs in a semi-detached configuration. Their expected number is small. However, they open a small chance to find Algol systems with mass flow from the currently more massive to the currently less massive star (e.g. VFTS 176, see Mahy et al. 2020a).

Figure 6 shows distribution of the absolute donor and accretor masses during the semi-detached phase. We see that the donor masses are significantly lower than the accretor masses, which is consistent with the fact that mostly the Roche-lobe filling star is the lower mass star of the binary. The highest probabilities for the lowest masses come from the combined effect of the IMF weight on the distribution functions and the fact that the lower mass donors spend more time in the Case A mass transfer phase. We see a broader range of accretor masses for a given donor mass since more massive systems avoid merging during Case A evolution for a larger initial mass ratio range (cf., Fig. F.1).

Notably, the increase in orbital period after the Case AB phase (Fig. F.6) is highest in the lower initial donor mass models because of the smaller core size of the lower mass donors. Owing to the higher envelope to core ratio, a comparatively larger fraction of mass is transferred in the lower mass models, which increases the mass ratio of the binary and the orbital period also increases more.

4.2. Surface abundances

In massive stars, the enrichment of helium and nitrogen is related, because both are products of the CNO-cycle
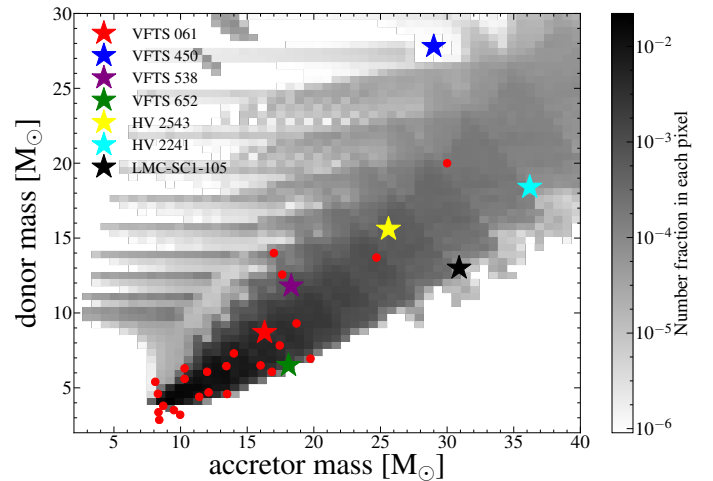
Fig. 6. Probability distribution of the donor and accretor masses that is predicted to be observed in the semi-detached configuration of the Case A mass transfer phase based on the model grid. The different coloured 'stars' denote the position of observed semi-detached systems in the LMC (Table 1). Grey-scale: see description in Fig. 7. The red circles denote the parameters for the Galactic Algol systems (Table 2).

(Kippenhahn & Weigert 1990). Within the convective core, CNO equilibrium is established quickly, such that nitrogen obtains its CNO equilibrium value while only little hydrogen has been converted into helium. However, the convective core of massive main sequence stars is receding with time, and leaves a transition region within which the hydrogen abundance drops from its initial value to the value currently inside the convective core. In stars above ∼15 $M_\odot$, this transition layer is slowly mixed with overlying unprocessed matter by semiconvection, which extends the transition layers to regions above the initial convective core, and leads to layers in which both, helium and nitrogen are enhanced, but with a nitrogen abundance below the CNO equilibrium value (Langer 1991). In addition to that, the temperature above even the extended transition layer is high enough to allow for incomplete CNO burning, where some carbon is
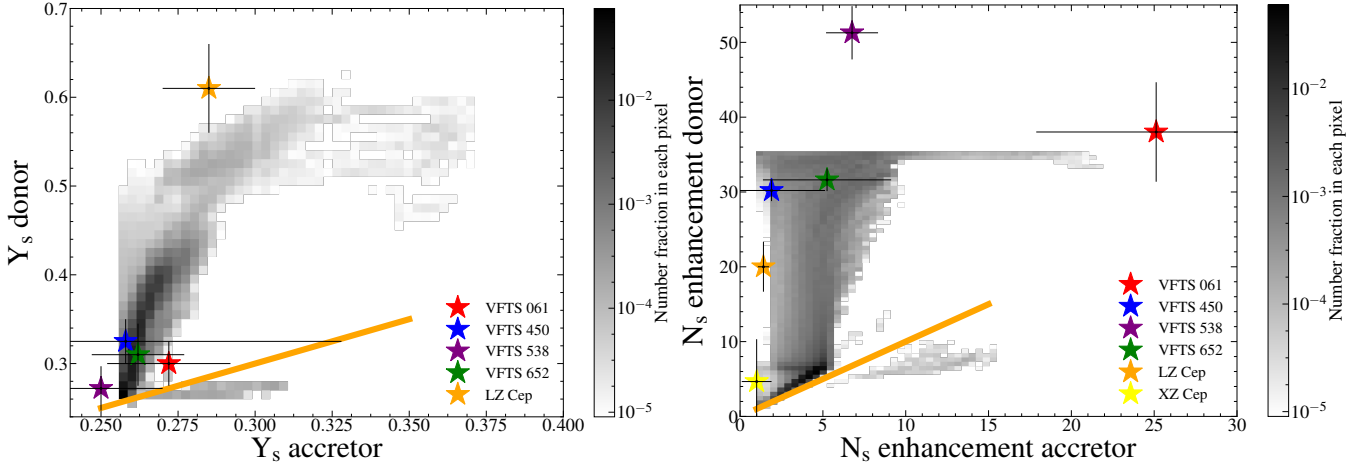
Fig. 7. Probability distribution of the surface helium mass fraction (Y_s, *left panel*) and surface nitrogen mass fraction (N_s) enhancement (*right panel*, see text) of donor vs. the accretor that is predicted to be observed in the semi-detached configuration of the Case A mass transfer phase based on the model grid. The different coloured 'stars' with error bars denote the position of the semi-detached systems of the TMBM survey and Galaxy. The surface nitrogen mass fraction enhancement of the LMC systems are evaluated w.r.t. to the LMC nitrogen abundance baseline, while the enhancement for LZ Cep and XZ Cep are evaluated w.r.t. to the Solar baseline. The grey-scale gives the probability fraction in each pixel. The total probability is normalised such that the integrated sum over the entire area is 1. The orange line indicates where the surface helium mass fraction or surface nitrogen enrichment of the donor and accretor is the same.

transformed into nitrogen, but oxygen is not. In our donor stars, all these layers appear successively at the surface and determine the abundances of the matter accreted by the accretor star, whose entire envelope undergoes thermohaline mixing as soon as even a small helium enrichment is present in the accreted matter.

Figure 7 shows the surface helium mass fraction (Y_s, left panel) and the ratio of the surface nitrogen mass fraction (N_s) to the initial surface nitrogen mass fraction (right panel, which we call surface nitrogen mass fraction enhancement), of our donor and accretor models in the semi-detached configuration. It shows that the mass donors emerge from fast Case A mass transfer with essentially all of the unenriched part of their envelopes removed. A mild nitrogen enrichment is present in almost all donors, which results from CN-processing occurring above the H/He-transition layers in the donor star. At the beginning of the semi-detached phase, helium is still practically unenriched at the mass donor's surface (cf., panel e of Fig. 2).

During the further evolution, mass transfer from the donor during the slow Case A phase gradually brings layers from the hydrogen-helium gradient region of the donor to its surface, which raises its surface helium mass fraction appreciably (see also Fig. 2). However, the helium surface mass fraction of the donor stars usually remain below $Y_s \simeq 0.45$. Correspondingly, the surface nitrogen mass fraction enhancement increases and eventually reaches the CNO equilibrium value of ~35 for the LMC during the slow Case A phase. This indicates that during slow Case A mass transfer, layers start to be uncovered which were part of the convective core earlier in the evolution.

The enrichment of the surface of the mass gainers is mediated by thermohaline mixing, and therefore remains significantly smaller than that of the donor. We see from Fig. 7 that their helium mass fraction remains mostly below $Y_s \simeq 0.29$ (the initial value is 0.256), whereas the nitrogen enrichment does not exceed a factor of 10 in the vast majority of cases. Core hydrogen burning in the accretors has already created a strong mean molecular weight gradient by the time the Roche-lobe overflow begins, which prevents a strong nitrogen enrichment due to rotational mixing even in rapidly rotating accretors (Wang et al. 2020).

In a small fraction of our models, the mass gainers reach rather high enrichment, that is, helium surface mass fractions in the range 0.30−0.38, and nitrogen mass fraction enhancements of up to 22 (Fig. 7). In Appendix B, we provide similar plots, but separately for three mass bins (Fig. B.2). This shows that the highly enriched mass gainers are restricted to systems with larger initial masses.

From investigating the Case A models that survive or eventually merge during slow Case A, separately, we find that the latter contain mass donors with surface nitrogen mass fraction enhancement below ~8 for ~75% of the time. Models that survive the slow Case A phase have donors whose surface nitrogen mass fraction enhancement is above ~8 for ~90% of the time they spend as semi-detached systems. Since both groups of binaries experience a nuclear timescale mass transfer phase, we expect observational counterparts to both these kinds of systems. In Sect. 3.2, we had shown that models that eventually merge during slow Case A phase contribute to ~70% of the predicted observable binaries in the semi-detached phase.

Now, the fraction of models that survive vs merge during the slow Case A phase depends on the response of accretor radius to mass accretion. We know that accretors with inefficient semi-convective mixing (as in our models) are larger in radius than accretors with efficient semiconvective mixing (cf., model 47 and 48 of Wellstein et al. 2001). This implies that our models are more likely to enter contact during slow Case A mass transfer than models with efficient semiconvection (such as the models of Menon et al. 2021). Hence, the predicted fraction of mergers during the slow Case A phase depends on, amongst other factors, the semiconvective efficiency.

Our binary models predict that in a sample of 100 observed massive Algol binaries, at least 52.5 (75% of 70% of 100 binaries) of the donors should show surface nitrogen mass fraction enhancement less than a factor of 8. On the other hand, at most 27 (90% of 30% of 100) donors can show surface nitrogen mass fraction enhancement greater than a factor of 8. If these number cut-offs ('at least 52.5' and 'at most 27') in the observed sample are largely different from our predictions, we can use this
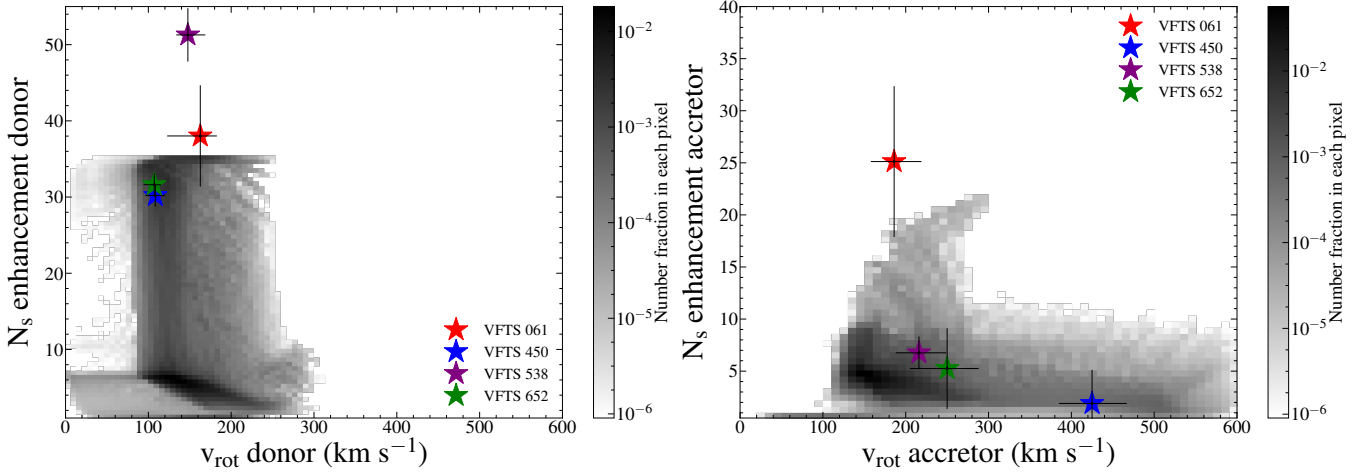
Fig. 8. Probability distribution of the surface nitrogen mass fraction enhancement vs rotational velocity of the donor (*left panel*) and accretor (*right panel*) during the semi-detached phase. The different coloured stars with error bars denote the position of the semi-detached systems of the TMBM survey (Table 3). Grey-scale: see description in Fig. 7.

as another observational constraint to constrain the efficiency of semiconvection used in stellar models, via the close massive binary evolution channel (see also Schootemeijer et al. 2019).

The small group of models below the orange lines in Fig. 7 arises from the small number of models undergoing inverse slow mass transfer (cf., Sect. 4.1). In these models, mass flows back to the original donor star from its currently more massive and less enriched companion. These binaries arise from very short period models and eventually merge via L2 overflow after a nuclear timescale inverse slow Case A mass transfer phase followed by a contact phase.

4.3. Effects of stellar rotation on nitrogen mass fraction enhancement

In single stars, the enhancement of surface nitrogen mass fraction gets higher with the increase in rotational velocity and mass of the rotating star, as internal mixing is more efficient in more massive and faster rotating stars (for a review, see Maeder & Meynet 2000). In binaries however, the donors can undergo envelope stripping which can expose layers of CNO processed material to the surface, increasing the surface abundance of nitrogen. Hence, it is essential to understand and differentiate between the contribution from internal mixing and envelope stripping to the observed surface nitrogen mass fraction enhancement in massive binaries.

Figure 8 shows the distribution of the surface nitrogen mass fraction enhancements of donor and accretor during the semi-detached phase as function of their surface rotational velocity. The surface rotational velocity of the donors is set by the orbital motion of the binaries, as their rotation is synchronised to the orbital revolution.

The shortest orbital period binaries have the highest surface rotational velocities in our grid, owing to tidal locking at short orbital periods and the fact that we initialise the initial spins of the binary components to be equal to that of the orbit. In contrast to the single star picture, the donors rotating the fastest do not show the highest surface nitrogen mass fraction enhancement because the nitrogen enhancement in these binary models is not an outcome of rotational mixing but of envelope stripping. The donors with the highest rotational velocities $(300 \, \text{km s}^{-1})$ during the semi-detached phase arise from binaries with the shortest

initial orbital period, go into a contact phase with an episode of inverse slow Case A mass transfer and eventually merge during their main sequence lifetime. It is hence likely that these models will not undergo significant envelope stripping by Case A mass transfer and do not show very high nitrogen enrichment until they merge.

Donors with surface rotational velocities between $\sim 100-250 \, \text{km s}^{-1}$ have relatively higher initial orbital periods, where the binaries survive the slow Case A mass transfer and the envelope of the donors are efficiently stripped and the surface nitrogen mass fraction enhancement reaches CNO equilibrium values towards the end of the slow Case A phase (see vertical column of increasing surface nitrogen abundance near $X \simeq 150-250 \, \text{km s}^{-1}$). We see two islands of higher probability of surface nitrogen enhancement, one at ordinate values of $\simeq 2-6$ and the other near the CNO equilibrium value for the LMC (i.e. $\simeq 35$). As already discussed, the lower enhancement peak comes from models that eventually merge during slow Case A and the high surface enhancement peak comes from models that survive the entire Case A mass transfer phase. Hence, we expect the lower enhancement to be the result of rotational mixing (see also Maeder & Meynet 2000), while the enhancement all the way up to CNO equilibrium is from envelope stripping.

Surface rotational velocities less than $90 \, \text{km s}^{-1}$ occur for a very brief time during the fast Case A mass transfer phase in our models when a large amount of mass is lost by the donor while tidal forces cannot instantaneously synchronise the rotation to the orbit. The light grey shading indicates that the amount of time spent in this region of the parameter space is very low. We also see two islands of surface nitrogen enhancement where the rotational velocity is below $90 \, \text{km s}^{-1}$. This dichotomy arises typically from low and high mass models whereby in lower mass models, the envelope is not very efficiently stripped, leading to low surface nitrogen mass fraction enhancement (cf., panel f in Fig. 2) during and just after the fast Case A phase. In higher mass models, the envelope stripping is much more efficient, owing to the larger core to envelope mass, such that the surface nitrogen enrichment becomes very high right from the fast Case A mass transfer phase.

The right panel of Fig. 8 shows the distribution of the surface nitrogen mass fraction enhancement of the accretor versus their equatorial rotation velocity. As we shall see (Fig. 9, right
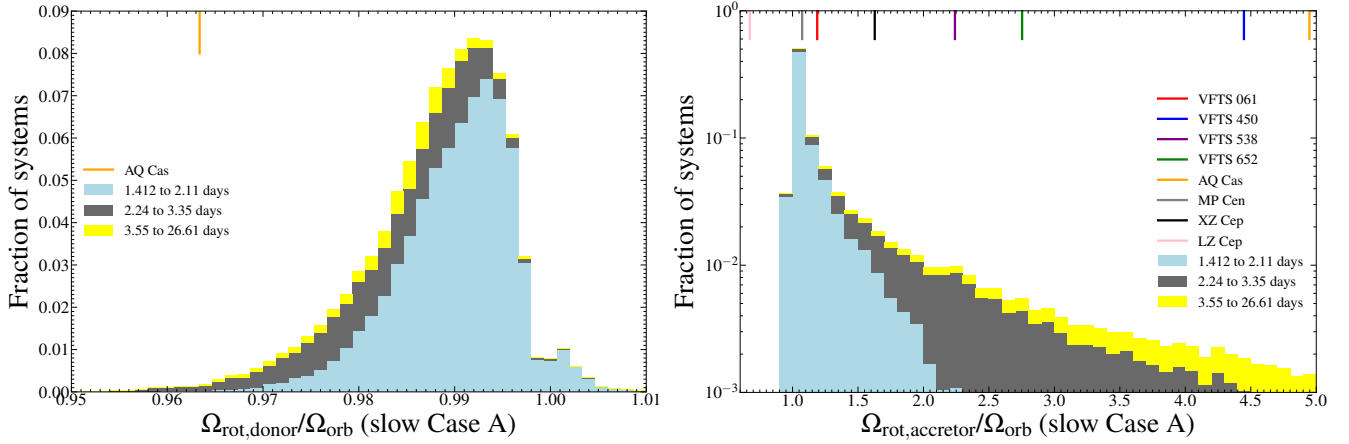
Fig. 9. Probability distribution of the ratio of spin to orbital angular velocity for the mass donor (*left panel*) and the mass accreting star (*right panel*) in our models during the semi-detached configuration, weighted by the birth probability of each system and the lifetime in the respective bin. The colour coding indicate the initial orbital period ranges indicated in the legend. The coloured vertical lines at the top of the right plot indicate the ratio of spin to orbital angular velocity of some of the observed massive Algol binaries where both parameters were found in the literature (Table 3). The *Y*-axis of the *right panel* is in log scale.

panel), most of the accretors in our grid are tidally locked during the slow Case A phase. The increase in surface rotational velocity around $200-250\,\mathrm{km\,s^{-1}}$ with the increase in surface nitrogen mass fraction enhancement from $15-22$ indicates that these accretor stars only spin up slightly, not up to critical rotation, towards the end of slow Case A mass transfer phase. These models having surface nitrogen enhancement >15 have orbital periods less than ~4 days and survive the Case A mass transfer phase. Hence, the secondaries are able to accrete the N-rich matter transferred by the donor while not spinning up all the way to critical rotation during the late stages of the slow Case A mass transfer phase.

Accretors with rotational velocities above $300\,\mathrm{km\,s^{-1}}$ are not found to be tidally locked. Hence they undergo inefficient slow Case A mass transfer (see Fig. F.2) and the surface nitrogen abundance is not as highly enhanced as for accretors that are rotating synchronously. We note that the probability fraction of accretors that are tidally synchronised is much higher than the accretors that are not tidally locked, consistent with Fig. 9 later.

4.4. Tidal synchronization

Our mass transfer efficiency depends on the extent to which tidal forces can halt the spin-up of the mass accreting star (Sect. 2). For very short period binaries, tides can be strong enough to keep the mass accreting star rotating synchronously with the orbital velocity, enabling conservative mass transfer in our model grid. The strength of tidal forces implemented in our models can be tested by comparing the degree of synchronisation of our accretors during the slow Case A mass transfer phase as a function of orbital period to the degree of synchronisation of the accretors in observed massive Algol systems.

The tidal synchronization timescale of a mass donor decreases as the star expands to fill its Roche lobe. Figure 9 (left panel) shows the distribution of the ratio between spin and orbital angular velocity of the mass-donating star during the semi-detached phase. As these stars persist to fill their Roche lobes during this phase, we see that all our donors are effectively rotating fully synchronised during the entire semi-detached phase.

The right panel of Fig. 9 shows the distribution of the degree of synchronization of the mass accreting star during the semi-

detached phase. We see that most of the mass accreting stars are rotating synchronously since the biggest contribution to the semi-detached phase comes from short period models where tidal interaction is strong. For higher orbital periods where tidal synchronization is inefficient, the accretors rotate super-synchronously. As expected, the degree of super-synchronicity is higher for longer orbital periods.

4.5. Orbital period derivatives

The orbital period derivative helps us assess the degree to which mass and angular momentum are lost from the binary and thus determine the efficiency of mass transfer in the binary system. Figure 10 shows the distribution of the orbital period and its time derivative during the slow Case A mass transfer phase. The period derivative value is very tightly constrained between $0.004-0.03\,\mathrm{s/year}$. This value of the orbital period derivative is related to the mass and angular momentum lost from the binary and the mass transfer efficiency during the slow Case A phase. We have seen that the mass transfer efficiency during the slow Case A phase in our models is largely conservative (Fig. 3).

The orbital period and its derivative if the entire Case A mass transfer was modelled as purely conservative or purely non-conservative with isotropic re-emission from the surface of the accretor can be analytically derived (Eqs. (29) or (30) of Quast et al. 2019, respectively), with deviations coming from the mass and angular momentum lost due to stellar winds. Both the orbital period and its derivative is higher for the case of totally conservative mass transfer (yellow dots) or totally non-conservative mass transfer with isotropic re-emission (orange dots) than our models.

We note that we implement non-conservative mass transfer in our models as an increase in wind mass loss rather than isotropic re-emission from the accretor (cf., Eqs. (14) and (15) of Quast et al. 2019). As such, the orbital period in our models do not increase to the same extent as for the case of isotropic re-emission from the accretor. Comparing Eqs. (29) and (30) of Quast et al. (2019) we can see that the orbital period derivative for the case of non-conservative mass transfer via isotropic re-emission becomes positive before the mass ratio is inverted and is higher than for the conservative case, as is seen in Fig. 10.
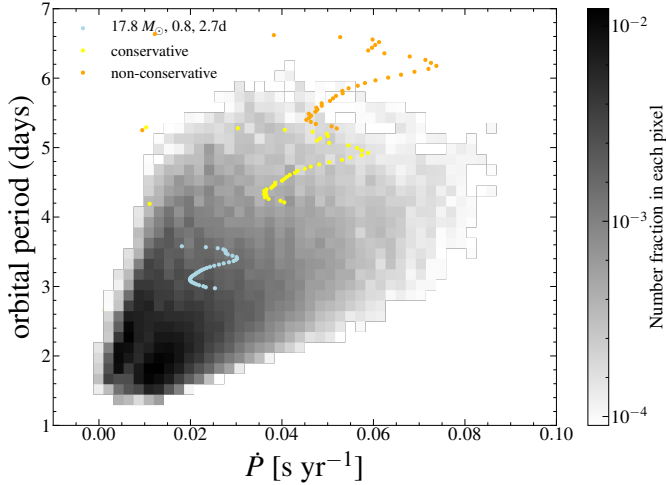
Fig. 10. Probability distribution of the orbital period and its derivative that is predicted to be observed in the semi-detached configuration of the Case A mass transfer phase based on the model grid. The lightblue coloured dots show the evolution of the orbital period and its derivative during the semi-detached phase for our example model in Fig. 2. The yellow and orange dots show the evolution for the same model if the mass transfer phase was modelled as totally conservative (Eq. (5)) or totally non-conservative with the mass lost via isotropic re-emission (Eq. (29) of Quast et al. 2019), respectively. The dots are placed at intervals of 50 000 years with the first dots of each colour having the lowest orbital period. Grey-scale: See description in Fig. 7.

Hence, one can expect to test the mass transfer efficiency during the slow Case A phase and the implementation of non-conservative mass transfer for the overall Case A mass transfer phase in our models from measurements of the orbital period derivative of observed Algol systems over a few years. We note that the orbital period measurements are more constrained (Mahy et al. 2020a) than the values of orbital period derivatives we find during the semi-detached phase. For the mass dependence of this orbital period derivative during the slow Case A phase, see Fig. E.1.

5. Binary properties after Case AB mass transfer

After the slow Case A mass transfer, which is terminated by core hydrogen exhaustion of the donor star (Fig. 2), the donor star's envelope still contains several solar masses of hydrogen-rich matter (Fig. F.5). The contracting helium core therefore leads to an envelope expansion, which initiates another thermal timescale mass transfer phase, named Case AB. We find that 99.2% of the models that survive the slow Case A mass transfer also survive the Case AB mass transfer.

While this paper focusses on the semi-detached phase of evolution, we also briefly discuss the properties of our binary models after the Case AB mass transfer here. At this stage, they consist of a main sequence star with a stripped-envelope star as companion. Observations of such binaries are difficult, since the stripped star is very hot and hard to detect next to the brighter OB companion (Wellstein et al. 2001; Schootemeijer et al. 2018; Götberg et al. 2020; Wang et al. 2021). Only for the most massive systems in our model grid, it is expected that the stripped stars develop an optically thick wind and appear as Wolf-Rayet stars. According to Pauli et al. (in prep.), who analyse the WR+O star phase for a model grid with primary masses of up to $\sim$90 $M_{\odot}$, this occurs for primary masses above $\sim$28 $M_{\odot}$ (see also, Shenar et al. 2020) at the metallicity of the LMC. In the following, we

do not distinguish stripped stars with and without optically thick winds.

In our models, no mass transfer occurs during core helium burning and hence their orbital period and mass ratio does not change significantly throughout the core helium burning phase of the mass donor (cf., Fig. 2, panels b and g). The orbital period increases slightly due to wind mass-loss while the mass ratio change remains small. Also, the surface properties of the individual binary components undergo only moderate changes. For our analysis, we sample the properties of our post Case AB models at a time when the core helium mass fraction of the mass donor (the stripped star) has decreased to 0.90 due to helium burning (except for Fig. G.1).

Figure 11 (top left panel) shows the orbital period and mass ratio distribution of our models after the Case AB mass transfer phase. Due to the additional mass transfer, the mass ratios of our post Case AB models are larger than during the slow Case A phase (cf., Fig. 5), with values up to $q = 5$. Since during Case AB, mass flows from a less massive to a more massive star (see panel h of Fig. 2), the orbital period also increases significantly compared to models in the slow Case A phase, to values of $\sim$15 days and more. At the same time, since the Case AB mass transfer in our models is highly non-conservative (cf., Fig. F.5), orbital periods and mass ratios in our models remain significantly smaller than in fully conservative models (e.g. Wellstein et al. 2001).

The top right panel of Fig. 11 displays the distribution of the surface helium mass fraction and stellar mass of our mass gainers. A comparison with Fig. 7 shows that the helium mass fraction is increased by a few percent compared to the semi-detached phase. Still, most mass gainers contain only a mild surface helium enrichment. However, more massive mass gainers tend to be more helium enriched, although there is a large spread for every considered mass. This is so because during core hydrogen burning, more massive stars have larger convective core mass fractions.

The surface helium mass fraction of the donors at the considered time is $0.70-0.90$, and is most drastically reduced for the most massive systems, in which the donors become Wolf-Rayet stars (cf., Pauli et al., in prep.). Figure 11 (bottom left panel) shows the distribution of remaining hydrogen mass in the post Case AB mass donors, as function of their mass. We compute the remaining hydrogen mass ($M_{\rm H}$) in the donor as $M_{\rm H} = \int_0^M X(m)\,{\rm d}m$. At most $\sim$0.4 $M_{\odot}$ of hydrogen remains in any of our models. We see the overall trend that the remaining hydrogen mass increases with the donor mass (see also, Yoon et al. 2017). The wind stripping during the core helium burning phase of the mass donor is illustrated by Fig. G.1. A comparison with Fig. 11 shows that many of the most massive donors manage to lose all their hydrogen, whereas some hydrogen remains in all donors below $\sim$12 $M_{\odot}$.

After Case AB mass transfer, many of the mass gainers may observationally appear as single stars because the high mass ratios and longer orbital periods make binary detection more elusive). Hence, it is interesting to consider the distribution of their surface nitrogen mass fraction enhancements and rotational velocities (Fig. 11, bottom right panel). The surface nitrogen mass fraction enhancement is higher then it was in the Algol phase (cf., Fig. 8), but far from its CNO equilibrium value of $\sim$35. Whereas the matter that is transferred during Case AB does contain CNO equilibrium abundances, the mass transfer efficiency is low (cf., Fig. 3), and thermohaline mixing dilutes the small amounts of accreted matter in the massive envelope of the accretor.
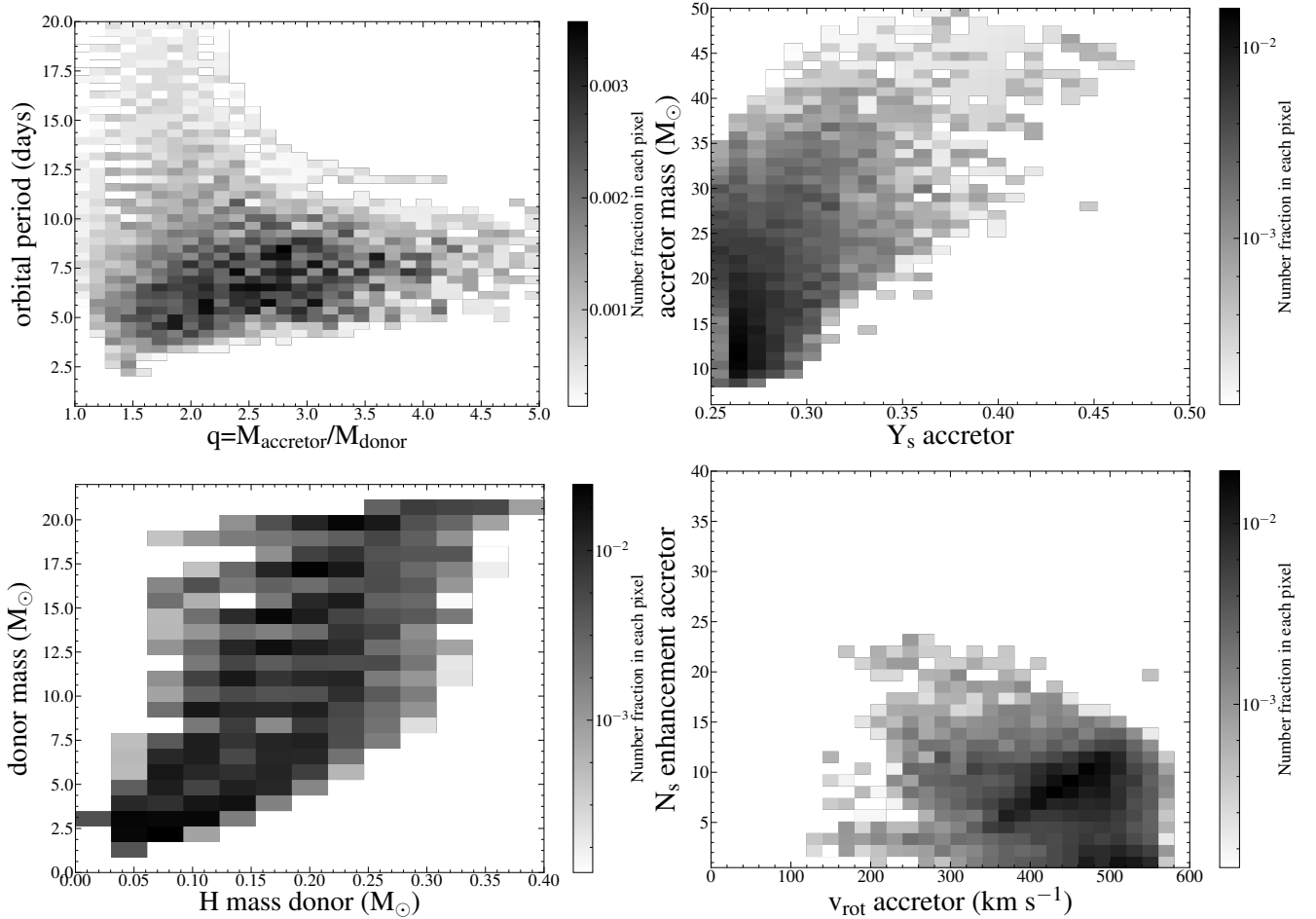
Fig. 11. Probability density distribution of several properties of our binary models after Case AB mass transfer, when the central helium mass fraction of the donor has decreased to 0.90: orbital period versus mass ratio (*top left*), surface helium abundance and mass of the mass gainer (*top right*), leftover hydrogen mass in the donor and donor mass (*bottom left*), and surface nitrogen mass fraction enhancement versus rotational velocity of the mass gainer (*bottom right*).

Compared to the semi-detached phase (Fig. 8), where most of the mass accretors are tidally locked, Fig. 11 shows that the Case AB mass transfer spins them up considerably. This is so because the orbital periods increase rapidly during the Case AB phase, rendering tidal braking inefficient in most cases. However, whereas many of our accretor models end Case AB mass transfer very close to critical rotation, tides remain strong enough to spin down most of our models over their core helium burning evolution (see Fig. G.1). For our most massive models, stellar winds also help to spin down the accretors. Therefore, our models provide only a small contribution to the overall population of Be stars, in particular compared to massive binary models undergoing mass transfer after core hydrogen burning (Case B, e.g. see Wang et al. 2020). We also note that the parameter space for Case A mass transfer is smaller than that for Case B mass transfer (Fig. 2 of Langer et al. 2020).

6. Comparison with observations

6.1. Observed Algol binaries in the LMC

The Tarantula Massive Binary Monitoring (TMBM) survey (Almeida et al. 2017; Mahy et al. 2020a,b) investigated ~100 massive binaries in the Tarantula region of the LMC. Mahy et al. (2020a,b) classified six of them as semi-detached. From those, we find four to be in the Algol configuration, where the less

massive star transfers mass to its more massive companion, and shows surface helium and nitrogen enrichment.

The other two systems (VFTS 176 and VFTS 094) have their more massive stars filling its Roche lobe, and are therefore not in the Algol configuration. Furthermore, none of the components shows any surface enrichment. Both systems have a very short orbital period (1.77 days and 2.25 days, respectively). It appears plausible that VFTS 176 and VFTS 094 evolved previously through a thermal timescale contact phase and are currently undergoing inverse nuclear timescale slow Case A mass transfer (see discussion in Sect. 4.1 for VFTS 176 and 'System 2' type evolution of contact binaries in Menon et al. 2021 for VFTS 094). Due to the lack of a concrete understanding of the current evolutionary stage of these two systems, we left these two systems out of our comparison with the predictions obtained from the model grid of binary models for the Algol phase. We list the observed properties of the classical TMBM Algol systems in Table 1, along with those of three massive Algols in the LMC described in the literature.

6.2. Observed Algol binaries in the Milky Way

In order to enhance the statistical basis of the comparison of our models with observations, we also consider observed Galactic massive Algol systems. We do this despite the metallicity difference between Milky Way and LMC, because the physics of mass

Table 1. Semi-detached double-lined eclipsing binaries observed in the LMC with at least one component having a mass greater than $8\,M_\odot$.

Name (colour in plots)	Period (d)	M_a ($M_\odot$)	M_d ($M_\odot$)	q	R_a ($R_\odot$)	R_d ($R_\odot$)	T_a (kK)	T_d (kK)	References (#)
VFTS 061 (red)	2.33	16.3 ± 1.4	8.7 ± 0.6	1.87	7.2 ± 0.2	7.30 ± 0.3	33.5 ± 0.9	32.9 ± 0.7	[1]
VFTS 652 (green)	8.59	18.1 ± 3.9	6.5 ± 1.1	2.78	15.4 ± 0.7	16.8 ± 0.7	32.1 ± 0.9	23.9 ± 0.5	[1]
VFTS 538 (purple)	4.15	18.3 ± 1.9	11.8 ± 1.4	1.55	7.9 ± 0.6	14.7 ± 1.0	35.6 ± 1.7	32.0 ± 0.3	[2]
HV 2543 (yellow)	4.83	25.6 ± 0.7	15.6 ± 1.0	1.64	15.5 ± 0.4	14.0 ± 0.4	35.3 ± 0.6	28.7 ± 0.5	[3]
VFTS 450 (blue)	6.89	29.0 ± 4.1	27.8 ± 3.9	1.04	13.0 ± 3.0	22.2 ± 0.4	33.8 ± 2.3	28.3 ± 0.3	[1]
SC1-105 (black)	4.25	30.9 ± 1.0	13.0 ± 0.7	2.37	15.1 ± 0.2	11.9 ± 0.2	35.0 ± 2.5	32.5 ± 2.5	[4]
HV 2241 (cyan)	4.34	36.2 ± 0.7	18.4 ± 0.7	1.96	14.9 ± 0.4	13.7 ± 0.4	38.4 ± 1.4	29.5 ± 1.2	[5]

Notes. Subscripts 'a' and 'd' denote the accretor and donor star respectively. The systems are ordered by increasing mass of the mass gainer.
References. (1) Mahy et al. (2020a), (2) Almeida et al. (2017), Mahy et al. (2020b), (3) Ostrov et al. (2000), (4) Bonanos (2009), (5) Ostrov et al. (2001).

transfer has no known direct metallicity dependence. However, we caution that an indirect impact of metallicity is possible, due to three effects. Firstly, stars of higher metallicity are slightly less compact (Brott et al. 2011a), such that longer orbital period binaries can contribute to the semi-detached phase at higher metallicity. Secondly, stellar winds are stronger in the Milky Way compared to the LMC (Mokiem et al. 2007), which may be relevant in particular for the most massive binaries discussed here. And thirdly, the most massive stars in our samples may be sufficiently close to the Eddington limit that envelope inflation may occur (Sanyal et al. 2015, 2017). While the first effect remains at the level of ~10% (Brott et al. 2011b), the other two effects may be larger, especially for the most massive binaries discussed here. No metallicity dependence in the orbital period-mass ratio distribution of massive contact binaries has been predicted by Menon et al. (2021) between the LMC and SMC, although they expect envelope inflation to play a role in explaining some of the observed long period (≥ 5 d) massive contact binaries in the Milky Way.

Malkov (2020) performed a comprehensive literature survey of semi-detached double line eclipsing binaries in the Milky Way. He listed 119 semi-detached systems, of which 32 have at least one component with a stellar mass above $8\,M_\odot$ (Table 2). Investigation into the individual systems (see systems with footnotes in Table 2) reveals that GT Cep is in triple system, RZ Sct and BY Cru have an accretion disc that makes accurate determination of their masses very challenging, the mass ratio of TU Mon is highly debated in the literature, V453 Cyg is now considered as a detached system, V729 Cyg is a potential contact system and BY Cru shows evidence of very heavy interactions and contain an F type supergiant donor. As such, we do not include these six systems in our analysis. These systems will be very interesting for follow-up observations.

For four galactic Algol systems, an estimate of the projected rotational velocities of the component stars and for the orbital inclination was available in the literature. We list their parameters, together with those of the four classical TMBM Algols, in Table 3. We assume that the inclination of the orbital plane is the same as the inclination of the stellar spin axes. As such, we calculate the rotational velocity of the binary components from the projected rotational velocity and the orbital inclination (see Fig. 8). The orbital inclinations for the Algol binaries are taken from the references given in Table 2.

6.3. The number of semi-detached binaries in the LMC

To compare the expected number of semi-detached binaries from our grid of binary models with observations, we note that the

Tarantula Massive Binary Monitoring (TMBM) survey (Almeida et al. 2017; Mahy et al. 2020a,b) has observations of 102 O type massive binary candidates with orbital periods in the range $1-1000$ days. The TMBM sample was based on binary detections in the Very Large Telescope Flames Tarantula survey (Evans et al. 2011). Sana et al. (2013) showed that the binary detection probability is a function of the orbital period. It goes from 95% at 2 d to 87% at 10 d to 70% at 100 d to 25% at 1000 d. It is however beyond the scope of this paper to find this in our analysis. Hence, we consider all models in our grid that have initial orbital periods of less than 1000 days. This includes many models that do not undergo Case A mass transfer. To filter out the semi-detached models, we only consider those in which mass transfer during core hydrogen burning lasts for more than three times the thermal timescale of the mass donor (calculated at the onset of mass transfer). This way we find that 16% of all models with orbital periods less than 1000 d to undergo nuclear timescale Case A mass transfer.

We then find the sum of the weighted duration of the Case A mass transfer phase relative to the main sequence lifetime for each model as

$$F2 = \frac{\sum_{m=1}^{N_g} \tau_{\text{Case A}} W_m}{\sum_{m=1}^{N_g} \tau_{\text{MS}} W_m}, \qquad (9)$$

where τ_{MS} is as defined for Eq. (8) (cf., Sect. 3.3 and Fig. 4), N_g is the number of models in the grid with initial orbital periods below 1000 days, and W_m represents the birth probability of each system according to Eq. (3). We find that $F2 \simeq 0.03$, which implies that we expect 3 out of every 100 main sequence binaries originating from initial donor masses between $10-40\,M_\odot$ and orbital periods of $1.41-1000$ days to be observed in the slow Case A mass transfer phase. This is in good agreement with the VFTS-TMBM survey, where we find four binaries to be in the Algol configuration amongst the 102 observed binaries.

Table 4 gives the contribution from each initial donor mass in our grid to the total of 3% (2nd column), in comparison to the expected contribution if it would simply scale with the Salpeter IMF (3rd column). It shows that while more massive systems contribute less to the total synthetic Algol population than less massive ones, their contribution is larger than expected according to the IMF, with $40\,M_\odot$ binaries contributing three times as much. This estimate needs to be amended by the fact that $10\,M_\odot$ stars live about five times longer than $40\,M_\odot$ stars, which implies a ~15 times larger contribution of our most massive systems than naively expected. It reflects the fact that, for a given initial

Table 2. Semi-detached double-lined eclipsing binaries observed in the Galaxy with at least one component exceeding 8 $M_\odot$.

Name	Period (d)	M_a ($M_\odot$)	M_d ($M_\odot$)	q	R_a ($R_\odot$)	R_d ($R_\odot$)	T_a (kK)	T_d (kK)	References (#)
TT Aur	1.33	8.10	5.40	1.50	3.90	4.20	24.8	18.2	[1]
μ_1 Sco	1.44	8.30 ± 1.00	4.60 ± 1.00	1.80	3.90 ± 0.30	4.60 ± 0.40	24.0 ± 1.0	17.0 ± 0.7	[2]
SV Gem	4.00	8.34	3.37	2.47	4.87	6.70			[3]
V454 Cyg	2.31	8.40	2.86	2.93	4.99	4.64			[1]
BF Cen	3.69	8.70	3.80	2.29	5.10	7.10	12.9	9.4	[1]
BM Ori	6.47	9.50	3.51	2.70	4.47	8.94			[3]
IZ Per	3.68	9.97 ± 0.55	3.20 ± 0.17	3.11	7.51 ± 0.13	6.90 ± 0.12	19.0 ± 0.5	9.5 ± 0.5	[4]
AI Cru	1.41	10.30 ± 0.20	6.30 ± 0.10	1.63	4.95 ± 0.06	4.43 ± 0.05	24.2 ± 0.5	17.7 ± 0.5	[5]
SX Aur	1.21	10.30 ± 0.40	5.60 ± 0.30	1.84	5.17 ± 0.09	3.90 ± 0.07			[3]
MP Cen	2.99	11.40 ± 0.40	4.40 ± 0.20	2.59	7.70 ± 0.10	6.60 ± 0.10	18.7 ± 0.4	12.4 ± 0.1	[6]
IU Aur	1.81	11.99 ± 0.08	6.07 ± 0.04	1.97	6.30 ± 0.20	5.20 ± 0.20	33.3 ± 0.1	28.8 ± 0.2	[7]
V356 Sgr	8.89	12.10	4.70	2.57	7.40	14.00	19.1	8.8	[1]
V Pup [a]	1.45	12.85 ± 0.50	6.33 ± 0.30	2.03	5.48 ± 0.18	4.59 ± 0.06	28.2 ± 1.0	26.6 ± 1.0	[8]
V498 Cyg	3.48	13.44	6.45	2.08	6.81	8.12			[1]
GN Car	4.34	13.49	4.59	2.94	7.14	8.29			[1]
LZ Cep	3.07	16.00 ± 9.80	6.50 ± 2.40	2.46	11.70 ± 3.30	9.40 ± 2.60	32.0 ± 1.0	28.0 ± 1.0	[9]
δ Pic	1.67	16.30	8.60	1.89	7.62	5.05	25.2	21.4	[10]
XX Cas	3.06	16.85	6.07	2.77	8.28	7.19			[1]
HH Car	3.23	17.00	14.00	1.21	6.10	10.70	35.5	29.9	[1]
V337 Aql	2.73	17.44 ± 0.31	7.83 ± 0.18	2.22	9.86 ± 0.06	7.48 ± 0.04	28.0 ± 0.5	23.6 ± 0.5	[11]
AQ Cas	11.70	17.63 ± 0.91	12.50 ± 0.81	1.41	13.40 ± 0.64	23.50 ± 0.73	27.0 ± 1.0	16.7 ± 0.4	[12]
XZ Cep	5.09	18.70 ± 1.30	9.30 ± 0.50	2.01	14.20 ± 0.10	14.20 ± 0.10	28.0 ± 1.0	24.0 ± 3.0	[13]
29 CMa [b]	4.39	19.00	16.00	1.20	10.00	13.00	29.0	33.7	[14]
AB Cru	3.41	19.75 ± 1.04	6.95 ± 0.65	2.84	10.50 ± 0.32	8.85 ± 0.32	35.8	27.2	[15]
V448 Cyg	6.51	24.70 ± 0.70	13.70 ± 0.70	1.80	7.80 ± 0.20	16.30 ± 0.30	30.5 ± 0.1	20.3 ± 0.1	[16]
QZ Car [c]	5.99	30.00 ± 3.00	20.00 ± 3.00	1.50	10.00 ± 0.50	20.00 ± 1.00	36.0	30.0	[17]
*GT Cep [d]	4.90	10.70 ± 0.50	2.58 ± 0.14	4.14	6.34 ± 0.19	6.98 ± 0.11	22.4 ± 1.0	10.9 ± 0.3	[18]
*RZ Sct [e]	15.20	11.70	2.49	4.68	15.00	15.90	19.0	6.5	[1]
*TU Mon [f]	5.04	12.00	2.50	4.80	5.50	7.20	19.0	8.1	[1]
*V453 Cyg [g]	3.89	14.36 ± 0.20	11.10 ± 0.13	1.29	8.55 ± 0.06	5.49 ± 0.06	26.6 ± 0.5	25.5 ± 0.8	[1]
*V729 Cyg [h]	6.60	36.00 ± 3.00	10.00 ± 1.00	3.60	27.00 ± 1.00	15.00 ± 0.60			[19]
*BY Cru [i]	106.40	9−11	1.80	5.30					[20]

Notes. Subscripts 'a' and 'd' refer to the mass accretor and mass donor, respectively. The list is adopted from the work of Malkov (2020) and Surkova & Svechnikov (2004). Systems without effective temperature estimates have only photometric orbit solutions and mass estimates. Comments on individual systems marked with superscripts: [a]Masses and radii taken from Budding et al. (2021). [b]May be a contact system (Mahy et al., in prep.). [c]Is a part of SB2+SB2 system, see Morrison & Conti (1979), Blackford et al. (2020). [d]Possibly a triple system, see discussion in text. [e]The more massive star is rapidly rotating and has an accretion disc. See Wilson et al. (1985). [f]Debate about the mass ratio of this system exists in the literature. See the discussion in Cester et al. (1977). [g]Recent studies now consider this as a detached system. See Southworth et al. (2004). [h]A potential contact system (Yaşarsoy & Yakut 2014) and a part of a hierarchical triple system (Rauw et al. 2019). [i]A highly interacting binary with an F type supergiant donor, with the accretor invisible due to an accretion disc around it. The long orbital period suggests it may be undergoing thermal timescale Case AB or Case B mass transfer. As such, we do not compare our model predictions with six (d,e,f,g,h,i) observed systems marked with an asterisk.

References. (1) Surkova & Svechnikov (2004), (2) Budding et al. (2015), (3) Budding et al. (2004), (4) Hilditch et al. (2007), (5) Bell et al. (1987), (6) Terrell et al. (2005), (7) Surina & Kang (2009), (8) Stickland et al. (1998), (9) Mahy et al. (2011), (10) Evans (1974), (11) Tüysüz et al. (2014), (12) Ibanoglu et al. (2013), (13) Martins et al. (2017), (14) Bagnuolo et al. (1994), (15) Lorenz et al. (1994), (16) Djurašević et al. (2009), (17) Walker et al. (2017), (18) Çakırlı (2015), (19) Rauw et al. (1999), (20) Daems & Waelkens (1997).

primary mass, the period and mass ratio range of surviving Case A binary models is much larger for larger initial primary mass, as can be seen when comparing the blue coloured areas in the upper and lower panels of Fig. F.1.

About 25% of all massive stars in the LMC are associated with the Tarantula region, with the estimated number of O-type stars being 570 (Doran et al. 2013; Crowther 2019). Extrapolating, we expect about 2000 O-type stars in the LMC. This accounts for a total of ~1000 O-type star binaries in the LMC, assuming a binary fraction of 50% (Sana et al. 2013). We found in our model grid that 3% of all massive main sequence binaries are in the semi-detached phase. Therefore, we expect around 30 binaries that contain an O-type star in the semi-detached phase in the LMC, from our binary parameter space.

At the same time, in our parameter space, the ratio of models expected to be observed in the contact phase to the semi-detached phase is ~1/19 (see discussion of Fig. 5). This implies that we expect ~1.6 O-type contact binaries in the LMC originating from our initial parameter space. However, our initial orbital period range does not cover the shortest period contact systems, which have the longest contact lifetimes (Menon et al. 2021). Therefore, our number is smaller than the result of

Table 3. Orbital velocities, rotational velocities, and luminosities of the semi-detached double-lined eclipsing binaries, whenever available.

Name	Period (d)	$v_{rot,a} \sin i$ (km s^{-1})	$v_{rot,d} \sin i$ (km s^{-1})	$\Omega_{rot,a}/\Omega_{orb}$	$\Omega_{rot,d}/\Omega_{orb}$	$\log L_a$ ($L_\odot$)	$\log L_d$ ($L_\odot$)	Inclination i (deg)
VFTS 061	2.33	174^{+33}_{-28}	152^{+20}_{-40}	1.18	1.02	4.77 ± 0.04	4.75 ± 0.05	$69.1^{+0.9}_{-0.9}$
MP Cen	2.99	140^{+12}_{-12}	95^{+15}_{-15}	1.07	0.85	3.80 ± 0.20	3.00 ± 0.20	$82.2^{+0.2}_{-0.2}$
LZ Cep	3.07	130^{+10}_{-10}	80^{+10}_{-10}	0.67	0.51	5.11 ± 0.19	4.69 ± 0.19	$48.1^{+2.0}_{-0.7}$
VFTS 538	4.15	158^{+28}_{-33}	108^{+14}_{-21}	2.24	0.82	4.96 ± 0.08	5.31 ± 0.06	$47.0^{+5.0}_{-5.0}$
XZ Cep	5.09	230^{+15}_{-15}	110^{+12}_{-12}	1.62	0.78	5.05 ± 0.06	4.79 ± 0.22	$80.0^{+2.0}_{-2.0}$
VFTS 450	6.89	380^{+42}_{-40}	97^{+12}_{-12}	4.44	0.66	5.30 ± 0.21	5.46 ± 0.04	$63.5^{+1.7}_{-1.2}$
VFTS 652	8.59	224^{+38}_{-45}	96^{+10}_{-13}	2.75	1.08	5.35 ± 0.06	4.92 ± 0.06	$63.7^{+0.9}_{-4.8}$
AQ Cas	11.70	287^{+10}_{-10}	98^{+11}_{-11}	4.94	0.96	4.94 ± 0.08	4.59 ± 0.05	$84.4^{+4.0}_{-4.0}$

Notes. The references to each individual system are the same as in Tables 1 and 2. The subscript 'a' denotes the accreting star and 'd' denotes the Roche lobe filling mass donating star.

Table 4. Contribution from models at each initial donor mass ($M_{d,i}$) to the total percentage (3%) of all massive main sequence binaries that is predicted to be found in the semi-detached configuration.

$M_{d,i}$ ($M_\odot$)	Fraction (%)	IMF (%)	Relative excess
10.0	0.33	0.33	1.0
11.2	0.31	0.28	1.1
12.6	0.29	0.24	1.2
14.1	0.27	0.20	1.3
15.8	0.26	0.18	1.4
17.8	0.26	0.15	1.7
19.9	0.24	0.13	1.8
22.4	0.21	0.11	1.9
25.1	0.20	0.09	2.2
28.2	0.18	0.08	2.3
31.6	0.17	0.07	2.4
35.5	0.16	0.06	2.7
39.8	0.15	0.05	3.0

Notes. The third column gives the relative IMF weights for the initial donor masses, normalised to 0.33% for $10\,M_\odot$. The last column gives the relative excess (Col. 2/Col. 3) of binaries predicted in the semi-detached configuration relative to the case where the contribution from the different masses would simply scale with the Salpeter IMF.

Menon et al. (2021), who, based on their evolutionary grids of contact binary models, and for a binary fraction of 50%, predict ~8 O-type contact binaries in the LMC. B stars above ~$10\,M_\odot$ live roughly twice as long as average O stars, and accounting for a Salpeter initial mass function, we expect about 60 Algol binaries and 3 contact binaries amongst the ~4000 B stars above $10\,M_\odot$ in the LMC.

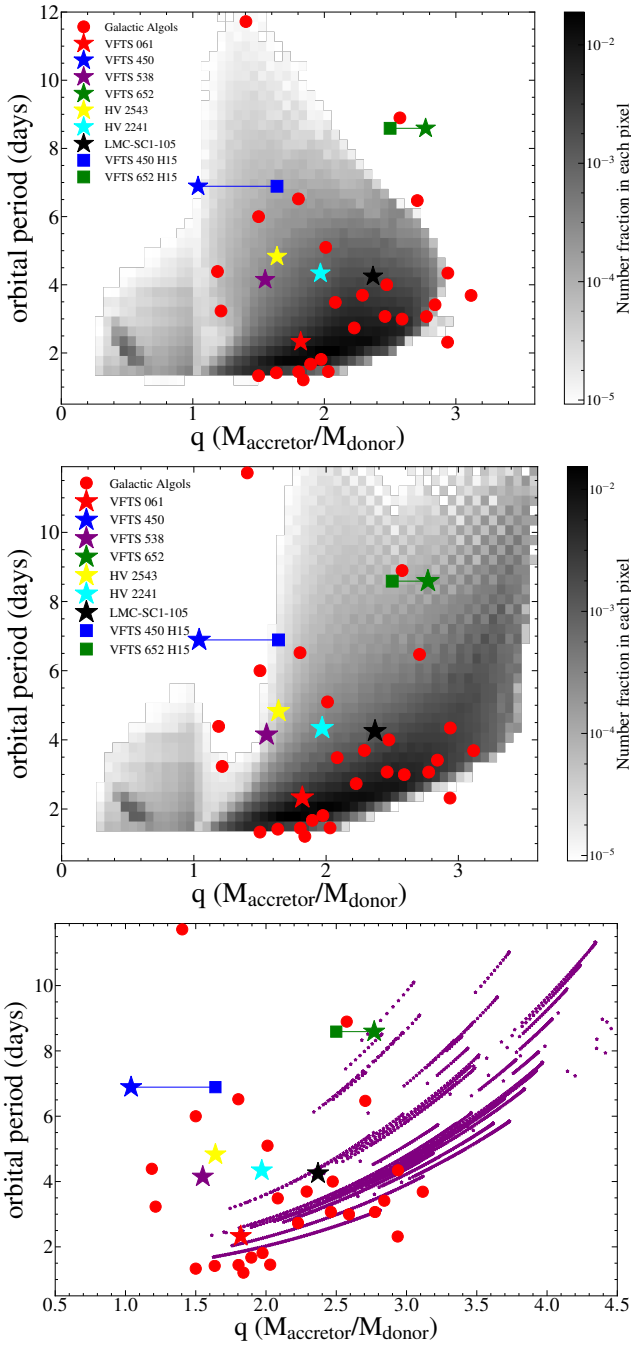## 6.4. Orbital periods and mass ratios

Figure 5 compares the observed orbital periods of the semi-detached binaries with the predicted period distribution. Whereas observed and predicted period ranges agree well, there are more system observed at larger period than expected from the theoretical distribution, in particular in the LMC sample. We note however that, while the distribution in Fig. 5 is dominated by the lower mass systems due to the steepness of the IMF, the observed Algol binaries in the LMC are very massive (see Fig. 6), and the predicted orbital period distributions stretch

to significantly larger values for higher masses (Fig. C.1). On the other hand, we find the peak of the distribution of the Galactic Algol systems to be in good agreement, but again have more high period systems than predicted. While the significance of this mismatch remains unclear due to the unknown observational biases, we find one systems in the LMC (VFTS 652) and two in the Galaxy (V356 Sgr and BM Ori) each with orbital periods above 8 d but with accretor masses below $20\,M_\odot$. Concerning the mass ratios, we find a reasonable match with most of the observed semi-detached binaries in the LMC and the Galaxy (Fig. 5). There is one systems (IZ Per) with a mass ratio above 3 that is not explained by our model grid.

Figure 12 (top panel) shows the probability distribution of the predicted orbital period and mass ratio of our Algol models simultaneously. We also estimate the distribution of Algol binaries from our models in the $P-q$-plane if, in retrospect, mass transfer had been assumed to be fully conservative (cf., Sect. 3.1; middle panel), and in the conservative models (of Wellstein et al. 2001, bottom panel). For our *pseudo* conservative approximation (middle panel), we assume that the binary will merge during Case A mass transfer if the mass transfer rate from the donor is greater than the mass divided by the thermal timescale of the accretor ($M_{acc}/\tau_{KH,acc}$).

We see that in all the three panels, there is a sharp borderline leading to an absence of predicted high mass ratio models at the shortest orbital periods. This occurs since the shortest-period models in our grid are nearly conservative, and the retained mass and angular momentum during the mass transfer leads to a simultaneous increase of mass ratio and orbital period. Figure 12 shows further that for orbital periods above ~4 d, our models predict a confinement of Algols to smaller mass ratios for larger periods (top panel). This occurs due to the fact that tides becomes weaker for larger periods, which leads to a smaller mass transfer efficiency (cf., Sect. 3). In the conservative case (middle and lower panel of Fig. 12), the opposite trend is seen.

We note that our *pseudo* conservative approximation predicts a maximum mass ratio of ~3.6 while the maximum mass ratio from self-consistent conservative models can go above 4. This is primarily because the conservative models of (Wellstein et al. 2001) do not include overshooting while our models do. This leads to the availability of a larger envelope mass of the donor that can be transferred to the accretor in the self-consistent conservative models and a lighter stripped donor star. This leads to a higher mass ratio for the self-consistent models towards the end of the slow Case A mass transfer.

Fig. 12. *Top panel*: probability distribution of orbital periods and mass ratios of our synthetic population of semi-detached binaries. For the grey scale, see description in Fig. 7. *Middle panel*: as the top panel, but with the retrospect assumption of fully conservative mass transfer (see text). *Bottom panel*: evolution of orbital period versus mass ratio during the semi-detached phase of the 41 conservative Case A models of Wellstein et al. (2001), with primary masses of 12 $M_\odot$, 16 $M_\odot$ and 25 $M_\odot$ is marked by small purple stars. The small purple stars are placed with a time difference of 50 000 yr. In all three plots, the different coloured star symbols denote the position of the semi-detached systems in the LMC (Table 1), and squares denote the binary parameters of VFTS 450 and 652 derived by Howarth et al. (2015). The colour coding is as in Fig. 5. Red circles denote the parameters for the Galactic Algol systems.

In a large unbiased observational sample, we expect to find ~90% of the semi-detached systems in the LMC in the orbital period range 1.5−5 d and with mass ratios between one and three. About 75% of the observed Algol binaries do fall into

these ranges. Of the remaining ones, we find four Galactic systems just below our short period cut-off of 1.4 d, which may have undergone a short-lived contact phase (Menon et al. 2021). However, while this means that the bulk of the observed systems are well reproduced by our models (top panel), we see that this is also true for the conservative models (middle panel).

A preference between the two sampled mass transfer efficiency assumptions must be based on those Algol systems which are outliers. Of these, V454 Cyg (P, q = 2.3 d,2.93) is missed in both cases. However, a handful of systems at the high mass ratio side, in particular IZ Per (P, q = 3.7 d,3.11), V356 Sgr (P, q = 8.9 d,2.57), and VFTS 652 (P, q = 8.6 d,2.78) are missed by our calculations but are well covered by the conservative models. On the other hand, several low-q systems are better reproduced by our non-conservative models, such as HH Car (3.2 d,1.21), 29 CMa (4.39 d,1.20), QZ Car (6.0 d,1.50), VFTS 450 (6.9 d,1.04), and AQ Cas (11.7 d,1.41).

An obvious cure to these discrepancies would be to assume that mass transfer is more efficient in the first group (at high mass ratio), while retaining the low mass transfer efficiency otherwise. Notably, recovering HH Car and VFTS 450 needs a very non-conservative evolution. We note that while one could tune the mass transfer efficiency directly in binary model calculations, assuming more efficient tidal coupling would likely serve the same purpose in our models, as it would diminish the spin-up of the accretor and thus allow for more accretion.

Recently, Justesen & Albrecht (2021) found evidence for a higher efficiency of tidal circularization in binaries with temperatures between 6250 K and 10 000 K. A higher efficiency of tidal coupling in the 4−10 d orbital period range than implemented in our models would lead to a higher mass transfer efficiency in this orbital period range, which could help reproduce the high mass ratio outliers in Fig. 12 (top panel).

We note from Fig. F.2 that the transition from conservative to non-conservative mass transfer in our Case A models is a function of all three initial binary parameters, the donor mass, orbital period and mass ratio. The self-consistently generated boundary line between conservative and non-conservative mass transfer is also different for different phases of the mass transfer (i.e. fast Case A, slow Case A and Case AB). These boundary lines essentially denote the orbital period (for binaries of a certain initial donor mass and mass ratio) at which tidal forces are unable to halt the spin-up of our accretor models.

The above self-consistently derived mass transfer efficiency from our models can be easily implemented as an orbital period dependent mass transfer efficiency prescription in rapid binary evolution models. Then, quick tests on the extent to which the strength of tidal interactions needs to be increased can be gauged so as to reproduce some of the highest mass ratio Algols. This can be done by varying the boundary between efficient and inefficient mass transfer in the rapid codes, and looking at the maximum mass ratios attained by the models during the Algol phase. We also note that a completely non-conservative mass transfer at all orbital periods would not fit the observations as then we would underpredict the mass ratios of the very short period (1−3 d) semi-detached models that undergo fairly conservative mass transfer in our original model grid.

When looking at the mass dependence of the predictions (Fig. C.1), for the most massive binary Algol systems we find that at the highest considered accretor masses (above 30 $M_\odot$) the peak in the mass ratio distribution is much closer to one, and the orbital period distribution predicts a considerable fraction of Algol binaries above 5 d. Indeed, Fig. C.1 does not reveal any problem with our mass transfer scheme, where most of the

observed Algols rather seem to be restricted to the lowest considered accretor mass interval (less than 20 $M_\odot$).

6.5. Surface abundances

The four Roche lobe filling donor stars of the TMBM sample which we assume to be in the slow Case A mass transfer phase have observed surface nitrogen abundances consistent with CNO cycle equilibrium (Fig. 7). These systems also show surface helium enrichment, signifying that their hydrogen-helium gradient region is exposed to the surface. We have shown (Fig. B.1) that the models that survive the Case A mass transfer phase show high surface nitrogen enrichment. We conclude that these systems will likely survive the Case A mass transfer without merging.

On the other hand, there are two more VFTS systems (VFTS 094 and VFTS 176) in the semi-detached phase which we did not include in our analysis (cf., Sect. 6.1) that do not show surface helium and nitrogen enrichment (Mahy et al. 2020b). These systems have very short orbital periods (Mahy et al. 2020a). As we have shown in Sect. 4.2, a very mild surface nitrogen mass fraction enhancement in our donor models occurs only in very short period model systems that undergo inverse mass transfer and subsequently a contact evolution before merging during the slow Case A phase. Hence, these two systems are likely not following the classical Case A evolution, and may be progenitors of binary mergers.

In our models, a surface nitrogen enrichment above 5 is usually associated with an increase in surface helium mass fraction, as the slow Case A mass transfer exposes the hydrogen-helium gradient region. But this is not seen in VFTS 538, where the donor is consistent with no helium enhancement, while its nitrogen enrichment is seemingly even above the CNO equilibrium value. On the other hand, VFTS 061 has a short orbital period and shows high nitrogen enrichment in both components. This is consistent with the region of our parameter space that predicts high surface nitrogen mass fraction enhancement in both donors and accretors (Fig. 7), which occurs in our most conservative models.

Carbon deficiencies have also been observed in the more massive components of Algol binaries (Tomkin et al. 1993), signifying that CNO cycled material has been transferred from the currently lower mass star. A high surface enrichment is also observed in several Galactic Algol binaries. Mahy et al. (2011) find that the Roche lobe filling component of the semi-detached system LZ Cep shows a strong helium and nitrogen mass fraction enhancement. HD 149404 (Raucq et al. 2016) and XZ Cep (Martins et al. 2017) contain Roche lobe filling stars with surface abundances close to CNO equilibrium.

Overall, these observations reflect the range of enhancements we find in our models. While our donor models slowly increase their surface nitrogen abundance during the slow Case A evolution (see Figs. B.1 and B.2), they can reach values near CNO equilibrium during the second half of Case A mass transfer (cf., Sect. 3.1; see also Wang et al. 2017). A statistically significant Algol sample is needed to test whether additional physics assumptions are required, such as tidally induced mixing in close binaries (Hastings et al. 2020), to understand their surface abundances.

6.6. Synchronization

For eight observed Algol binaries (Table 3), the projected rotational velocities and inclination angles are available in the liter-

ature. For those, we determine the deviation of both components from synchronous rotation. We obtain the spin angular velocity ($v_{\rm rot,a/d}$) from the measured projected rotational velocity ($v_{\rm rot,a/d} \sin i$), the stellar radius and the inclination angle i, while the orbital angular velocity is derived from orbital period and orbital separation.

We find that the spins of three of the Roche lobe filling donors, VFTS 061, VFTS 652 and AQ Cas, to be synchronised with the orbit to within 10%. The remaining five donor stars seem to rotate slower than synchronous, by $15-50\%$. In our models, the donors do not deviate by more than 4% from synchronous rotation (Fig. 9, left panel). The largest deviations are found for Galactic Algols (most extreme for LZ Cep) for which the derived radius my depend on the adopted distance. The resolution of this discrepancy needs a deeper investigation than is done here.

The vertical dashes on the top in the right panel of Fig. 9 denote the asynchronicities of the observed accretors (Table 3). All but one (LZ Cep) rotate super-synchronously, with an average value of 2.4 times synchronous rotation, and a maximum value of 5. Also a trend of stronger super-synchronicity with larger orbital period is apparent from the data (Table 3), which could imply that in closer systems, the accretion-induced spin-up is reduced by tidal interaction. Notably, the observed range of super-synchronicities, and its trend with orbital period, appears to be well reproduced by our models (Fig. 9, right panel). We note, however, that Dervişoğlu et al. (2010) found in Algols of much lower mass, that the accretor rotates only at $10-40\%$ of their critical velocity, even though their orbital periods exceed 5 d.

6.7. Overluminosity

We compare the luminosity of the individual stellar components of the observed semi-detached binaries in the LMC and Galaxy to the luminosity of a single star that has the same mass and effective temperature. For this, we use the single star models of Brott et al. (2011a) with initial rotational velocity of $\sim$200 km s^{-1}. We create 50 000 points with random masses between $3-80\,M_\odot$ and random ages between zero and terminal age main sequence. Through interpolation we assign a luminosity and effective temperature to each of the 50 000 points. Finally, we use the mass and effective temperature of an observed Algol binary component to find the nearest point on the stellar mass-effective temperature plane and note its luminosity. The ratio of the observed luminosity to this single star luminosity defines our overluminosity.

Table 5 lists the luminosities of the observed semi-detached binaries and the derived overluminosities; see also Fig. 13. We find that the observed mass donors are generally significantly overluminous for their mass. Exceptions are AI Cru and δ Pic, but their underluminosity is so small (10 and 20%, respectively) that an overluminosity can not be excluded. On average, the donors are overluminous by a factor of seven, with the record holder (VFTS 652) showing a factor of 30.

Such large overlumnosities are expected for stars whose average mean molecular weight μ is much larger than in single stars, since for chemical homogeneous stellar models of mass M, their luminosity L behaves as $L \sim M^\alpha \mu^\beta$ (Kippenhahn & Weigert 1990), where, in the mass range $10-30\,M_\odot$, the exponent β is $5-2.5$ (Gräfener et al. 2011; Köhler et al. 2015). As the mean molecular weight in the stellar core increases by a factor of $\sim$2.2 during hydrogen burning, and as the donor stars may be almost entirely stripped of their hydrogen envelope, we expect

Table 5. Overluminosity of observed Algol binaries in the Galaxy and the LMC, whenever available.

Name	Period (d)	M_a ($M_\odot$)	M_d ($M_\odot$)	$\log L_a$	$\log L_d$	L_a/L_{single}	L_d/L_{single}	$\log (L_a/M_a)$	$\log (L_d/M_d)$	Ref.
TT Aur	1.33	8.10	5.40	3.72	3.24	1.7	1.7	2.81	2.51	[1]
μ_1 Sco	1.44	8.30 ± 1.00	4.60 ± 1.00	3.66	3.20	1.4	3.5	2.74	2.54	[2]
BF Cen	3.69	8.70	3.80	2.82	2.55	0.06	1.3	1.88	1.97	[1]
IZ Per	3.68	9.97 ± 0.55	3.20 ± 0.17	3.85	2.57	0.5	2.3	2.85	2.06	[3]
AI Cru	1.41	10.30 ± 0.20	6.30 ± 0.10	3.88	3.24	0.6	0.9	2.87	2.44	[4]
MP Cen	2.99	11.40 ± 0.40	4.40 ± 0.20	3.80	3.00	0.25	2.63	2.74	2.35	[5]
IU Aur	1.81	11.99 ± 0.08	6.07 ± 0.04	4.64	4.22	3.4	9.9	3.56	3.43	[6]
V356 Sgr	8.89	12.10	4.70	3.81	3.02	0.3	2.3	2.73	2.35	[1]
V Pup	1.45	14.00 ± 0.50	7.30 ± 0.30	4.28	3.97	1.7	8.1	3.13	3.10	[7]
δ Pic	1.67	16.30	8.60	4.32	3.68	0.4	0.8	3.10	2.74	[8]
HH Car	3.23	17.00	14.00	4.73	4.91	1.8	4.8	3.50	3.76	[1]
V337 Aql	2.73	17.44 ± 0.31	7.83 ± 0.18	4.73	4.20	1.1	4.7	3.49	3.30	[9]
AQ Cas	11.70	17.63 ± 0.91	12.50 ± 0.81	4.94	4.59	1.48	1.1	3.69	3.49	[10]
XZ Cep	5.09	18.70 ± 1.30	9.30 ± 0.50	5.05	4.79	1.3	11	3.78	3.82	[11]
AB Cru	3.41	19.75 ± 1.04	6.95 ± 0.65	5.21	4.58	2.5	20.6	3.91	3.74	[12]
V448 Cyg	6.51	24.70 ± 0.70	13.70 ± 0.70	4.63	4.57	0.3	1.1	3.23	3.43	[13]
QZ Car	5.99	30.00 ± 3.00	20.00 ± 3.00	5.18	5.46	0.9	5.2	3.70	4.16	[14]
VFTS 061	2.33	16.30 ± 1.40	8.70 ± 0.60	4.77	4.75	1.9	14	3.55	3.81	[15]
VFTS 652	8.59	18.10 ± 3.90	6.50 ± 1.10	5.35	4.92	5.8	31	4.09	4.10	[15]
VFTS 538	4.15	18.30 ± 1.90	11.80 ± 1.40	4.96	5.31	2.4	20	3.70	4.24	[15]
VFTS 450	6.89	29.00 ± 4.10	27.80 ± 3.90	5.30	5.46	1.3	1.5	3.84	4.01	[15]

Notes. We give here the luminosity of the accretors (L_a) and donors (L_d) of massive semi-detached double-lined eclipsing binaries in the Galaxy and the LMC, and derive the ratio of their respective luminosity to that of single star models (L_{single}) of the same mass and effective temperature. Masses and luminosities are in Solar units.

References. (1) Surkova & Svechnikov (2004), (2) Budding et al. (2015), (3) Hilditch et al. (2007), (4) Bell et al. (1987), (5) Terrell et al. (2005), (6) Surina & Kang (2009), (7) Stickland et al. (1998), (8) Evans (1974), (9) Tüysüz et al. (2014), (10) Ibanoglu et al. (2013), (11) Martins et al. (2017), (12) Lorenz et al. (1994), (13) Djurašević et al. (2009), (14) Walker et al. (2017), (15) Mahy et al. (2020a,b).
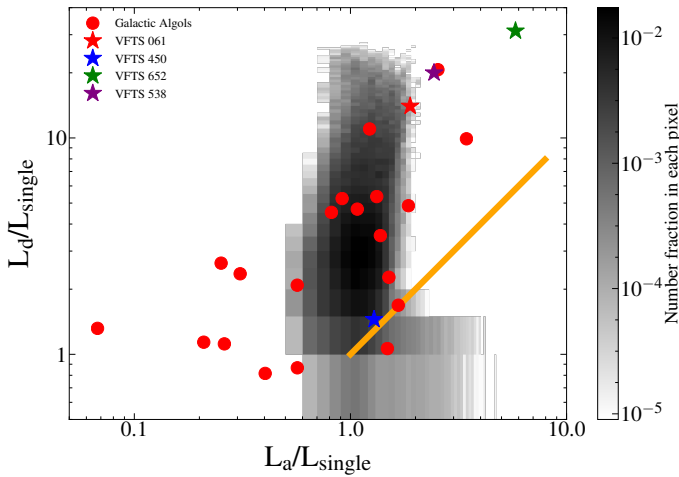
Fig. 13. Probability distribution of the ratios of the luminosities of the Algol donor and accretor models over the luminosities of single star models of the same mass and effective temperature (grey-scale, cf., description in Fig. 7). Red circles and coloured star symbols denote the corresponding parameters for the Galactic and LMC Algol systems, respectively (see Table 5). The orange line shows where the luminosity ratios of donor and accretor are equal.

overluminosities of up to a factor of 50 for the donor stars (Wellstein et al. 2001). The observed large overluminosities are therefore a direct confirmation of the loss of a large fraction of the envelope of the Roche-lobe filling components of the Algol systems.

For the accretors, we expect a much smaller effect, since most of the transferred matter from the donor is comprised of its unenriched envelope. The accretor could be slightly underluminous in case it does not undergo complete rejuvenation (Braun & Langer 1995), or it could be slightly overluminous due to the accretion of some helium-enriched material, but both effects are expected to be small.

Figure 13 shows the distribution of the overluminosities of our Algol model components in comparison with the observed values. We see that the accretors cluster around an overluminosity factor of one. However, we find several stars with significantly smaller and larger values. Here, we can only speculate about the reasons for this mismatch. One interesting feature is that the smallest overluminosity factors of the accretors occur in systems which also have small overluminosities of their donors, and the most overluminous accretors are accompanied by the most overluminous donors. The cloud of points is stretched in the direction parallel to the yellow line, which indicates equal donor and accretor mass. Potentially, any error in the distance would move observed points in this direction. While such errors could well affect the location of the Galactic Algols in this diagram, this is unlikely for the VFTS binaries in the LMC. On the other hand we note that most of the observational data for the Galactic Algols has been obtained and analysed several decades ago[3]. As it stands, the average of the observationally derived

---

[3] For example, McSwain et al. (2008) note on the most extreme outlier in Fig. 13, BF Cen, that 'Even the eclipsing double-lined spectroscopic binary BF Centauri (=HD 100915), a member of NGC 3766, has been largely neglected by modern spectroscopic observations'.

overluminosities of the accretors does agree with our model prediction, but the observed distribution is much broader.

7. Comparison with earlier work

7.1. Properties before Case AB mass transfer

Previous studies on the Case A mass transfer phase were focussed on low to intermediate mass Algol binaries having masses $0.1-8\,M_\odot$ (Mennekens & Vanbeveren 2017; Negu & Tessema 2018). Mennekens & Vanbeveren (2017) compared the observed Algol systems having B-type companions with binary stellar evolution models in the solar neighbourhood. We note that while their models reached up to $17\,M_\odot$ for the initial donor mass, the observed binaries that they compare their models to reached a maximum mass of $\sim 8\,M_\odot$. They found evidence for non-conservative mass transfer.

In the low to intermediate star mass range, their models predict a peak in orbital periods of Algols between $5-10\,d$, and mass ratios (inverting their definition of mass ratio to match with ours) around 2. While their predicted mass ratio distribution matches with ours, we note that the most probable orbital periods are higher in their predictions. At the same time, the orbital period distribution of the observed Algol binaries, that they compare their model predictions to, has a peak between $2.5-4\,d$, which is closer to our predicted distribution of orbital periods. They conclude that the mass transfer in the intermediate-mass Algol binaries is non-conservative (see also van Rensbergen et al. 2010).

Evidence of low mass transfer efficiency was found in the study by Petrovic et al. (2005), who compare observations of three short-period WR+O binaries with their binary models. Investigation into the mass transfer efficiency (Fig. 3) of our models also reveals that models that do not merge during the main sequence have typically low mass transfer efficiencies and, as an outcome of how our mass transfer is calculated, decreases with increasing orbital period. However, we note that we predict the shortest period observed Algol binaries might have undergone a largely conservative mass transfer and is destined to eventually merge later during the slow Case A mass transfer phase.

Evidence of an orbital period dependent mass transfer efficiency was found by de Mink et al. (2007), who compared observed massive Algol binaries in the Small Magellanic Cloud to detailed binary evolution models. They found that the mass transfer efficiency of their models, that can reproduce the observations, has to decrease with increasing orbital period. We have shown that our accretor spin-up dependent mass transfer efficiency does reproduce this orbital period dependency naturally (Fig. 3), giving additional credibility to our modelling of the mass transfer phase.

de Mink et al. (2014) studied the effects of a binary population on a synthetic massive star population assuming a binary fraction of 0.7. They assumed that, in their standard simulation, binaries with initial mass ratios less than 0.65 merge. They found that 3% of their total population of models to be binaries in the semi-detached phase. We also predicted the same fraction of such systems from our binary model grid, which can be said to be well in harmony with the former study, when the uncertainties related to mass transfer efficiency, angular momentum loss are taken into consideration. In our models, the dividing line (in initial mass ratio) between stable and unstable mass transfer depends on the initial donor mass (cf., Fig. 1, upper and lower panels of Fig. F.1), with more low initial mass ratio binaries undergoing stable Case A mass transfer at higher initial donor masses. By inspection, we found that lower initial mass ratio

models spend less time in the slow Case A mass transfer phase, such that the overall prediction of the properties of Algol systems are not significantly affected by the smaller initial mass ratio models that also undergo stable mass transfer in our binary grid.

The predicted velocity semi-amplitude of the semi-detached models in de Mink et al. (2014, Fig. 2) matches well with the orbital velocity distribution of the accretors in our model grid (Fig. D.1). However, the orbital velocities of the donor are considerably higher on average than predicted by the former study. This is in part be due to the fact that de Mink et al. (2014) accounted for the random 3D orientation of the plane of the orbit, while we only report the absolute value of the orbital velocity.

However, incorporating this randomness in orientation will also reduce the average orbital velocity of the accretors and the resolution of this conflict requires a deeper investigation than we do here. We also note that the calculation of this phase in de Mink et al. (2014) was done using a rapid binary stellar evolution code, which does not calculate in detail through the mass transfer phase but rather uses fitting recipes (Tout et al. 1997; Hurley et al. 2002) to simulate the properties of the stars during and after the mass transfer phase.

The general properties of our models (Sect. 2.3) are in agreement with the binary models of Pols (1994) who find that their models having initial donor mass of $16\,M_\odot$ and orbital periods below $1.6\,d$ enter into contact during the slow Case A mass transfer phase (cf., Fig. F.1). Moreover, as in Pols (1994), we also see that our models having low orbital periods and low mass ratios enter into a thermal timescale contact during the fast Case A mass transfer phase (compare hatching in bottom panel of Fig. F.1 with black frames around coloured squares in right-middle panel of Fig. F.2).

7.2. Properties after Case AB mass transfer

Recently, Langer et al. (2020) investigated the properties of black hole+OB star binaries in the LMC using the same grid of binary evolution models as is used in our work. Comparing their predictions of the mass ratio and orbital period of black hole+OB binaries arising from Case A mass transfer (Figs. 4 and 6), we find that our prediction of the most probable mass ratios and orbital periods (Fig. 11) after the Case AB mass transfer phase are very similar to their predicted distribution. We expect this to be the case because the models do not go through any more mass transfer phases, before the collapse of the initially more massive star, that can significantly alter the binary properties (see however Laplace et al. 2020). Likewise, predictions of surface nitrogen mass fraction enhancement and rotational velocity of the mass accretor after the Case AB mass transfer (Fig. 11) are very similar to the corresponding properties of the OB star companions to the BHs in Langer et al. (2020, Figs. 8 and 9).

8. Conclusions

Semi-detached binaries pose a crucial test for massive binary evolution models. On one hand, their evolution is typically simpler than that of the shortest period binaries, whose components may swap mass back-and-forth and evolve through long-lived contact stages (Marchant et al. 2016; Menon et al. 2021). On the other hand, longer-period binaries undergo thermal timescale mass transfer after the donor star has exhausted hydrogen in its core, after which their binary nature remains elusive (de Mink et al. 2014).

The nuclear timescale semi-detached phase leads to the prediction that about 3% of all massive binaries in the LMC, with initial donor masses $10-40\,M_\odot$ and orbital periods above 1.4 d, should be found in this stage, which corresponds to a significant population in any star-forming galaxy. They are easily identified, since they are photometrically variable and show large radial velocity variations. While they undergo nuclear-timescale mass transfer currently, they underwent a phase of thermal timescale mass transfer previously. It is the latter which leads to the most drastic changes of the binary properties. This thermal timescale mass transfer is crucial for all mass transferring binaries, and the semi-detached binaries allow us to examine its consequences.

Based on our large grid of $\sim 10\,000$ detailed binary evolution models (Marchant 2017), we predict the distribution functions of the orbital properties of massive semi-detached binaries (orbital period, period derivative, orbital velocities, mass ratio) as well as the surface properties of both stellar components (luminosity, temperature, chemical composition, spin). A comparison with the available observations evidently confirms the classical Algol scenario (Crawford 1955; Kopal 1971) for most of the observed massive semi-detached systems, most spectacularly by the observed large overluminosities of the donor stars by up to a factor of 30 (Fig. 13). These, as most other observables, are found in fair agreement with the model predictions.

Some necessary corrections of our models are also signified by the observations. The observed period and mass ratio distribution demonstrates that some semi-detached binaries did undergo nearly conservative mass transfer, while others can only be explained assuming very non-conservative evolution (Fig. 12). This empirical range of accretion efficiencies is well reproduced by our models (cf., Appendix F). But a more efficient mass accretion in the lowest considered mass range ($10-20\,M_\odot$; Fig. C.1), perhaps mediated by a stronger tidal coupling than the one adopted here, could help to understand the Algol systems with the highest mass ratios. New binary models are required to explore this.

However, the impetus from the current models can not yet be fully harvested, since the number of well observed massive Algol systems is small. For the LMC, large progress has been made by the TMBM (Almeida et al. 2017) and BBC (Villaseñor et al. 2021) surveys. Through detailed analyses, Mahy et al. (2020a,b) derived the most relevant observational constraints for our models for four TMBM targets. However, in agreement with our predictions, the Algol binaries comprise only a few percent of the targets in these surveys. Of the putative 90 LMC Algols above $10\,M_\odot$, we have basic data for seven, and highest quality analyses for four. While we know more massive Algols in the Milky Way, the data here is scarce, very heterogeneous and often without error estimates. This calls for a high quality multi-epoch survey dedicated to massive Algol binaries.

When confronted with the results of such a survey, we expect more crisp constraints on the input physics of our models (see Appendix A). In addition, model grids for solar and sub-LMC metallicity would form a big step forward to understand the impact of metallicity on the mass transfer process. While parameter variations are difficult for model grids as large as the one analysed here, the best studied Algol binaries could be attempted to be reproduced by tailored models where the input physics could be varied. As semi-detached massive binaries may be progenitors of magnetic main sequence stars (Schneider et al. 2016, 2019; Takahashi & Langer 2021), hydrogen-poor supernovae (Yoon et al. 2010; Dessart et al. 2020; Stanway et al. 2020), neutron star and black hole binaries (Tauris & van den Heuvel 2006; Van Bever & Vanbeveren 2000; Langer et al.

2020), and double-compact binary mergers (Eldridge & Stanway 2016; Kruckow et al. 2018), pursuing these routes promises to be fruitful.

References

Abbott, B. P., Abbott, R., Abbott, T. D., et al. 2019, Phys. Rev. X, 9, 031040
Abdul-Masih, M., Sana, H., Sundqvist, J., et al. 2019, ApJ, 880, 115
Almeida, L. A., Sana, H., Taylor, W., et al. 2017, A&A, 598, A84
Asplund, M., Grevesse, N., & Sauval, A. J. 2005, in Cosmic Abundances as Records of Stellar Evolution and Nucleosynthesis, eds. T. G. Barnes, III, & F. N. Bash, ASP Conf. Ser., 336, 25
Bagnuolo, W. G., Jr., Gies, D. R., Hahula, M. E., Wiemker, R., & Wiggs, M. S. 1994, ApJ, 423, 446
Banyard, G., Sana, H., Mahy, L., et al. 2022, A&A, 658, A69
Belczynski, K., Kalogera, V., Rasio, F. A., et al. 2008, ApJS, 174, 223
Bell, S. A., Kilkenny, D., & Malcolm, G. J. 1987, MNRAS, 226, 879
Blackford, M., Walker, S., Budding, E., et al. 2020, J. Am. Assoc. Var. Star Obs., 48, 3
Böhm-Vitense, E. 1960, in Aerodynamic Phenomena in Stellar Atmospheres, ed. R. N. Thomas, IAU Symp., 12, 338
Bonanos, A. Z. 2009, ApJ, 691, 407
Braun, H., & Langer, N. 1995, A&A, 297, 483
Breivik, K., Coughlin, S., Zevin, M., et al. 2020, ApJ, 898, 71
Brott, I., de Mink, S. E., Cantiello, M., et al. 2011a, A&A, 530, A115
Brott, I., de Mink, S. E., Cantiello, M., et al. 2011b, VizieR Online Data Catalog: J/A+A/530/A115
Budding, E., Erdem, A., Çiçek, C., et al. 2004, A&A, 417, 263
Budding, E., Butland, R., & Blackford, M. 2015, MNRAS, 448, 3784
Budding, E., Love, T., Blackford, M. G., Banks, T., & Rhodes, M. J. 2021, MNRAS, 502, 6032
Cantiello, M., & Langer, N. 2010, A&A, 521, A9
Çakırlı, Ö. 2015, New Astron., 35, 71
Cester, B., Fedel, B., Giuricin, G., Mardirossian, F., & Pucillo, M. 1977, A&A, 61, 469
Choi, J., Dotter, A., Conroy, C., et al. 2016, ApJ, 823, 102
Clark, J. S., Ritchie, B. W., Najarro, F., Langer, N., & Negueruela, I. 2014, A&A, 565, A90
Crawford, J. A. 1955, ApJ, 121, 71
Crowther, P. A. 2019, Galaxies, 7, 88
Daems, K., & Waelkens, C. 1997, A&A, 327, 640
de Mink, S. E., Pols, O. R., & Hilditch, R. W. 2007, A&A, 467, 1181
de Mink, S. E., Cantiello, M., Langer, N., et al. 2009, A&A, 497, 243
de Mink, S. E., Langer, N., Izzard, R. G., Sana, H., & de Koter, A. 2013, ApJ, 764, 166
de Mink, S. E., Sana, H., Langer, N., Izzard, R. G., & Schneider, F. R. N. 2014, ApJ, 782, 7
Dervişoğlu, A., Tout, C. A., & Ibanoğlu, C. 2010, MNRAS, 406, 1071
Deschamps, R., Braun, K., Jorissen, A., et al. 2015, A&A, 577, A55
Dessart, L., Yoon, S.-C., Aguilera-Dena, D. R., & Langer, N. 2020, A&A, 642, A106
Detmers, R. G., Langer, N., Podsiadlowski, P., & Izzard, R. G. 2008, A&A, 484, 831
Djurašević, G., Vince, I., Khruzina, T. S., & Rovithis-Livaniou, E. 2009, MNRAS, 396, 1553
Doran, E. I., Crowther, P. A., de Koter, A., et al. 2013, A&A, 558, A134
Dunstall, P. R., Dufton, P. L., Sana, H., et al. 2015, A&A, 580, A93
Eldridge, J. J., & Stanway, E. R. 2016, MNRAS, 462, 3302
Eldridge, J. J., Stanway, E. R., Xiao, L., et al. 2017, PASA, 34, e058
Evans, R. G. 1974, MNRAS, 167, 517

Evans, C. J., Taylor, W. D., Hénault-Brunet, V., et al. 2011, A&A, 530, A108
Ge, H., Webbink, R. F., Chen, X., & Han, Z. 2020, ApJ, 899, 132
Giacobbo, N., Mapelli, M., & Spera, M. 2018, MNRAS, 474, 2959
Gorda, S. Y., & Svechnikov, M. A. 1998, Astron. Rep., 42, 793
Götberg, Y., Korol, V., Lamberts, A., et al. 2020, ApJ, 904, 56
Gräfener, G., Vink, J. S., de Koter, A., & Langer, N. 2011, A&A, 535, A56
Hastings, B., Langer, N., & Koenigsberger, G. 2020, A&A, 641, A86
Heger, A., Langer, N., & Woosley, S. E. 2000, ApJ, 528, 368
Heger, A., Woosley, S. E., & Spruit, H. C. 2005, ApJ, 626, 350
Hilditch, R. W., Howarth, I. D., & Harries, T. J. 2005, MNRAS, 357, 304
Hilditch, R. W., Hill, G., & Lister, T. A. 2007, The Observatory, 127, 33
Howarth, I. D., Dufton, P. L., Dunstall, P. R., et al. 2015, A&A, 582, A73
Hurley, J. R., Tout, C. A., & Pols, O. R. 2002, MNRAS, 329, 897
Ibanoglu, C., Çakırlı, Ö., & Sipahi, E. 2013, New Astron., 25, 68
Iglesias, C. A., & Rogers, F. J. 1996, ApJ, 464, 943
Izzard, R. G., Dray, L. M., Karakas, A. I., Lugaro, M., & Tout, C. A. 2006, A&A, 460, 565
Janssens, S., Shenar, T., Mahy, L., et al. 2021, A&A, 646, A33
Johnston, C., Pavlovski, K., & Tkachenko, A. 2019, A&A, 628, A25
Justesen, A. B., & Albrecht, S. 2021, ApJ, 912, 123
Kippenhahn, R., & Weigert, A. 1990, Stellar Structure and Evolution (Berlin: Springer-Verlag)
Kobulnicky, H. A., Kiminki, D. C., Lundquist, M. J., et al. 2014, ApJS, 213, 34
Köhler, K., Langer, N., de Koter, A., et al. 2015, A&A, 573, A71
Kopal, Z. 1971, PASP, 83, 521
Kruckow, M. U., Tauris, T. M., Langer, N., Kramer, M., & Izzard, R. G. 2018, MNRAS, 481, 1908
Langer, N. 1991, A&A, 252, 669
Langer, N. 1997, in Luminous Blue Variables: Massive Stars in Transition, eds. A. Nota, & H. Lamers, ASP Conf. Ser., 120, 83
Langer, N. 2012, ARA&A, 50, 107
Langer, N., Wellstein, S., & Petrovic, J. 2003, in A Massive Star Odyssey: From Main Sequence to Supernova, eds. K. van der Hucht, A. Herrero, & C. Esteban, IAU Symp., 212, 275
Langer, N., Schürmann, C., Stoll, K., et al. 2020, A&A, 638, A39
Laplace, E., Götberg, Y., de Mink, S. E., Justham, S., & Farmer, R. 2020, A&A, 637, A6
Lorenz, R., Mayer, P., & Drechsel, H. 1994, A&A, 291, 185
Lubow, S. H., & Shu, F. H. 1975, ApJ, 198, 383
Maeder, A., & Meynet, G. 2000, ARA&A, 38, 143
Mahy, L., Martins, F., Machado, C., Donati, J. F., & Bouret, J. C. 2011, A&A, 533, A9
Mahy, L., Almeida, L. A., Sana, H., et al. 2020a, A&A, 634, A119
Mahy, L., Sana, H., Abdul-Masih, M., et al. 2020b, A&A, 634, A118
Malkov, O. Y. 2020, MNRAS, 491, 5489
Mandel, I., & de Mink, S. E. 2016, MNRAS, 458, 2634
Marchant, P. 2017, PhD Thesis, University of Bonn, Germany
Marchant, P., Langer, N., Podsiadlowski, P., Tauris, T. M., & Moriya, T. J. 2016, A&A, 588, A50
Marchant, P., Pappas, K. M. W., Gallegos-Garcia, M., et al. 2021, A&A, 650, A107
Martins, F., Mahy, L., & Hervé, A. 2017, A&A, 607, A82
Massey, P. 1981, ApJ, 244, 157
Massey, P., Penny, L. R., & Vukovich, J. 2002, ApJ, 565, 982
McSwain, M. V., Huang, W., Gies, D. R., Grundstrom, E. D., & Townsend, R. H. D. 2008, ApJ, 672, 590
Mennekens, N., & Vanbeveren, D. 2017, A&A, 599, A84
Menon, A., Langer, N., de Mink, S. E., et al. 2021, MNRAS, 507, 5013
Milone, A. P., Marino, A. F., Di Criscienzo, M., et al. 2018, MNRAS, 477, 2640
Moe, M., & Di Stefano, R. 2017, ApJS, 230, 15
Mokiem, M. R., de Koter, A., Vink, J. S., et al. 2007, A&A, 473, 603
Morrison, N. D., & Conti, P. S. 1979, in Mass Loss and Evolution of O-Type Stars, eds. P. S. Conti, & C. W. H. De Loore, 83, 277
Negu, S. H., & Tessema, S. B. 2018, Astron. Nachr., 339, 709
Nelson, C. A., & Eggleton, P. P. 2001, ApJ, 552, 664
Niemela, V. S., & Moffat, A. F. J. 1982, ApJ, 259, 213
Ostrov, P. G., Lapasset, E., & Morrell, N. I. 2000, A&A, 356, 935
Ostrov, P. G., Morrell, N. I., & Lapasset, E. 2001, A&A, 377, 972
Packet, W. 1981, A&A, 102, 17
Pavlovski, K., Southworth, J., & Tamajo, E. 2018, MNRAS, 481, 3129
Pavlovskii, K., Ivanova, N., Belczynski, K., & Van, K. X. 2017, MNRAS, 465, 2092
Paxton, B., Bildsten, L., Dotter, A., et al. 2011, ApJS, 192, 3
Paxton, B., Cantiello, M., Arras, P., et al. 2013, ApJS, 208, 4

Paxton, B., Marchant, P., Schwab, J., et al. 2015, ApJS, 220, 15
Paxton, B., Schwab, J., Bauer, E. B., et al. 2018, ApJS, 234, 34
Petrovic, J., Langer, N., & van der Hucht, K. A. 2005, A&A, 435, 1013
Podsiadlowski, P., Joss, P. C., & Hsu, J. J. L. 1992, ApJ, 391, 246
Pols, O. R. 1994, A&A, 290, 119
Pols, O. R., Tout, C. A., Schröder, K.-P., Eggleton, P. P., & Manners, J. 1997, MNRAS, 289, 869
Qin, Y., Marchant, P., Fragos, T., Meynet, G., & Kalogera, V. 2019, ApJ, 870, L18
Quast, M., Langer, N., & Tauris, T. M. 2019, A&A, 628, A19
Raucq, F., Rauw, G., Gosset, E., et al. 2016, A&A, 588, A10
Rauw, G., Vreux, J. M., & Bohannan, B. 1999, ApJ, 517, 416
Rauw, G., Nazé, Y., & Campos, F. 2019, A&A, 627, A2
Ritchie, B. W., Clark, J. S., Negueruela, I., & Langer, N. 2010, A&A, 520, A48
Salpeter, E. E. 1955, ApJ, 121, 161
Sana, H., de Mink, S. E., de Koter, A., et al. 2012, Science, 337, 444
Sana, H., de Koter, A., de Mink, S. E., et al. 2013, A&A, 550, A107
Sanyal, D., Grassitelli, L., Langer, N., & Bestenlehner, J. M. 2015, A&A, 580, A20
Sanyal, D., Langer, N., Szécsi, D., Yoon, S.-C., & Grassitelli, L. 2017, A&A, 597, A71
Schneider, F. R. N., Podsiadlowski, P., Langer, N., Castro, N., & Fossati, L. 2016, MNRAS, 457, 2355
Schneider, F. R. N., Ohlmann, S. T., Podsiadlowski, P., et al. 2019, Nature, 574, 211
Schootemeijer, A., Götberg, Y., de Mink, S. E., Gies, D., & Zapartas, E. 2018, A&A, 615, A30
Schootemeijer, A., Langer, N., Grin, N. J., & Wang, C. 2019, A&A, 625, A132
Shenar, T., Gilkis, A., Vink, J. S., Sana, H., & Sander, A. A. C. 2020, A&A, 634, A79
Soberman, G. E., Phinney, E. S., & van den Heuvel, E. P. J. 1997, A&A, 327, 620
Southworth, J., Maxted, P. F. L., & Smalley, B. 2004, MNRAS, 351, 1277
Spera, M., Mapelli, M., Giacobbo, N., et al. 2019, MNRAS, 485, 889
Stanway, E. R., Eldridge, J. J., & Chrimes, A. A. 2020, MNRAS, 497, 2201
Stevenson, S., Vigna-Gómez, A., Mandel, I., et al. 2017, Nat. Commun., 8, 14906
Stickland, D. J., Lloyd, C., Pachoulakis, I., & Koch, R. H. 1998, The Observatory, 118, 356
Surina, F., & Kang, Y. W. 2009, in Absolute Dimensions of Four Eclipsing Binaries, eds. S. J. Murphy, & M. S. Bessell, ASP Conf. Ser., 404, 178
Surkova, L. P., & Svechnikov, M. A. 2004, VizieR Online Data Catalog: V/115
Takahashi, K., & Langer, N. 2021, A&A, 646, A19
Tauris, T. M., & van den Heuvel, E. P. J. 2006, Formation and Evolution of Compact Stellar X-ray Sources (Cambridge, UK: Cambridge University Press), 623
Terrell, D., Munari, U., Zwitter, T., & Wolf, G. 2005, MNRAS, 360, 583
Tomkin, J., Lambert, D. L., & Lemke, M. 1993, MNRAS, 265, 581
Torres, G., Andersen, J., & Giménez, A. 2010, A&ARv, 18, 67
Tout, C. A., Aarseth, S. J., Pols, O. R., & Eggleton, P. P. 1997, MNRAS, 291, 732
Tüysüz, M., Soydugan, F., Bilir, S., et al. 2014, New Astron., 28, 44
Ulrich, R. K., & Burger, H. L. 1976, ApJ, 206, 509
Valsecchi, F., Glebbeek, E., Farr, W. M., et al. 2010, Nature, 468, 77
Van Bever, J., & Vanbeveren, D. 2000, A&A, 358, 462
van der Hucht, K. A. 2001, New Astron. Rev., 45, 135
van Rensbergen, W., De Greve, J. P., Mennekens, N., Jansen, K., & De Loore, C. 2010, A&A, 510, A13
Vanbeveren, D., De Loore, C., & Van Rensbergen, W. 1998, A&ARv, 9, 63
Villaseñor, J. I., Taylor, W. D., Evans, C. J., et al. 2021, MNRAS, 507, 5348
Walker, W. S. G., Blackford, M., Butland, R., & Budding, E. 2017, MNRAS, 470, 2007
Walter, R., Lutovinov, A. A., Bozzo, E., & Tsygankov, S. S. 2015, A&ARv, 23, 2
Wang, J., Song, H., & Li, Z. 2017, Sci. China Phys. Mech. Astron., 60, 59521
Wang, C., Langer, N., Schootemeijer, A., et al. 2020, ApJ, 888, L12
Wang, L., Gies, D. R., Peters, G. J., et al. 2021, AJ, 161, 248
Wellstein, S., & Langer, N. 1999, A&A, 350, 148
Wellstein, S., Langer, N., & Braun, H. 2001, A&A, 369, 939
Williams, S. J., Gies, D. R., Henry, T. J., et al. 2008, ApJ, 682, 492
Wilson, R. E., van Hamme, W., & Pettera, L. 1985, ApJ, 289, 748
Yaşarsoy, B., & Yakut, K. 2014, New Astron., 31, 32
Yoon, S. C., Woosley, S. E., & Langer, N. 2010, ApJ, 725, 940
Yoon, S.-C., Dessart, L., & Clocchiatti, A. 2017, ApJ, 840, 10
Zahn, J. P. 1977, A&A, 500, 121

Appendix A: Discussion and uncertainties

A.1. Envelope inflation

Sanyal et al. (2015) investigated the single star models of Brott et al. (2011a) at LMC metallicity and found that models exceeding $\sim 40\,M_\odot$ reach their Eddington limit inside the stellar envelope during core hydrogen burning. This leads to a large expansion of the stellar envelope, which makes the star grow to red supergiant proportions during core hydrogen burning. Our models, with very similar physics assumptions as those of Brott et al. (2011a), are also expected to show similar behaviour. Indeed, for the next higher initial donor mass to be considered ($44.7\,M_\odot$), the envelope of the donor inflates and leads to unstable mass transfer which MESA is unable to calculate through. In this sense, the upper limit on the initial donor mass in our grid is a computational result. For a more comprehensive discussion of this topic, we refer the interested readers to Sect. 4.1 of Langer et al. (2020). We discuss the parts relevant to our work.

The implication of inflation above $\sim 40\,M_\odot$ at the LMC metallicity is that all binary models having initial donor masses above $\sim 40\,M_\odot$ will undergo Case A mass transfer since the donors will expand to red supergiant proportions during core hydrogen burning. Such donors have inflated convective envelopes at the onset of Roche-lobe overflow (Sanyal et al. 2015). The subsequent mass transfer due to Roche-lobe overflow from stars with convective envelopes is expected to be unstable as the radius of a star with convective envelope increases when mass is lost from the envelope (Quast et al. 2019; Ge et al. 2020). Langer et al. (2020) assume that, in the absence of detailed model calculations, mass transfer due to Roche-lobe overflow from an inflated mass donor will lead to an unstable mass transfer and the binary would merge.

Due to inflation and the inability of MESA to calculate through the mass transfer phase of such models, our models cannot predict the observable properties of binary systems in semi-detached configurations originating from initial donor masses greater than $\sim 40\,M_\odot$. In the TMBM sample of semi-detached systems, we find a system VFTS 094 in which both components have masses around $\sim 30\,M_\odot$. This might be an observed system which shows evidence of stable mass transfer during fast Case A when the mass of the donor was arguably greater than $\sim 40\,M_\odot$. However, the error bars are too big to draw any conclusive arguments. The system VFTS 450 also shows that both components have high dynamical masses $\sim 30\,M_\odot$ and is a possible candidate to have undergone stable mass transfer above the cut-off mass for inflation to set in our models.

We find another system LH 54-425 (Williams et al. 2008) in which the more massive component is estimated to have a mass of $\sim 47 \pm 2\,M_\odot$. The binary system R136-38 (Massey et al. 2002) is estimated to have a star with mass $\sim 56.9 \pm 0.6\,M_\odot$. We note that the 04f + 06V eclipsing binary system Sk-67°105 is found to have one component which has mass greater than $40\,M_\odot$, and both the components are nearly filling their Roche lobe. The existence of these observed high mass systems provides a motivation for a comprehensive investigation of the mass transfer phase in mass donors with inflated envelopes.

However, we note that inflation at LMC metallicity sets in at $40\,M_\odot$ during the late stage of core hydrogen burning and the estimated age of LH 54-425 and R136 is 1.5-2 Myrs. Hence, these systems might not have inflated yet. On the other hand, the authors that studied Sk-67°105 reported that it is in a very distorted configuration and is likely that its components are undergoing very strong interactions.

If inflated stars do undergo stable mass transfer in nature, then the orbital period distribution of our semi-detached models can be taken as skewed to lower periods. However, the initial mass function and the empirical determination of the distribution of orbital periods in binaries are heavily weighted towards lower masses and orbital periods. Moreover, the time spent in Case A mass transfer phase decreases with the increase in the initial orbital period of the binary. Hence, we do not expect a significant impact on the predicted orbital period distributions as a whole. However, the properties of very massive binaries ($>\sim 30\,M_\odot$) in the Algol configuration can be quite different than comparatively lower mass Algol binaries (see for eg. Fig. 5).

A.2. Mass transfer efficiency and stability of mass transfer

Observations of binary systems which have undergone a mass transfer phase indicate that the mass transfer efficiency varies from binary to binary. While some binaries require models to have low mass transfer efficiency (Langer et al. 2003), others indicate a need for higher mass transfer efficiency (Wellstein & Langer 1999). It has also been argued that binaries with lower mass ratio experience lower mass transfer efficiency (Petrovic et al. 2005). de Mink et al. (2007) also find hints for a low mass transfer efficiency for higher period binaries. However, a recent study by Deschamps et al. (2015) reported that direct observational imprints of mass loss due to non-conservative mass transfer might not be visible in Algol systems.

Our mass transfer model based on the principle of decreasing mass transfer efficiency with increasing rotation of the mass accreting star does in theory take into consideration these variations and we do see a trend of decreasing mass transfer efficiency with increasing period and decreasing mass ratios. This model needs excess mass to be removed from the binary so that the mass gainer does not exceed critical rotation. We model this by requiring that the combined photon energy from both the stars in the binary is larger than the gravitational energy needed to remove the excess unaccretable mass due to the accretor reaching critical rotation. If this condition fails, the evolution of the model is stopped and assumed to merge. However, as already demonstrated, our mass transfer scheme is able to reproduce the observed population of Algol binaries in the Galaxy and LMC.

Our criterion to determine the stability of mass transfer is simple. The dividing line between stable and unstable mass transfer in our models is a function of the initial orbital period and mass ratio for a particular initial donor mass of the binary. For a discussion, we direct the interested reader to Fig. 2 of Langer et al. (2020).

Wang et al. (2020) has shown that a large fraction of the Be star population in NGC 330 (Milone et al. 2018) is well represented by binary evolution models. To correctly predict their numbers in comparison to the number of mergers, however, they posit that the boundary between stable and unstable mass transfer has to be relaxed such that there are more models that can undergo stable mass transfer. Doing such would increase the number of Case A mass transfer systems with lower initial mass ratios. Inspection of our model grid shows that the time spent in the semi-detached phase decreases with lower mass ratios, such that models having initial mass ratio less than 0.5 spend less than 10% of their main sequence lifetime in the semi-detached phase. Hence, relaxing the criterion for stable mass transfer will not significantly affect the results we derive in this work.

A.3. Semiconvection

We are aware that recent studies on single star models (Schootemeijer et al. 2019) argue for a higher efficiency of semiconvection in stellar models. We note that a higher

semiconvective efficiency than what is implemented in our models will make the mass gaining stars rejuvenate (Braun & Langer 1995) and develop a core-envelope structure similar to that of a single star (Braun & Langer 1995). The core mass and stellar radius of rejuvenated accretors will be larger and smaller, respectively, compared to our nonrejuvenated models (compare model 47 and 48 of Wellstein et al. 2001). This implies that our binary models enter into a contact configuration and can undergo L2 overflow (purple models in Fig. 1) at longer orbital periods compared to models calculated with a higher semiconvective efficiency, due to the larger radii of our accretors (compare Fig. 1 to Fig. A1 of Menon et al. 2021).

Rejuvenated accretors also have a greater remaining core hydrogen burning lifetime than nonrejuvenated accretors. Accordingly, our binary models are more likely to undergo inverse mass transfer from a post main sequence accretor onto a main sequence donor (orange models in Fig. 1 than binary models calculated using a high semiconvective efficiency. After Case AB mass transfer, our nonrejuvenated accretors may live their core helium burning lifetime as a blue supergiant instead of a red supergiant (Podsiadlowski et al. 1992). However, the amount of increase in the core masses of mass gainers due to rejuvenation depends on the amount of mass that can be successfully accreted (Braun & Langer 1995). We showed that the mass transfer efficiency is low in most of our models that survive the Case A mass transfer phase (Fig. 3).

From the above discussion, we can speculate that more short period binaries will contribute to our predicted Algol popula-

tion for models with efficient semiconvection. As such, the peak in the predicted orbital period distribution may be shifted to a lower value, although we cannot quantify it. The maximum lifespan of the slow Case A phase is also expected to increase since fewer models will merge due to L2 overflow during slow Case A mass transfer. This may increase our predicted number of Algol binaries in the LMC. As less binaries will undergo contact and inverse slow Case A mass transfer, the peak in the predicted surface abundance is also expected to increase to higher values, especially the nitrogen surface enhancement. Since shorter period binaries undergo more conservative Case A mass transfer in our mass transfer scheme, we expect more contribution from models that undergo conservative mass transfer to the population of WR/He+OB star binaries.

Appendix B: Additional figures for surface abundances during slow Case A

Here, we show the prediction of surface helium mass fraction and surface nitrogen mass fraction enhancement for only the models that survive the Case A mass transfer phase (Fig. B.1) or only for models that merge during the Case A mass transfer (Fig. B.1). We also provide additional figures of the surface helium mass fraction and nitrogen mass fraction enhancement of donors and accretors during the slow Case A mass transfer phase, for different ranges of accretor masses of the binary during the semi-detached configuration (Fig. B.2).
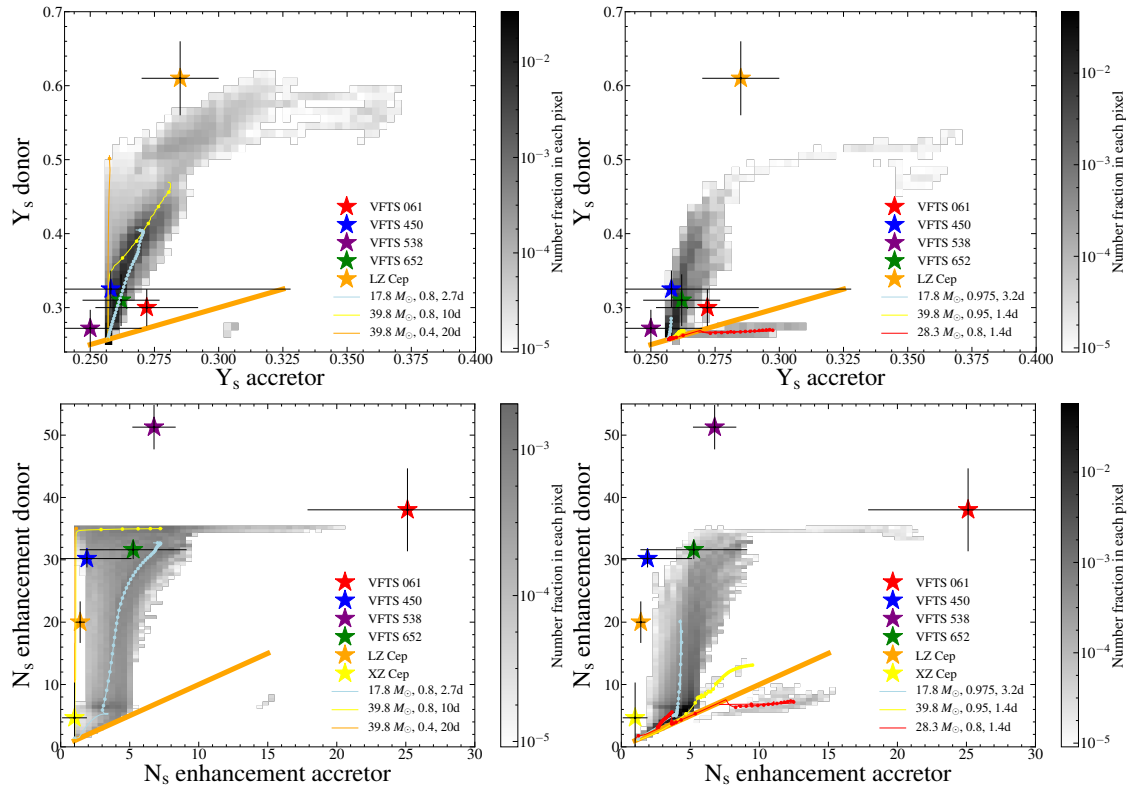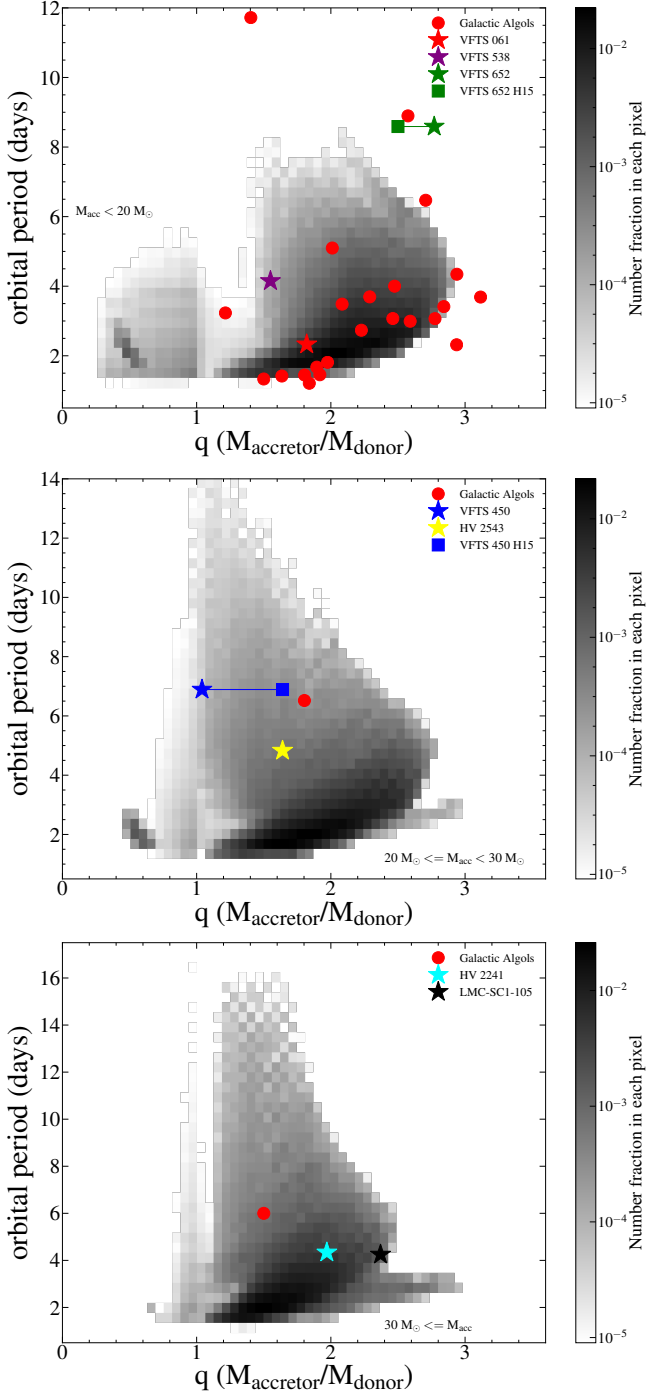

Fig. B.1. Probability distribution of the surface helium mass fraction (top panels) and surface nitrogen mass fraction enhancement (bottom panels) of donor vs the accretor that is predicted to be observed in the semi-detached configuration of the Case A mass transfer phase. The left panels show the contribution to Fig. 7 from models that survive the Case A mass transfer phase while the right panels show the contribution to Fig. 7 from models that eventually merge during the slow Case A phase. The different coloured 'stars' with error bars denote the position of the semi-detached systems of the TMBM survey (Mahy et al. 2020b) and Galaxy. The thick orange line indicates where the surface helium mass fraction or surface nitrogen enrichment of the donor and accretor is the same. The thin coloured lines show the evolution of surface abundances during the main sequence with initial parameters (donor mass, mass ratio, period) as given in the legend. The corresponding coloured dots are at 50 000 years during the semi-detached phase. The grey-scale gives the probability fraction in each pixel. The total probability is normalised such that the integrated sum over the entire area is 1.
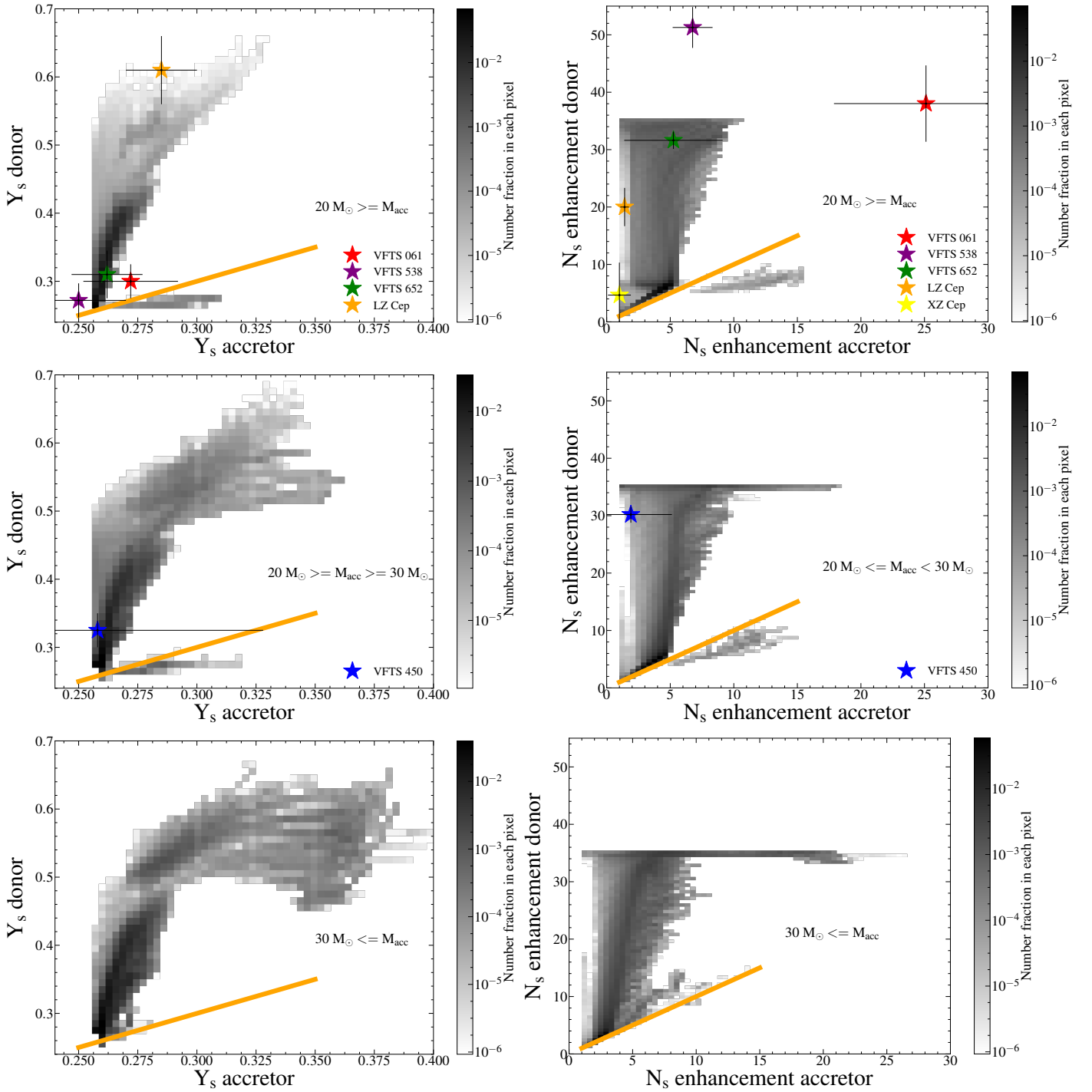
Fig. B.2. Probability distribution of the surface helium mass fraction (left three panels) and surface nitrogen mass fraction enhancement factors (right three panels) of the donor vs the accretor for different ranges of accretor masses during the semi-detached phase: below 20 $M_\odot$ (top panels), 20-30 $M_\odot$ (middle panels) and above 30 $M_\odot$ (bottom panels). The different coloured stars symbols with error bars denote the positions of the semi-detached systems from the TMBM survey (Mahy et al. 2020a,b). The orange line indicates where the donor and accretor abundances are the same. The grey-scale gives the probability fraction in each pixel. The total probability is normalised such that the sum over the entire area equals unity.

Appendix C: Mass dependence of orbital period and mass ratio during slow Case A

Here, we provide additional figures of the orbital period and mass ratio during the slow Case A mass transfer phase, for different ranges of accretor masses of the binary.

Appendix D: Orbital velocities

Figure D.1 shows the probability distribution of the orbital velocities of the two components during the semi-detached phase. In the darker shaded regions, we see that the donor has a higher orbital velocity than the accretor. This indicates that the donor is currently the less massive component of the system.
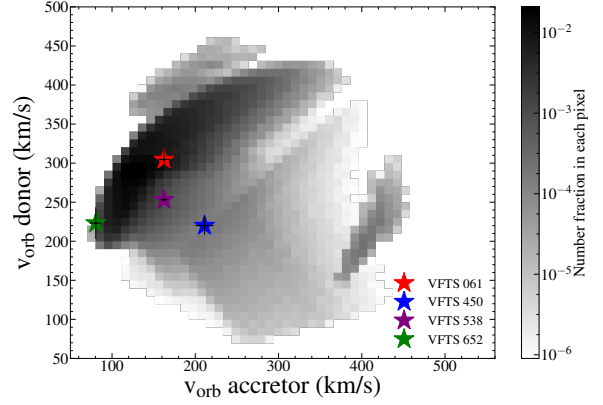
Fig. D.1. Probability distribution of the orbital velocities of the donor and the accretor in the semi-detached configuration. The different coloured stars with error bars denote the position of the semi-detached systems of the TMBM survey (Almeida et al. 2017). Grey-scale: See description in Fig. 7.

Appendix E: Orbital period derivatives

Figure E.1 shows the orbital period derivatives during the semi-detached phase for different ranges of initial donor masses.

Fig. C.1. Probability distribution of the orbital period and mass ratio that is predicted to be observed in the semi-detached configuration of the Case A mass transfer phase for models with accretor mass below 20 $M_\odot$ (top panel), 20-30 $M_\odot$ (middle panel) and above 30 $M_\odot$ (bottom panel). The grey-scale gives the probability fraction in each pixel. The total probability is normalised such that the sum over the entire area is 1.

Fig. E.1. Same as Fig. 10, but only for initial donor mass of 10-15 $M_\odot$ (top panel) and 30-40 $M_\odot$ (bottom panel).

Appendix F: Summary of the outcome of binary models for different initial donor masses in our grid

We present the summary plots for different initial donor masses in our grid. Our work is mainly focussed on the systems that survive the Case A mass transfer phase (light blue models) or undergo an extended phase of interaction (orange and purple models) before merging on the main sequence (Fig. F.1).
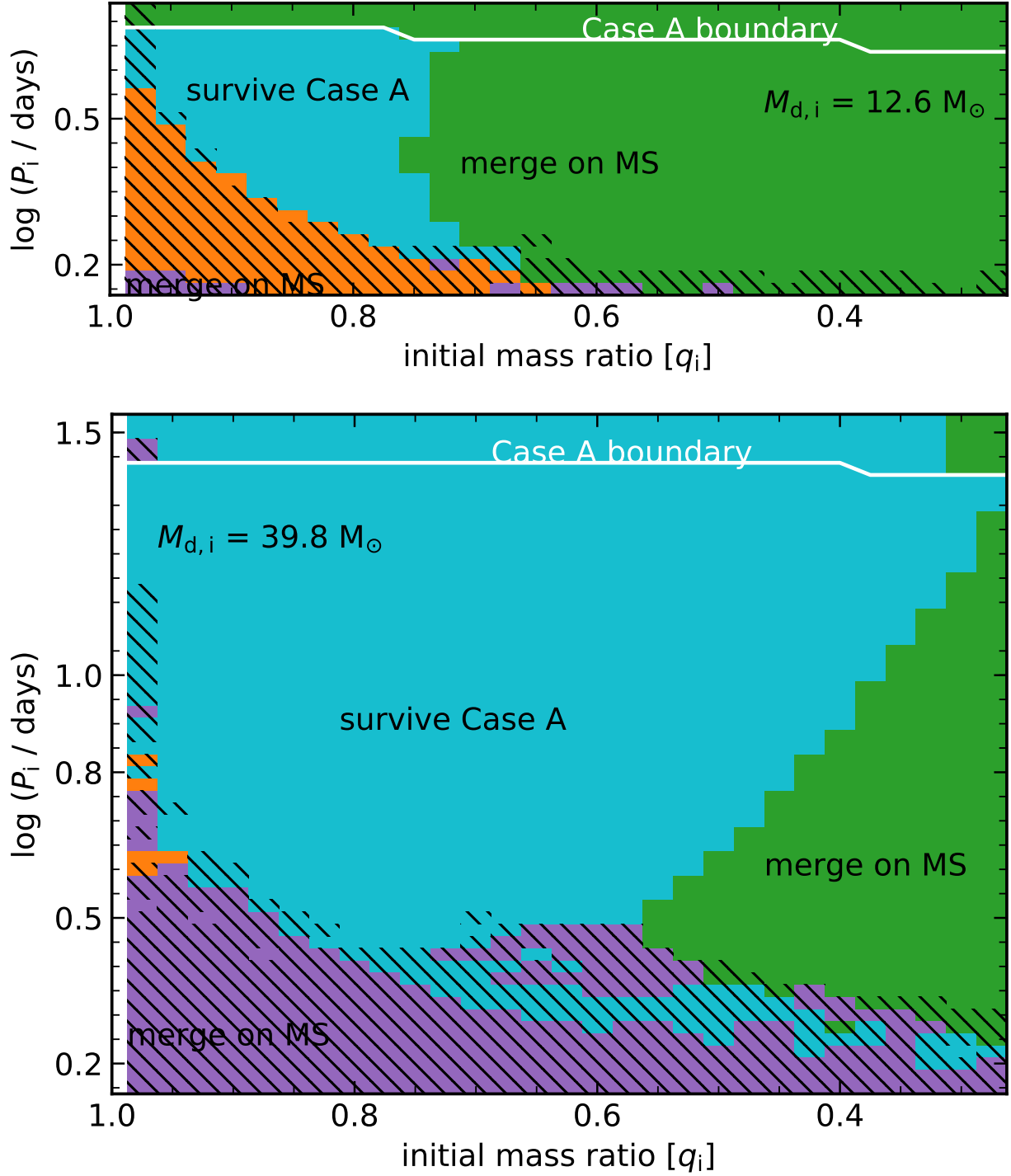

Fig. F.1. Summary plot, same as Fig. 1, but for an initial donor mass of $M \simeq 12.6\,M_\odot$ (top plot) and $M \simeq 39.8\,M_\odot$ (bottom plot).
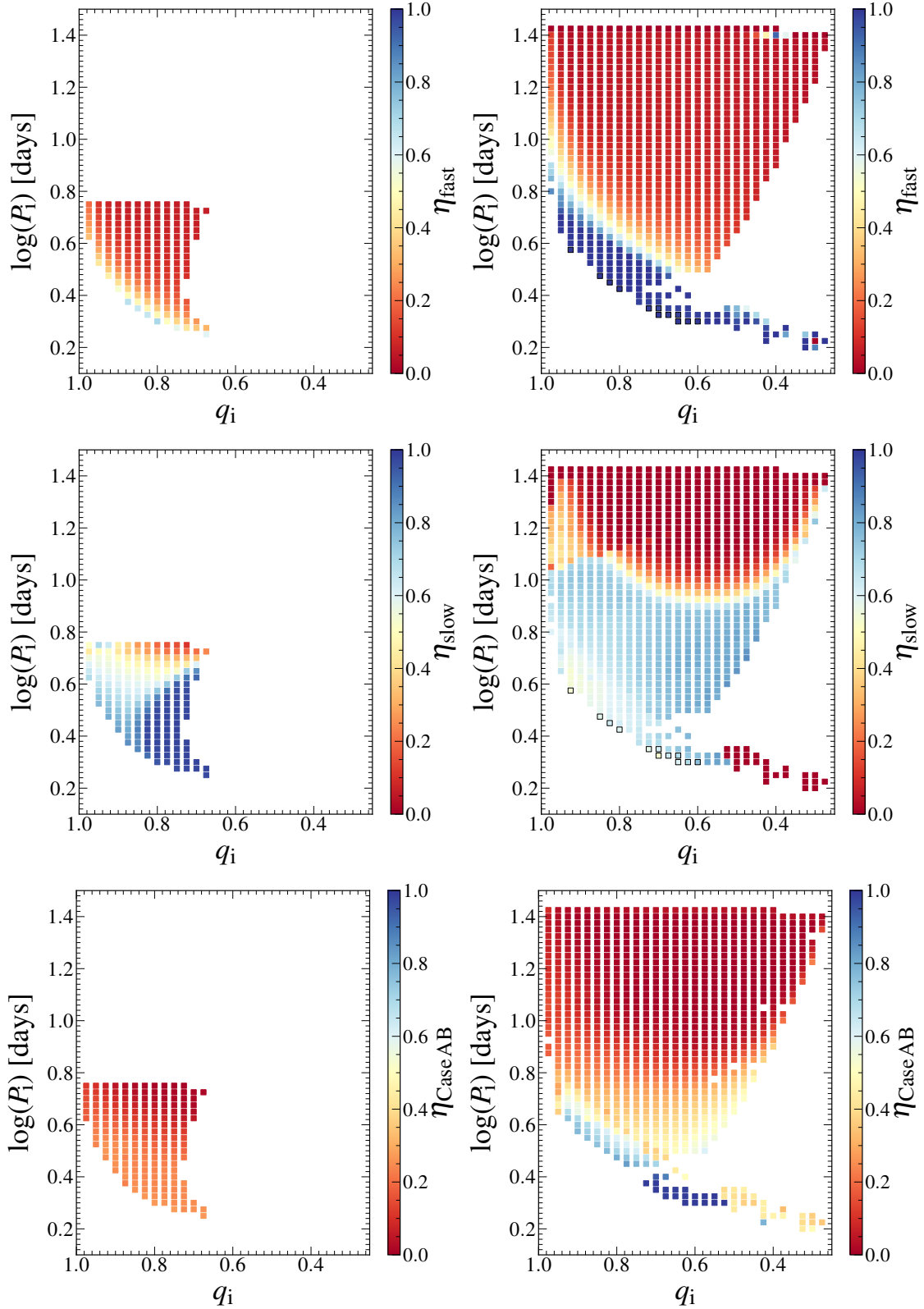
Fig. F.2. Mass transfer efficiency η (colour coded) during fast (top panels) and slow (middle panels) Case A, and during Case AB (bottom panels) as function of initial orbital period and initial mass ratio, for systems with initial donor masses of $\sim 16\,M_\odot$ and $\sim 40\,M_\odot$ in the left and right panels, respectively. Each coloured square represents one binary evolution model, with the colour denoting the mass transfer efficiency. Black frames around coloured square indicate models that has undergone a contact phase lasting more than three thermal timescales of the mass donor.
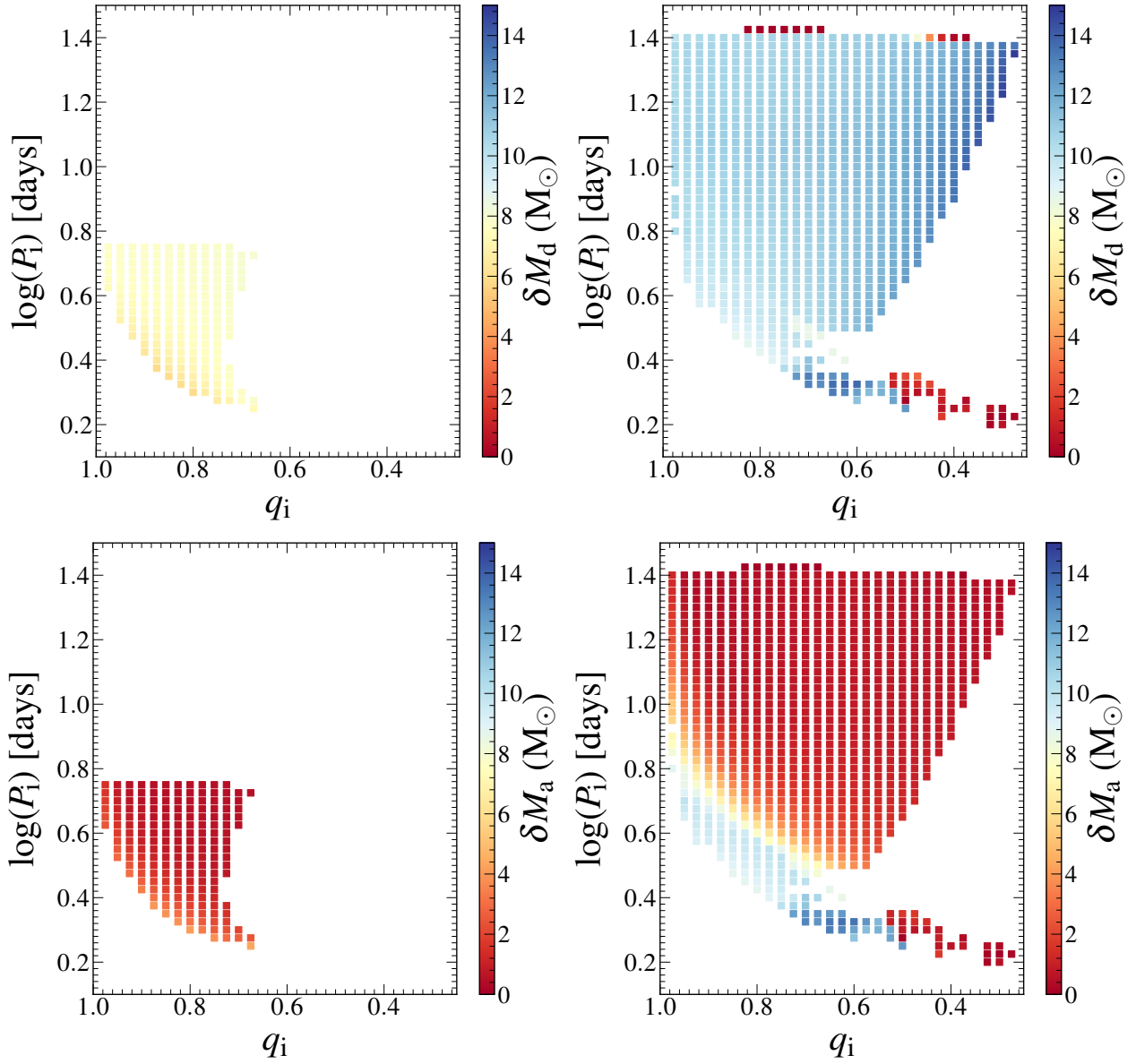
Fig. F.3. Amount of mass lost by the donor stars δM_d (top panels) and gained by the accretor δM_a (bottom panels) during fast Case A mass transfer phase, for systems with initial donor masses of $\sim 16\,M_\odot$ and $\sim 40\,M_\odot$ in the left and right panels, respectively.
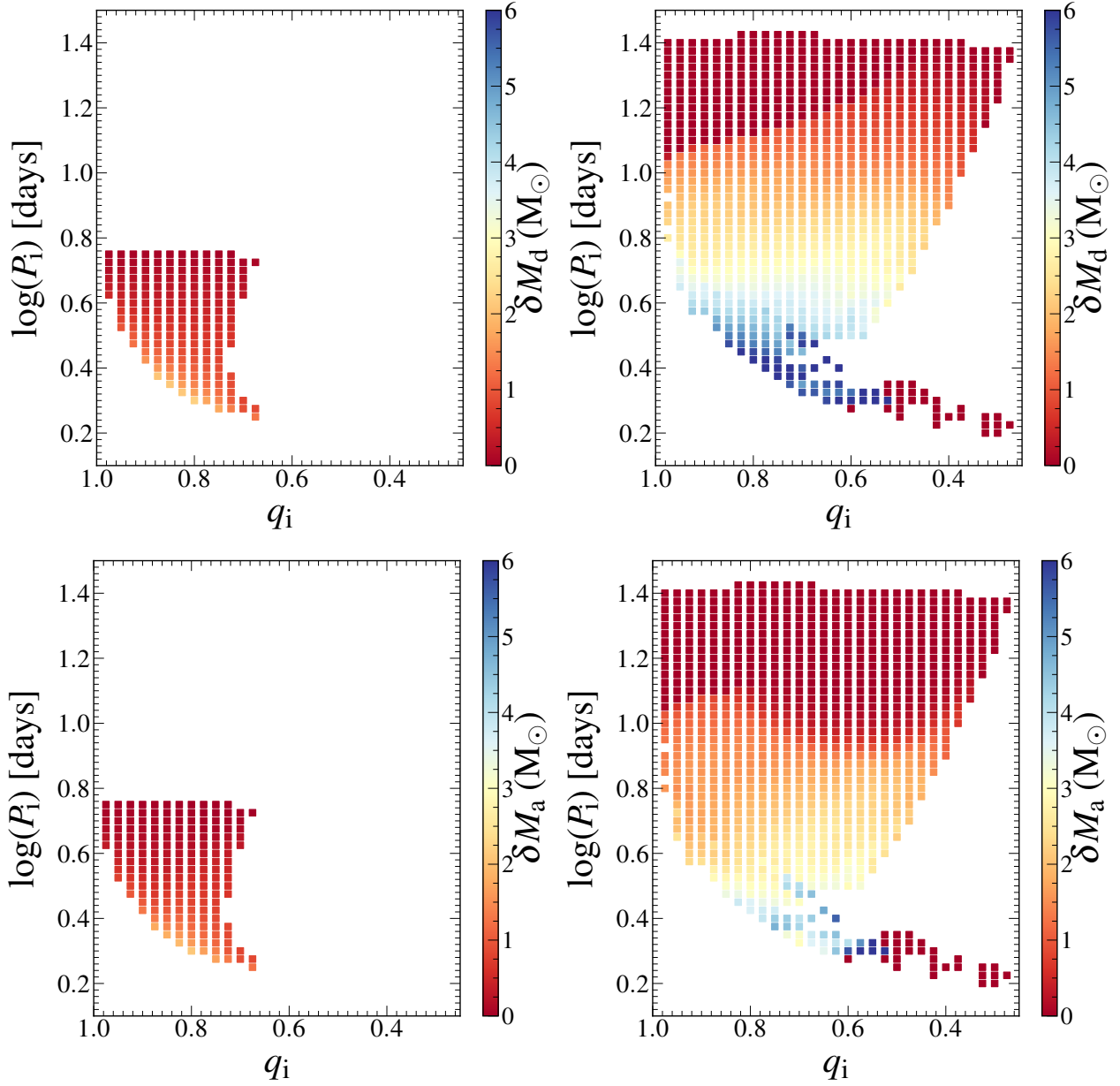
Fig. F.4. Amount of mass lost by the donor stars δM_d (top panels) and gained by the accretor δM_a (bottom panels) during slow Case A mass transfer phase, for systems with initial donor masses of $\sim 16\,M_\odot$ and $\sim 40\,M_\odot$ in the left and right panels, respectively.
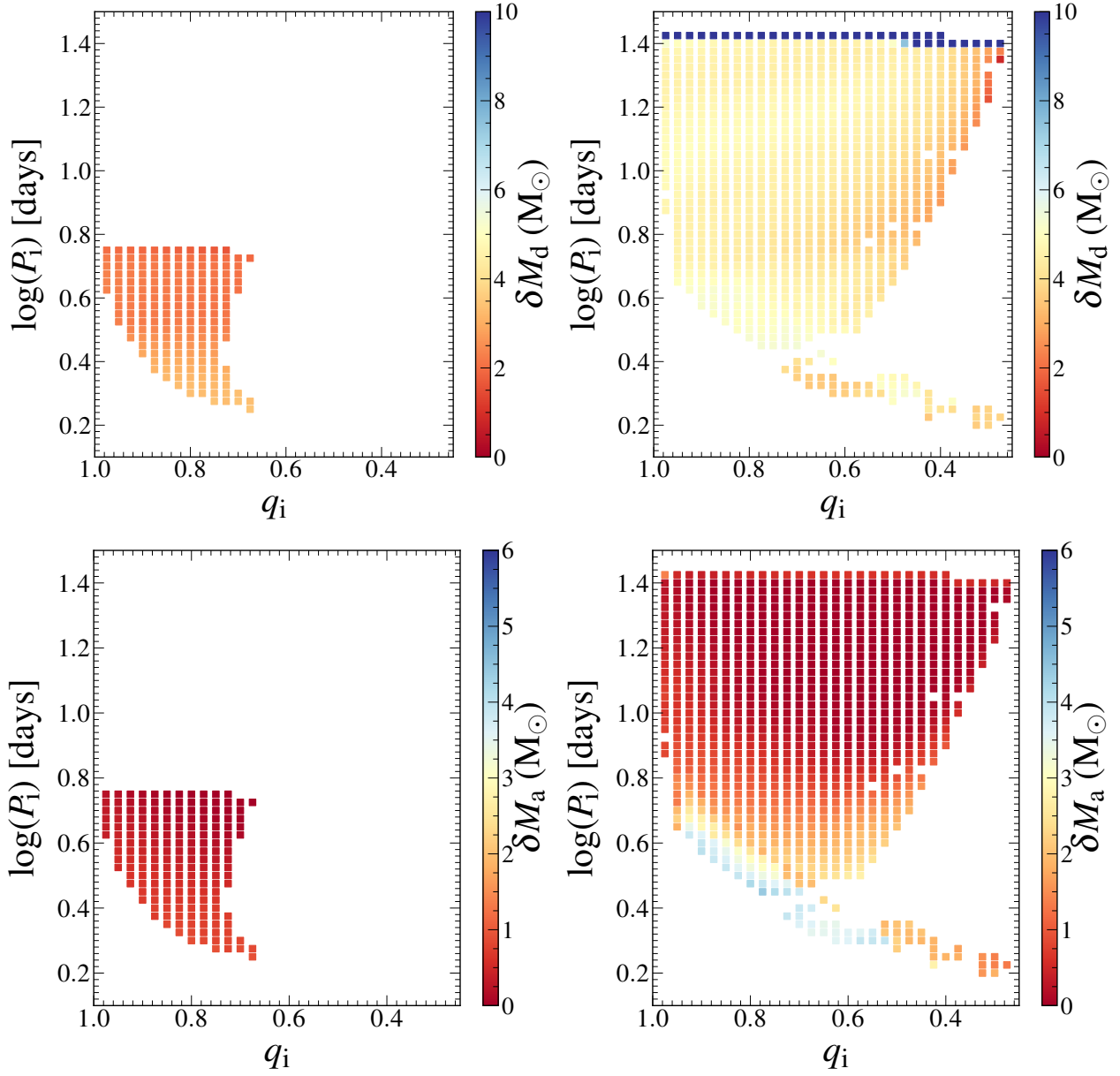
Fig. F.5. Amount of mass lost by the donor stars δM_d (top panels) and gained by the accretor δM_a (bottom panels) during Case AB mass transfer phase, for systems with initial donor masses of $\sim 16\,M_\odot$ and $\sim 40\,M_\odot$ in the left and right panels, respectively.
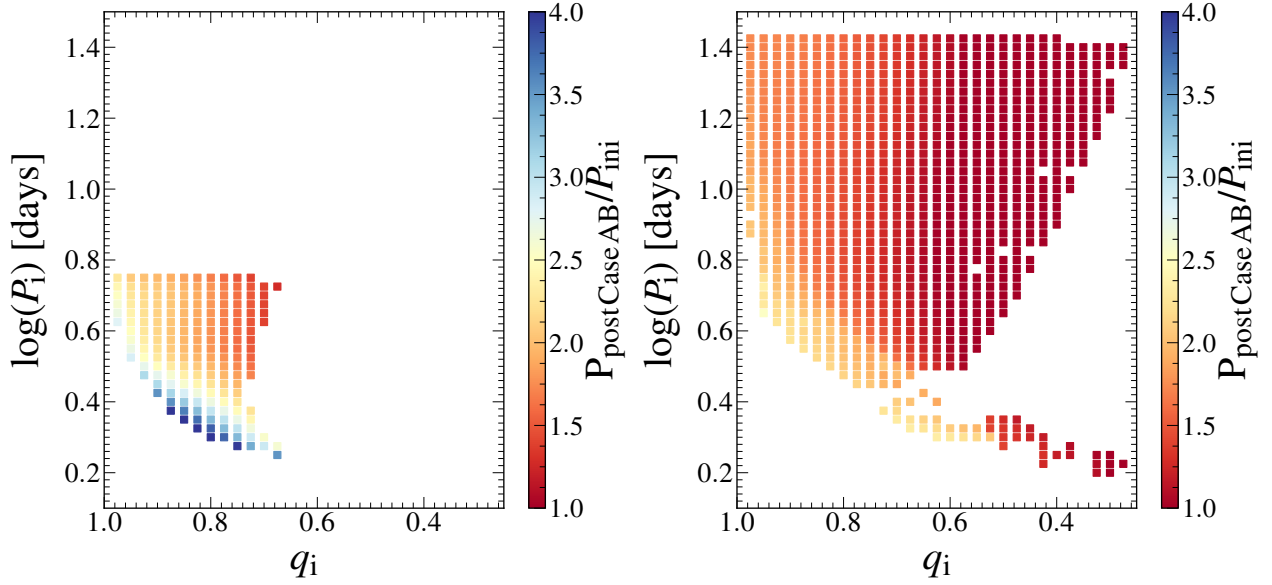
Fig. F.6. Ratio of the binary orbital period after Case AB mass transfer phase to the initial orbital period (colour coded) as function of initial orbital period and initial mass ratio, for systems with initial donor masses of $\sim16\,M_\odot$ and $\sim40\,M_\odot$ in the left and right panels, respectively.

Appendix G: Binary properties after Case AB mass transfer

Here, we show the binary properties of post Case AB models when the central helium mass fraction of the donor is 0.10.
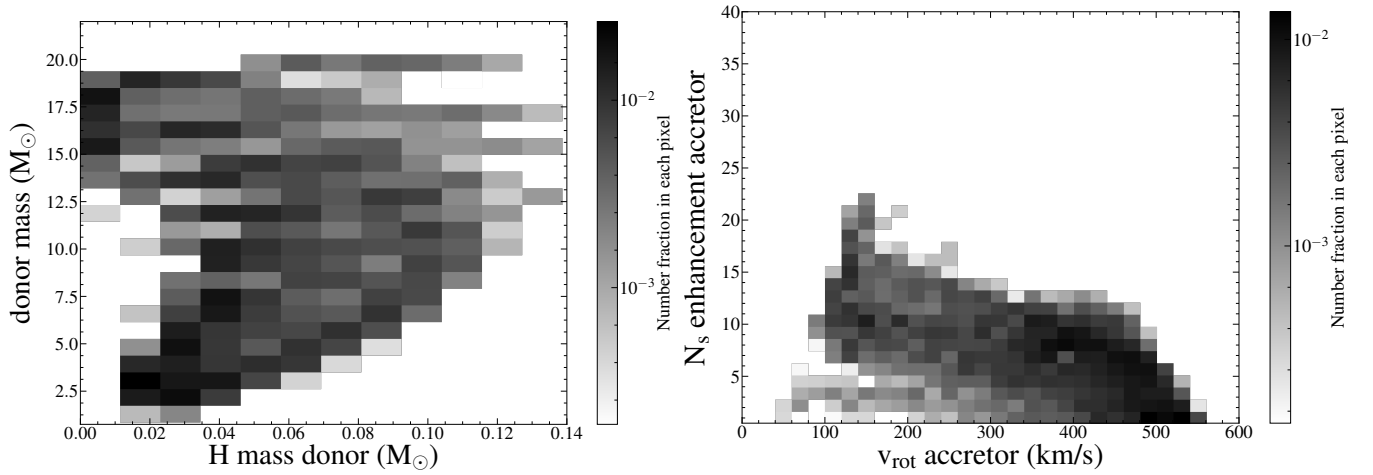
Fig. G.1. Probability density distribution the leftover hydrogen mass vs total stellar mass of the donor (left panel) and of the surface nitrogen mass fraction enhancement and rotational velocity for the mass gainer, for our binary models after the Case AB mass transfer phase. In contrast to Fig. 11, which depicts the same models at a time where the central helium mass fraction of the donors is 0.9, here we display the information for a donor central helium mass fraction of 0.1.

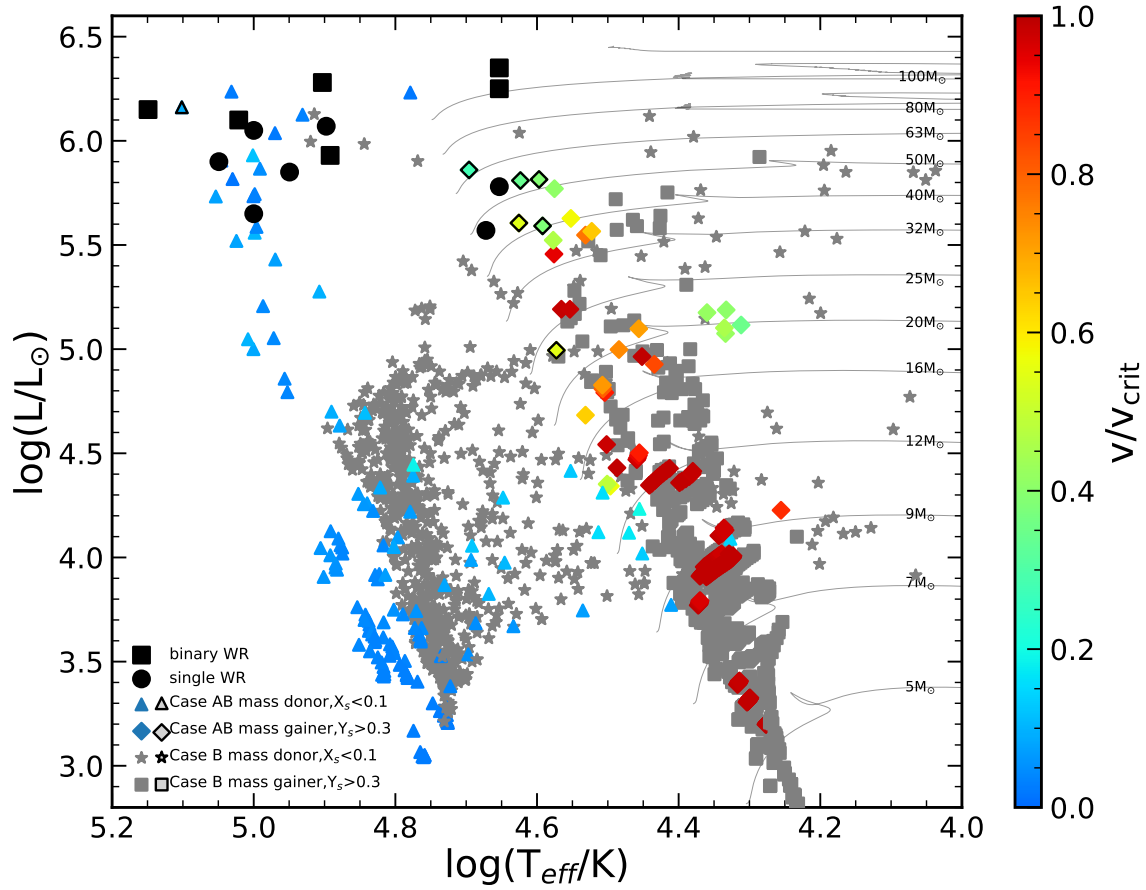# Appendix to Chapter 3

B.1 More efficient semiconvection

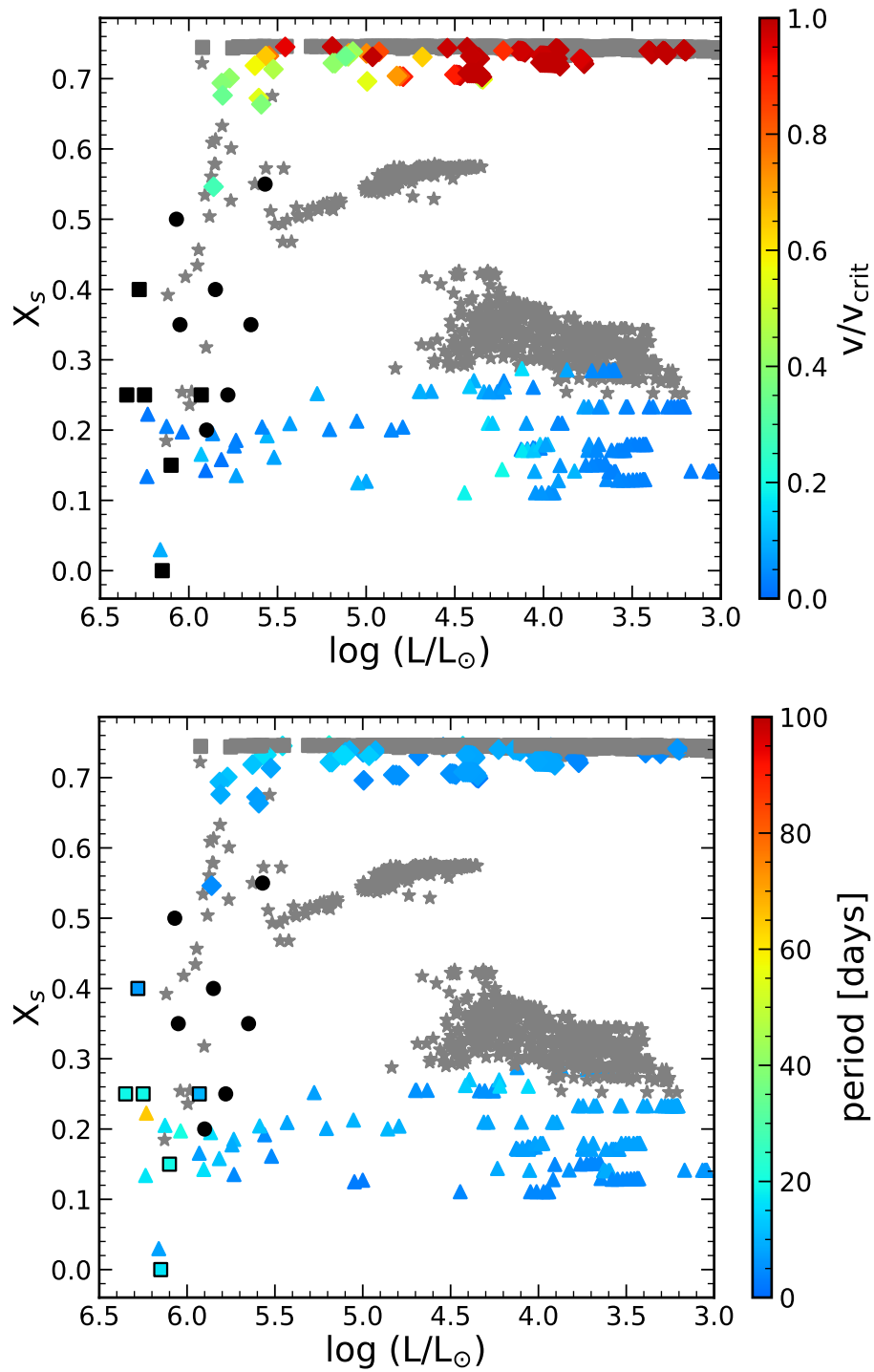
Figure B.1: Same as Fig. 3.12 but for α_{sc}=10.

Figure B.2: Same as Fig. 3.13 (top and bottom panel corresponds to left and right panel respectively) but for α_{sc}=10.

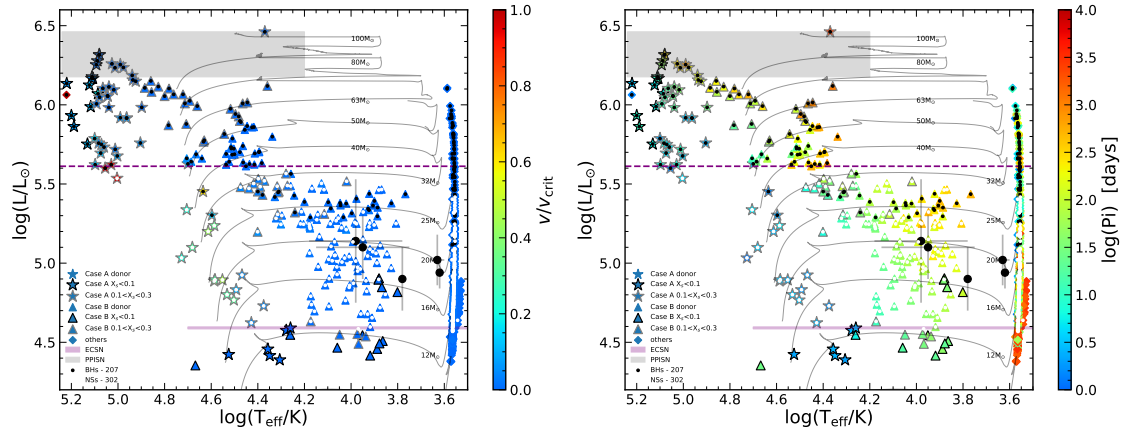# Appendix to Chapter 4

C.1 Additional plots

Figure C.1: Same as Fig. 4.2 but with the colourbar showing the ratio of rotational velocity to the critical rotational velocity of the individual binary components prior to CC (left panel) and the initial orbital period of the binary model (right panel).

Appendix to Chapter 5

Astronomy
&
Astrophysics

X-ray emission from BH+O star binaries expected to descend from the observed galactic WR+O binaries

K. Sen[1,2,*] , X.-T. Xu[1,2,*], N. Langer[1,2], I. El Mellah[3], C. Schürmann[1,2], and M. Quast[1]

[1] Argelander-Institut fur Astronomie, Universitat Bonn, Auf dem Hugel 71, 53121 Bonn, Germany
  e-mail: ksen@astro.uni-bonn.de
[2] Max-Planck-Institut fur Radioastronomie, Auf dem Hugel 69, 53121 Bonn, Germany
[3] Univ. Grenoble Alpes, CNRS, IPAG, 414 Rue de la Piscine, 38400 Saint-Martin-d'Hères, France

ABSTRACT

Context. In the Milky Way, ~18 Wolf-Rayet+O star (WR+O) binaries are known with estimates of their stellar and orbital parameters. Whereas black hole+O star (BH+O) binaries are thought to evolve from WR+O binaries, only one such system is known in the Milky Way. To resolve this disparity, it was suggested recently that upon core collapse, the WR stars receive large kicks such that most of the binaries are disrupted.
Aims. We reassess this issue, with a particular emphasis on the uncertainty in predicting the X-ray emission from wind-accreting BHs in BH+O binaries, which is key to identifying such systems.
Methods. BH+O systems are thought to be X-ray bright only when an accretion disk forms around the BHs. We followed the methodology of previous work and applied an improved analytic criterion for the formation of an accretion disk around wind accreting BHs. We then used stellar evolutionary models to predict the properties of the BH+O binaries which are expected to descend from the observed WR+O binaries if the WR stars would form BHs without a natal kick.
Results. We find that disk formation sensitively depends on the O stars' wind velocity, the amount of specific angular momentum carried by the wind, the efficiency of angular momentum accretion by the BH, and the spin of the BH. We show that whereas the assumption of a low wind velocity may lead to the prediction that most of the BH+O star binaries will have an extended X-ray bright period, this is not the case when typical wind velocities of O stars are considered. We find that a high spin of the BH can boost the duration of the X-ray active phase as well as the X-ray brightness during this phase. This produces a strong bias for detecting high mass BH binaries in X-rays with high BH spin parameters.
Conclusions. We find that large BH formation kicks are not required to understand the sparsity of X-ray bright BH+O stars in the Milky Way. Probing for a population of X-ray silent BH+O systems with alternative methods can likely inform us about BH kicks and the necessary conditions for high energy emission from high mass BH binaries.

Key words. stars: massive – stars: evolution – stars: black holes – X-rays: binaries – binaries: close

1. Introduction

The detection of gravitational waves by LIGO/VIRGO in the last decade has opened a new window to look at our Universe. Since the first observation by LIGO in 2015 (Abbott et al. 2016, 2019), most of these, now routine, events are associated with merging stellar mass black holes (BHs, Abbott et al. 2019). Thereby, the interest in the study of BHs has been revitalised (de Mink & Mandel 2016; Marchant et al. 2016; Belczynski et al. 2020; Woosley et al. 2020; du Buisson et al. 2020). But the evolution of massive star binaries towards binary compact object mergers is still riddled with uncertainties (Langer 2012; Crowther 2019).

Apart from gravitational wave signals from compact object mergers and direct imaging of the supermassive BH shadows (Akiyama 2019), BHs can be detected via microlensing (Minniti et al. 2015; Masuda & Hotokezaka 2019; Wyrzykowski & Mandel 2020), tidal disruption events (Perets et al. 2016; Kremer et al. 2019), and X-ray emission due to accretion on the BH. In the latter case, the source of material can be a dense interstellar medium (Fujita et al. 1998;

Tsuna et al. 2018; Scarcella et al. 2021), or an orbiting stellar companion (Orosz et al. 2011).

A large number of binary population synthesis studies have been undertaken to predict the event rate of merging compact objects (Mennekens & Vanbeveren 2014; Belczynski et al. 2014; Stevenson et al. 2015; de Mink & Belczynski 2015; Kruckow et al. 2018). One of the major uncertainties in population synthesis studies (for a discussion, see O'Shaughnessy et al. 2008) is whether the formation of a BH is preceded by a supernova (SN) explosion and if so, whether the BH receives a natal kick high enough to disrupt the binary in which the BH formed (Mandel & Müller 2020; Mandel et al. 2021; Woosley et al. 2020). As expected, the presence or absence of a substantial kick during BH formation significantly affects the BH-BH merger rates calculated by population synthesis calculations (Mennekens & Vanbeveren 2014; Belczynski et al. 2016).

Direct evidence towards high or low BH kicks is inconclusive (Özel et al. 2010; Farr et al. 2011; Belczynski et al. 2012). On the one hand, in Galactic low mass X-ray binaries containing a BH, BHs were found to have formed with low or modest kick velocities (Brandt et al. 1995; Willems et al. 2005; Fragos et al. 2009; Wong et al. 2012). Belczynski et al. (2016) (table 7, and references therein) have given empirical evidence for low BH natal kicks. On the other hand, Repetto et al. (2012,

* The first two authors have contributed equally to this work.

Article published by EDP Sciences

A138, page 1 of 14

2017) found that their binary models can adequately explain the observed population of low mass BH binaries above the Galactic plane when high BH kick velocities, similar to the ones assumed for the formation of neutron stars (Hobbs et al. 2005), are adopted during BH formation. Moreover, some works have suggested a BH mass-dependent natal kick distribution (Mirabel & Rodrigues 2003; Dhawan et al. 2007), with more massive BHs receiving lower kicks.

Several teams have studied whether very massive stars can explode at the end of their lifetime (O'Connor & Ott 2011; Ugliano et al. 2012). Sukhbold et al. (2018) and Woosley (2019) predict that most of the hydrogen-free helium stars having masses between 7–30 $M_\odot$, which also manifest as Wolf-Rayet (WR) stars during helium burning, do not explode with an associated supernova but instead implode into BHs. Mirabel & Rodrigues (2003) provided evidence that WR stars might become BHs with little or no kick.

Langer et al. (2020) predict to find that approximately three out of every 100 massive binary stars host a BH. The average lifetime of the WR+O phase (~0.4 Myrs, given by the lifetime of the WR phase) is much smaller than the lifetime of the BH+O phase (which is given by the remaining main sequence lifetime of the O star). Hence, if the transition from the WR+O stage to the BH+O stage happens without the binary being disrupted, we expect the Milky Way to host more binaries containing BHs than WR stars. However, the observed number of WR+O star binaries are much larger than BH+O star binaries.

Vanbeveren et al. (2020) (hereafter V20) assessed this problem with the following two assumptions: (i) WR stars collapse to form BHs with no natal kick and (ii) a BH+O binary is detectable if the BH has an accretion disk and the X-ray flux emitted from the accretion disk is above the detection threshold of current X-ray telescopes. They predict to find over 200 wind-fed BH high mass X-ray binaries (HMXBs) in the Milky Way. There is only one observed in the Milky Way (Cygnus X-1, see e.g., Hirsch et al. 2019).

The large discrepancy between the predicted and observed number of wind-fed BH HMXBs led V20 to conclude that most of the WR stars must explode in a supernova to form neutron stars with an associated large natal kick that disrupts the binaries, or BH formation itself is associated with a high kick velocity that disrupts most of the progenitor WR+O binaries at the time of BH formation. This conclusion would greatly affect the merger rates of BH-BH and BH-NS mergers as many population synthesis results assume low kick velocities for BH formation.

In this work, we follow Shapiro & Lightman (1976) to formulate a condition for the formation of accretion disks and detectability of a BH+O system as a wind-fed BH HMXB. We investigate the effect of the stellar wind velocity, efficiency of angular momentum accretion from the stellar wind, and the spin of the BH on our prediction of the number of wind-fed BH HMXBs. We also revisit the assumptions and definitions of stellar parameters used to derive the accretion disk formation criterion in the work of V20.

In Sect. 2, we outline the definitions and assumptions used to derive our accretion disk formation criterion. We then predict the population of BH+O binaries and study the effect of uncertain parameters on our predictions in Sect. 3. We compare the assumptions and results in our work with the literature in Sect. 4. In Sect. 5, we critically discuss the implications of the uncertainties that are present in the calculation of the X-ray active lifetime of BH+O binaries and outline our main conclusions from this work in Sect. 6.

Table 1. Stellar parameters of the anticipated BH+O binaries obtained by V20 at BH formation, in order of increasing orbital period.

Progenitor system	Distance (kpc)	O star mass ($M_\odot$)	BH mass ($M_\odot$)	Orbital period (days)	$L/L_{\rm Edd}$ of O star
WR 155	2.99	30	12	2.6	0.161
WR 151	5.38	28	10	3.4	0.076
WR 139	1.31	28	6	5.0	0.101
WR 31	6.11	24	7	6.1	0.140
WR 42	2.44	27	14	8.7	0.156
WR 47	3.49	47	20	10.5	0.317
WR 79	1.37	24	7	10.7	0.076
WR 127	3.09	20	6	11.8	0.076
WR 21	3.99	37	10	11.8	0.341
WR 9	4.57	32	8	15.0	0.299
WR 97	2.15	30	9	18.3	0.304
WR 30	5.09	34	14	20.4	0.303
WR 113	1.80	22	8	35.9	0.054
WR 141	1.92	26	18	43.1	0.076
WR 35a	5.84	19	10	68.2	0.054
WR 11	0.34	31	8	86.8	0.107
WR 133	1.85	34	9	158.0	0.107

Notes. The BH is assumed to have formed at the end of core helium depletion of the WR star in the progenitor WR+O binaries.

2. Method

2.1. Sample selection

In the Milky Way, there are about ~53 observed WR+O type binaries[1] (van der Hucht 2001, 2006; Crowther et al. 2015; Rosslowe & Crowther 2015). Of them, 38 are designated as double-lined spectroscopic binaries (SB2). V20 consider a sub-population of 17 SB2 binaries that have estimates of the masses of both components and orbital period of the binary. The present masses of both components and the orbital period of the selected sample of 17 binaries can be found in table 1 of V20. We find one more SB2 system, WR 22, that has estimates of its component masses and orbital period (Schweickhardt et al. 1999). This system has an orbital period around ~80 days. In this work, we further look at the distance of the systems from Earth using the catalogue of galactic WR stars (Rosslowe & Crowther 2015) (Table 1). To be consistent with the analysis of V20, we chose to analyse the sub-sample of the 17 WR+O binaries. We also explain later that the addition of WR 22 to the sample of 17 SB2 binaries reinforces the conclusions we derive from our work.

The orbital period distribution of WR+O binaries in the Large Magellanic Cloud (LMC) is expected to peak at ~100 days (Langer et al. 2020), which can be expected to be similar in the Milky Way. Observationally, short-period WR+O star binaries are much easier to detect than long-period ones. This implies that the sub-sample of ~17 mostly short-period WR+O binaries considered in this work may indeed account for nearly all short-period WR+O binaries expected for the ~53 WR+O binaries observed in the Milky Way. We see below that only short-period WR+O binaries can manifest as X-ray bright BH+O systems. In this sense, the sub-sample of 17 WR+O binaries can be used as a suitable proxy to analyse the detectability of anticipated BH+O binaries in the Milky Way.

---

[1] http://pacrowther.staff.shef.ac.uk/WRcat/index.php

2.2. Binary evolution

We describe the further modelling of the chosen WR+O binaries in the following sub-sections.

2.2.1. WR+O binary evolution up to BH formation

We adopt the stellar and orbital parameters of the anticipated BH+O binaries derived by V20 at the time of BH formation (Table 1). We describe the modelling of the evolution of the WR+O star binaries performed by V20 up to the point of BH formation briefly in the following paragraph.

The orbital periods of the considered WR+O star binaries suggest that most of them did in fact undergo mass transfer in the past, which stripped the hydrogen-rich envelope of the donor stars and the O star companions may have been rejuvenated due to accretion (Braun & Langer 1995). The expected masses of the WR stars at core helium depletion were calculated using the evolutionary tracks of hydrogen deficient, post-Roche Lobe overflow, core helium burning star models of Vanbeveren et al. (1998b). For a WR star of the nitrogen sequence (i.e., WN star), the WR star was assumed to be at the beginning of the helium burning. On the other hand, if a WR star was of the carbon sequence (WC star), the calculation was started from the point during core helium burning at which helium burning products appear at the stellar surface due to wind mass loss. This assumption neither affects the main results of V20 nor this study (see appendix of V20 for a discussion). Following this evolution, the expected mass of the WR star at the end of core helium burning was calculated. The orbital periods of the WR+O binaries at the end of core helium burning of the WR stars were estimated using the close binary evolutionary models of Vanbeveren et al. (1998a).

At the end of core helium depletion, we assumed that the WR stars will directly collapse into BHs of the same mass without any natal kick. This means that we did not account for the binary disruption which might be induced by high natal kicks. We also neglected the changes in orbital separation and eccentricity provoked by natal kicks. We thus expect the number of wind-fed BH HMXBs predicted from our analysis to be an upper limit on the actual number. Below, we test this assumption a posteriori by comparing our predicted number of wind-fed BH HMXBs with observations. We note that a small natal kick may not lead to the binary being disrupted, but introduce an eccentricity in the orbit that may result in the production of X-ray at periastron passage. In such a case, the X-ray emission is expected to be periodic and active only for a small fraction of the orbital period. Therefore, we do not expect a small natal kick to significantly alter our results.

2.2.2. The BH+O phase

After the formation of the BH, orbital evolution is driven by the mass loss from the O star companion, which reduces the mass of the O star and carries away orbital angular momentum (Quast et al. 2019; El Mellah et al. 2020a). Whether the orbit shrinks or expands depends on the mass ratio and the fraction of wind material escaping from the system (see Fig. 10 in El Mellah et al. 2020a). In our case, the ratio of O star masses to BH masses are below 5, and more than ~99% of wind material escapes from the binary (see Fig. A.1). This implies that we can assume that the orbital parameters remain unchanged during the BH+O phase. Considering the fact that most of these systems might have undergone a mass transfer episode in the past, we also assumed that the orbit is circular.

We followed the subsequent evolution of the O star companions in the BH+O binaries by interpolating in the massive single star models of Ekström et al. (2012). Due to past mass transfer from the WR progenitors to the O star companions, the O stars can be found to be younger than the age of the binaries, by the process of rejuvenation (Braun & Langer 1995). This is the so-called rejuvenated ages of the O stars. The rejuvenated ages of the O stars were obtained by V20 from their observed mass, spectral type, and luminosity class. Here, we estimated the rejuvenated ages of the O stars at the time of BH formation by reproducing the results of V20 with their assumptions. For the systems that are not expected to become detectable BH+O binaries by V20, the rejuvenated ages of the O stars at the time of BH formation were set to be zero. This did not affect our results as we also found no X-ray emission from those systems during the BH+O phase. We assume that the BH+O phase lasts until the O stars leave the main sequence or fill their Roche lobes, whichever is earlier. On the other hand, V20 assumed that the BH+O phase lasts until the O stars fill its Roche lobes.

2.3. Wind-captured disks during the BH+O phase

Due to the gravitational field of the BH, a fraction of the stellar wind from the O star can be captured by the BH (Illarionov & Sunyaev 1975). As a result, a wind-captured disk may form around the BH (Shapiro & Lightman 1976; Iben & Tutukov 1996). Due to turbulent viscosity produced by instabilities such as the magneto-rotational instability (Balbus & Hawley 1991), accreting material moves inwards in an optically thick and geometrically thin accretion disk in which gravitational energy is efficiently converted into thermal energy, producing X-ray emission (Shakura & Sunyaev 1973).

2.3.1. Wind velocity

The O star wind velocity (v_{wind}) at the location of the BH can be approximated as

$$v_{\mathrm{wind}} = v_{\infty} \left(1 - \frac{R_{\mathrm{O}}}{a} \right)^{\beta},$$ (1)

where a is the orbital separation, v_{∞} is the terminal velocity of stellar wind, and R_{O} is the radius of the O star. For O stars (effective temperature higher than 30 kK), the value of β is 0.8–1 (Groenewegen & Lamers 1989; Puls et al. 1996) and the terminal velocity is given by (Vink et al. 2001)

$$v_{\infty} \simeq 2.6 \, v_{\mathrm{esc}},$$ (2)

where v_{esc} is the modified escape velocity of the O star

$$v_{\mathrm{esc}} = \sqrt{\frac{2GM_{\mathrm{O}}}{R_{\mathrm{O}}} (1 - \Gamma)},$$ (3)

where Γ is the Eddington factor and M_{O} is the mass of the O star companion.

2.3.2. Disk formation

A necessary condition for the formation of a wind-captured disk around a BH is

$$\frac{R_{\mathrm{disk}}}{R_{\mathrm{ISCO}}} > 1,$$ (4)

where R_{ISCO} is the radius of the innermost stable orbit and R_{disk} is the circularisation radius of a Keplerian accretion disk, which is defined by

$$R_{disk} = \frac{j^2}{GM_{BH}}, \tag{5}$$

where j is the specific angular momentum of the captured wind material, G is the gravitational constant, and M_{BH} is the mass of the BH. The radius of the innermost circular orbit around a BH is evaluated by

$$R_{ISCO} = \frac{6GM_{BH}}{c^2}\gamma_{\pm}, \tag{6}$$

where c is the speed of light and $\gamma_{\pm}$ represents the modification caused by the BH spin with respect to the disk on the location of the innermost stable circular orbit. It ranges from 1/6 for a maximally rotating BH surrounded by a prograde disk to 3/2 for a maximally rotating BH surrounded by a retrograde disk, assuming the disk and BH angular momenta are aligned (El Mellah 2017). For a non-rotating BH, $\gamma_{\pm} = 1$. Qin et al. (2018) found that the spin of the first formed BH in a binary is usually very low. For a considerable change in the spin, the BH needs to accrete an amount of mass of the order of its own mass (Wong et al. 2012). Regardless of the birth spin of the BH, we assume that the spin of the BH does not change during the BH+O phase as only a small fraction of the BH mass is accreted during this phase.

The specific angular momentum (j) accreted by the BH from the O star wind can be written as (Shapiro & Lightman 1976, eq. 7)

$$j = \frac{1}{2}\eta\Omega_{orb}R_{acc}^2, \tag{7}$$

where Ω_{orb} is the orbital angular velocity, η is a numerical factor which quantifies the efficiency of specific angular momentum accretion by the BH from the available wind matter, and R_{acc} is the accretion radius which is the typical distance to the BH at which the wind trajectory and/or speed is significantly altered by the gravitational field of the BH. It can be written as (Davidson & Ostriker 1973)

$$R_{acc} = \frac{2GM_{BH}}{v_{rel}^2}, \tag{8}$$

where $v_{rel} = \sqrt{v_{wind}^2 + v_{orb}^2}$ is the relative velocity of the stellar wind with respect to the BH for a circular orbit, v_{wind} is the wind velocity of the O star companion, and v_{orb} is the relative velocity of the BH with respect to the O star, that is, $v_{orb} = \Omega_{orb}a$.

Equation (7) was obtained under the assumption that the wind velocity is considerably larger than the orbital velocity, which is consistent with our further analysis (see Fig. B.1). If all wind material entering the accretion radius can be accreted by the BH, $\eta = 1$ (Shapiro & Lightman 1976). Detailed hydrodynamical simulations suggest that this efficiency factor can be lower, $\sim 1/3$ (Livio et al. 1986; Ruffert 1999). In what follows, we consider these two values.

In defining the mass ratio $q = M_O/M_{BH}$ and combining Eqs. (5)–(8), the disk formation criterion can be converted into the dimensionless form

$$\frac{2}{3}\frac{\eta^2}{(1+q)^2} > \left(\frac{v_{orb}}{c}\right)^2\left(1 + \frac{v_{wind}^2}{v_{orb}^2}\right)^4\gamma_{\pm}, \tag{9}$$

or equivalently

$$\frac{R_{disk}}{R_{ISCO}} = \frac{2}{3}\frac{\eta^2}{(1+q)^2}\left(\frac{v_{orb}}{c}\right)^{-2}\left(1 + \frac{v_{wind}^2}{v_{orb}^2}\right)^{-4}\gamma_{\pm}^{-1} > 1. \tag{10}$$

Equations (9) and (10) suggest that a wind-captured disk can form around a BH if the captured material carries enough angular momentum, if the wind speed is low compared to the orbital speed, and if the orbital speed is high.

2.4. X-ray luminosity

We can distinguish the following three cases for the morphology of the accretion flow: sub-Eddington accretion via a disk, super-Eddington accretion via a disk, and spherical accretion. The first two happen only if enough angular momentum is carried by the accretion flow (see Sect. 2.3). Super-Eddington accretion occurs when the mass accretion rate is so high that the X-ray luminosity it produces exceeds the Eddington luminosity of the BH. Although super-Eddington accretion onto neutron stars has been observed in ultra-luminous X-ray sources (Bachetti et al. 2014; Fürst et al. 2016; Israel et al. 2017; Chandra et al. 2020), the typical mass accretion rate calculated in our study is much smaller than the Eddington accretion rate for the individual systems (Fig. A.1). Accretion disks with a sub-Eddington mass accretion rate are thought to be geometrically thin and optically thick, centrifugally-maintained structures (Shakura & Sunyaev 1973; Novikov & Thorne 1973). Notwithstanding minor relativistic corrections, such a disk around a BH mostly radiates in X-rays, and the maximum associated luminosity is (Frank et al. 2002; El Mellah 2017):

$$L_X = \frac{1}{2}\frac{GM_{BH}\dot{M}_{acc}}{R_{ISCO}}, \tag{11}$$

where $\dot{M}_{acc}$ is the mass accretion rate.

In order to evaluate the mass accretion rate, we rely on the wind accretion formula introduced by Davidson & Ostriker (1973) (see also the review by Edgar 2004). It is valid in binary systems provided the wind speed at the binary orbital separation is larger than the orbital speed (El Mellah & Casse 2017). In this case, the fraction of the accreted wind can be approximated by

$$\frac{\dot{M}_{acc}}{\dot{M}_{wind}} = \frac{1}{4}\left(\frac{R_{acc}}{a}\right)^2\frac{v_{rel}}{v_{wind}}, \tag{12}$$

where $\dot{M}_{wind}$ is the O star wind mass loss rate.

Finally, in the case of spherical accretion, the mass accretion rate is not an independent variable. Instead, it is set by the location of the sonic point as described in the 1D spherical Bondi model (Bondi 1952). Without an accretion disk, thermal bremsstrahlung dominates the radiation from the optically thin wind material, which makes spherical accretion radiatively inefficient (Shapiro & Teukolsky 1983). We do not expect this regime to produce any X-ray emission above detectable levels.

2.5. Detectability of a BH+O system

The X-ray active lifetime (τ_{L_X}) of each BH+O binary model considered is defined as the amount of time during the BH+O phase when the system is detectable as a wind-fed BH HMXB. We assume that this is only the case when an accretion disk forms, that is, Eq. (10) is satisfied, and when the calculated X-ray luminosity (Eq. (11)) and the distance to the source yield a flux
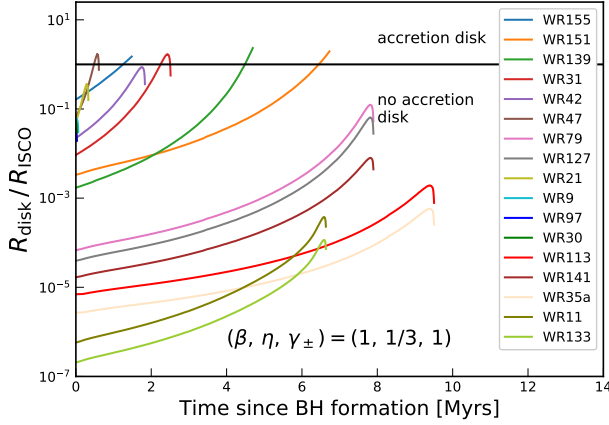
Fig. 1. Evolution of the ratio of the circularisation radius $R_{\rm disk}$ to the radius of the innermost stable circular orbit $R_{\rm ISCO}$ during the BH+O phase as a function of the time since the formation of the BH for $(\beta, \eta, \gamma_\pm) = (1, 1/3, 1)$. The black horizontal line shows the dividing line above which an accretion disk is expected. The colour coding in the legend identifies the 17 progenitor WR+O star systems that are expected to give rise to the BH+O binaries.

above a detection threshold that we set to $\sim 10^{-11}\,{\rm erg\,s^{-1}\,cm^{-2}}$. Our adopted threshold is similar to the flux detection limit of non-focussing X-ray telescopes with typical integration times (Wood et al. 1984; Bradt et al. 1991; In't Zand et al. 1994). We discuss the relevance of the X-ray flux threshold in the light of the sensitivity of current all-sky monitoring X-ray instruments in Sect. 5.

3. Results

3.1. Fiducial parameter set

Figure 1 shows the evolution of the ratio of the circularisation radius ($R_{\rm disk}$) to the radius of the innermost stable circular orbit ($R_{\rm ISCO}$) during the BH+O phase for the 17 progenitor WR+O star binaries. For our fiducial case, we adopted the value of $\beta = 1$ (Vink et al. 2001), $\eta = 1/3$ (El Mellah 2017), and $\gamma_\pm = 1$ (Qin et al. 2018). The O star expands during core hydrogen burning, leading to a decrease in its wind velocity, which makes the formation of a wind-captured disk easier during the late stages of its main sequence evolution. In most systems, there is a small decrease in the ratio of the circularisation radius to the innermost stable circular orbit towards the end of the BH+O star phase, which is related to the shrinkage of massive stars when they approach their core hydrogen depletion. WR139, WR151, and WR155 do not present this feature since their BH+O phases are terminated due to the Roche Lobe filling condition before their O stars complete core hydrogen burning. While the mass ratio of WR 139 suggests this system will merge at this time, the other two could undergo an SS433-like evolution leading to short-period WR+BH binaries (van den Heuvel et al. 2017), which lies outside the scope of our paper.

We find that no accretion disk forms in 12 of our BH+O models. Among them, three systems are not visible in this plot since the estimated rejuvenated age of their O stars are very close to the O stars' main sequence lifetime, such that the duration of their BH+O phase is very small. Importantly, we find that only in five BH+O models, all with orbital periods ≤ 10 days, can an accretion disk form for a small fraction of the total BH+O phase. For systems with higher orbital periods, an accretion disk does not form at all for the entire BH+O phase. Noting that the orbital
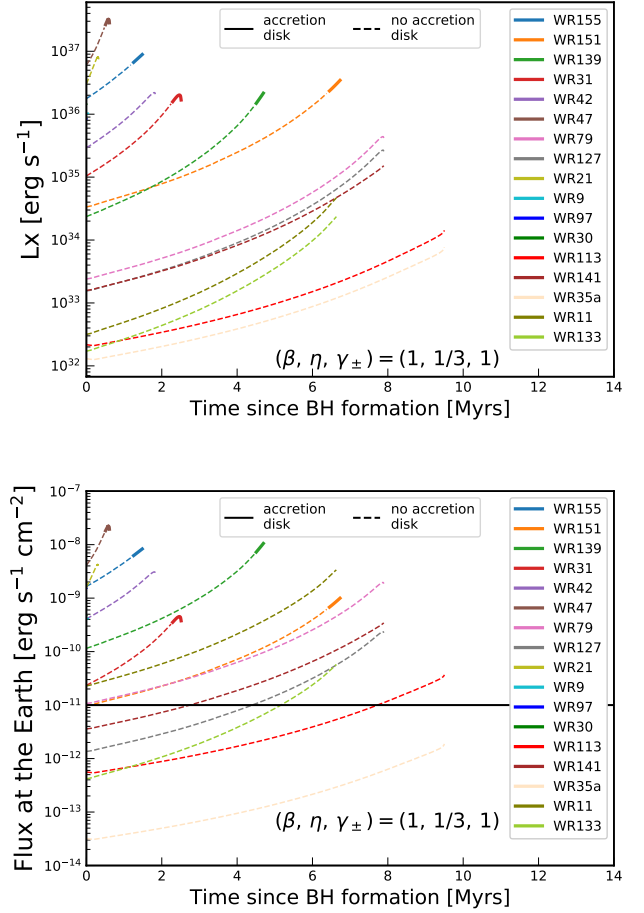
Fig. 2. Evolution of X-ray luminosity (*upper panel*) calculated using Eq. (11) and the corresponding X-ray flux at Earth (*lower panel*) for our BH+O models when an accretion disk can form according to our criterion (solid line). The dashed lines indicate the X-ray luminosity and flux evolution if an accretion disk could form for the entire BH+O phase. The black horizontal line shows our adopted flux detection limit.

period of WR 22 is ~ 80 days, we do not expect that the BH+O binary anticipated to form from WR 22 will be X-ray bright at any time.

Figure 2 shows the X-ray luminosity (top panel) and its corresponding flux at Earth (bottom panel), calculated using Eq. (11) for our BH+O models. We find that when an accretion disk can form, the predicted X-ray flux at Earth is well above the flux detection limit we have assumed. In other words, the X-ray luminosity from the accretion disk is not a bottleneck for our BH+O models to be detectable in X-rays. We note that Eq. (11) only holds when an accretion disk is present such that the dashed lines are only indicative of the X-ray luminosity and flux if an accretion disk could form for the entire BH+O phase. The X-ray luminosity from a BH+O system without an accretion disk is expected to be orders of magnitude lower than what is predicted by Eq. (11) (see discussion in Sect. 2.4).

For each system where an accretion disk can form, we calculated the duration for which it will be detectable as a wind-fed BH HMXB (i.e., the X-ray active lifetime). To predict the number of wind-fed BH HMXB systems that we expect based on the 17 progenitor WR+O star systems, we assume (as in V20) that the observed numbers of WR+O binaries and wind-fed BH HMXBs are proportional to the lifetime in the respective phases. One WR+O binary is thus representative of $\tau_{\rm Lx}/\tau_{\rm WR}$ wind-fed

Table 2. Predicted X-ray active lifetime ($\tau_{\mathrm{L_X}}$, in millions of years) of each of the 17 BH+O binary models and expected number of wind-fed BH HMXBs (N_{XRBs}, last line), for various combinations of β, η, and $\gamma_\pm$.

$\gamma_\pm$	$(\beta,\eta)^{(a)} = (1,1)$			$(\beta,\eta) = (0.8,1)$			$(\beta,\eta) = (1,1/3)$			$(\beta,\eta) = (0.8,1/3)$		
	1/6	1	3/2	1/6	1	3/2	1/6	1	3/2	1/6	1	3/2
WR155	1.5	1.5	1.4	1.5	1.2	0.9	1.4	**0.2**	0.0	0.9	0.0	0.0
WR151	3.6	1.6	1.3	2.9	1.1	0.8	1.3	**0.3**	0.1	0.8	0.0	0.0
WR139	2.0	1.0	0.8	1.6	0.6	0.5	0.8	**0.2**	0.1	0.5	0.0	0.0
WR31	1.9	1.0	0.8	1.6	0.7	0.6	0.8	**0.2**	0.1	0.6	0.0	0.0
WR42	1.8	0.8	0.7	1.7	0.6	0.5	0.7	**0.0**	0.0	0.5	0.0	0.0
WR47	0.6	0.4	0.4	0.6	0.4	0.3	0.4	**0.1**	0.0	0.3	0.0	0.0
WR79	0.8	0.1	0.0	0.6	0.0	0.0	0.0	**0.0**	0.0	0.0	0.0	0.0
WR127	0.6	0.0	0.0	0.4	0.0	0.0	0.0	**0.0**	0.0	0.0	0.0	0.0
WR21	0.3	0.2	0.1	0.3	0.1	0.1	0.1	**0.0**	0.0	0.1	0.0	0.0
WR9	0.1	0.0	0.0	0.1	0.0	0.0	0.0	**0.0**	0.0	0.0	0.0	0.0
WR97	0.0	0.0	0.0	0.0	0.0	0.0	0.0	**0.0**	0.0	0.0	0.0	0.0
WR30	0.0	0.0	0.0	0.0	0.0	0.0	0.0	**0.0**	0.0	0.0	0.0	0.0
WR113	0.0	0.0	0.0	0.0	0.0	0.0	0.0	**0.0**	0.0	0.0	0.0	0.0
WR141	0.0	0.0	0.0	0.0	0.0	0.0	0.0	**0.0**	0.0	0.0	0.0	0.0
WR35a	0.0	0.0	0.0	0.0	0.0	0.0	0.0	**0.0**	0.0	0.0	0.0	0.0
WR11	0.0	0.0	0.0	0.0	0.0	0.0	0.0	**0.0**	0.0	0.0	0.0	0.0
WR133	0.0	0.0	0.0	0.0	0.0	0.0	0.0	**0.0**	0.0	0.0	0.0	0.0
$N_{\mathrm{XRBs}}{}^{(b)}$	33.0	16.6	13.4	28.3	11.8	9.0	13.4	**2.5**	0.7	9.0	0.0	0.0

Notes. The bold highlighted column represents our fiducial case. $^{(a)}$See Eqs. (1) and (7) for the definition of β and η, respectively. $^{(b)}N_{\mathrm{XRBs}}$ is the predicted number of wind-fed BH high mass X-ray binaries by considering 0.4 Myr to be the typical lifetime of WR stars. See Sect. 3 for more details.

BH HMXBs, where τ_{WR} is the duration of the WR+O binary phase. Considering $\tau_{\mathrm{WR}} = 0.4$ Myrs to be the typical lifetime of a WR star (V20), we expect ~2.5 wind-fed BH HMXBs from the 17 WR+O binaries. Accounting for the observational and theoretical bias in the population of WR+O binaries (see discussion in Sect. 2.1), it is likely that the number of wind-fed BH HMXBs in the entire Milky Way would be ~2–3.

3.2. Effects of parameter variations

The predicted number of wind-fed BH HMXBs is sensitive to the uncertainties in the parameters we have assumed. We explore the results computed using reasonable variations to our fiducial parameter set in Table 2. For a non-rotating BH ($\gamma_\pm = 1$), by varying (β,η) from (0.8, 1/6) to (1, 1/2), the predicted number of wind-fed BH HMXBs out of 17 WR+O binaries varies from 0 to 16.6. Considering a maximally spinning BH with a prograde accretion disk, the predicted number can be boosted up to 33, suggesting an observational bias in favour of wind-fed BH HMXBs containing maximally rotating BHs surrounded by a prograde disk. In the following sub-sections, we discuss the effects of these parameters individually.

3.2.1. Efficiency of specific angular momentum accretion

From Eq. (10), the ratio of the circularisation radius to the radius of the innermost stable orbit varies with the square of the efficiency of specific angular momentum accretion

$$\frac{R_{\mathrm{disk}}}{R_{\mathrm{ISCO}}} \propto \eta^2. \tag{13}$$

The predicted X-ray luminosity when an accretion disk can form does not depend on the efficiency parameter. So, the likelihood of the formation of an accretion disk in our BH+O models increases

with the increase in the efficiency of angular momentum accretion by the BH. In Fig. 3, we show the variation of the two above-mentioned quantities with the efficiency of specific angular momentum accretion for the BH+O model corresponding to WR 31. We find that the amount of time an accretion disk can form during the BH+O phase is significantly longer when the efficiency of angular momentum accretion increases by a factor of 3. On the other hand, the X-ray luminosity predicted from Eq. (11) is unaffected. From Table 2, we find that the number of predicted wind-fed BH HMXBs increases by 6.5 times when the η increases from 1/3 to 1, and the other two parameters are at their fiducial value.

3.2.2. BH spin

Our definition of the radius of the innermost stable circular orbit around a BH (Eq. (6)) accounts for the effect of the spin of the BH on the formation of an accretion disk (via $\gamma_\pm$). The spin parameter of BHs in observed wind-fed HMXBs can be quite high, as in Cyg X-1 (Gou et al. 2011; Zhao et al. 2021; Miller-Jones et al. 2021). To account for the spin of the BH, we calculated the predicted number of wind-fed BH HMXB derived from the 17 progenitor WR+O binaries for the following three cases (see Table 2): i) when the BHs are maximally rotating with a prograde accretion disk, ii) when the BHs are maximally rotating with a retrograde accretion disk, and iii) for a non-spinning BH.

Both the ratio of the circularisation radius to the radius of the innermost stable orbit, and the X-ray luminosity from an accretion disk vary inversely with our BH spin parameter

$$\frac{R_{\mathrm{disk}}}{R_{\mathrm{ISCO}}} \propto \gamma_\pm^{-1} \tag{14}$$

and

$$L_{\mathrm{X}} \propto \gamma_\pm^{-1}. \tag{15}$$
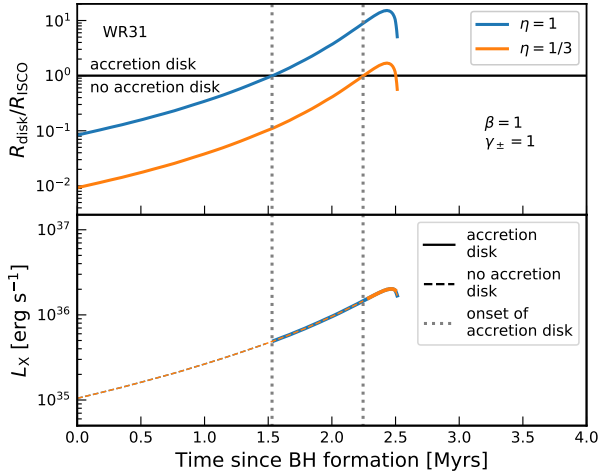
Fig. 3. Effects of η parameter on the ratio of the circularisation radius to the radius of the innermost stable circular orbit (*upper panel*) and the X-ray luminosity (*lower panel*). We take the BH+O binary derived from WR31 as an example. The η parameter is considered to be 1 and 1/3 (colour coded), and $(\beta, \gamma_\pm) = (1, 1)$. The line styles in the *lower panel* have the same meaning as in Fig. 2.
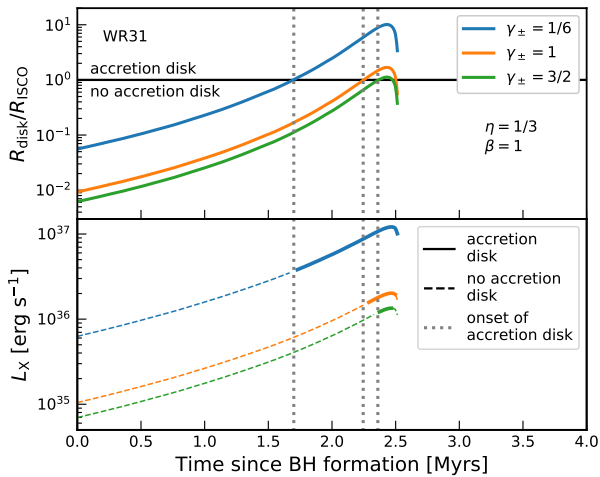
Fig. 4. Effects of the $\gamma_\pm$ parameter. The same as Fig. 3, but $\gamma_\pm$ is considered to be 1/6, 1, and 3/2 (colour coded), and $(\beta, \eta) = (1, 1/3)$. The line styles in the *lower panel* have the same meaning as in Fig. 2.

Figure 4 shows the effect of the BH spin on the formation of an accretion disk and the emitted X-ray luminosity during the BH+O phase of WR 31. For a BH maximally rotating with a prograde accretion disk, both the amount of time for which an accretion disk can form and the X-ray luminosity predicted from the accretion disk increase significantly. In Table 2, we find that the predicted number of wind-fed HMXBs increases by a factor of ~5 for the case of a maximally rotating BH with a prograde disk, and it decreases by a factor of ~3.5 for a maximally rotating BH with a retrograde disk, compared to a non-rotating BH, with the other two parameters being at their fiducial values.

The fact that we predict a short X-ray active lifetime for non-spinning BHs in BH+O systems, while the only observed wind-fed BH HMXB in the Milky Way is known to have high spin parameter, hints to the possibility that only BHs that were born with a very high spin are likely to be detectable as an X-ray source if they are associated with an O star in a close binary configuration. Qin et al. (2019) show that high spin BHs can be
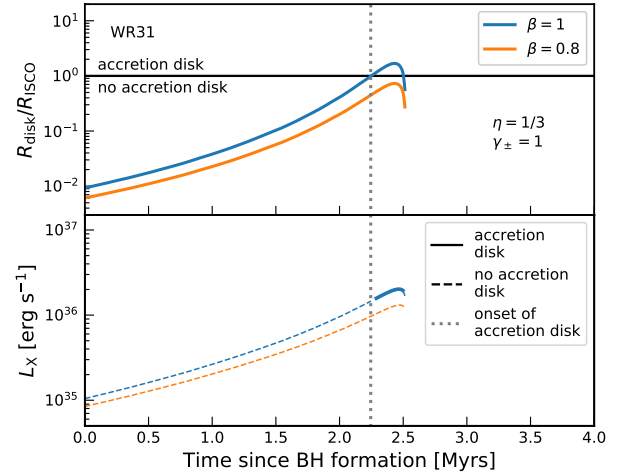
Fig. 5. Effects of the β parameter. The same as Fig. 3, but the β parameter is considered to be 0.8 and 1 (colour coded), and $(\eta, \gamma_\pm) = (1/3, 1)$. The line styles in the *lower panel* have the same meaning as in Fig. 2.

produced only if the efficiency of angular momentum transport in stellar models is reduced. As such, BHs with high birth spins might be rare, as is the case for observed wind-fed BH HMXBs.

3.2.3. O star wind velocity law

The exponent β in the wind velocity law for O stars is constrained from observations to be 0.8–1 (Groenewegen & Lamers 1989; Lamers et al. 1995; Puls et al. 1996). Since wind velocity is always larger than orbital velocity in our work, Eqs. (10) and (11) suggest the following dependencies:

$$\frac{R_{\text{disk}}}{R_{\text{ISCO}}} \propto v_{\text{wind}}^{-8} \propto \left(1 - \frac{R_O}{a}\right)^{-8\beta}, \tag{16}$$

and

$$L_X \propto v_{\text{rel}}^{-3} \propto \left(1 - \frac{R_O}{a}\right)^{-3\beta}. \tag{17}$$

In our analysis, the ratio between the O star radius (obtained from the stellar tracks of Ekström et al. 2012) and orbital separation is generally below 0.4. Therefore, changing β from 1 to 0.8 can maximally reduce the ratio of the circularisation radius to the radius of the innermost stable circular orbit by a factor of ~2, making the formation of the accretion disk more difficult. Likewise, the predicted X-ray luminosity from Eq. (11) is also decreased.

We present the effects of the β parameter on the formation of an accretion disk and the X-ray luminosity emitted from the disk in Fig. 5, where we use the BH+O model derived from WR 31 as an example. We find that even the change in the assumed β value from 1 to 0.8 makes the BH+O model of WR 31 become X-ray inactive due to the inability to form an accretion disk. The predicted X-ray luminosity and thereby the X-ray flux from an accretion disk, if it were to form, is also decreased, but not as significantly as to fall beyond our flux detection limit.

From Table 2, we see that when we change the value of the β from 1 to 0.8, while the other parameters remain at their fiducial values, our BH+O binary models do not have any X-ray bright phase. The predicted number of wind-fed BH HMXBs decreases from ~2.5 to zero. This shows that the X-Ray active lifetime of the BH+O binaries analysed in our work is very sensitive to the assumed wind velocity of the O star companion.
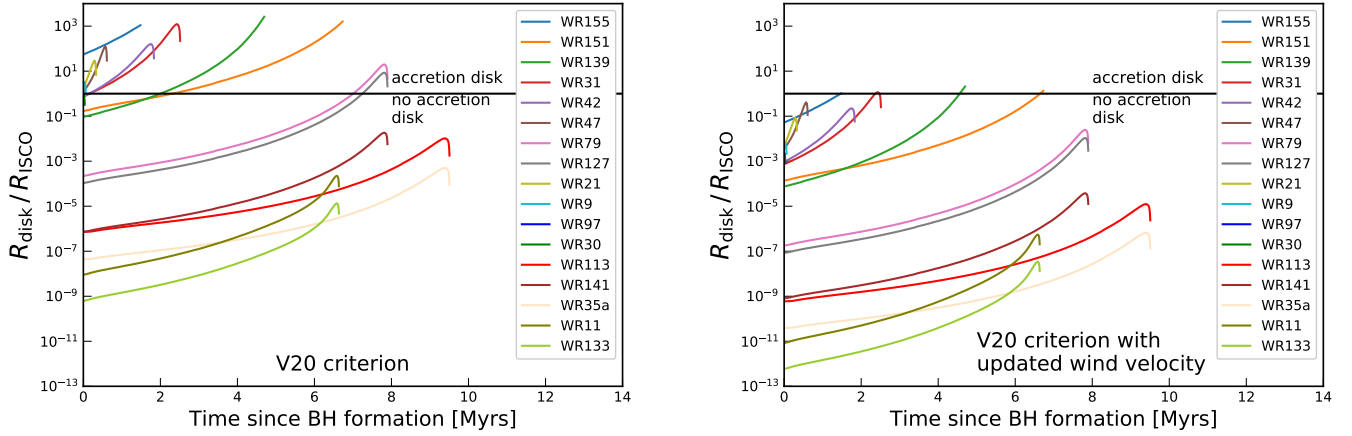
Fig. 6. Evolution of the ratio of the circularisation radius of the accreted wind matter from the O star to the radius of the innermost stable circular orbit of the BH for the 17 BH+O star binary models as a function of the time since the formation of the BH. *Left panel*: evolution as calculated by V20, which does not account for the orbital velocity of the companion and the typical wind velocity of O stars. *Right panel*: same evolution when we use the typical O star wind velocity (Eq. (1)), the mass of the BH, and the orbital velocity of the O star companion. The black horizontal line in both panels show the dividing line above which an accretion disk can form. The colour coding in the legend identifies the 17 progenitor WR+O star systems that are expected to give rise to the BH+O binaries.

4. Comparison with earlier work

Starting from the same 17 WR+O binaries, V20 performed a similar analysis and predicted to find over 200 wind-fed BH HMXBs in the Milky Way. Here, we compare the analysis of V20 with our work and discuss the factors that led to the difference in the predicted numbers.

V20 adopted the accretion disk formation criterion derived by Iben & Tutukov (1996). Iben & Tutukov (1996) primarily modelled accretion onto degenerate white dwarfs from red giant donors and their central idea remained the same in the sense that they assumed that an accretion disk forms when the specific angular momentum of the accreted matter exceeds that of the innermost stable circular orbit radius of the BH. Iben & Tutukov (1996) assumed that the specific angular momentum (j) accreted by the degenerate dwarf from the stellar wind of the giant companion is given by

$$j \sim \Omega_g R_g^2 \left(\frac{R_{\mathrm{acc}}}{a}\right)^2,\tag{18}$$

where Ω_g and R_g are the angular velocity and radius of the giant star, respectively. Iben & Tutukov (1996) defined the accretion radius R_{acc} as

$$R_{\mathrm{acc}} = \frac{2GM_{\mathrm{dd}}}{v_{\mathrm{wind}}^2},\tag{19}$$

where M_{dd} is the mass of the degenerate dwarf. They further assumed that the companion star is tidally locked and the binary mass is dominated by the giant star mass (M_g). Comparing our work and V20, we note the difference of a factor $\sim R_g^2/a^2$ in the definition of specific angular momentum accretion, and the omission of the relative velocity of the BH with respect to the main sequence companion in the definition of the accretion radius. For the wind velocity, Iben & Tutukov (1996) assumed that the wind velocity from the giant companions is given by

$$v'_{\mathrm{wind}} = v'_{\mathrm{esc}} \left(1 - \frac{R_g}{a}\right),\tag{20}$$

where $v'_{\mathrm{esc}} = \sqrt{2GM_g/R_g}$ is the escape velocity from the companion star. Effectively, they assumed that the terminal wind

velocity is equal to the escape velocity from the surface of the star, and $\beta = 1$. They also did not take the Eddington factor into account.

Observational studies of the terminal wind velocities of O stars show that their terminal velocities are larger than their escape velocities, such that the appropriate expression for the wind velocity from O stars is given by Eq. (1) (Vink et al. 2001). However, V20 did not account for the typical wind velocity of the O stars when they adopted the disk formation criterion derived by Iben & Tutukov (1996) for their BH+O systems, that is, the terminal wind velocities used by V20 in their disk formation criterion are underestimated by a factor of 2.6.

Figure 6 shows the evolution of the ratio of the circularisation radius to the radius of the innermost stable circular orbit during the BH+O phase of the 17 progenitor WR+O binaries, with (right panel, Eq. (C.1)) and without (left panel, Eq. (C.3)) taking into consideration the typical O star wind velocity, the mass of the O star, and the orbital velocity in the definition of accretion radius. Comparing the left- and right-hand side panels, we see that in using the appropriate O star wind velocity, the fraction of the BH+O star phase when an accretion disk can form greatly decreases. This shows that the X-ray active lifetime is very sensitive to the wind velocity considered in the disk formation criterion.

From the modified criterion (Eq. (C.1)), we see that only four out of 17 progenitor WR+O binaries are to become wind-fed BH HMXBs for a short period during their lifetime as a BH+O star binary. All of them are close binaries with orbital periods of less than 10 days. The only observed wind-fed BH+O in the Milky Way, Cyg X-1, also has an orbital period of around ~5.6 days (Orosz et al. 2011; Hirsch et al. 2019). From the modified criterion, we expect to find approximately three wind-fed BH HMXBs for the 17 progenitor WR+O binaries instead of 44 as calculated in V20.

In the definition of the accretion radius (Eq. (19)), Iben & Tutukov (1996) only accounted for the wind velocity of the giant star companion and not for the relative velocity between the compact object and the red giant star. We find that this assumption does not play a significant role in most of our BH+O systems as the wind velocity is much larger than the orbital velocity (Fig. B.1). But for systems where the wind

velocity can be comparable to the orbital velocity, the inclusion of the orbital velocity can further reduce the X-ray active lifetime.

Iben & Tutukov (1996) also assumed the total mass of the binary system to be approximately equal to the mass of the giant star companion (see their Eq. (65)). Their work was primarily aimed at white dwarf or neutron star+red giant binary systems and hence this was a reasonable approximation. However, that approximation breaks down for BH+O systems. V20 did not correct for the mass of the BH in the equation of the orbital velocity. The inclusion of the mass of the BH in the expression for orbital velocity reduces the predicted X-ray active lifetime of the BH+O models for systems where the mass of the BH formed is comparable to the mass of the O star, which is most readily seen in Eq. (C.2). For an equal mass BH+O binary, accounting for the mass of the BH introduces a factor of ~1.34 on the right-hand side of Eq. (C.2), which means that the radius of the O star has to be larger for an accretion disk to form, while all other parameters are fixed.

The luminosity of massive O stars can be a finite fraction of its Eddington luminosity (see Table 1). Accounting for this Eddington factor, defined as the ratio of the luminosity of the O star to its Eddington luminosity, in the wind velocity of O stars leads to a decrease in the calculated O star wind velocity. However, in many of our considered WR+O binaries, the Eddington factor of the O star is low (≤0.1). Hence, the inclusion of the Eddington factor does not have a significant effect on the predicted X-ray active lifetime of most of our BH+O models. On the other hand, for the few systems which have Eddington factors ~0.3, accounting for the Eddington factor increased the X-ray active lifetime, but not as significantly so as to compensate for the updated O star terminal wind velocity.

For the X-ray emission from a BH+O model with an accretion disk to be detectable from Earth, V20 assumed a luminosity cut-off of 10^{35} erg s^{-1} for all the 17 systems regardless of their individual distances from Earth. But most of the 17 WR+O binaries considered are not located within 3–4 kpc. In our work, we assume a flux cut-off of ~10^{-11} erg s^{-1} cm^{-2} and take the distance of each source from Earth into consideration individually. The consideration of the individual distances does not affect our results as the calculated X-ray flux is above our flux detection threshold for all the models that are predicted to have an X-ray active phase (Fig. 2).

The end of the BH+O phase in V20 is considered to be the point when the companion star fills its Roche lobe. This can lead to an over-prediction of τ_{Lx} for comparatively wide systems where the O star can complete hydrogen burning and yet not fill its Roche lobe. Since the wind velocity of post-MS stars are low as well, some of these systems in the post-MS phase of the O star can become strong X-ray emitters, but they do not necessarily fall under the class of wind-fed BH HMXBs. Hence, V20 may have over-predicted the X-ray active lifetime for some of the progenitor WR+O binaries by including the post-MS phase.

A recent population synthesis study by Shao & Li (2020) based on the rapid binary evolution code predicted about 10–30 wind-fed BH HMXBs in the Milky Way (see also, Wiktorowicz et al. 2020). The mass loss rate in Vink et al. (2001) was adopted, and the accretion rate was evaluated by the Bondi-Hoyle-Lyttleton accretion model (Bondi & Hoyle 1944; Belczynski et al. 2008). To evaluate the detectability of their BH+O binary models, they also adopted the same threshold for X-ray luminosity at 10^{35} erg/s as V20. We note that they did not take the criterion for the formation of an accretion disk into account. Our work suggests that accretion disks can only exist

for a limited period of the main sequence lifetime of the O stars, which mainly determines the X-ray active lifetime of the BH+O star binaries. Therefore, Shao & Li (2020) have likely overestimated the number of wind-fed BH HMXBs in the Milky Way.

5. Discussion

Here, we discuss the uncertainties in the predicted X-ray active lifetimes of our BH+O binary models.

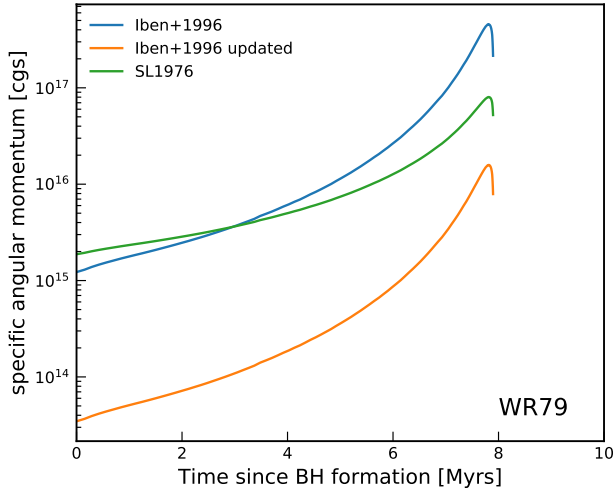### 5.1. Specific angular momentum accretion

The discrepancy between the predicted wind-fed BH HMXB populations of V20 and our work shows that the criterion for accretion disk formation is sensitive to variations of the parameters in the theory. In particular, accounting for a larger O star wind velocity changes the prediction of V20 drastically. More factors such as the accretion efficiency and the approximation of the specific angular momentum carried by the accreted matter introduce further uncertainties for the computation of the X-Ray bright lifetime of the BH+O star binaries (Sect. 3). Livio et al. (1986) and Soker et al. (1986) studied accretion onto compact objects using detailed hydrodynamic simulations and found that while the mass accretion rate is similar to that predicted by the Bondi-Hoyle theory, the amount of specific angular momentum accreted was only a few percent of that predicted by the analytical approximation obtained from the Bondi-Hoyle theory. A similar conclusion was drawn by Ruffert (1999).

Owing to these calculations, El Mellah (2017) adopted the analytical expression for specific angular momentum from Shapiro & Lightman (1976, Eq. (7)), but they introduced an efficiency factor of 1/3 to account for the reduced specific angular momentum accretion found in the detailed numerical hydrodynamic studies. We captured this uncertainty and studied its effects through our efficiency parameter η. Therefore, we need to compare the analytical approximations to the specific angular momentum carried by the accreted matter used in V20 and our work to detailed 3D numerical hydrodynamic simulations in order to assess the reliability of the approximations.

As a preliminary exercise, in Fig. 7, we compare the expression for specific angular momentum carried by the wind matter used in V20 (Eq. (62) of Iben & Tutukov 1996) to the analytical form derived by Shapiro & Lightman (1976) that is assumed in our work. We see that there are significant differences between the two definitions and to the third, which includes the typical O star wind velocity in expression for specific angular momentum carried by the wind matter given by Iben & Tutukov (1996).

Due to the line-deshadowing instability and sub-photospheric turbulence, stellar winds from hot stars are prone to form overdense regions called 'clumps' (Owocki & Rybicki 1984; Owocki et al. 1988; Feldmeier 1995; Grassitelli et al. 2015). These clumps produce stochastic variations in the instantaneous amount of specific angular momentum of the accreted material. These variations take place on time scales of the order of hundreds to thousands of seconds, much shorter than the evolutionary time scales (Grinberg et al. 2017; El Mellah et al. 2020b). For clump sizes derived from first principles (Sundqvist et al. 2018), clumps are small compared to the accretion radius when they reach the orbital separation (El Mellah et al. 2018). As a consequence, they induce a limited peak-to-peak variability. However, when the wind is sufficiently fast, the net amount of angular momentum provided to the flow is so small (and so is the accretion radius) that the serendipitous capture of clumps becomes relatively more important and can

Fig. 7. Comparison of the specific angular momentum of the accreted wind matter used in V20 (Eq. (18), Iben+1996) to the analytical value derived by Shapiro & Lightman (1976) (SL1976) for the stellar and binary parameters of WR79, as a function of the time since BH formation. We also show the decrease in the amount of specific angular momentum carried by the wind when the typical wind velocity for O type stars is introduced in Eq. (18), denoted by 'Iben+1996 updated'.

produce a transient accretion disk. However, in Cygnus X-1, the wind-captured disk is permanent and so far, the only wind-fed HMXB where a transient wind-captured disk has been observed is Vela X-1 (Liao et al. 2020). In the latter case, the disk formation is believed to be associated with variations at the periastron induced by the slightly eccentric orbital motion, rather than with clump capture (Kretschmar et al. 2021). Therefore, including wind clumping is not expected to significantly modify the results obtained in this paper.

5.2. Properties of the WR star companion

In many of the investigated WR+O star binaries, in particular in the shorter-period ones, the WR star likely formed via Roche-lobe overflow from its progenitor O star (e.g., Vanbeveren et al. 1998a; Wellstein & Langer 1999). The companion O star may thus accrete mass from the WR star progenitor, which could lead to properties which are different from those of single O stars. Important properties in this respect are the helium abundance and spin of the mass gaining O star.

An enhancement of the surface helium mass fraction of the mass gainer of a few percent is predicted from conservative (Wellstein & Langer 1999) as well as non-conservative (Petrovic et al. 2005a; Langer et al. 2020) massive binary evolution models. This enrichment leads to a slight overluminosity of the mass gainer (Langer 1992), which may affect the stellar wind properties. However, quantitatively, this effect is not expected to exceed the uncertainty in the average wind properties of O stars (Vink & Sander 2021).

Independent of the mass transfer efficiency, the angular momentum gain of the accretor during the mass transfer is expected to spin up the mass gainer significantly (Packet 1981; Petrovic et al. 2005b; Langer et al. 2020). The observed population of Be/X-ray binaries (Reig 2011) signifies that this spin-up may achieve near-critical rotation, with strong consequences for the mass outflow from the spun-up star, and the mass accretion onto the compact companion. The Galactic and LMC WR+O binaries do indeed also contain rapidly rotating O

stars (Vanbeveren et al. 2018; Shara et al. 2020). However, while faster than average O stars, the analysed WR companions rotate on average with less than 50% of their critical rotational velocity, implying that the centrifugal force remains below 25% of the surface gravity at the stellar equator. Whereas this may lead to a slight wind anisotropy, a disk-like outflow is not expected in this case.

In our analysis above, we adopted a wind velocity of the O star companions as expected for single stars. However, in Be/X-ray binaries (Waters et al. 1988) as well as in supergiant X-ray binaries (Manousakis et al. 2012), abnormally slow stellar winds are observed. While in the first case, this may relate to the stars' extreme rotation, a reduced wind acceleration due to the X-ray irradiation of the stellar atmosphere is thought to be responsible in the latter case (see also, Vilhu et al. 2021). For the conclusions we draw above, the consequences would be small, since neither of the two effects is expected in the majority of the investigated binaries. For the few cases where disk formation and significant X-ray emission is predicted, a slower wind would, however, lead to an increased accretion rate and a higher X-ray luminosity.

5.3. Other uncertainties

The lifetime of the WR+O star binary phase is considered to be constant for all the different considered WR+O binaries, whereas it actually depends on the core helium burning lifetime of the WR star, which in turn depends on the individual masses of the WR star. However, we do not expect this simplifying assumption to affect our predicted number of wind-fed BH HMXBs significantly. The mass of the WR stars at the end of core helium depletion is also uncertain due to the uncertainty about the mass loss rate during the WR phase (Neijssel et al. 2021). In both works, that is ours and V20, it is assumed that the properties of the WR stars do not change after core helium depletion. However, it has been shown recently (Laplace et al. 2020) that WR stars that have an outer hydrogen envelope may expand after helium depletion and the binary can undergo another mass transfer phase before core collapse (see also Laplace et al. 2021). Therefore, the formation of wind-fed BH HMXBs needs further investigation, both using detailed binary evolution models that calculate the binary evolution up to the core collapse of the WR star as well as into accurate modelling of the physics of accretion onto BHs.

We have shown (Fig. A.1) that the predicted mass accretion rates calculated for the anticipated BH+O binaries are much lower than the Eddington mass accretion rates. Hence, we do not consider super-Eddington accretion to be relevant for our work. Due to the same reason, the X-ray emission should be isotropic and we do not need to consider the case of beaming (King 2008). LOBSTER eye telescopes can reach a flux cut-off of 10^{-12} erg s^{-1} cm^{-2} (Priedhorsky et al. 1996; Hudec et al. 2007). The recently launched eROSITA X-ray telescope is stated to have a flux detection threshold of $\sim 10^{-14}$ erg s^{-1} cm^{-2} (Merloni et al. 2012) in the average all-sky survey mode. However, changing the flux limit to these lower values does not change our predicted X-ray active lifetime since once a wind-captured disk can form around the BH, the expected to X-ray flux at Earth is higher than 10^{-11} erg s^{-1} cm^{-2} (Fig. 2). On the other hand, if there is significant extinction at X-ray wavelengths in the Galactic plane, our predicted X-ray active lifetime of the BH+O binary models can get reduced.

The predicted X-ray luminosity of an accreting BH in our models is a few percent of the Eddington luminosity. In such a case, the X-ray spectrum can switch from a soft state to a

hard state and the X-ray emission becomes radiatively inefficient (Yuan & Narayan 2014). This is well-described by a distended and tenuous advection-dominated accretion flow (ADAF, see Narayan & Yi 1994, 1995a,b). In this accretion regime, the bulk of the accretion energy is carried by the accreting gas in the form of thermal energy, which can vanish through the event horizon of the BH. Hence, the BHs in the ADAF regime can be fainter by a factor of ~100–1000 (Narayan & McClintock 2008). In such a case, we do not expect the binary to be detectable in X-rays. The inclusion of this effect can only reduce our prediction of the X-ray active lifetime during the BH+O phase.

6. Conclusion

WR+O binaries are expected to be progenitors of BH+O binaries. V20 investigated 17 galactic WR+O star binaries and predicted that there should be more than 200 wind-fed BH HMXBs in the Milky Way, while only one has been observed. They concluded that BHs receive much higher natal kick velocities or WR stars explode with supernova explosions to form neutron stars, which lead to a break-up of the binary systems.

We applied a similar methodology as in V20 with an improved analytical criterion to study the formation of accretion disks around BHs in BH+O binaries and the detectability of X-ray emission from such systems. We also investigated the effect of uncertain physics parameters, such as the β value in the O star wind velocity law, the efficiency of angular momentum accretion (η) and the spin of the BH ($\gamma_{\pm}$) on the predicted number of wind-fed BH HMXBs. We find that this calculated number is sensitive to plausible variations in the assumed parameters.

For our fiducial parameter set $(\beta, \eta, \gamma) = (1, 1/3, 1)$ (see Sect. 3, and Fig. 1), we predict only approximately two to three wind-fed BH HMXBs based on the 17 progenitor WR+O systems. While we still over-predict the number of wind-fed BH HMXBs, accounting for the theoretical and observational biases in the population of WR+O binaries (see Sect. 2.1) suggest that we should expect approximately two to three wind-fed BH HMXBs in the entire Milky Way. We remind the reader that only one wind-fed BH+O X-ray binary has been observed (Cyg X-1).

We then revisited the derivation of the accretion disk formation criterion used by V20 and found that, in particular, the assumed O star wind velocity was underestimated. Accounting for the appropriate O star wind velocity (Vink et al. 2001), we find most of BH+O binary models will have negligible X-ray bright lifetimes due to the absence of an accretion disk around the BH (see Fig. 6). As such, any conclusion drawn from the seemingly discrepant number of observed WR+O binaries and wind-fed BH HMXBs has to be re-evaluated.

Furthermore, our analysis shows that a high BH spin parameter can lead to significantly longer and brighter X-ray phases in wind-accreting BH+O binaries. The corresponding bias in detecting such binaries with rapidly spinning BHs may help to alleviate the tension between the rather low BH spin values generally predicted from binary stellar evolution models (Qin et al. 2018) and the high BH spin values observationally deduced from BH+O binaries in the Local Group (Qin et al. 2019).

We conclude that high BH formation kicks are not necessary to understand the number discrepancy between the populations of observed WR+O binaries and wind-fed BH HMXBs in the Milky Way. With our current understanding of O star wind velocities, we have shown that possibly the vast majority of Galactic BH+O star binaries may not form BH accretion disks and hence remain undetected in X-Ray surveys. Recent studies have shown that the *Gaia* satellite offers an excellent opportunity

to observe such X-ray quiet BH+O binaries via periodic astrometric variations (Breivik et al. 2017; Mashian & Loeb 2017; Yalinewich et al. 2018; Yamaguchi et al. 2018; Andrews et al. 2019). Furthermore, BH+O binaries can also be detected from photometric variability of the O star induced by the BH companion (Zucker et al. 2007; Masuda & Hotokezaka 2019), or spectroscopically via the periodic shift in radial velocity of the O star.

References

Abbott, B. P., Abbott, R., Abbott, T. D., et al. 2016, Phys. Rev. X, 6, 041015
Abbott, B. P., Abbott, R., Abbott, T. D., et al. 2019, Phys. Rev. X, 9, 031040
Andrews, J. J., Breivik, K., & Chatterjee, S. 2019, ApJ, 886, 68
Bachetti, M., Harrison, F. A., Walton, D. J., et al. 2014, Nature, 514, 202
Balbus, S. A., & Hawley, J. F. 1991, ApJ, 376, 214
Belczynski, K., Kalogera, V., Rasio, F. A., et al. 2008, ApJS, 174, 223
Belczynski, K., Wiktorowicz, G., Fryer, C. L., Holz, D. E., & Kalogera, V. 2012, ApJ, 757, 91
Belczynski, K., Buonanno, A., Cantiello, M., et al. 2014, ApJ, 789, 120
Belczynski, K., Repetto, S., Holz, D. E., et al. 2016, ApJ, 819, 108
Belczynski, K., Klencki, J., Fields, C. E., et al. 2020, A&A, 636, A104
Bondi, H. 1952, MNRAS, 112, 195
Bondi, H., & Hoyle, F. 1944, MNRAS, 104, 273
Bradt, H. V., Swank, J. H., & Rothschild, R. E. 1991, Adv. Space Res., 11, 243
Brandt, W. N., Podsiadlowski, P., & Sigurdsson, S. 1995, MNRAS, 277, L35
Braun, H., & Langer, N. 1995, A&A, 297, 483
Breivik, K., Chatterjee, S., & Larson, S. L. 2017, ApJ, 850, L13
Chandra, A. D., Roy, J., Agrawal, P. C., & Choudhury, M. 2020, MNRAS, 495, 2664
Crowther, P. A. 2015, in Wolf-Rayet Stars, eds. W. R. Hamann, A. Sander, & H. Todt, 21
Crowther, P. A. 2019, Galaxies, 7, 88
Davidson, K., & Ostriker, J. P. 1973, ApJ, 179, 585
de Mink, S. E., & Belczynski, K. 2015, ApJ, 814, 58
de Mink, S. E., & Mandel, I. 2016, MNRAS, 460, 3545
Dhawan, V., Mirabel, I. F., Ribó, M., & Rodrigues, I. 2007, ApJ, 668, 430
du Buisson, L., Marchant, P., Podsiadlowski, P., et al. 2020, MNRAS, 499, 5941
Edgar, R. 2004, New Astron. Rev., 48, 843
Ekström, S., Georgy, C., Eggenberger, P., et al. 2012, A&A, 537, A146
El Mellah, I. 2017, ArXiv e-prints [arXiv:1707.09165]
El Mellah, I., & Casse, F. 2017, MNRAS, 467, 2585
El Mellah, I., Sundqvist, J. O., & Keppens, R. 2018, MNRAS, 475, 3240
El Mellah, I., Bolte, J., Decin, L., Homan, W., & Keppens, R. 2020a, A&A, 637, A91
El Mellah, I., Grinberg, V., Sundqvist, J. O., Driessen, F. A., & Leutenegger, M. A. 2020b, A&A, 643, A9
Event Horizon Telescope Collaboration (Akiyama, K., et al.) 2019, ApJ, 875, L1
Farr, W. M., Sravan, N., Cantrell, A., et al. 2011, ApJ, 741, 103
Feldmeier, A. 1995, A&A, 299, 523
Fragos, T., Willems, B., Kalogera, V., et al. 2009, ApJ, 697, 1057
Frank, J., King, A., & Raine, D. J. 2002, Accretion Power in Astrophysics (Third Edition)
Fujita, Y., Inoue, S., Nakamura, T., Manmoto, T., & Nakamura, K. E. 1998, ApJ, 495, L85
Fürst, F., Walton, D. J., Harrison, F. A., et al. 2016, ApJ, 831, L14
Gou, L., McClintock, J. E., Reid, M. J., et al. 2011, ApJ, 742, 85
Grassitelli, L., Fossati, L., Simón-Díaz, S., et al. 2015, ApJ, 808, L31
Grinberg, V., Hell, N., El Mellah, I., et al. 2017, A&A, 608, A143
Groenewegen, M. A. T., & Lamers, H. J. G. L. M. 1989, A&AS, 79, 359
Hirsch, M., Hell, N., Grinberg, V., et al. 2019, A&A, 626, A64
Hobbs, G., Lorimer, D. R., Lyne, A. G., & Kramer, M. 2005, MNRAS, 360, 974
Hudec, R., Pina, L., Šimon, V., et al. 2007, Nucl. Phys. B Proc. Suppl., 166, 229
Iben, I. J., & Tutukov, A. V. 1996, ApJS, 105, 145
Illarionov, A. F., & Sunyaev, R. A. 1975, A&A, 39, 185
In't Zand, J. J., Priedhorsky, W. C., Moss, C. E., et al. 1994, in Advances in Multilayer and Grazing Incidence X-Ray/EUV/FUV Optics, eds.

R. B. Hoover, & A. B. Walker, Society of Photo-Optical Instrumentation Engineers (SPIE) Conference Series, 2279, 458
Israel, G. L., Belfiore, A., Stella, L., et al. 2017, Science, 355, 817
King, A. R. 2008, MNRAS, 385, L113
Kremer, K., Lu, W., Rodriguez, C. L., Lachat, M., & Rasio, F. A. 2019, ApJ, 881, 75
Kretschmar, P., El Mellah, I., Martínez-Núñez, S., et al. 2021, A&A, 652, A95
Kruckow, M. U., Tauris, T. M., Langer, N., Kramer, M., & Izzard, R. G. 2018, MNRAS, 481, 1908
Lamers, H. J. G. L. M., Snow, T. P., & Lindholm, D. M. 1995, ApJ, 455, 269
Langer, N. 1992, A&A, 265, L17
Langer, N. 2012, ARA&A, 50, 107
Langer, N., Schürmann, C., Stoll, K., et al. 2020, A&A, 638, A39
Laplace, E., Götberg, Y., de Mink, S. E., Justham, S., & Farmer, R. 2020, A&A, 637, A6
Laplace, E., Justham, S., Renzo, M., et al. 2021, A&A, submitted [arXiv:2102.05036]
Liao, Z., Liu, J., Zheng, X., & Gou, L. 2020, MNRAS, 492, 5922
Livio, M., Soker, N., de Kool, M., & Savonije, G. J. 1986, MNRAS, 222, 235
Mandel, I., & Müller, B. 2020, MNRAS, 499, 3214
Mandel, I., Müller, B., Riley, J., et al. 2021, MNRAS, 500, 1380
Manousakis, A., Walter, R., & Blondin, J. M. 2012, A&A, 547, A20
Marchant, P., Langer, N., Podsiadlowski, P., Tauris, T. M., & Moriya, T. J. 2016, A&A, 588, A50
Mashian, N., & Loeb, A. 2017, MNRAS, 470, 2611
Masuda, K., & Hotokezaka, K. 2019, ApJ, 883, 169
Mennekens, N., & Vanbeveren, D. 2014, A&A, 564, A134
Merloni, A., Predehl, P., Becker, W., et al. 2012, ArXiv e-prints [arXiv:1209.3114]
Miller-Jones, J. C. A., Bahramian, A., Orosz, J. A., et al. 2021, Science, 371, 1046
Minniti, D., Contreras Ramos, R., Alonso-García, J., et al. 2015, ApJ, 810, L20
Mirabel, I. F., & Rodrigues, I. 2003, Science, 300, 1119
Narayan, R., & Yi, I. 1994, ApJ, 428, L13
Narayan, R., & Yi, I. 1995a, ApJ, 444, 231
Narayan, R., & Yi, I. 1995b, ApJ, 452, 710
Narayan, R., & McClintock, J. E. 2008, New Astron. Rev., 51, 733
Neijssel, C. J., Vinciguerra, S., Vigna-Gómez, A., et al. 2021, ApJ, 908, 118
Novikov, I. D., & Thorne, K. S. 1973, in Black Holes (Les Astres Occlus), 343
O'Connor, E., & Ott, C. D. 2011, ApJ, 730, 70
Orosz, J. A., McClintock, J. E., Aufdenberg, J. P., et al. 2011, ApJ, 742, 84
O'Shaughnessy, R., Kim, C., Kalogera, V., & Belczynski, K. 2008, ApJ, 672, 479
Owocki, S. P., & Rybicki, G. B. 1984, ApJ, 284, 337
Owocki, S. P., Castor, J. I., & Rybicki, G. B. 1988, ApJ, 335, 914
Özel, F., Psaltis, D., Narayan, R., & McClintock, J. E. 2010, ApJ, 725, 1918
Packet, W. 1981, A&A, 102, 17
Perets, H. B., Li, Z., Lombardi, J. C., Jr., & Stephen, R. M., Jr. 2016, ApJ, 823, 113
Petrovic, J., Langer, N., & van der Hucht, K. A. 2005a, A&A, 435, 1013
Petrovic, J., Langer, N., Yoon, S. C., & Heger, A. 2005b, A&A, 435, 247
Priedhorsky, W. C., Peele, A. G., & Nugent, K. A. 1996, MNRAS, 279, 733
Puls, J., Kudritzki, R. P., Herrero, A., et al. 1996, A&A, 305, 171
Qin, Y., Fragos, T., Meynet, G., et al. 2018, A&A, 616, A28
Qin, Y., Marchant, P., Fragos, T., Meynet, G., & Kalogera, V. 2019, ApJ, 870, L18
Quast, M., Langer, N., & Tauris, T. M. 2019, A&A, 628, A19
Reig, P. 2011, Ap&SS, 332, 1
Repetto, S., Davies, M. B., & Sigurdsson, S. 2012, MNRAS, 425, 2799
Repetto, S., Igoshev, A. P., & Nelemans, G. 2017, MNRAS, 467, 298
Rosslowe, C. K., & Crowther, P. A. 2015, MNRAS, 447, 2322
Ruffert, M. 1999, A&A, 346, 861
Scarcella, F., Gaggero, D., Connors, R., et al. 2021, MNRAS, 505, 4036
Schweickhardt, J., Schmutz, W., Stahl, O., Szeifert, T., & Wolf, B. 1999, A&A, 347, 127
Shakura, N. I., & Sunyaev, R. A. 1973, A&A, 500, 33
Shao, Y., & Li, X.-D. 2020, ApJ, 898, 143
Shapiro, S. L., & Lightman, A. P. 1976, ApJ, 204, 555
Shapiro, S. L., & Teukolsky, S. A. 1983, Black holes, white dwarfs, and neutron stars : the physics of compact objects
Shara, M. M., Crawford, S. M., Vanbeveren, D., et al. 2020, MNRAS, 492, 4430
Soker, N., Livio, M., de Kool, M., & Savonije, G. J. 1986, MNRAS, 221, 445
Stevenson, S., Ohme, F., & Fairhurst, S. 2015, ApJ, 810, 58
Sukhbold, T., Woosley, S. E., & Heger, A. 2018, ApJ, 860, 93
Sundqvist, J. O., Owocki, S. P., & Puls, J. 2018, A&A, 611, A17
Tsuna, D., Kawanaka, N., & Totani, T. 2018, MNRAS, 477, 791
Ugliano, M., Janka, H.-T., Marek, A., & Arcones, A. 2012, ApJ, 757, 69
van den Heuvel, E. P. J., Portegies Zwart, S. F., & de Mink, S. E. 2017, MNRAS, 471, 4256
van der Hucht, K. A. 2001, VizieR Online Data Catalog:III/215
van der Hucht, K. A. 2006, A&A, 458, 453
Vanbeveren, D., De Donder, E., Van Bever, J., Van Rensbergen, W., & De Loore, C. 1998a, New Astron., 3, 443
Vanbeveren, D., De Loore, C., & Van Rensbergen, W. 1998b, A&ARv, 9, 63
Vanbeveren, D., Mennekens, N., Shara, M. M., & Moffat, A. F. J. 2018, A&A, 615, A65
Vanbeveren, D., Mennekens, N., van den Heuvel, E. P. J., & Van Bever, J. 2020, A&A, 636, A99
Vilhu, O., Kallman, T. R., Koljonen, K. I., & Hannikainen, D. C. 2021, A&A, 649, A176
Vink, J. S., & Sander, A. A. C. 2021, MNRAS, 504, 2051
Vink, J. S., de Koter, A., & Lamers, H. J. G. L. M. 2001, A&A, 369, 574
Waters, L. B. F. M., van den Heuvel, E. P. J., Taylor, A. R., Habets, G. M. H. J., & Persi, P. 1988, A&A, 198, 200
Wellstein, S., & Langer, N. 1999, A&A, 350, 148
Wiktorowicz, G., Lu, Y., Wyrzykowski, Ł., et al. 2020, ApJ, 905, 134
Willems, B., Henninger, M., Levin, T., et al. 2005, ApJ, 625, 324
Wong, T.-W., Valsecchi, F., Fragos, T., & Kalogera, V. 2012, ApJ, 747, 111
Wood, K. S., Meekins, J. F., Yentis, D. J., et al. 1984, ApJS, 56, 507
Woosley, S. E. 2019, ApJ, 878, 49
Woosley, S. E., Sukhbold, T., & Janka, H. T. 2020, ApJ, 896, 56
Wyrzykowski, Ł., & Mandel, I. 2020, A&A, 636, A20
Yalinewich, A., Beniamini, P., Hotokezaka, K., & Zhu, W. 2018, MNRAS, 481, 930
Yamaguchi, M. S., Kawanaka, N., Bulik, T., & Piran, T. 2018, ApJ, 861, 21
Yuan, F., & Narayan, R. 2014, ARA&A, 52, 529
Zhao, X., Gou, L., Dong, Y., et al. 2021, ApJ, 908, 117
Zucker, S., Mazeh, T., & Alexander, T. 2007, ApJ, 670, 1326

Appendix A: Mass accretion rate
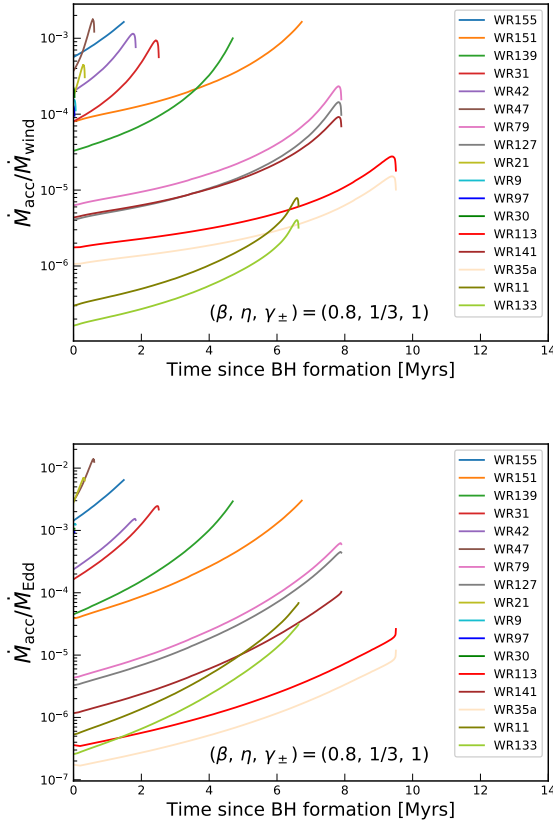
Fig. A.1. Comparison of mass accretion rate $\dot{M}_{acc}$, mass loss rate of the O star $\dot{M}_{wind}$, and Eddington accretion rate of the BH $\dot{M}_{Edd}$ during the BH+O binary phase modelled from the 17 observed progenitor WR+O binaries for $(\beta,\eta,\gamma_\pm) = (0.8,1/3,1)$. The *upper and lower panels* present $\dot{M}_{acc}/\dot{M}_{wind}$ and $\dot{M}_{acc}/\dot{M}_{Edd}$, respectively. The colour coding in the legend denotes the 17 WR+O systems that are expected to form BH+O binaries.

Figure A.1 presents the comparison among the mass accretion rate, mass loss rate from the O star, and the Eddington accretion rate of the BH. The Eddington mass accretion rate is defined as

$$\dot{M}_{Edd} = \frac{L_{Edd}\,R_{ISCO}}{G\,M_{BH}}, \tag{A.1}$$

where R_{ISCO} is the radius of the innermost stable circular orbit around BH, G is the gravitational constant, M_{BH} is the mass of BH, and L_{Edd} is the Eddington luminosity, evaluated by

$$L_{Edd} = L_\odot \frac{65335}{1+X} \frac{M_{BH}}{M_\odot}, \tag{A.2}$$

where X is the hydrogen abundance in the accreted material, which is expected to be the hydrogen abundance at the surface of the donor star.

The upper panel shows that over 99% of wind material escapes the BH+O system, which means the typical timescale of orbital evolution $|a/\dot{a}|$ is longer than that of mass loss from the O star $|M_O/\dot{M}_O|$ (El Mellah et al. 2020a). The mass loss rate of the O star is about 10^{-7}–10^{-6} $M_\odot$ yr^{-1}. Therefore the orbital period of BH+O binary models can be safely treated as constant. The lower panel shows that the $\dot{M}_{acc}$ is far below $\dot{M}_{Edd}$. Hence super-Eddington winds from the accretor do not occur in our models.

Appendix B: Ratio of O star wind velocity to the orbital velocity
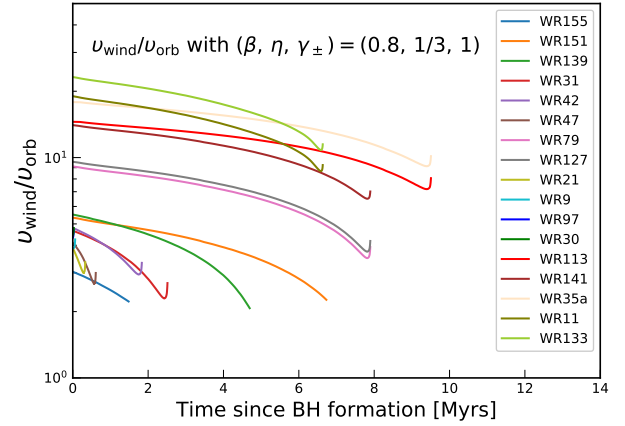
Fig. B.1. Evolution of the ratio of the O star wind velocity to the orbital velocity during the BH+O binary phase modelled from the 17 observed progenitor WR+O binaries for $(\beta,\eta,\gamma_\pm) = (0.8,1/3,1)$. The colour coding in the legend denotes the 17 WR+O systems that are expected to form BH+O binaries.

Figure B.1 presents the ratio wind velocity divided by orbital velocity $\upsilon_{wind}/\upsilon_{orb}$. The specific angular momentum obtained by SL76 only works in the fast-wind regime ($\upsilon_{wind}/\upsilon_{orb} > 1$), which is consistent with our model that we always have $\upsilon_{wind} > \upsilon_{orb}$.

Appendix C: Modifications on the disk formation criterion from Iben & Tutukov (1996)

Adopting the specific angular momentum as shown in Eq. (18) (Iben & Tutukov 1996) as well as the updated wind velocity from Eqs. (1)–(3), the ratio of R_{disk}/R_{ISCO} is

$$\frac{R_{disk}}{R_{ISCO}} = \frac{8}{3} \frac{(R_O/a)^4}{(1+q)^2} \left(\frac{\upsilon_{orb}}{c}\right)^{-2} \left(1 + \frac{\upsilon_{wind}^2}{\upsilon_{orb}^2}\right)^{-4} \gamma_\pm^{-1}, \tag{C.1}$$

where $q = M_O/M_{BH}$. Comparing this with Eq. (10), the efficiency parameter η for angular momentum accretion is replaced by $(R_O/a)^4$. For the WR+O binaries considered in this work, $(R_O/a)^4$ is much smaller than η. Hence, we expect that this updated criterion Eq. (C.1) predicts fewer wind-fed BH HMXBs than that by Eq. (10).

Taking the β parameter for wind velocity law and the BH spin parameter $\gamma_\pm$ to be equal to 1 in Eq. (C.1), the accretion disk formation criterion (Eq. (4)) can be rewritten as

$$\frac{R_O}{a} \geq \left(2.6\sqrt{1-\Gamma}\right)^{8/7} \left(\frac{R_{ISCO}}{R_O}\right)^{1/7} (1+q)^{3/7} \left(1 - \frac{R_O}{a}\right)^{8/7}. \tag{C.2}$$

The wind velocity defined by Iben & Tutukov (1996) does not take into account the effect of the Eddington factor on the escape velocity and it underestimates the ratio of the terminal velocity to the escape velocity. Furthermore, assuming that the binary mass is equal to the mass of the non-compact companion, we obtain

$$\frac{R_{disk}}{R_{ISCO}} = \frac{8}{3} \left(\frac{R_O}{a}\right)^4 q^{-2} \left(\frac{\upsilon'_{orb}}{c}\right)^{-2} \left(\frac{\upsilon'_{wind}^2}{\upsilon'_{orb}^2}\right)^{-4}, \tag{C.3}$$

where υ'_{orb} is the orbital velocity assuming the binary mass is equal to the donor star mass and υ'_{wind} is the wind velocity

defined by Iben & Tutukov (1996), that is Eq. (20). Combining Eqs. (4) and (C.3) leads to the disk formation criterion obtained by Iben & Tutukov (1996) (c.f. Eq. (2) of V20),

$$\frac{R_O}{a} \geq \left(\frac{R_{ISCO}}{R_O}\right)^{1/7} q^{3/7} \left(1 - \frac{R_O}{a}\right)^{8/7}, \quad \text{(C.4)}$$

which makes the disk formation much easier than Eq. (C.2). For example, in the BH+O model corresponding to WR 155, with $\Gamma = 0.16$ and $q = 2.5$ at the BH formation time, taking $\gamma_{\pm} = 1$ and $\beta = 0.8$, adopting the typical O star wind velocity reduces the ratio of R_{disk}/R_{ISCO} obtained from Eq. (C.1) by three orders of magnitude in comparison to that predicted from Eq. (C.3).

List of Publications

First author papers, refereed

I **Koushik Sen**, Rodrigo Fernandez & Aristotle Socrates — *2018, MNRAS, 477, 2286S* — Subphotospheric fluctuations in magnetized radiative envelopes: contribution from unstable magnetosonic waves.

II **K. Sen**, X.-T. Xu, Norbert Langer, Ileyk El Mellah, Christoph Schürmann & Martin Quast — *2021, A&A, 652, A138* — X-ray emission from BH+O star binaries expected to descend from the observed galactic WR+O binaries.

III **K. Sen**, N. Langer, P. Marchant, A. Menon, S. E. de Mink, C. Schümann, L. Mahy, H. Sana, A. Schootemeijer, K. Nathaniel, X.-T. Xu, C. Wang and B. Hastings — *2022, A&A, 659, A98* — Detailed models of interacting short-period massive binary stars.

Second-or-later author papers, refereed

i J. Puls, F. Najarro, J. O. Sundqvist, & **K. Sen** — *2020, A&A, 642, A172* — Atmospheric NLTE models for the spectroscopic analysis of blue stars with winds

ii Athira Menon, Norbert Langer, Selma E de Mink, Stephen Justham, **Koushik Sen**, Dorottya Szécsi, Alex de Koter, Michael Abdul-Masih, Hugues Sana, Laurent Mahy & Pablo Marchant — *2021, MNRAS, 507, 5013* — Detailed evolutionary models of massive contact binaries I. Model grids and synthetic populations for the Magellanic Clouds

iii N. Langer, C. Schürmann, K. Stoll, P. Marchant, D. J. Lennon, L. Mahy, S. E. de Mink, M. Quast, W. Riedel, H. Sana, P. Schneider, A. Schootemeijer, C. Wang, L. A. Almeida, J. M. Bestenlehner, J. Bodensteiner, N. Castro, S. Clark, P. A. Crowther, P. Dufton, C. J. Evans, L. Fossati, G. Grafener, L. Grassitelli, N. Grin, B. Hastings, A. Herrero, A. de Koter, A. Menon, L. Patrick, J. Puls, M. Renzo, A. A. C. Sander, F. R. N. Schneider, **K. Sen**, T. Shenar, S. Simon-Dias, T. M. Tauris, F. Tramper, J. S. Vink & X.-T. Xu — *2020, A&A, 638, A39* — Properties of OB star-black hole systems derived from detailed binary evolution models

Curriculum Vitae

Personal Details

Name	Koushik Sen
Date of Birth	13-07-1995
Email	ksen@astro.uni-bonn.de, senkoushik1995@gmail.com

Education

2013–2018	Integrated BSc & MSc in Physics, Indian Institute of Technology Kharagpur, West Bengal, India.
2018–2022	PhD in Astrophysics, Rheinische Friedrich-Wilhelms-Universität, Bonn, Germany.

Professional Experience

2016	Summer Research Intern at Universitäts-Sternwarte München, Bavaria, Germany.
2017	Summer Research Intern at the University of Alberta, Canada.
2018	Summer Research Intern at the Max Planck Institute for Quantum Optics, Garching, Germany.
2018-present	Online Tutor at Chegg India, Physics, New Delhi, India.
2018-2022	Doctoral work at the University of Bonn, Germany.
2019-2021	Teaching assistant for various Astrophysics and Computer Programming graduate university courses. Rheinische Friedrich-Wilhelms-Universität, Bonn, Germany.

Languages

Bengali	Native speaker
English	Fluent
Hindi	Intermediate
German	Basic